Development of Molecular Photosensitizers for Luminescence Sensing and Catalytic Applications

A Thesis submitted to the

UPES

For the Award of

Doctor of Philosophy

in

Chemistry

By

Sudhanshu Naithani

July 2025

Supervisor

Dr. Sushil Kumar

Co-Supervisor

Dr. Tapas Goswami

Department of Chemistry

School of Advanced Engineering (SOAE)

UPES

Dehradun- 248007: Uttarakhand, INDIA

Development of Molecular Photosensitizers for Luminescence Sensing and Catalytic Applications

A Thesis submitted to the

UPES

For the Award of

Doctor of Philosophy

in

Chemistry

By

Sudhanshu Naithani

July 2025

Supervisor

Dr. Sushil Kumar

Sr. Associate Professor

School of Advanced Engineering, UPES

Co-Supervisor

Dr. Tapas Goswami

Sr. Associate Professor

School of Advanced Engineering, UPES

Department of Chemistry

School of Advanced Engineering (SOAE)

UPES

Dehradun- 248007: Uttarakhand, INDIA

DECLARATION

I declare that the thesis entitled "**Development of molecular photosensitizers for luminescence sensing and catalytic applications**" has been prepared by me under the guidance of **Dr. Sushil Kumar** (Supervisor), Sr. Associate Professor, Department of Chemistry, UPES, Dehradun and **Dr. Tapas Goswami** (Co-supervisor), Sr. Associate Professor, Department of Chemistry, UPES, Dehradun. No part of this abstract has formed the basis for the award of any degree or fellowship previously.

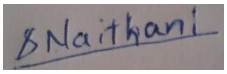

Sudhanshu Naithani
Department of Chemistry, SoAE
UPES, Dehradun
248007

UPES
UNIVERSITY OF TOMORROW

Great Place To Work. Certified FEB 2025 - FEB 2026 INDIA

CERTIFICATE

I certify that **Sudhanshu Naithani** has prepared his thesis entitled **"Development of molecular photosensitizers for luminescence sensing and catalytic applications"** for the award of PhD degree from the University under my guidance. He has carried out the work at the Department of Chemistry, UPES, Dehradun.

Signature of Supervisor 15.07.25

Name of Supervisor: **Dr. Sushil Kumar**
Department: Chemistry
Designation: Sr. Associate Professor
School of Advanced Engineering, UPES, Dehradun, INDIA
Date:

Signature of Co-supervisor 15/07/25

Name of Co-supervisor: **Dr. Tapas Goswami**
Department: Chemistry
Designation: Sr. Associate Professor
School of Advanced Engineering, UPES, Dehradun, INDIA
Date:

ABSTRACT

Small analytes, such as metal ions and anions, are vital to human health, material science, industrial applications, and biological systems. However, their improper use and mishandling have led to serious environmental contamination, particularly in soil and water bodies. This highlights the need for highly selective and efficient detection methods to monitor these analytes in biological and environmental samples, ensuring both human and ecological safety. Optical sensing, particularly fluorescence-based molecular probes, has emerged as a powerful approach due to its simplicity, rapid response, high sensitivity, and cost-effectiveness. By integrating suitable receptor and signaling units, these probes hold significant promise for applications across chemical, biological, and environmental disciplines. In this context, the current research work explores the development of new molecular probes for their potential applications in the optical detection of such analytes, as well as in catalysis, to address critical environmental and biological challenges.

To illustrate, a dual-functional naphthalene-derived Schiff base (**NpSb**) probe has been synthesized and evaluated for its fluorescence and chromogenic response to metal ions. It demonstrated selective recognition of Al^{3+} and Zn^{2+} in an aqueous-organic solvent system, producing a "turn-on" fluorescence response *via* the chelation-enhanced fluorescence (CHEF) effect. The detection limits for Al^{3+} and Zn^{2+} were determined to be 38.0 nM and 43.0 nM, respectively, with binding constants of 1.18×10^6 M^{-1} and 3.5×10^5 M^{-1}. Additionally, **NpSb** functioned as a colorimetric sensor for Al^{3+}, inducing a visible color change from colorless to pale green. The binding mechanism was confirmed through ESI-mass, Job's plot, NMR, and DFT studies, while reversibility experiments with F^- and EDTA facilitated the construction of logic gate. **NpSb** was successfully applied for Al^{3+} detection in real samples, including tap water, distilled water, and soil samples.

Expanding on this approach, a pyridyl-benzimidazole based luminescent probe (**RSB1**) has been developed for the selective detection of

perchlorate (ClO_4^-) ions. **RSB1** exhibited high selectivity for ClO_4^- in an aqueous-acetonitrile system, even in the presence of potential interferents. It displayed a "turn-on" fluorescence response, with enhanced emission at 363 nm upon excitation at 300 nm. The detection limit and binding constant were determined to be 0.121 μM and 2.6×10^5 M^{-1}, respectively. The binding mechanism was validated using Job's plot, NMR, and DFT analyses, and the probe was effectively employed for perchlorate detection in real samples, including tap water, distilled water, and soil.

Furthermore, a monometallic Ru(II) complex (**Ru-1**), incorporating an imidazo-phenanthroline moiety, has been designed and developed as a highly selective luminescent probe for CN^- detection in pure water. **Ru-1** also exhibited sensing capabilities for F^-, AcO^-, and $H_2PO_4^-$ when pure acetonitrile was chosen as a solvent. The binding constant and detection limit for CN^- were determined to be 3.05×10^6 M^{-1} and 12.8 nM, respectively. The high selectivity of **Ru-1** for CN^- was attributed to the proximity of its N-H site to the Ru(II) center and its pronounced acidity. Job's plot and DFT analyses further confirmed the binding mechanism. Time-resolved fluorescence (TRF) spectroscopy was conducted to investigate cyanide-induced emission lifetime changes. To explore practical applicability, **Ru-1** was incorporated into paper-based strips capable of detecting CN^- in the mM range under 365 nm light illumination. The probe was successfully applied for CN^- detection in human breast cancer MCF-7 cell lines and in natural food sources such as apple seeds and sprouting potatoes.

In the field of photocatalysis, a bioinspired heterobimetallic photocatalyst, $\mathbf{Ru^{II}_{phot}–Cu^{II}_{cat}}$, was developed for visible-light-driven C-H bond oxidation of hydrocarbons using O_2 as the oxygen source. The Ru^{II} center efficiently absorbed visible light at 460 nm, facilitating electron transfer to the Cu^{II} center and generating a catalytically active high-valent copper-oxo species. This oxo species enabled a range of oxidation reactions in the presence of triethanolamine (TEOA) as a sacrificial electron donor.

Overall, this thesis presents a comprehensive study on the design and application of novel optical cation/anion sensing probes and photocatalysts, offering significant contributions to advancements in environmental and biological technologies.

ACKNOWLEDGEMENT

First of all, I would like to express my sincere gratitude to my Ph.D supervisors, **Dr. Sushil Kumar** and **Dr. Tapas Goswami**, for their guidance and encouragement throughout this journey. Their support has been instrumental in helping me to achieve my research goals, and their expertise has significantly influenced my academic growth.

I am also thankful to **Dr. Ranjeet Kumar Brajpuriya** (Cluster Head), **Dr. Shalendra Kumar**, and **Dr. Bhawna Yadav Lamba** (Ph.D Coordinators) for their constructive feedback, which has strengthened and refined my research. I deeply appreciate **Dr. Pankaj Kumar** (Associate Dean) for continuous guidance and helping me to attain SRF scholarship. I am grateful to my DRC members, Dr. Sravendra Rana, Dr. Shikha Wadhwa, Dr. Bhawna Yadav Lamba and Dr. Subhankar Das, for their valuable feedback and guidance, which played a key role in shaping my research. I am also thankful to Dr. Franck Thetiot, Dr. Jimmy Mangalam, Dr. Ritesh Dubey, Dr. Samar Layek, Dr. Parteek Prasher and Dr. Tridib Kumar Sinha for their insightful discussions and constructive suggestions, which helped to improve my work.

The support of my colleagues and friends in the lab has been invaluable throughout this journey. I am truly grateful to Vikas Yadav, Nidhi Goswami, Pooja Sharma, Sandeep Singh, Anjali Varshney, Udisha Duhan, and Heena for their thoughtful discussions, and steady support. I also acknowledge Dr. Devendra Rawat, Mr. Charu Chandra Pant, Mr. Tijendra Kumar, Mr. Keshav Kumar Surya, Mr. Abhishek Goel, and Ms. Neeta Rawat for their technical assistance throughout the experimental work. My sincere thanks to Vikas Yadav for facilitating access to characterization facilities at IIT Delhi, which was crucial for specific experimental stages.

I am grateful to UPES for financial support, and to CIC and R&D, UPES Dehradun, for fostering a supportive academic environment. I also acknowledge the instrumental support from IIT Roorkee and IIT Mandi, which contributed

significantly to my research. I extend my sincere gratitude to all the faculty members of my department for their valuable guidance and constant encouragement. Above all, I am profoundly thankful to my father, Dr. N. P. Naithani; my beloved late mother, Mrs. Geeta Naithani; my brother, Dr. Divyanshu Naithani; and my sister-in-law, Dr. Ranjana Naithani. Their unwavering support, belief in my abilities, and enduring presence have been the true foundation of my journey.

Finally, being part of the UPES community has been a rewarding experience, contributing to both my academic and personal growth. The time spent in my lab, filled with learning and challenges, will always hold a special place in my memories.

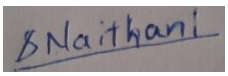

(Sudhanshu Naithani)

TABLE OF CONTENT

LIST OF TABLES

LIST OF FIGURES

LIST OF SCHEMES

LIST OF SYMBOLS/ABBREVIATIONS

Symbol	Abbreviation
atomic absorption spectroscopy	AAS
aggregation-induced emission	AIE
Benesi-Hildebrand	B-H
chelation enhanced fluorescence	CHEF
Dichloromethane	DCM
excited-state intramolecular proton transfer	ESIPT
ethylenediamine tetraacetate	EDTA
Förster resonance energy transfer	FRET
hard and soft acids and bases	HSAB
hierarchical cluster analysis	HCA
highest occupied molecular orbital	HOMO
lowest unoccupied molecular orbital	LUMO
high performance liquid chromatography	HPLC
imidazo-phenanthroline	imidazo-phen
inductively coupled plasma mass spectrometry	ICP-MS
inductively coupled plasma optical emission spectrometry	ICP-OES
intraligand charge transfer	ILCT
internal conversion	IC
intersystem crossing	ISC
intramolecular charge transfer	ICT
Stern-Volmer constant	K_{sv}
ligand-centred	LC
limit of detection (or detection limit)	LoD
metal-to-ligand charge transfer	MLCT
near-infrared	NIR
principal component analysis	PCA
photodynamic therapy	PDT
photoinduced electron transfer	PeT
reactive oxygen species	ROS
relative standard deviation	R.S.D.
single-crystal X-ray diffraction	SC-XRD

surface enhanced Raman spectroscopy	SERS
singlet state	S_1
ground state	S_0
triplet state	T_1
N,*N*,*N*′,*N*′-tetrakis(2-pyridylmethyl)ethylenediamine	TPEN
2-thenoyltrifluoroacetone	TTA
Ultraviolet	UV
Visible	Vis
X-ray fluorescence	XRF

ANNEXURE I

LIST OF FIGURES/TABLES

CHAPTER 1

INTRODUCTION

1.1. Photosensitizers

Photosensitizers are light-responsive molecular entities capable of absorbing photons, typically in the ultraviolet (UV) to visible spectral range, and converting the absorbed energy into heat, light, or chemical energy. This process closely resembles the natural photophysical behavior of chlorophyll during photosynthesis, where solar energy is harnessed and utilized to drive biochemical transformations (Lv et al., 2023; Ravi and Tan, 2015). Upon photon absorption, the photosensitizer transitions from its ground state to an electronically excited state, usually the singlet excited state (S_1). From this state, the molecule may undergo intersystem crossing (ISC) to form the long-lived triplet excited state (T_1), which plays a central role in initiating subsequent energy or electron transfer reactions (Feng et al., 2020). The design and selection of an efficient photosensitizer are dictated by several critical parameters. Key among them are the absorption characteristics (broad and intense absorption in the UV-Vis region), photostability (resistance to photobleaching under prolonged irradiation), and quantum efficiency for energy and/or electron transfer processes (Shon and Teets, 2019; Zhao, Liu, et al., 2021). A desirable feature of high-performance photosensitizers is a short-lived singlet state, which ensures a rapid and efficient ISC to the triplet state. This suppresses competitive nonradiative pathways such as fluorescence, internal conversion (IC), or undesirable photochemical side reactions, thereby enhancing the triplet yield (Quina and Silva, 2021). An optimal photosensitizer should also exhibit a sufficiently long-lived triplet state, typically in the microsecond range under oxygen-free conditions, to facilitate efficient interaction with substrate molecules or target analytes (Quina and Silva, 2021; Zeng et al., 2024). For triplet-triplet energy transfer (TTET) to be

thermodynamically favorable, the triplet energy level of the photosensitizer must be at least ~12 kJ/mol (or ~3 kcal/mol) higher than that of the acceptor. This energetic difference ensures irreversible energy transfer and suppresses back energy transfer, thereby enhancing the reaction specificity (Turro et al., 2010).

From an environmental and biomedical standpoint, ideal photosensitizers should also possess low toxicity, minimal dark cytotoxicity, and good biocompatibility, especially for applications involving biological systems or green chemistry (Lan et al., 2019; Pham et al., 2021). Common classes of photosensitizers include porphyrins, phthalocyanines, transition metal complexes (notably ruthenium(II)-polypyridyl derivatives), and various organic fluorophores such as rhodamines and coumarins. These molecular scaffolds are valued for their tunable photophysical properties and robust chemical architectures (Evangelista et al., 2025; Fillaut, 2024; O'Connor et al., 2009; Wong et al., 2019; Zhao, Liu, et al., 2021). Photosensitizers have found widespread applications across diverse scientific domains including photodynamic therapy (PDT), photocatalysis, and luminescence sensing (Kumar et al., 2022; Lan et al., 2019; Xue and Chao, 2024). In PDT, they serve as the key agents for generating reactive oxygen species (ROS) upon light irradiation, enabling localized destruction of cancer cells (Yang et al., 2019; Zhou et al., 2016). In photocatalysis, they facilitate redox transformations under mild conditions, contributing to the development of sustainable and energy-efficient chemical processes. Meanwhile, in luminescence-based sensing platforms, photosensitizers allow for the highly sensitive and selective detection of biologically or environmentally relevant analytes, both *in vitro* and *in vivo*, through changes in fluorescence intensity, wavelength shifts, or lifetime modulation (Berezin and Achilefu, 2010; Lovell et al., 2010).

1.2. Photosensitizers in Optical Sensors

Photosensitizers play a pivotal role in the development of optical chemosensors due to their capacity to transduce chemical or biological interactions into detectable optical signals, such as changes in fluorescence intensity, emission wavelength, phosphorescence, or visible color shifts (Suárez

et al., 2019). These luminescence-based changes occur in response to interactions with specific analytes, making photosensitizers highly valuable in analytical and diagnostic applications (Chen et al., 2023; Zhang and Yuan, 2020). Photosensitizer-based optical sensors are widely applied in various domains. In biomedical diagnostics, they serve as biosensors for the detection of biomarkers such as metal ions, pH changes, nucleic acids, or reactive oxygen species, offering real-time and non-invasive monitoring in complex biological matrices (Du and Dong, 2017; Lin et al., 2023; Nosaka and Nosaka, 2017; Zhang and Yuan, 2020). In environmental monitoring, these sensors are employed to detect hazardous pollutants, such as heavy metals, nitrates, or volatile organic compounds, thereby supporting efforts in pollution control and public health surveillance (Hojjati-Najafabadi et al., 2022; Jalal et al., 2018; Rathi et al., 2021). Additionally, in industrial and chemical processes, photosensitizer-based sensors facilitate the detection of key intermediates or trace contaminants with high precision (Ateia et al., 2024; Chen et al., 2024; Zulkifli et al., 2018). The sensing capability of photosensitizers is fundamentally based on the modulation of their photophysical properties (such as fluorescence, phosphorescence, or delayed emission) in the presence of target analytes. These optical changes can be exploited for both qualitative and quantitative detection. Continued advancements in molecular design and sensor engineering have led to the development of new-generation optical sensors with enhanced efficiency, photostability, and selectivity, expanding their potential utility in real-world applications (Manna et al., 2025; Yao et al., 2014).

Typically, a molecular optical sensor consists of three key components: (i) a photosensitizer unit that serves as the signal generator; (ii) a receptor or recognition site that selectively binds the analyte; and (iii) a spacer or linker that connects these two domains, facilitating communication between them (**Scheme 1.1**). The interaction between the analyte and the receptor triggers an optical response through either energy transfer, electron transfer, or conformational change, resulting in a detectable signal. The first fluorescent chemosensor was reported by F. Goppelsröder in 1867 for the detection of aluminum ions (Al^{3+}) via the formation of a highly fluorescent morin-aluminum

complex (Czarnik, 1993). However, the field gained significant momentum in the 1980s due to pioneering work by A.P. de Silva and Anthony W. Czarnik, who are widely regarded as the foundational figures of modern chemosensor research (Wu et al., 2017). Optical chemosensors can generally be classified into two categories: (i) binding-based sensors which rely on reversible, non-covalent interactions (e.g., hydrogen bonding, electrostatic forces, π-π stacking) between the analyte and the receptor without significant structural changes in the sensing system and (ii) reaction-based sensors that utilize specific chemical reactions that result in covalent modifications of the sensing unit, leading to permanent and highly selective detection of the target analyte. Though often irreversible, these sensors offer exceptional selectivity (Singha et al., 2019; You et al., 2015). Modern optical chemosensors are extensively used for the detection of a wide array of species, including metal cations, anions, and small neutral molecules. Their versatility, combined with the ability to fine-tune the photophysical behavior of the photosensitizer, continues to drive innovation in the field of optical sensing (Nestoros et al., 2025).

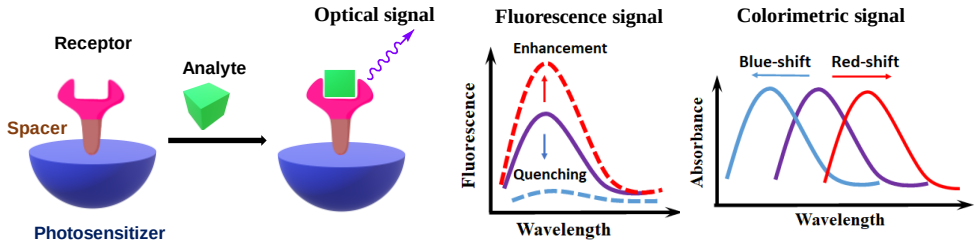

Scheme 1.1. Design of an optical chemosensor.

1.2.1. Fluorogenic sensors

Fluorogenic sensors are a subclass of optical chemosensors that operate by modulating their fluorescence response upon interaction with specific analytes. These sensors are highly valued for their exceptional sensitivity, selectivity, rapid signal response, and ability to detect trace amounts of analytes both qualitatively and quantitatively (Kolanowski et al., 2018; Yao et al., 2014; Zhang et al., 2014). Their utility extends across diverse fields, including environmental monitoring, medical diagnostics, and biological imaging, where

real-time and non-invasive sensing is often required (Balas, 2009). Furthermore, fluorogenic systems can offer mechanistic insights into chemical and biochemical transformations by tracking changes in the fluorescence signal associated with dynamic molecular events (H. Singh et al., 2019). The phenomenon of fluorescence was first documented by George Gabriel Stokes in 1852 (Jameson, 2025), when he observed blue luminescence from the mineral fluorite under ultraviolet illumination, a discovery that laid the foundation for modern fluorescence spectroscopy.

The basic photophysical principles underlying fluorogenic sensors can be represented by a Jablonski diagram (**Scheme 1.2**). Upon irradiation, the photosensitizer or fluorophore absorbs a photon within an ultrafast timescale ($\sim 10^{-15}$ s), resulting in excitation from S_0 to S_1. The molecule can then return to the ground state *via* two main pathways: (i) radiative decay, in which the excess energy is emitted as a photon (fluorescence), typically occurring within nanoseconds ($\sim 10^{-9}$ s); and (ii) non-radiative decay, which involves dissipation of energy as heat through internal conversion or vibrational relaxation. An alternative route includes ISC from the S_1 state to a lower-energy T_1, followed by a slower radiative return to the ground state, known as phosphorescence. Due to the spin-forbidden nature of $T_1 \rightarrow S_0$ transitions, phosphorescence exhibits significantly longer lifetimes (on the order of micro- to milliseconds, $\sim 10^{-4}$ s or more) compared to fluorescence. In the context of chemosensing, analyte-induced changes in the local electronic environment, molecular conformation, or intramolecular charge distribution can either enhance or quench the fluorescence signal (Lee et al., 2015). These variations form the basis for designing *turn-on*, *turn-off*, or ratiometric fluorogenic sensors, each providing different analytical advantages depending on the sensing mechanism.

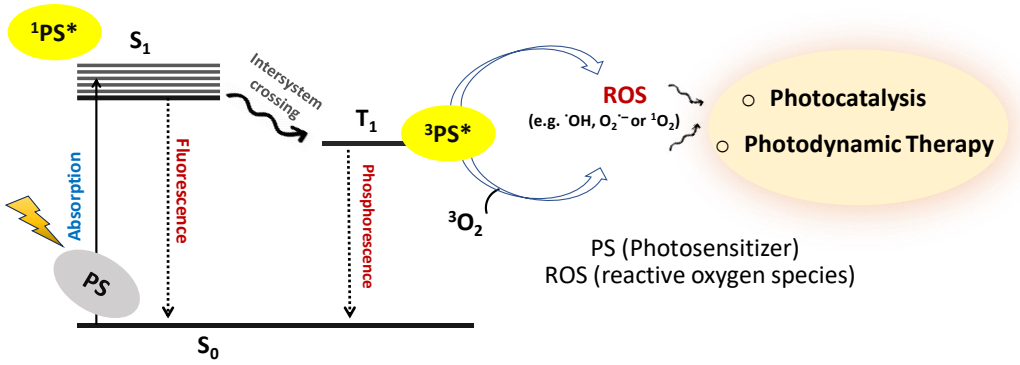

Scheme 1.2. Simplified Jablonski diagram and mechanistic routes for photocatalysis and PDT (Kumar et al., 2022).

Fluorogenic chemosensors can detect analyte *via* various pathways including intramolecular charge transfer (ICT) (Pal et al., 2021), photoinduced electron transfer (PeT) (Niu et al., 2023), Förster resonance energy transfer (FRET) (Wu et al., 2020), chelation enhanced fluorescence (CHEF) (Goshisht et al., 2022), aggregation-induced emission (AIE) (Chua et al., 2023), and excited-state intramolecular proton transfer (ESIPT) (Sedgwick et al., 2018). ICT fluorescent probes employ a Donor (D)–π–Acceptor (A) system where degree of charge transfer between D and A is primarily responsible for photophysical behavior or tunable emission (Chen and Fang, 2020). Analyte interaction modulates charge transfer efficiency consequently resulting in blue or red shifted fluorescence band serving as a measurable signal. CHEF probes enable selective metal ion detection through coordination induced fluorescence enhancement. The coordination restricts non-radiative decay and enhanced π-conjugation resulting in fluorescence enhancements (Yang et al., 2025). AIE active materials remains weakly emissive however upon aggregation they turn into bright fluorophores via restriction of intramolecular motions. Analyte interaction may produce notable changes either by disaggregating the probe or forming stable ground-state complexes (Chua et al., 2023). FRET typically involves non-radiative energy transfer between D–A pair via long range dipole-dipole interaction. The energy transfer from excited state donor to a ground-state acceptor occurs at a separation of 1-10 nm (Kaur et al., 2020). Probes exhibiting intramolecular H-bond between a proton donor (OH or NH_2) and proton acceptor (=N or =O moiety) can display ESIPT (Li et al., 2025).

Photoexcitation triggers proton transfer forming tautomeric excited state producing significant shift in the emission spectra when compared to the excited state. In PeT, a receptor is linked to a fluorophore and it quenches the emission band due to excited state electronic transfer (Daly et al., 2015). PeT is a very versatile mechanism and most commonly employed for designing fluorescent probe, and therefore it is discussed in details in the next paragraph.

A typical PeT probe consists of three important components, i.e., a signaling unit (i.e., luminophore), a spacer unit (i.e., linker) and a receptor (i.e., ionophore or binding unit) (**Scheme. 1.3**) (Wu et al., 2017). Usually, the ionophore is an electron (e^-) donor such as thio- or amino- containing groups, whereas the luminophore acts as an e^- acceptor. In the case of the free probe (without guest analyte) ((**Scheme. 1.3(a)**), the e^- present in the HOMO (highest-occupied-molecular-orbital) of its luminophore is promoted to the LUMO (lowest-unoccupied-molecular-orbital) with the absorption of a photon of suitable wavelength (excited luminophore). If the energy level of the HOMO of the free ionophore is slightly higher than the HOMO of the luminophore, spatial electron transfer will take place from the ionophore to the luminophore through HOMOs (**(Scheme. 1.3(a)**). Consequently, the transition of the excited electron from the LUMO to HOMO of the luminophore is blocked; this quenching of emission is defined as the PeT process (Daly et al., 2015; de Silva et al., 2009; Tarai et al., 2021a). Metal ion binding to the ionophore results in a decrease in the HOMO energy of the ionophore below the HOMO level of the luminophore, ultimately restoring the luminescence response of the probe (**(Scheme. 1.3(b)**). This phenomenon of luminescence recovery's also known as the metal-chelation-enhanced-luminescence effect. The restoration of the luminescence and the emission of the resultant metal complex is often attributed to the $\pi \rightarrow \pi^*$ excited-state relaxation of the luminescence. Notably, the protonation of the ionophore group may also block the PeT event (Naithani et al., 2024).

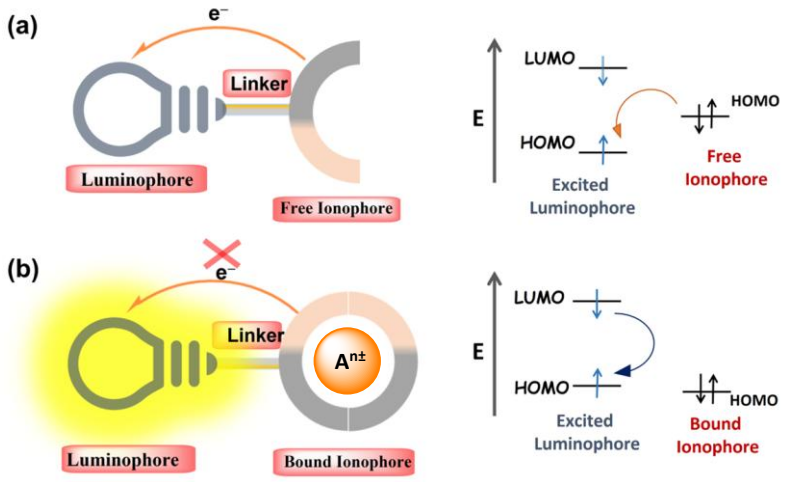

Scheme 1.3. Schematic "turn-on" sensing mechanism in PeT based luminescent probes; (a) free probe and (b) probe with target analyte (Naithani et al., 2024).

1.2.2. Colorimetric sensors

Distinctly from the luminescent receptors, the colorimetric sensors are associated with the changes observed in their electronic properties in the form of inter/intra-molecular charge transfer (ICT) e.g., charge-transfer transitions. A molecular sensor with D–π–A system is commonly used to accomplish the colorimetric sensing (Liu et al., 2020). Furthermore, a D–π–A molecular system can be obtained by introducing both electron donor (D) as well as electron acceptor (A) groups in the molecular sensor at suitable positions. Binding of metal ion to either D or A in the molecular probe occurs *via* covalent and non-covalent interactions. In general, analyte binding to D reduces its electron donating ability that ultimately converts the D–π–A molecular system into A_1–π–A_2; as a result, the conjugation of the system is reduced leading to a blue-shift in the absorption spectrum of the probe. Comparatively, the binding of metal ion to A moiety provides a remarkable strength to the D–π–A system leading to an increase in the push-pull ICT effect with a concomitant red-shift in UV-Vis spectrum (Caricato et al., 2013; Kaur and Singh, 2023). Such kinds of analyte induced transitions along with ICT contribute to the color changes observed after binding with the target (**Scheme 1.4**).

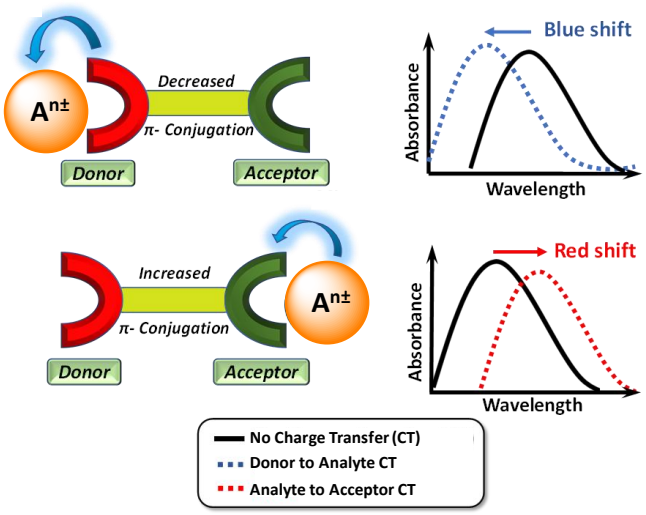

Scheme 1.4. Distinct binding effects of metal ions on D–π–A systems of colorimetric probes (Naithani et al., 2024).

1.3. Optical probes for heavy metal ions

Metal ions play crucial roles in various biological, environmental and industrial processes but they can also pose significant environmental and biological risks (Geng et al., 2022; Krämer et al., 2022b; Pal et al., 2021; Tarai et al., 2021b; Wu et al., 2020). They are essential for maintaining homeostasis, supporting metabolic activities, facilitating biomineralization, mediating cell signaling, and catalyzing key biochemical reactions. They also contribute to the stabilization of biomolecular conformations, act as enzyme cofactors, and function as intracellular signal transducers, thereby supporting a wide range of physiological processes (Broering et al., 2013; Li and Zamble, 2009; Mulrooney and Hausinger, 2003). For instance, Na^{+}/K^{+} and Ca^{2+}/Mg^{2+} gradients across cell membranes regulate osmotic pressure, membrane potential, and cellular excitability. These biologically essential metal ions are typically classified as trace elements. On the other hand, heavy metal ions have emerged as a serious global environmental concern, primarily due to their extensive use in industrial processes and non-biodegradable nature (Shrestha et al., 2021). Toxic metals such as lead (Pb^{2+}), mercury (Hg^{2+}), copper (Cu^{2+}), cadmium (Cd^{2+}), zinc (Zn^{2+}), aluminum (Al^{3+}), and platinum (Pt^{2+}) are harmful to living organisms even at trace concentrations and tend to bioaccumulate (Amiard et al., 1987;

Collin et al., 2022; Novaes et al., 2018; Rainbow and Luoma, 2011; Szynkowska et al., 2018). Consequently, there is an urgent need for the development of highly specific, sensitive, user-friendly, and real-time metal ion sensors for environmental and biological monitoring. To monitor heavy metal ions, a series of analytical techniques have been developed, including inductively coupled plasma mass spectrometry (ICP-MS), atomic absorption spectroscopy (AAS), surface enhanced Raman spectroscopy (SERS), and inductively coupled plasma optical emission spectrometry (ICP-OES) (Goswami et al., 2023; Kang et al., 2017). These methods are known for their high sensitivity and precision; however, they often involve expensive instrumentation, labor-intensive procedures, and are unsuitable for rapid or on-site detection therefore, optical sensors are gaining widespread attention (Chopra et al., 2022; Naithani et al., 2023a; She et al., 2021). To date, a wide array of probes has been reported for detection of metal ions based on organic and/or inorganic materials, a few of them have been covered in subsequent sections.

1.3.1. Design principles for metal ion responsive probes

The design of the receptor unit is a critical factor in achieving high selectivity for a specific metal ion (i.e., the targeted analyte) over other competing species. To enhance receptor-cation interactions and analyte selectivity, several key aspects must be carefully considered:

(i) Size of the receptor pocket: The effective ionic radius of targeted cation, number and nature of coordinating ligands, and size of the receptor pocket can be carefully tailored as it may exclude the risk of probe response/affinity towards larger or shorter cations or any other competing species (Naithani et al., 2025).

(ii) The nature and number of donor atoms in the receptor unit and (iii) the geometry of the receptor pocket: Transition metal ions, particularly those from the first-row of the d-block, often exhibit diverse coordination geometries such as tetrahedral, square planar, and octahedral, depending on their electronic configuration, oxidation state, and the nature of the ligands involved. The geometry and stability of these metal-ligand complexes are strongly influenced

by ligand field effects, which govern the distribution of d-electrons and the resulting spin state. To achieve high selectivity and strong binding affinity, the design of a cation-responsive probe must account for the preferred coordination environment of the target metal ion. This typically involves incorporating donor groups (such as amines, carbonyls, pyridines, bipyridines, or phenanthrolines) into the receptor framework, aligned in geometries that complement the metal's coordination preferences. Furthermore, factors such as ligand denticity, backbone rigidity, and electronic properties of the receptor play critical roles in tuning the selectivity and sensitivity of the sensor system (Naithani et al., 2025; Naithani et al., 2024).

(iv) The hard and soft basicity of donor atoms in the receptor: The strength and selectivity of cation-receptor interactions are dependent on intrinsic properties of the metal ion and the coordinating donor atoms within the receptor framework. The Hard and Soft Acids and Bases (HSAB) principle offers a fundamental strategy for rational probe design, facilitating the selection of appropriate donor groups to match the hardness or softness of the targeted metal ion (Ho, 1975; LoPachin et al., 2012). Hard metal ions (e.g., Al^{3+}, Fe^{3+}) typically prefer oxygen-based donors like carboxylates or hydroxyls, whereas soft metal ions (e.g., Hg^{2+}, Ag^{+}) exhibit stronger affinities for sulfur- or phosphorus-containing ligands. Borderline metal ions (e.g., Zn^{2+}, Cu^{2+} and Ni^{2+}) favor nitrogen-donor ligands such as imidazoles, pyridines, and amines. Therefore, selecting the correct donor types is critical for achieving selectivity and strong binding affinity. Additionally, factors such as solvent polarity, pH, and the presence of competing or interfering species in the sensing environment significantly influence metal-receptor interactions (Naithani et al., 2025; Naithani et al., 2024; Wu et al., 2015). Minor changes in these parameters can alter coordination geometry, probe solubility, or binding efficiency, ultimately affecting the overall sensing performance. Thus, an all-rounded approach considering both molecular design and environmental context is essential for developing effective and selective metal ion sensors. This will enable these sensors to work in real scenarios rather than being mere academic curiosities.

1.3.2. Organic probes

Organic molecular probes have emerged as versatile tools for the detection of metal ions, offering several key advantages such as structural diversity (e.g., pyridine, anthracene, pyrene, naphthalene, quinoline, coumarin, rhodamine, phenolphthalein), ease of functionalization, excellent reproducibility, and well-understood sensing mechanisms (Li et al., 2022; Pramanik, 2025). Among them, Schiff bases, characterized by their imine (>C=N-) linkage, have been extensively explored for the detection of heavy metal ions (Taha et al., 2024). This is largely attributed to their straightforward synthesis, good chemical stability, and tunable electronic and steric environments, which allow for selective and sensitive interaction with one or more metal ions (Afrin and Swamy, 2023; Kumar et al., 2023; Taha et al., 2024). Typically, metal ion coordination induces significant changes in the photophysical properties of the probe, often leading to a marked enhancement in fluorescence. Hence, rational design of the probe scaffold is essential to ensure effective binding and signal transduction upon coordination with the target cation. Kim and co-workers (Kim et al., 2015) developed a julolidine-based probe **1** capable of detecting multiple metal ions *via* both fluorogenic and chromogenic pathways (**Fig. 1.1**). Probe **1** alone exhibited weak fluorescence emission in DMF. A wide range of metal ions, including Ga^{3+}, Al^{3+}, Zn^{2+}, In^{3+}, Cu^{2+}, Cd^{2+}, $Fe^{2+/3+}$, Cr^{3+}, Hg^{2+}, Ag^{+}, Mg^{2+}, Ni^{2+}, Co^{2+}, K^{+}, Na^{+}, Mn^{2+}, Pb^{2+}, and Ca^{2+}, were screened, but only Al^{3+} and Zn^{2+} induced significant fluorescence enhancement, with emission bands observed at 448 nm and 418 nm, respectively. This fluorescence enhancement was attributed to multiple factors: inhibition of excited-state proton transfer, suppression of >C=N isomerization, and the CHEF effect, which provides structural rigidity to the formed metal complexes. In UV-Vis experiments, the addition of Zn^{2+} resulted in a decrease in the absorption band at 351 nm and an increase at 374 nm, along with a clear isosbestic point at 358 nm, indicating complex formation. For Al^{3+}, the absorption peak at 352 nm decreased, and a new peak appeared at 380 nm with an isosbestic point at 363 nm. Job's plot revealed a 1:1 binding stoichiometry, further corroborated by ESI-MS and ^{1}H NMR spectroscopy. The association

constants for the Zn^{2+} and Al^{3+} complexes, determined using the Benesi-Hildebrand (B-H) equation, were 2.9×10^4 M^{-1} and 8.5×10^3 M^{-1}, with corresponding limits of detection (LoD) of 1.59 μM and 1.34 μM, respectively. Interference studies revealed that Cu^{2+}, Ga^{3+}, and Fe^{3+} significantly competed with Zn^{2+}, while Al^{3+} detection was hindered in the presence of Cu^{2+}, In^{3+}, Ga^{3+}, $Fe^{2+/3+}$, Co^{2+}, and Cr^{3+} ions. Further fluorogenic studies were carried out in a DMF-bis-tris buffer system (95: 5, v/v). Initially, probe **1** again exhibited weak fluorescence at 440 nm (λ_{ex} = 355 nm), which was significantly enhanced upon the addition of Zn^{2+} ions. Interestingly, Al^{3+} failed to produce a notable enhancement under these aqueous conditions, likely due to its hard acid nature and strong interaction with water, which suppressed coordination with the probe. Interference studies in this medium identified $Fe^{2+/3+}$, Cr^{3+}, Co^{2+}, Cu^{2+}, and Al^{3+} as major competing species. The reversibility of the sensing was demonstrated by the successful use of ethylenediaminetetraacetic acid (EDTA) to restore the probe's original fluorescence. Practical application of probe **1** was validated by spiking tap water samples with Zn^{2+} ions, which showed good recovery values. In this environment, the binding constant and LoD were calculated to be 7.7×10^3 M^{-1} and 3.74 μM, respectively. The lower affinity and higher LoD were attributed to strong interference from water molecules. Lastly, the chromogenic response of probe **1** was examined in a methanol-buffer solution at room temperature. Only Fe^{2+} and Fe^{3+} ions caused noticeable spectral changes and visible color shifts from pale yellow to dark green. Upon $Fe^{2+/3+}$ addition, the absorption band at 378 nm decreased while a new band appeared at 456 nm, attributed to metal-to-ligand charge transfer transitions.

Two isosbestic points at 363 nm and 429 nm confirmed complex formation. Binding constants and LoDs determined by UV–Vis titration were 1.1×10^4 M^{-1} and 0.21 μM for Fe^{2+}, and 1.2×10^4 M^{-1} and 0.22 μM for Fe^{3+}, respectively. While Zn^{2+} and Al^{3+} showed excellent fluorometric responses, they exhibited no visible spectral changes in this chromogenic setting. Job's plot, ^1H NMR, and ESI-MS analyses confirmed a 1:1 stoichiometry and strong complexation. Finally, the detection of Fe^{3+} in real water samples was

successfully demonstrated, yielding good recovery and low relative standard deviation (R.S.D.) values.

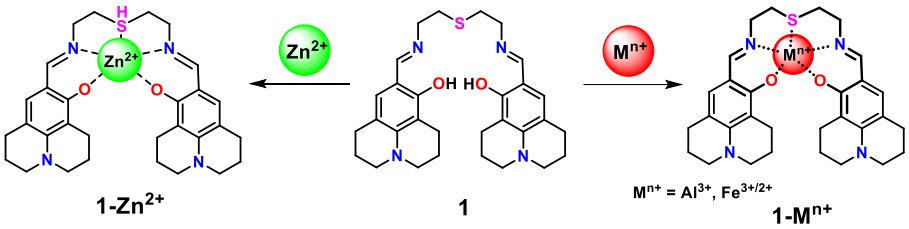

Fig. 1.1. Binding mode of Zn^{2+}, $Fe^{2+/3+}$ and Al^{3+} in DMF with probe **1** (10 μM) having julolidine-based fluorophore (Kim et al., 2015).

In 2016, Castro *et* al. developed a pyrene-based probe, **2a**, and systematically investigated its response toward various metal ions (**Fig. 1.2**) (de Castro et al., 2016). UV-Vis absorption studies revealed a characteristic pyrene absorption band at 360 nm in dichloromethane. Fluorescence studies showed two emission bands at 394 nm and 511 nm. Upon incremental addition of Pb^{2+} ions (up to 50 equiv.), a quenching of the 394 nm emission band was observed over 69 minutes. Beyond this point, a new broad emissive band emerged in the 420-500 nm range, attributed to the formation of a pyrene dimer. The fluorescence lifetime of the probe was ~25 ns, with only nominal changes upon Pb^{2+} coordination, indicating a non-radiative quenching pathway. In addition to Pb^{2+}, the response of probe **2a** was examined against other metal ions including Cu^{2+}, Zn^{2+}, Ag^{+}, Hg^{2+}, and Cd^{2+}, all of which induced significant variations in both absorption and emission spectra. To better interpret these complex spectral patterns and distinguish among the metal ions, hierarchical cluster analysis (HCA) and principal component analysis (PCA) were employed. These multivariate statistical tools demonstrated that probe **2a** could effectively discriminate between Ag^{+}, Cd^{2+}, and Pb^{2+}. However, differentiating between Zn^{2+}, Hg^{2+}, and Cu^{2+} remained a challenge due to their similar spectral responses. Furthermore, an analogue probe **2b** incorporating a diethylenetriamine binding motif was also synthesized and evaluated. While this analogue showed improved selectivity between Ag^{+} and Pb^{2+}, it failed to

clearly differentiate between Zn^{2+} and Cd^{2+}, as well as between Cu^{2+} and Hg^{2+} ions.

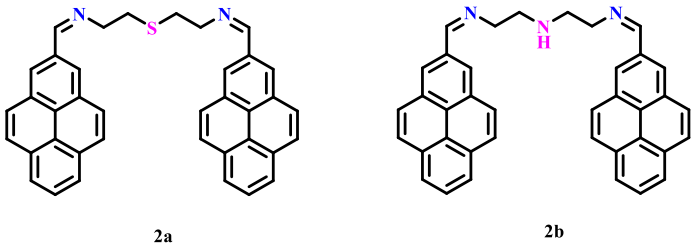

2a 2b

Fig. 1.2. Chemical structures of probes **2a** and **2b** (de Castro et al., 2016).

Yoon and co-workers (Hu et al., 2015) modified probe **2a** by incorporating -OH functionality to design pyrene-based probes **3a** and its 2,2′-oxybis(ethylamine) analogue **3b** (**Fig. 1.3**). Fluorescence studies revealed that the probe **3a** exhibited a turn-on emission response at 550 nm in the presence of Zn^{2+} ions upon excitation at 355 nm in a DMSO-H_2O (1: 1, v/v) mixture. The quantum yield of **3a** increased significantly from 1.56% to 21.33% upon Zn^{2+} coordination. The selectivity of the probe was evaluated against a broad range of metal ions, including Ca^{2+}, Ag^{+}, Co^{2+}, Cd^{2+}, Cr^{3+}, Cs^{+}, Fe^{2+}/Fe^{3+}, Cu^{2+}, Hg^{2+}, K^{+}, Sr^{2+}, Mg^{2+}, Li^{+}, Na^{+}, Mn^{2+}, Pb^{2+}, and Ni^{2+}, none of which induced a turn-on response. UV-Vis absorption spectra of **3a** showed pronounced bathochromic shifts upon Zn^{2+} addition, accompanied by a distinct visual change from pink to orange, indicating a clear colorimetric response. Job's plot confirmed a 1:1 binding stoichiometry between **3a** and Zn^{2+} ions, suggesting that the receptor site comprises two oxygen atoms from the fluorophore, two imine nitrogen atoms, and one sulfur donor, forming a suitable coordination environment for Zn^{2+}. The association constant of probe **3a** with Zn^{2+} was determined to be 3.90×10^5 M^{-1}, with a detection limit of 1.24 μM based on fluorescence titration experiments. Probe **3a** was further applied for intracellular Zn^{2+} detection in mouse NIH-3T3 embryonic fibroblast and HeLa cells. Upon incubation with **3a** followed by Zn^{2+} addition, significant fluorescence enhancement was observed. Introduction of tetrakis(2-pyridylmethyl)ethylenediamine (TPEN), a well-known Zn^{2+} chelator, led to dramatic fluorescence quenching, confirming Zn^{2+}-specific binding. As Zn^{2+} ions are released from intracellular proteins during

apoptosis, H_2O_2 was used to induce cell apoptosis, which led to strong fluorescence enhancement in the incubated cells, that was again quenched upon TPEN addition. Analogue **3b** displayed a similar fluorescence response, with a slightly higher binding constant of 6.69×10^5 M^{-1} and an improved detection limit of 0.85 μM, suggesting enhanced performance over **3a**.

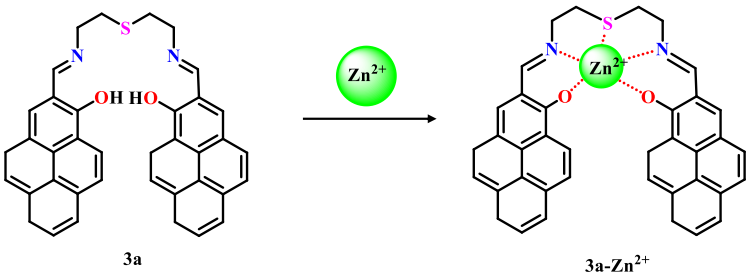

Fig. 1.3. Binding mode of Zn^{2+} in DMSO-H_2O (1:1, v/v) with probe **3a** (10 μM) having hydroxy-pyrene as fluorophore (Hu et al., 2015).

In 2018, Kim and co-workers (Lee et al., 2018) developed a hydroxy-naphthaldehyde-based probe **4** for the detection of In^{3+} and Fe^{3+} ions (**Fig. 1.4**). The fluorescence sensing behavior of probe **4** was evaluated against a variety of metal ions, including Mg^{2+}, Fe^{3+}, Ag^{+}, Na^{+}, Ga^{3+}, K^{+}, Al^{3+}, Co^{2+}, Cu^{2+}, Cd^{2+}, Zn^{2+}, Cr^{3+}, In^{3+}, Fe^{2+}, Ni^{2+}, Pb^{2+}, and Mn^{2+} in CH_3CN. The probe exhibited a significant enhancement in fluorescence intensity at 450 nm in the presence of In^{3+} ions. UV-Vis absorption studies revealed that probe **4** displayed three absorption bands at 290 nm, 340 nm, and 430 nm. Upon addition of In^{3+}, the bands at 290 nm and 340 nm intensified, and two new bands emerged at 320 nm and 370 nm. Meanwhile, the absorption band at 430 nm decreased, and the appearance of an isosbestic point at 270 nm suggested complex formation. Job's plot analysis confirmed a 1:1 binding stoichiometry between probe **4** and In^{3+} ions.

The association constant was calculated to be 2.4×10^3 M^{-1} using the B-H equation, and the LoD for In^{3+} ions was determined to be 5.89 μM. Interestingly, UV-Vis studies also revealed a distinct colorimetric response in the presence of Fe^{3+} ions. A new absorption band appeared at 600 nm, accompanied by a visible color change from colorless to pale violet. An

isosbestic point at 431 nm further supported the formation of a 1:1 complex between probe **4** and Fe^{3+} ions, as corroborated by Job's plot and ESI-MS analysis. The binding constant for Fe^{3+} was higher than that for In^{3+}, calculated to be 2.4 × 10^5 M^{-1}, and the corresponding LoD was significantly lower, determined to be 0.30 μM. The practical applicability of probe **4** was demonstrated through colorimetric detection of Fe^{3+} using low-cost test strips, which retained sensing capability for up to three cycles with EDTA regeneration.

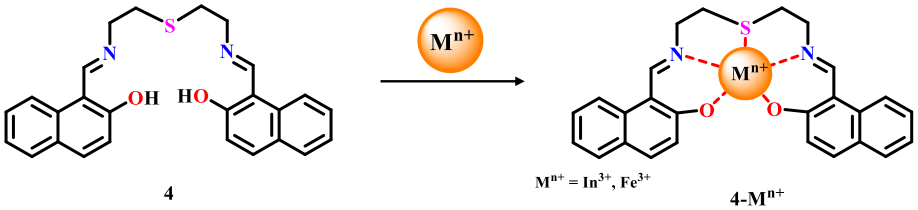

Fig. 1.4. Binding mode of In^{3+} and Fe^{3+} in CH_3CN with probe **4** (20 μM) having hydroxy-naphthalene as fluorophore (Lee et al., 2018).

In 2020, Yoon and co-workers (Kwon et al., 2020) synthesized pyrene-based probes **5a** and **5b** (**Fig. 1.5**). Upon excitation at 350 nm, both probes exhibited characteristic monomeric emission at 390 nm and excimer emission at 450 nm. The fluorescence sensing behavior of the probes was evaluated against a panel of metal ions, and a significant quenching response was observed in the presence of Cu^{2+} and Fe^{2+} ions, attributed to their well-known paramagnetic nature. Notably, Ni^{2+} and Hg^{2+} also induced considerable fluorescence quenching. Among the two, probe **5b** demonstrated a particularly strong quenching response toward Cu^{2+} ions. Job's plot analysis confirmed a 1:1 binding stoichiometry for both probes with Cu^{2+}. The association constants of probes **5a** and **5b** with Cu^{2+} were determined to be 4.47 × 10^{15} M^{-1} and 1.33 × 10^{12} M^{-1}, respectively. To assess biocompatibility and specificity, several amino acids and nucleoside phosphates, including Hcy, GSH, Leu, Ala, Cys, Glu, Phe, ATP, ADP, AMP, GTP, and PPi, were tested with the probe **5a**-Cu^{2+} and **5b**-Cu^{2+} complexes. Upon addition of Cu^{2+} ions to living cells, probe **5a**

exhibited fluorescence quenching, and the probe **5a**-Cu^{2+} ensemble was successfully utilized for imaging biothiols in live cells.

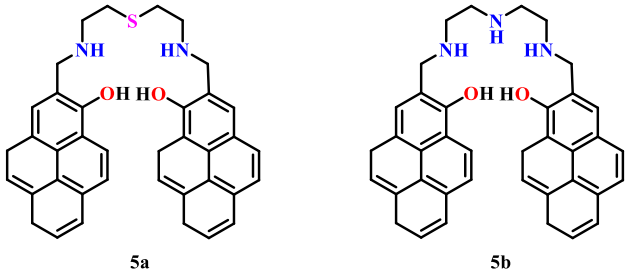

Fig. 1.5. Chemical structures of probes **5a** and **5b** (Kwon et al., 2020).

In 2024, Goswami *et* al. (Goswami et al., 2024) employed probe **6** by incorporating N-heterocyclic ring in ligand framework to synthesize a quinoline-based Schiff base (**Fig. 1.6**). The UV-Vis spectrum of the probe in CH_3CN/H_2O (4: 1, v/v) displayed absorption peaks at 242 nm (π→π* transition) and 287 nm (n→π* transition). A weak emission band at 422 nm was observed upon excitation at 310 nm, attributed to low ICT and C=N isomerization. Upon the addition of Al^{3+} ions, the absorption bands redshifted to 245 nm and 302 nm, respectively, and the emission intensity at 422 nm showed a 20-fold enhancement. The spectral changes were reversible upon treatment with EDTA, and probe **6** maintained its sensing ability over three consecutive cycles. Importantly, other metal ions including Mg^{2+}, Zn^{2+}, Pb^{2+}, Cd^{2+}, Ca^{2+}, Cu^{2+}, Fe^{3+}, Ni^{2+}, Sn^{2+}, Hg^{2+}, Fe^{2+}, Cr^{3+}, and In^{3+} showed no significant interference, demonstrating the probe's high selectivity for Al^{3+}. The probe exhibited a response time of 20 min and operated effectively within the biological pH range. Al^{3+} detection was further demonstrated in the solid state using low-cost paper strips coated with the probe solution. A 1:1 binding stoichiometry was confirmed by Job's plot, ESI-MS, DFT calculations, and ^1H NMR spectroscopy. The observed spectral changes were attributed to Al^{3+} coordination within the binding pocket, which inhibited ICT and suppressed C=N isomerization.

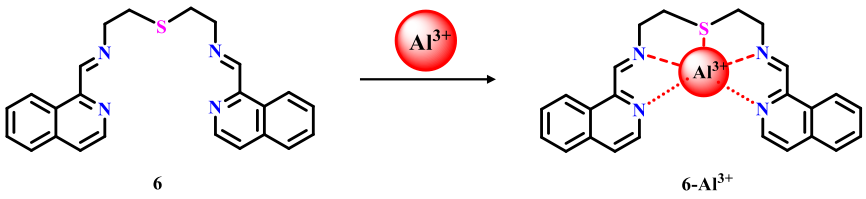

Fig. 1.6. Binding mode of Al^{3+} in CH_3CN/H_2O (4:1; v/v) with probe **6** (1 μM) incorporating quinoline as a fluorophore (Goswami et al., 2024).

1.3.3 Metal complexes based probes

Conventional organic sensors often face critical limitations such as small Stokes shifts, significant spectral overlap, low signal-to-noise ratios, and poor photostability, which collectively hinder their performance in real-world sensing applications (Jiang et al., 2024; Liu et al., 2024). These limitations can be particularly problematic in complex biological or environmental matrices, where background interference and rapid photobleaching are common. In contrast, metal-based probes provide several compelling advantages, including larger Stokes shifts, enhanced photostability, and long-lived emissive states that enable time-gated detection with minimal background noise (Chang et al., 2023; Ning et al., 2022). Furthermore, their modular coordination chemistry and intrinsic structural versatility allow for fine-tuning of photophysical properties and selective recognition of specific metal ions. This makes them particularly attractive for designing robust and responsive sensors tailored to diverse analytical environments. The following section highlights key examples of inorganic probes developed for the selective and sensitive detection of metal ions.

In year 2021, Hishimone *et* al. (Hishimone et al., 2021) reported a Cd^{2+}-based probe **7** incorporating a thiosemicarbazone moiety within the ligand framework (**Fig. 1.7**). In DMF solution, UV-Vis studies of probe **7** revealed a strong intraligand charge transfer (ILCT) band centred at 410 nm, accompanied by a weaker MLCT band near 535 nm. Additionally, a moderate-intensity absorption peak was observed at 306 nm, likely arising from a ligand-centred (LC) $\pi \rightarrow \pi^*$ transition. The response of probe **7** to various nitrate salts of metal cations, including Fe^{3+}, Ag^{+}, Zn^{2+}, Mn^{2+}, Cu^{2+}, Co^{2+}, Ni^{2+}, Cd^{2+}, Cr^{3+}, Pb^{2+}, and Hg^{2+}, were systematically investigated. Upon the addition of 5.0 equiv. of Ni^{2+}

ions to a ~10^{-5} M solution of the probe in DMF, the ILCT band at 410 nm decreased significantly, and a new absorption band emerged near 500 nm, indicating the formation of a new species. This spectral change was accompanied by the appearance of an isosbestic point at 437 nm and a visible color change from yellow to brown, clearly perceptible to the naked eye. Similar spectral and colorimetric responses were observed with Cu^{2+}, Co^{2+}, and Hg^{2+} ions, suggesting that these metal ions can also form analogous adducts with probe **7**. The formation of the **7**-Ni^{2+} complex was further corroborated by ESI-MS and NMR spectroscopy. Notably, no significant spectral changes were observed upon the addition of various anions, including F^-, OH^-, CN^-, AcO^-, Cl^-, Br^-, I^-, and HSO_4^-, indicating good selectivity toward Ni^{2+}. The binding constant and LoD for the **7**-Ni^{2+} complex was determined to be 1.55 × 10^2 M^{-1} and 1.30 × 10^{-10} M, respectively.

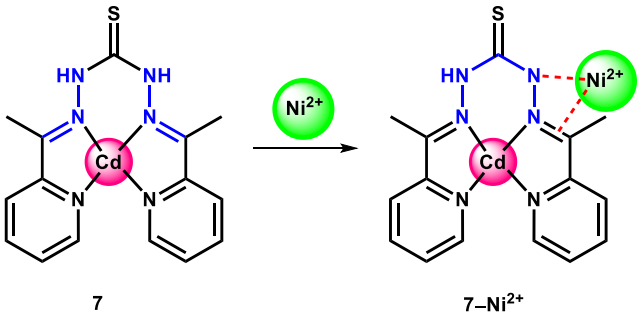

Fig. 1.7. Binding mode of Ni^{2+} in water with Cd(II)-based probe **7** (10 μM) (Hishimone et al., 2021).

Later in the same year (2021), Han and co-workers (Han et al., 2021) reported a water-soluble zinc(II)-based coordination compound **8**, capable of detecting Fe^{3+}, Cu^{2+}, Ni^{2+}, and CrO_4^{2-} ions among a broad panel of cations and anions (**Fig. 1.8**). Probe **8** exhibited an emission maximum at 371 nm upon excitation at 335 nm in aqueous solution. Among the various metal ions investigated, Fe^{3+} induced the most significant luminescence quenching at 371 nm, which was attributed to energy transfer processes and the broad absorption spectrum (200-400 nm) of Fe^{3+} that overlapped with the probe's excitation range. In contrast, the quenching mechanisms for Ni^{2+} and Cu^{2+} ions were

ascribed to spectral overlap between the excitation band of the probe and the absorption spectra of the respective metal ions. The Stern-Volmer constant (K_{sv}) for Ni^{2+} was determined to be 2.68×10^4 M^{-1}, and the LoD was calculated as 0.491 µM.

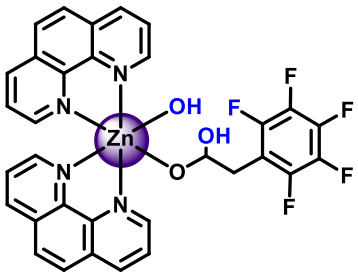

8

Fig. 1.8. Chemical structure of probe **8** (Han et al., 2021).

In 2014, Kumar *et* al. (Kumar et al., 2014) reported the synthesis of a Ru(II)-based probe **9** for the selective detection of Pd^{2+} ions in aqueous environments (**Fig. 1.9**). The UV-Vis absorption spectrum of probe **9** revealed a strong LC ($\pi \rightarrow \pi^*$) transition at 283 nm and a broad MLCT band at 428 nm in water. Upon introduction of 50 ppm Pd^{2+}, the LC band underwent a hypochromic shift (approximately 1.8-fold decrease in intensity), while the MLCT band exhibited both a hypsochromic shift of up to 16 nm and a hyperchromic enhancement (~1.5-fold increase). Additionally, a new absorption band emerged at 565 nm, accompanied by three well-defined isosbestic points at 364, 432, and 503 nm, indicating the formation of a new species in solution. These spectral changes, characterized as a "turn-on" and "turn-left" response, were visually corroborated by a distinct color change from orange to dark red. Probe **9** also displayed luminescent properties with an emission peak at 670 nm upon excitation at 428 nm. The presence of Pd^{2+} led to pronounced quenching of this emission, which was attributed to the paramagnetic character of Pd^{2+}. Collectively, these findings confirmed the generation of a heterobimetallic complex between probe **9** and Pd^{2+}. The probe exhibited high selectivity for Pd^{2+} over a wide range of competing metal ions, including Zn^{2+}, Pb^{2+}, Ni^{2+}, Hg^{2+}, Mn^{2+}, Ag^{+}, Au^{3+}, Cu^{2+}, Co^{2+}, Cd^{2+}, Fe^{2+}, and

even platinum-group elements such as Pt^{2+}, Rh^{3+}, and Ru^{3+}. Stoichiometric analysis *via* Job's plot indicated a 1:1 binding ratio for the **9**-Pd^{2+} complex. The probe demonstrated a low detection limit of 1.54×10^{-6} M and a binding constant of 1.89×10^{3} M^{-1}. Formation of the dinuclear complex was further supported by single-crystal X-ray diffraction (SC-XRD), mass spectrometry, and electrochemical measurements. Finally, as a proof-of-concept application, **9** was successfully utilized for the detection of Pd^{2+} in real water samples (tap and pool water) and exhibited over 90% accuracy in identifying unknown Pd^{2+} samples.

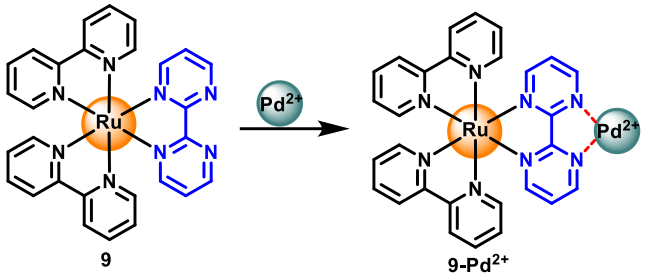

Fig. 1.9. Binding mode of Ru(II)-based probe **9** (10 µM) in water with Pd^{2+} ion (Kumar et al., 2014).

In 2023, Liu *et* al. (Liu et al., 2023) synthesized two near-infrared (NIR) iridium-based metal complexes, **10a** and **10b**, functionalized with amino and allyl groups for the detection of Pd^{0} and Pd^{2+} ions (**Fig. 1.10**). Both complexes exhibited LC $\pi \rightarrow \pi^*$ transitions in the range of 250-320 nm, along with MLCT bands between 320-400 nm. Complex **10a** showed excitation at 260 nm and emitted at 685 nm, while **10b** exhibited excitation at the same wavelength with an emission maximum at 618 nm. The photoluminescence lifetimes were reported to be 314.8 ns for **10a** and 74.7 ns for **10b**, with quantum yields of 6.41% and 1.12%, respectively. Although both probes demonstrated high selectivity towards palladium species, only **10a** was discussed in detail due to its NIR activity. Sensing studies were conducted in a 9:1 acetonitrile/HEPES buffer system. Upon addition of Pd^{0}, fluorescence quenching of **10a** at 685 nm occurred within 5 minutes. The probe demonstrated a low detection limit of 0.50 µM. Interference studies were performed using various amino acids, including

serine, histidine, asparagine, methionine, homocysteine, and cysteine, as well as a broad panel of metal ions: Li^+, K^+, Ag^+, Na^+, Ba^{2+}, Ca^{2+}, Ni^{2+}, Fe^{2+}, Mn^{2+}, Co^{2+}, Zn^{2+}, Cu^{2+}, Cd^{2+}, Cr^{3+}, Al^{3+}, Fe^{3+}, and Au^{3+}. Minor fluorescence quenching and slight interference were observed for Cr^{3+} and Fe^{3+}, likely due to weak coordination, and for Au^{3+} due to its affinity for allyl groups. However, the strongest quenching response was observed for Pd^0, confirming the probe's high selectivity. Probe **10a** also successfully detected Pd^0 in real water samples collected from the Xi'an Moat. Additionally, live-cell imaging studies were carried out using HeLa cells. Probe **10a** exhibited low cytotoxicity, with an IC_{50} value of 19.65 μM after 6 hours of incubation. Upon exposure to increasing concentrations of Pd^0 and Pd^{2+} ions, the bright red fluorescence of **10a** was significantly quenched. Notably, the probe localized within the mitochondria and demonstrated excellent photostability. This was confirmed by co-staining with MitoTracker Green, a commercial mitochondrial dye, and monitoring under a 405 nm laser. While the fluorescence of MitoTracker faded after 420 seconds, probe **10a** retained strong luminescence, underscoring its robustness under prolonged irradiation.

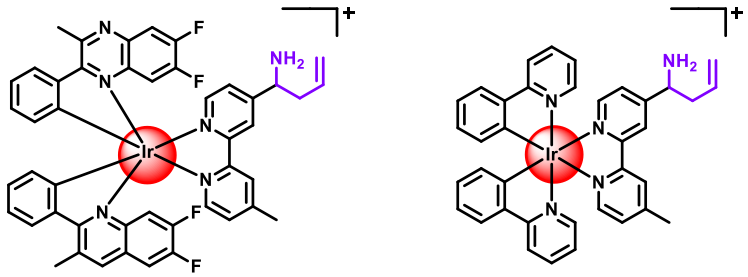

Fig. 1.10. Chemical structures of Ir(III)-based probes **10a** and **10b** (Liu et al., 2023).

In 2021, Song *et* al. (Song et al., 2021) reported a novel inorganic fluorescent sensor, probe **11**, with 1,10-phenanthroline derivative, and 2-thenoyltrifluoroacetone (TTA) as ligand (**Fig. 1.11**). The Eu^{3+} ion is in eight-coordinated state, bonded to six O atoms from TTA and two N atoms from the phen derivative. Probe **11** in CH_3OH exhibited broad absorption bands peaks at 274, 289, and 337 nm. These peaks are seen as a combination of the absorption

of the component parts, slightly altered by the coordination to the Eu^{3+} ion. The absorption spectrum of complex **11** was shifted to a longer wavelength when compared to the individual ligands, suggesting stabilization of ligand orbitals and the formation of extended conjugated chelate systems upon complexation with metal ion. The addition of Al^{3+} or Zn^{2+} ions, resulted in significant red shift in the absorption spectrum band specifically to 278, 307, and 353 nm with Al^{3+}, and to 279, 299, and 342 nm with Zn^{2+} ions. The phen derivative ligand showed a broad emission band at 490 nm when excited at 350 nm in the solid state. However, **11**, in both solid state and solution, exhibited the distinctive narrow emission bands of the Eu(III) ion when excited at 340 nm at 580, 591, 612, 652, and 702 nm, corresponding to the $^5D_0 \rightarrow {}^7F_0$, $^5D_0 \rightarrow {}^7F_1$, $^5D_0 \rightarrow {}^7F_2$, $^5D^0 \rightarrow {}^7F_3$, and $^5D_0 \rightarrow {}^7F_4$ transitions respectively. The intense peak at 612 nm, corresponded to the electric dipole $^5D_0 \rightarrow {}^7F_2$ transition, is significantly stronger than the magnetic dipole $^5D_0 \rightarrow {}^7F_1$ transition at 591 nm, which strongly suggests that the Eu^{3+} ions are in a low-symmetry environment without inversion centers, consistent with crystal structure analysis. The absence of the broad ligand emission band around 490 nm in the spectrum of **11** indicated effective energy transfer from the ligand's excited states to the Eu^{3+} ion's excited states, which contributes to the complex's luminescence properties, including a long lifetime (0.29 ms) and high quantum yield (20.42% in solid, 21.58% in methanol solution). The complex displayed a red colour in both solid and methanol solution, as indicated by the CIE chromaticity coordinates (x = 0.67, y = 0.33 in solid; x = 0.65, y = 0.33 in methanol). The emission spectra of **11** undergo significant emission changes when Al^{3+} was introduced into a methanolic solution of probe. The characteristic Eu^{3+} emission bands at 612 nm completely quenched, and simultaneously a ligand-based emission band appeared at 388 nm with a colour change from red to bright blue in UV light.

Similarly, the addition of Zn^{2+} also caused Eu^{3+} emission band to vanish. A ligand-based emission band again emerges, but unlike in case of Al^{3+}, emission band was seen at 485 nm. This results in a change in fluorescent colour from red to ivory. These distinct colour changes in probe **11** allowed for naked-eye detection and discrimination of Al^{3+} and Zn^{2+} ions. The sensor exhibits high

sensitivity, with calculated detection limits of 588 nM for Al^{3+} and 76.78 nM for Zn^{2+}. The sensing mechanism was primarily attributed to a displacement process where Al^{3+}/Zn^{2+} ions could successfully displace the Eu^{3+}, forming a new emissive species with distinct emission features.

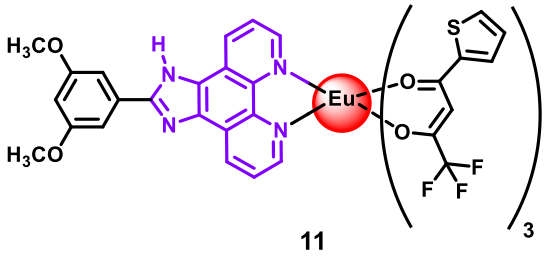

11

Fig. 1.11. Chemical structure of Eu(III)-based probe **11** (Song et al., 2021).

1.4. Optical Probes for Anions

In the past two decades, there has been a growing interest in the development of synthetic molecular probes responding selectively to anions (Beer and Gale, 2001; Busschaert et al., 2015). Drawing attention from researchers across multiple scientific domains this heightened focus is largely driven by the critical role anions play in a wide array of biological, environmental, aquatic, and industrial processes. Many of these necessitate accurate detection and identification of specific anionic species through optical sensing strategies. Biologically relevant anions such as fluoride (F^-), chloride (Cl^-), hydrogen phosphate (HPO_4^{2-}), and carbonate (CO_3^{2-}) are associated with various physiological functions and pathological conditions, including fluorosis and cystic fibrosis, making them priority targets for molecular recognition systems (Al-Abadleh et al., 2005; Berend et al., 2012; Takeda et al., 2004; Wu et al., 2022). Despite their significance, the effective sensing of anions remains inherently challenging due to their structural diversity and high solvation energies in aqueous media (Bodman and Butler, 2021; Butler and Parker, 2013).

Traditional detection techniques, ICP-MS, AAS, high performance liquid chromatography (HPLC), reflection X-ray fluorescence analysis (XRF), attenuate total reflectance chromatography and electrochemical methods, offer high accuracy but are often limited by the need for expensive instrumentation

and labor-intensive sample preparation (Arienzo and Capasso, 2000; Hatsis and Lucy, 2002; Hatzistavros and Kallithrakas-Kontos, 2011; Hein et al., 2020b). In response, optical sensors have emerged as promising alternatives owing to their synthetic tunability, cost-effectiveness, fast response times, ease of use, and remarkable sensitivity and selectivity (Butt et al., 2024; Rasheed et al., 2024).

However, the design of anion-specific sensors is more complex compared to cation recognition, primarily due to the lower charge-to-radius ratios of anions, which typically result in weaker binding affinities with receptor systems (Carreira-Barral et al., 2014; Patrick et al., 2024). Therefore, the development of effective anion-responsive probes demands meticulous molecular engineering that takes into account a range of non-covalent interactions such as electrostatic attractions, hydrogen bonding, π–π stacking, and hydrophobic effects to ensure both selectivity and sensitivity in target detection (Molina et al., 2017; Wang and Wang, 2020). To advance anion sensing, a diverse range of luminescent probes has been developed in recent years, encompassing synthetic organic and inorganic compounds, graphene quantum dots, functional group-doped nanomaterials, and metal-organic frameworks (MOFs) (Chang et al., 2015; Goshisht and Tripathi, 2021; Mandal et al., 2018; Mao et al., 2015).

1.4.1. Probe design for anion recognition

A central strategy in the design of molecular luminescent probes involves the covalent integration of a chromophore (serving as the signaling unit) with a supramolecular receptor (the binding site), enabling selective and high-affinity interactions with target analytes. Performance of probe relies on close spatial proximity and efficient electronic communication between the photoactive chromophore and the receptor, leading to measurable optical changes upon analyte binding (Czarnik, 1994; Gale and Caltagirone, 2015; Yoon et al., 2006). As a result, a wide array of molecular probes has been developed for anion sensing, demonstrating success in both purely organic and mixed aqueous-organic media. Despite substantial progress in this field, achieving high selectivity in anion recognition particularly under aqueous and physiological conditions remains a persistent challenge (Butler and Parker, 2013; Gale and

Caltagirone, 2015; Kubik, 2010). This difficulty stems from several inherent characteristics of anions, including their diffuse charge distributions (in contrast to isoelectronic cations), structural diversity (e.g., linear, spherical, trigonal planar, tetrahedral geometries), sensitivity to pH, and strong solvation in polar solvents (Bodman and Butler, 2021; Butler and Parker, 2013; Naithani et al., 2023b). To overcome these limitations, various design strategies have been proposed over the past two decades, with noncovalent interactions, especially hydrogen bonding, emerging as one of the most effective and extensively studied approaches. Hydrogen bonding, typically involving a donor-hydrogen-acceptor (D-H···A) arrangement, forms the basis for many supramolecular recognition systems (Desiraju, 2011). In anion sensing, receptors often incorporate N-H groups as hydrogen bond donors. Early examples of such systems featured cationic ammonium motifs to promote electrostatic interactions with anions (Park and Simmons, 1968). Since then, a wide range of amine-based receptors have been introduced, with amides and ureas being among the most commonly used due to their synthetic accessibility. However, the presence of carbonyl groups (>C=O) in these molecules, which can also act as hydrogen bond acceptors, may compromise anion binding by competing with target species (Molina et al., 2017). To address this issue, the design of alternative hydrogen bond donor frameworks has gained traction. Moreover, successful anion recognition has been achieved via hydroxyl group (Bao et al., 2009).

Heterocyclic units such as pyrroles and imidazoles have been increasingly employed due to their favorable binding characteristics (Molina et al., 2012; Sessler et al., 2003). Additionally, 1,2,3-triazole-containing systems have emerged as valuable motifs for anion recognition (Kashyap et al., 2020). The polarization of the C-H bond by the three nitrogen atoms in the triazole ring generates a pronounced dipole moment along the C5-H axis, enhancing the ability of the probe to engage in strong directional interactions with anionic species.

1.4.2. Organic probes

Anion sensing has gained significant attention due to the crucial roles anions play in biological, environmental, and industrial systems (Beer and Gale, 2001; Busschaert et al., 2015). Organic probes are widely employed for anion detection because of their structural tunability, high sensitivity, and selectivity (Goshisht and Tripathi, 2021; Lee et al., 2015). They can be rationally designed to incorporate specific recognition sites (e.g., amide, urea, thiourea, or pyridinium groups) that interact with anions via hydrogen bonding, electrostatic, or coordination interactions. Additionally, many organic probes exhibit optical responses (fluorescence or color change) upon anion binding, enabling real-time, non-invasive, and low-cost detection (Lee et al., 2015; Schmidtchen and Berger, 1997). Their versatility and adaptability make them good candidates for developing efficient chemosensors for a wide range of anions.

Bhaskar *et* al. (Bhaskar et al., 2022) employed a previously reported a fluorescent probe **12** which was previously employed for Cd detection and was derived from quinoline (**Fig. 1.12**). Quinoline was chosen as a fluorophore due to their strong chelating abilities and distinctive photophysical properties. Initially, free probe **12** exhibited emission band at 500 nm when excited at 380 nm in CH_3CN/H_2O (7: 3, v/v). However, the addition of F^- ions to the **12**-solution resulted in a significant increase in fluorescence intensity at 500 nm. This fluorescence enhancement was highly selective for fluoride ions, as other tested anions did not produce the same effect. Competitive studies further confirmed that fluoride could be recognized without interference from other anions or metal ions. The fluorescence enhancement was caused by a hydrogen bonding interaction between the F^- ion and the hydrazine-NH and phenolic-OH groups of the probe. At low fluoride concentrations, N-H----F^- and O-H----F^- hydrogen bonding occurs, and with increasing fluoride, leads to deprotonation of the probe's -NH and -OH groups. The emission quantum yield of **12** (Φ_{em} = 0.021) was notably enhanced upon binding with fluoride (Φ_{em} = 0.11). The fluoresce titration experiments were utilized to determine the detection limit for F^- ions (0.128 μM). The binding constant was determined from the Benesi-

Hildebrand (B-H) plot to be 7.88 × 10^{-3} M^{-1}. Job's plot, derived from spectroscopic data suggested a 1:1 binding stoichiometry between **12** and F^-. The influence of pH on the probe's fluorescence response was studied across the range of 1 to 11. The emission of **12** remained stable across this pH range, indicating its stability, while the fluorescence of the probe-fluoride complex varied, showing capability for fluoride sensing within the pH ranges of 1-11 however best results were obtained in between pH 6-9.

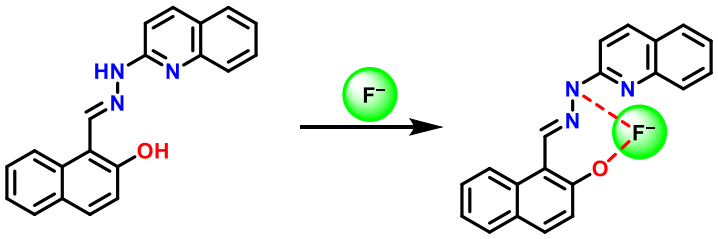

12 **12-F⁻**

Fig. 1.12. Binding mode of **12** (50 μM) (7:3 V/V) with F^- in CH_3CN/H_2O (Bhaskar et al., 2022).

A new probe **13** was developed by Sahu *et* al. (Sahu et al., 2019) for detecting F^- ions. In ACN solution, **13** initially appeared yellow **(Fig. 1.13)**. The UV-Vis titration experiment showed an absorption band at 363 nm for **13**. Introduction of F^- ions to probe solution resulted in the gradual emergence of a new absorption band at 506 nm. This new band corresponded to the observed color shift from yellow to orange, which is highly specific to the addition of F^-. Concomitantly, absorption bands at 363 nm fell, and isosbestic points were observed at 406 nm and 285 nm. The absorption titration profile was saturated after adding 10 equiv. of F^-. The LoD for F^- ions calculated was 6 μM. The color change and the appearance of the new band at 506 nm were attributed to the deprotonation of the -NH proton in the thiosemicarbazone moiety of probe by the F^- anion. This deprotonation triggers an ICT phenomenon, leading to increased electron density on the quinoxaline part of **13** and the appearance of a new band at 506 nm. Other common ions did not interfere, although a slight color change was observed with OAc^-. Computational studies using TD-DFT

supported these experimental findings, suggesting only F^- could effectively deprotonate **13** among investigated anions. The probe's reversibility was also tested by adding Ca^{2+} to the probe solution containing F^-. This reversibility suggests that **13** can be used over multiple cycles. Furthermore, the ability of **13** to detect F^- visually was also successfully demonstrated in real-world samples like toothpaste, test paper, and gel form.

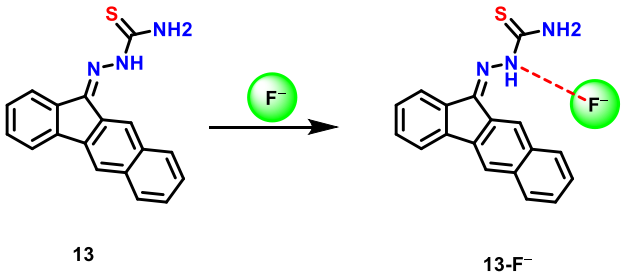

Fig. 1.13. Binding mode of **13** (10 μM) with F^- in CH_3CN (Sahu et al., 2019).

Mu *et* al. (Mu et al., 2022) designed probe **14** with perylene monoimide chromophore due to its high fluorescence quantum yield and good photostability (**Fig. 1.14**). The large π-conjugate system and electron-withdrawing nature of this chromophore facilitate the construction of a strong donor-π-acceptor (D-π-A) structure, which is intended to cause a significant red shift in the absorption band upon interaction with analyte. Moreover, an -OH group was introduced as the recognition unit in framework due to its strong affinity for anions, while a tertiary amine group was added to improve solubility. In THF, **14** exhibited a maximum absorption peak at 520 nm and fluorescence emission peak at 600 nm upon excitation at 520 nm. The addition of F^-, resulted in remarkable red shift in the absorption band from 520 nm to 742 nm (~ 220 nm red shift). This change was also accompanied by a significant color change of the solution from pink to green. Concurrently, the fluorescence of **14** at 600 nm was also substantially quenched and fluorescence quantum yield also exhibited significant reduction from 14.8% to 1.6% after the addition of F^-. The LoD calculated from the absorbance ratios (A_{742}/A_{520}) was 0.994 μM. From the fluorescence intensity changes, a lower LoD of 0.495 μM was calculated within the linear range of 2.0 to 9.0 μM. The detection mechanism

was proposed to involve strong H-bonding interactions between F^- and the OH group, leading to eventual deprotonation. The deprotonation significantly enhances the electron-donating ability of **14**, resulting in the significant red shift of the absorption band and the high-contrast color change. The change in electron density upon deprotonation was further conformed by DFT studies. The disappearance of the OH stretching vibration peak in IR spectra after F^- addition also supports the deprotonation process due to $F^-\cdots$H-O interactions. **14** was also successfully applied to detect fluoride in real water samples. The reversibility of **14** was also confirmed, showing that the spectral changes induced by F^- could be reversed by adding certain metal ions like Ag^+, which destroys the H-bonding interactions, possibly due to the poor solubility of metal fluorides in THF.

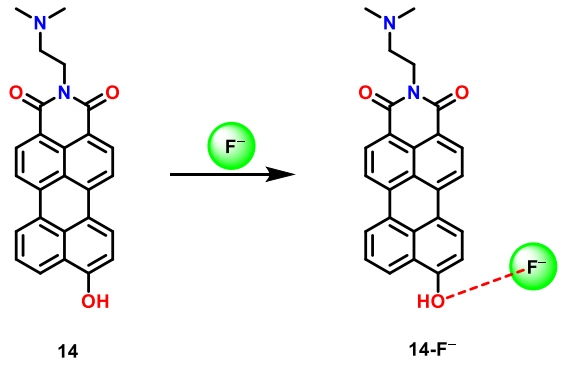

Fig. 1.14. Binding mode of **14** (10 μM) with F^- in THF (Mu et al., 2022).

Yilmaz *et* al. (Yilmaz et al., 2022a) developed probe **15** a fluorogenic naphthalene-based receptor, for the detection of CN^- (**Fig. 1.15**). UV-Vis studies revealed probe solution in DMF/H_2O solution (1:1, v/v) exhibited an absorption band at around 450 nm which is characteristic of the naphthalene ring. Moreover, when excited at 460 nm, probe exhibited a strong emission peak at 520 nm. Upon introduction of the cyanide ions, the absorption at 450 nm sharply decreased, whereas a corresponding increase in absorption was noted at approximately 480 nm and 340 nm. A clear isosbestic point was observed at 378 nm and saturation point was reached at 2 equiv. of cyanide ion. The binding stoichiometry was determined to be 1:2 by UV-Vis, fluorescence titration experiment and Job's method. The pH studies indicated that **15** recognition of

CN^- is minimally affected by pH in the range of 4 to 10, which is important for its potential use in biological systems. The addition of cyanide ion also significantly affected the emission spectra of probe. The emission band was significantly quenched after the addition of cyanide ion whereas other ions failed to produce any notable changes. Based on absorption titration studies, LoD for cyanide was calculated to be 0.21 µM. Probe was also successfully applied for bio-imaging of cyanide in living cells. Experiments with human epithelial cells (HEK 293) showed that probe exhibited strong fluorescence within the cells when present alone. Upon the addition of cyanide ions, a dramatic decrease in fluorescence intensity was observed. This demonstrated that **15** can detect cyanide ions inside living cells and exhibits an "off-on" fluorescence response in this context.

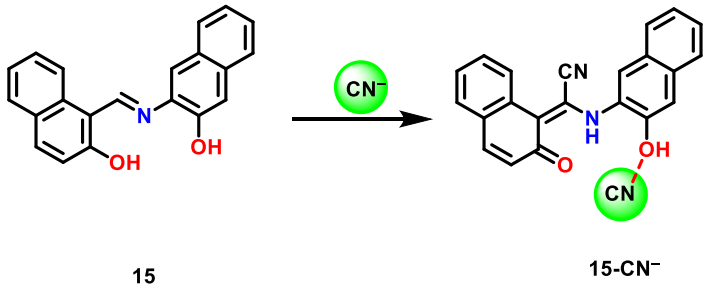

Fig. 1.15. Binding mode of **15** (10 µM) with CN^- in DMF/H_2O (1:1 v/v) (Yilmaz et al., 2022a).

1.4.3. Metal complexes based probes

Probes incorporating both hydrogen bond-donating amine functionalities (specifically the N-H group of the imidazole ring) and metal-coordinating imine nitrogen atoms (derived from the phenanthroline scaffold) have attracted considerable research interest (Chang et al., 2015). Importantly, the imidazole N-H group serves as a biologically relevant hydrogen bond donor, commonly found in natural systems. For instance, the imidazole rings present in histidine residues and Vitamin B compounds play essential roles in mediating hydrogen bonding interactions within various biochemical processes (Deepak and Sankararamakrishnan, 2016; Sundberg, 1974). It is well established that the presence of a strongly electron-withdrawing group at this position, particularly

in conjunction with an electron-deficient metal center (i.e., a strong Lewis acid), enhances the acidity of the N-H proton in the imidazole ring. This increase in proton acidity, in turn, reinforces the hydrogen bonding interaction between the N-H group and the target anion, thereby improving the probe's binding affinity and sensing efficiency. These inorganic probes exhibit increased water solubility, large stokes shift, and long-lived excited states making them ideal candidates for anion recognition (Chang et al., 2015; Naithani et al., 2023b).

The substituent at the 2-position of the imidazole ring plays a crucial role in modulating the anion selectivity of imidazo-phenanthroline (imidazo-phen) based receptors. In this context, Ye and co-workers (Mo et al., 2012) synthesized a series of luminescent Ru(II) complexes, designated as **16a-16d**, incorporating imidazo-phen ligands with phenyl rings bearing different substituents at the imidazole 2-position (**Fig. 1.16**). These complexes exhibited characteristic Ru(II)-centered absorption and emission bands in the ranges of 456-462 nm and 593-596 nm, respectively. Their sensing capabilities were evaluated against a panel of anions, including AcO^-, F^-, Cl^-, Br^-, I^-, NO_3^-, HSO_4^-, ClO_4^-, $H_2PO_4^-$, HCO_3^-, N_3^-, and SCN^-, in both DMSO and HEPES buffer (pH 7.5). Among the series, probe **16a** showed a selective luminescence quenching response toward CN^-, with a 31% decrease in emission intensity accompanied by a ~6.0 nm red-shift in the emission maximum in HEPES buffer. This selectivity was attributed to multipoint hydrogen bonding interactions involving the imidazole N-H and phenyl C-H protons. Job's plot analysis confirmed a 1:1 binding stoichiometry for the **16a**-CN^- complex. In aqueous medium, the binding constant for **16a** was estimated to be 345 ± 21 M^{-1}, with a K_{SV} of 0.069 ± 0.004 M^{-1} and a bimolecular quenching rate constant of 1.61 × 10^5 $M^{-1}s^{-1}$. The LoD for CN^- using probe **16a** was determined to be 100 μM. A pH-dependent luminescence study revealed a decrease in emission intensity by 37%, 36%, 37%, and 38% for **16a-16d**, respectively, as the pH was lowered from 6.0 to 3.0. Probes **16b-16d** failed to detect CN^- in aqueous media; however, slight emission quenching and minor red shifts (up to 4 nm) were observed for **16c** (~34% decrease) and **16d** (~32% decrease) in DMSO. The presence of five methyl groups in probe **16d** likely reduced the acidity of the

imidazole N-H proton, resulting in a lower binding constant ($1.16 \pm 0.07 \times 10^6$ M^{-1}) compared to probe **16b** ($2.15 \pm 0.15 \times 10^6$ M^{-1}). Interestingly, probe **16c** exhibited a higher binding constant ($6.54 \pm 0.41 \times 10^6$ M^{-1}) than both **16b** and **16d**, possibly due to the increased availability of the phenyl C-H group for hydrogen bonding with the target anion.

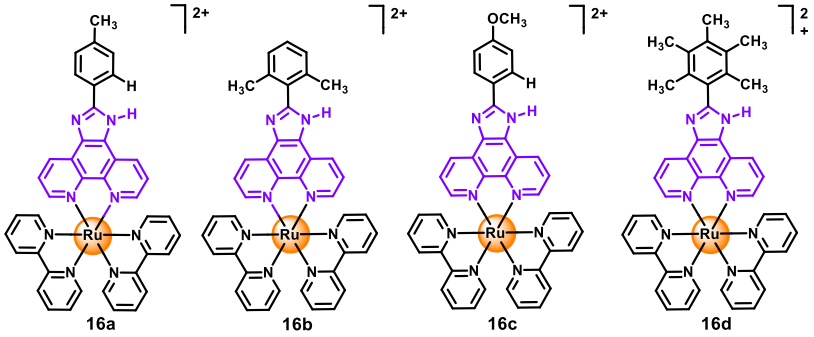

Fig. 1.16. Chemical structures of Ru(II)-based probes **16a-16d** (Mo et al., 2012).

An imidazo-phen based colorimetric sensor (**17**) incorporating an azo-coupled salicylaldehyde scaffold was developed by Khanmohammadi *et* al. (Khanmohammadi and Rezaeian, 2014) for the selective recognition of fluoride (F^-) ions in commercially available vinegar and mouthwash samples (**Fig. 1.17**). Both the ligand and its corresponding Ru(II) complex were evaluated for their anion sensing capabilities using UV-Vis and fluorescence spectroscopy. The presence of electron-deficient Ru(II) centers along with a strongly electron-withdrawing nitro ($-NO_2$) group in probe **17** was found to enhance the acidity of the N-H proton, thereby facilitating stronger hydrogen bonding interactions with anions. Upon addition of 5.0 equiv. of F^-, AcO^-, or $H_2PO_4^-$ ions to a DMSO solution of **17** (2×10^{-5} M), a distinct color change from light orange to dark brown was observed, indicating effective anion binding. In contrast, other anions such as Cl^-, Br^-, I^-, ClO_4^-, N_3^-, NO_3^-, and HSO_4^- did not induce any visible color change. The UV-Vis spectrum of **17** displayed two strong absorption bands at 289 nm and 355 nm corresponding to intraligand $\pi \rightarrow \pi^*$ transitions, along with a MLCT band at 461 nm. Upon addition of F^-, AcO^-, and $H_2PO_4^-$, a new absorption band emerged at 560 nm, accompanied by a

decrease in intensity of the 289 and 355 nm bands. The progressive increase in absorbance at 560 nm with further anion addition suggested a strong host-guest interaction. Fluorescence spectral studies showed a significant enhancement in the emission intensity at 735 nm upon the addition of 5.0 equiv. of F^-, AcO^-, or $H_2PO_4^-$, further confirming strong probe-anion interactions. Notably, the binding constants for **17** (1.04×10^5 M^{-1} - 2.66×10^5 M^{-1} in DMSO) were significantly higher than those of the free ligand (6.57×10^4 M^{-1} - 8.20×10^4 M^{-1}), highlighting the role of the electropositive Ru(II) center in modulating the acidity of the N-H proton. A 1:1 stoichiometric interaction between the probe and anion was established through Job's plot and B-H analyses. The LoD for F^-, AcO^-, and $H_2PO_4^-$ were determined to be 1.55×10^{-6} M, 1.27×10^{-6} M, and 2.27×10^{-6} M, respectively. Comparable spectral and colorimetric changes were observed in DMSO-water mixtures (9: 1, v/v), indicating minimal interference from water, a typically competitive medium for anion binding. For real-world applications, probe **17** demonstrated practical utility in detecting F^- and AcO^- ions in commercial mouthwash and vinegar samples, respectively. Upon addition of a single drop of either sample, a visible color change occurred immediately. This observation was further validated by the appearance of the 560 nm band in the UV-Vis spectrum. ^1H NMR studies supported a mechanism involving deprotonation of the phenolic -OH group by the anion, followed by stabilization of the resulting phenoxide via intermolecular hydrogen bonding.

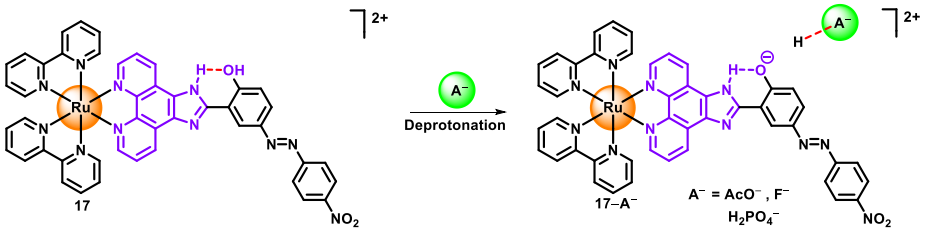

Fig. 1.17. Chemical structures of Ru(II)-based probe **17** (20 μM) and its binding with anions in DMSO (Khanmohammadi and Rezaeian, 2014).

Most imidazo-phen derived Ru(II) probes reported to date incorporate electron-withdrawing substituents on the imidazole ring, primarily to enhance the acidity of the N-H proton and thereby strengthen anion-receptor interactions. In contrast, systems bearing electron-donating substituents are

relatively scarce. Alreja and co-workers (Alreja and Kaur, 2016a) synthesized probe **18**, featuring an electron-rich 2-methoxyphenyl group at the imidazole moiety (**Fig. 1.18**). Probe **18** exhibited a characteristic MLCT absorption band at 456 nm, along with a high-energy ILCT band at 289 nm. Upon excitation at 285 nm, the emission maximum appeared at 603 nm. UV-Vis spectral studies revealed minimal changes in the MLCT band of probe **18** even upon the addition of 100 equiv. of various anions. However, a slight enhancement at 289 nm was observed, suggesting the involvement of a PeT process. Emission studies indicated significant quenching of luminescence at 603 nm upon the addition of F^-, AcO^-, CN^-, $H_2PO_4^-$, and SO_4^{2-} ions. The most pronounced quenching occurred with AcO^-, followed by F^-, CN^-, $H_2PO_4^-$, and SO_4^{2-}. In contrast, little to no response was observed for Cl^-, Br^-, I^-, and HSO_4^- ions. Notably, the red luminescence of probe **18** was completely quenched in the presence of acetate ion in DMSO under UV light, consistent with visual detection. The emission quenching was attributed to deprotonation of the imidazole N-H group, which facilitates PET from the excited Ru(II) center to the imidazo-phen scaffold. A 1:1 binding stoichiometry between the probe and the anion was supported by both Job's plot and B-H analyses. The LoD for acetate ion was determined to be 5.25×10^{-7} M. Among the tested anions, AcO^- exhibited the strongest interaction, as reflected in the highest luminescence quenching and association constant values. This selectivity is likely due to the trigonal geometry and high basicity of AcO^-, which promotes strong hydrogen bonding with the imidazole ring. These findings were further corroborated by DFT calculations.

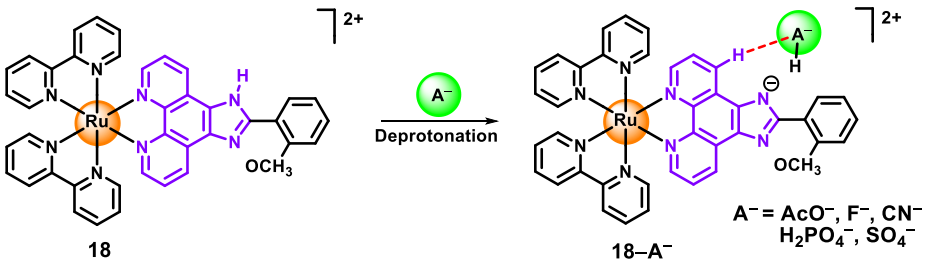

Fig. 1.18. Chemical structure of Ru(II)-based probe **18** (10 μM) and its binding with anion A^- in DMSO (Alreja and Kaur, 2016a).

Ru(II)–Cu(II) ensembles, namely **19a**-Cu^{2+} and **19b**-Cu^{2+}, incorporating a 2-hydroxyphenyl imidazole moiety, have been employed by Zheng and co-workers (Zheng et al., 2017) for the selective detection of CN^- in aqueous media (**Fig. 1.19**). In these systems, Cu^{2+} serves as a key mediator due to its strong affinity for cyanide anions. Although the formation of the **19b**–Cu^{2+} complex was initially reported by Zhang *et* al., its application in anion sensing was first explored in detail by Zheng's group. The sensing capabilities of the **19a**-Cu^{2+} and **19b**-Cu^{2+} ensembles toward CN^- were investigated using UV-Vis and fluorescence spectroscopy in aqueous HEPES buffer (20 mM, pH 7.2). Upon stepwise addition of CN^- to **19a**-Cu^{2+}, the absorption intensities at approximately 285 nm, 360 nm, and 460 nm increased, while bands near 320 nm and 490 nm gradually diminished. Furthermore, a pronounced luminescence "turn-on" response was observed: the emission intensity near 589 nm increased by approximately 15-fold for **19a**-Cu^{2+} and 7-fold for **19b**-Cu^{2+} upon CN^- addition. This luminescence enhancement was visibly detectable under UV illumination.

Selectivity studies confirmed that the fluorescence response of both ensembles to CN^- was not significantly influenced by the presence of other competing anions such as F^-, $H_2PO_4^-$, and AcO^-. Notably, both systems displayed a rapid response time of less than 2 minutes, outperforming previously reported ensembles that required either a higher concentration of CN^- or prolonged incubation times (>10 minutes). The detection limits for CN^- were determined to be 0.36 µM and 0.62 µM for **19a**-Cu^{2+} and **19b**-Cu^{2+}, respectively, in 99% aqueous solution. The practical utility of probe **19a**-Cu^{2+} was demonstrated through recovery experiments in tap water, where CN^- at concentrations of 1.50 µM, 3.00 µM, and 5.00 µM was successfully detected with recovery rates exceeding 90%.

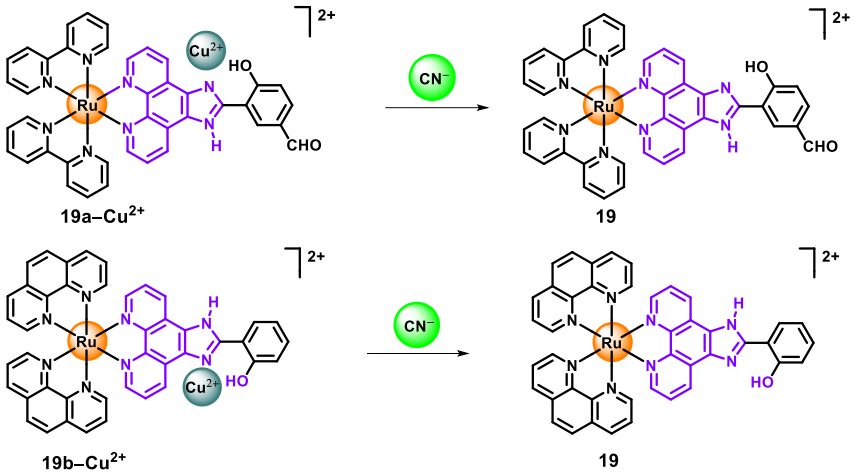

Fig. 1.19. Chemical structures of Ru(II)-based probes **19a**-Cu^{2+} and **19b**-Cu^{2+} and their interaction with CN^- ion in water (Zheng et al., 2017).

In 2020, Obali (Obali, 2020b) reported the development of two Ru(II)-based chemosensors, designated as **20a** and **20b**, featuring hydroxy- and methoxy-substituted polypyridyl ligands for the detection of CN^- in aqueous media (**Fig. 1.20**). Both complexes exhibited three characteristic absorption bands near 285 nm, 335 nm, and 460 nm. The first two high-energy bands were attributed to ligand-centered ($\pi \rightarrow \pi^*$) transitions, while the band around 460 nm corresponded to a typical MLCT transition involving $d\pi(Ru^{2+}) \rightarrow \pi^*$(ligand) orbitals. The anion sensing capabilities of these probes were systematically evaluated using UV-Vis and fluorescence spectroscopy. Upon the addition of CN^-, noticeable changes were observed in the absorption band at 285 nm for both **20a** and **20b**, suggesting the involvement of an ICT mechanism. Under excitation at 270 nm, probe **20a** exhibited emission bands at 387 nm, 501 nm, and 710 nm, while probe **20b** showed emission at 380 nm, 490 nm, and 712 nm. Introduction of CN^- ions resulted in a significant enhancement of luminescence intensity in both probes, accompanied by redshifts of approximately 75 nm for **20a** and 50 nm for **20b**.

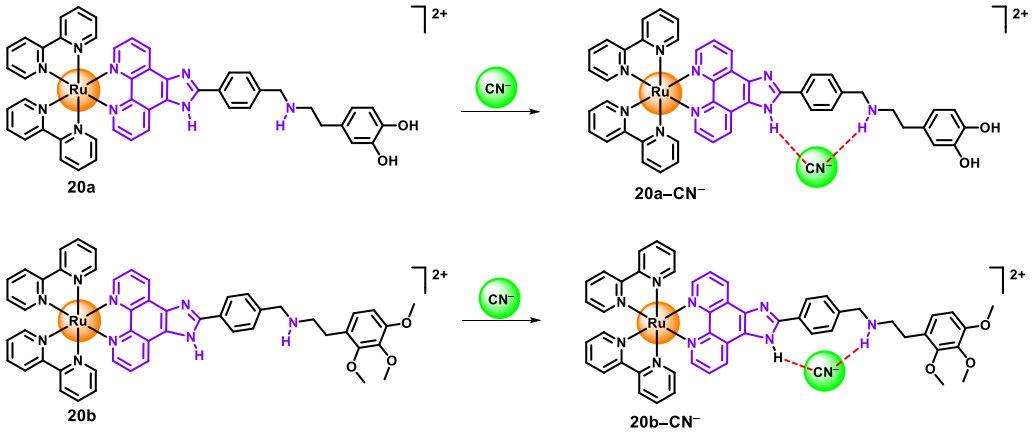

Fig. 1.20. Chemical structures of Ru(II)-based probes **20a** and **20b** (10 μM) and their H-bonding interaction with the CN^- ion in water (Obali, 2020b).

1.5. Photosensitizers in Photocatalysis

In photoredox catalysis, photosensitizers play a crucial role by initiating photoinduced electron or energy transfer events upon light absorption (Ghosh et al., 2017; Yadav et al., 2024). This excitation process triggers a cascade of mechanistic pathways, often involving highly reactive and short-lived radical intermediates. As a result, deciphering the underlying mechanisms remains a complex challenge, particularly when competing pathways coexist or when transient species are difficult to isolate or monitor (Lang et al., 2016; Pitre et al., 2016). Despite these intricacies, the efficiency and applicability of a photosensitizer in a given photoredox transformation are primarily dictated by three key parameters: (i) light absorption characteristics, which determine the extent to which the sensitizer can harvest photons in the desired spectral region; (ii) excited-state redox potentials, which govern the thermodynamic feasibility of photoinduced electron transfer events; and (iii) excited-state lifetime, which controls the temporal window available for productive interactions before deactivation to the ground state (Arias-Rotondo and McCusker, 2016; Chauhan et al., 2025). In addition to these intrinsic photophysical parameters, the chemical and photostability of the photosensitizer under operational conditions is crucial. A stable catalyst ensures sustained activity over time, allowing for low catalyst loadings and improved turnover numbers. Furthermore, the stability of the redox states involved is essential for efficient diffusion and for

completing the catalytic cycle without degradation or side reactions (D. Kim et al., 2024; Ravetz et al., 2020).

Another critical factor that shapes the performance of photocatalysts is the quantum yield of the photoinduced electron or energy transfer processes (Hagfeldt et al., 2010). This yield is significantly influenced by the fate of the radical ion pairs generated immediately after photoinduced electron transfer. These ion pairs typically form within a solvent cage, and for the photoredox cycle to proceed productively, cage escape must occur- allowing the oxidized or reduced species to diffuse and participate in subsequent chemical steps. Without effective cage escape, even highly efficient quenching processes can lead to recombination or unproductive pathways, ultimately diminishing the overall quantum efficiency of the system (Kim et al., 2024; Ravetz et al., 2020).

A diverse array of photosensitizers has been reported in the literature, spanning organic dyes, inorganic complexes, and organometallic species (Knör and Monkowius, 2011; Smith et al., 2022; Wang et al., 2024). Among these, transition metal polypyridyl complexes (particularly those of ruthenium and iridium) have historically dominated the field due to their favorable absorption in the visible range, robust redox properties, photostability, and long-lived MLCT excited states (Angerani and Winssinger, 2019; Kärkäs et al., 2014; Marzo et al., 2018; Prier et al., 2013; B. Zhang and Sun, 2019). Complexes such as $[Ru(bpy)_3]^{2+}$ and $[Ir(ppy)_3]$ have thus served as benchmark systems in photoredox catalysis. However, efforts to expand the library of metal-based photosensitizers remain relatively limited. While Pt^{2+} and Pd^{2+} complexes exhibit well-characterized photoluminescent behavior, their integration into photoredox processes and single-electron transfer (SET) catalysis is still underexplored. Similarly, Cu^{+} complexes have attracted growing interest as earth-abundant alternatives, but they often suffer from challenges such as Jahn-Teller distortions upon oxidation, which can lead to ligand dissociation or structural rearrangement, particularly in heteroleptic systems (Cerfontaine et al., 2020; Iwamura et al., 2007; Shaw et al., 2007; Zhao, Hou, et al., 2021). Reports of photoluminescent Ni^{2+} complexes are even scarcer, with only a few documented examples demonstrating utility in photocatalytic contexts. Given

these limitations, Ru(II)-polypyridyl complexes continue to serve as model systems for developing new photocatalytic methodologies. Their well-defined photophysical behavior, redox tunability, and long-lived MLCT states make them ideal candidates for driving a wide range of redox transformations under visible light (Lechner et al., 2022; Li et al., 2023).

1.5.1. Photoredox catalysis: Bimolecular mixture *vs.* single molecular assembly

A central goal in catalysis is the development of efficient and sustainable methods for activating small molecules, such as molecular oxygen (O_2). Among the various strategies explored, visible-light-driven photoredox catalysis has gained significant attention for enabling the activation of organic and inorganic substrates under mild conditions (Liu and Wu, 2017; Yang et al., 2020). This approach benefits from the ability of certain transition metal complexes and organic dyes to undergo photoinduced SET event with substrates upon light absorption, thus enabling a wide range of redox reactions (Deng et al., 2018; Prier et al., 2013; Romero and Nicewicz, 2016; Wasielewski, 1992). Notably, Ru(II)-polypyridyl complexes, particularly Ru-bpy derivatives, have been widely employed as photosensitizers in photoredox catalysis due to their excellent photophysical and redox properties. These systems have found broad utility in synthetic organic chemistry, materials science, and inorganic transformation processes (Arias-Rotondo and McCusker, 2016; Prier et al., 2013).

Bimolecular systems: modular but diffusion-limited

Traditionally, many photoredox systems are based on a bimolecular mixture, consisting of a discrete photosensitizer (Ru_{phot}) and a separate catalytic unit (M_{cat}) often involving a transition metal complex such as Ru^{2+}, $Fe^{2+/3+}$, Cu^{2+}, Mo^{4+}, or Mn^{2+} (**Scheme 1.5**) (Arcudi et al., 2022; Company et al., 2014; Deng et al., 2018; Fukuzumi et al., 2011; Tao et al., 2017). In such systems, Ru_{phot} absorbs visible light and enters an excited state, enabling it to transfer an electron to or from the catalytic unit M_{cat}, thereby initiating substrate activation (Ting et al., 2020). The redox interplay between these two components forms the basis for metallaphotoredox catalysis. One of the principal advantages of

this bimolecular design is its modularity- the ability to tune and combine different photosensitizer and catalyst pairs for a desired transformation. Varying the ligand environment of either component allows for precise tuning of redox potentials, electronic communication, and catalytic behavior. The molar ratio of Ru_{phot} to M_{cat} can also be optimized to maximize catalytic efficiency, and this flexibility facilitates high-throughput screening for new functional systems (Amaro-Gahete et al., 2021; Chauhan et al., 2025).

However, this approach also suffers from several inherent limitations. The efficiency of electron transfer in bimolecular systems is diffusion-limited, requiring that the two molecular entities come into close proximity in solution. This can lead to kinetic constraints and reduced overall reactivity, particularly when the excited-state lifetime is short. Additionally, back electron transfer within solvent cages, quenching by solvent molecules, or non-productive energy loss during diffusion can diminish quantum efficiency. These drawbacks become especially pronounced at low catalyst concentrations or in media with limited mobility, ultimately reducing the overall photocatalytic performance (Amaro-Gahete et al., 2021; Gotico et al., 2021; Vidal et al., 2021).

Covalent dyads: enhancing intramolecular communication

To address the shortcomings of bimolecular systems, a growing body of research focuses on the development of covalently linked **Ru_{phot}–M_{cat}** assemblies. In these supramolecular architectures, commonly referred to as dyads (for dinuclear complexes) or triads (for trinuclear systems), the photosensitizer and catalytic fragment are joined through a covalent linker or bridging ligand, forming a single, well-defined molecular entity (Chao and Fu, 2013; Herrero et al., 2015; Mühldorf et al., 2020; Phungsripheng et al., 2017). Such intramolecular assemblies provide several key advantages. By tethering the two metal centers in close spatial proximity, they facilitate rapid and efficient intramolecular electron transfer upon photoexcitation, eliminating the need for diffusion-based encounters. This spatial control enhances the reaction kinetics, improves selectivity, and often leads to increased catalytic turnover (Ducrot et al., 2016; Singh et al., 2021).

The bridging ligand plays a critical role in dictating the photophysical behavior of the dyad (Cui et al., 2024; Morimoto and Ishitani, 2017). It modulates excited-state energies, electron-transfer rates, and charge-separation lifetimes. Two main types of linkers are typically employed: i) Rigid linkers, such as π-conjugated systems (e.g., alkynes, aryl groups), which provide well-defined geometries and efficient pathways for electron/hole transport, and ii) Flexible linkers, which allow for dynamic conformations but often at the expense of electronic coupling and spatial precision. Rigid, planar linkers are generally favored as they enable shorter and more directed electron-transfer pathways, facilitating stronger electronic communication and longer-lived charge-separated states, critical features for high-performance photoredox systems.

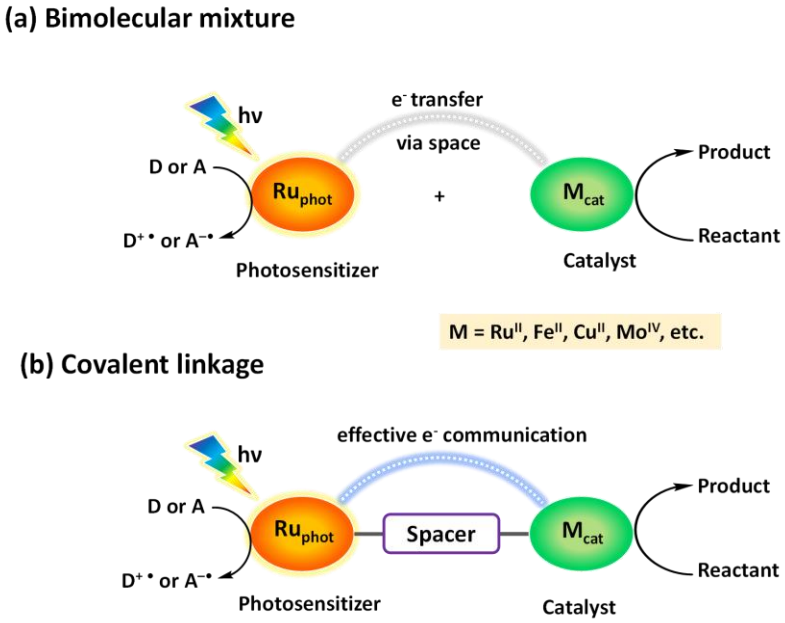

Scheme 1.5. Photoredox catalysis using Ru(II)-based photosensitizers: Bimolecular mixture vs. covalently bound single molecular assembly. A and D stand for sacrificial electron acceptor and electron donor, respectively (Chauhan et al., 2025).

Excited-state dynamics in dyads

Covalently tethered dyads frequently exhibit reduced luminescence quantum yields compared to the parent Ru_{phot} complexes. This quenching is typically indicative of photoinduced electron or energy transfer from the excited Ru_{phot} unit to the catalytic M_{cat} site. Time-resolved spectroscopy often reveals a

bi-exponential decay profile for the excited-state, with a short-lived component reflecting rapid intramolecular electron transfer, and a longer-lived component associated with the residual radiative decay of the ^{3}MLCT state. This change in excited-state behavior serves as a diagnostic marker for efficient intramolecular charge transfer and can be further optimized through careful design of the linker and metal coordination environments (Herrero et al., 2015; Iali et al., 2015).

Role of sacrificial reagents

In both bimolecular and dyad-based photoredox systems, sacrificial electron donors or acceptors are often employed to regenerate the ground-state Ru_{phot} species and complete the catalytic cycle. These reagents interact with either the oxidized or reduced form of the photosensitizer, depending on the nature of the transformation. For instance, reductive quenching pathways commonly use triethanolamine (TEOA), triethylamine (TEA), or ascorbic acid as electron donors, especially in hydrogen evolution or CO_2 reduction while the oxidative quenching mechanisms utilize agents such as persulfate ($S_2O_8^{2-}$) or $[Co(NH_3)_5Cl]Cl_2$ for oxidative organic transformations (Elgrishi et al., 2017; Kalita et al., 2011; Schulze et al., 2016; Streb, 2012). However, the use of stoichiometric sacrificial agents poses several challenges, including poor atom economy, generation of side products, and increased process complexity. As a result, significant research efforts are now directed toward developing catalytic systems that function without sacrificial reagents, relying instead on internal redox cycling or pairing with complementary half-reactions to maintain electron balance.

1.5.2. Unimolecular dyads for catalytic oxidation

Inspired by the various copper-based metalloenzymes found in nature, Iali *et* al. (2015) synthesized a hetero-dinuclear Ru^{II}_{phot}–Cu^{II}_{cat} complex, $[(bpy)_2Ru(bpbpa)Cu(OTf)(CH_3CN)]^{3+}$ (**21**) where bpbpa = *N*-(4-((5H-dipyrido[3,2-c:2’,3’-e]azepin-6(7H)-yl)methyl)benzyl)-1-(pyridin-2-yl)-*N*-(pyridin-2-ylmethyl)methanamine, incorporating a flexible linker (**Fig. 1.21**) (Iali et al., 2015). The complex displayed a ligand-centered π→π* transition at 290 nm and a Ru^{II}_{phot} based MLCT band between 445–455 nm. A weak d–d transition corresponding to the Cu^{II}_{cat} center was observed around 615 nm.

Electrochemical analysis revealed feasible PeT from $*Ru^{II}_{phot}$ to Cu^{II}_{cat}, evidenced by two quasi-reversible redox waves at +1.57 V and +0.42 V.

The emission band for dyad **21** appeared at 618 nm; however, its luminescence intensity and quantum yield were significantly reduced compared to the Ru^{II}_{phot} unit alone, likely due to PET quenching. While Ru^{II}_{phot}– exhibited a mono-exponential excited-state decay (~153 ns) in air-equilibrated solution, dyad **21** demonstrated biexponential decay kinetics, with a short-lived component (16 ns) and a longer-lived component (148 ns). The longer component was assigned to radiative deactivation of the triplet MLCT state, as inferred by comparison with the parent photosensitizer.

Upon light excitation and in the presence of TEOA as a sacrificial reductant, the complex underwent SET from Ru^{II}_{phot}-Cu^{II}_{cat}, yielding Cu^{I}_{cat}. This heterodinuclear dyad effectively catalyzed the selective oxidation of sulfides and triphenylphosphine without generating sulfone byproducts, demonstrating high selectivity and good turnover numbers (TONs). Furthermore, the complex was capable of oxidizing alkenes such as indene, cyclohexene, and cis-cyclooctene, yielding cis-diols (ca. 37%) and α- and β-unsaturated ketones, respectively. The proposed mechanism involves photoexcitation of Ru^{II}_{phot}-Cu^{II}_{cat}, followed by SET to form Ru^{III}_{phot}-Cu^{I}_{cat}. Regeneration of Ru^{II}_{phot} occurred via electron donation from TEOA, while Cu^{I}_{cat} formed a Cu^{II}-O_2 adduct, which served as the oxidizing species for substrate transformation.

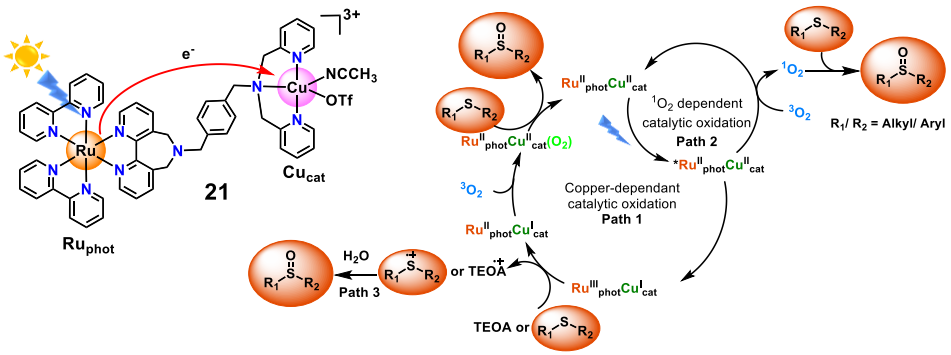

Fig. 1.21. Proposed catalytic mechanism for photocatalytic oxidation of organic substrates using hetero-dinuclear complex **21** with proposed catalytic mechanism (Iali et al., 2015).

Although the use of external sacrificial redox agents is essential for completing the photoredox catalytic cycle, their involvement often compromises atom economy due to the formation of undesired byproducts. Consequently, recent research efforts have been directed toward developing photocatalytic systems that operate without sacrificial agents. In 2017, Chao and Zhao (Chao and Zhao, 2017) reported **22** a Ru^{II}_{phot}-Cu^{II}_{cat} hetero-dinuclear dyad, $[Ru(deeb)_2(bpy\text{-}tpy)CuCl_2]^{2+}$, where deeb = 4,4′-diethylester-2,2′-bipyridine, for the aerobic oxidation of sulfides in the absence of any sacrificial redox agents (**Fig. 1.22**). UV-Vis spectroscopic studies revealed moderate absorption between 400 and 500 nm. The Ru^{II}_{phot} moiety alone exhibited a strong emission band at 650 nm, which was significantly quenched upon conjugation with the catalytic Cu^{II}_{cat} unit, indicating PeT from the excited photosensitizer to the catalytic center. Electrochemical measurements identified two semi-reversible redox waves at +0.54 V and +1.49 V (vs. SCE), corresponding to the Cu^{I}/Cu^{II} and Ru^{II}/Ru^{III} redox couples, respectively. The oxidation potential of $*Ru^{II}/Ru^{III}$ was determined to be approximately –0.53 V, confirming the thermodynamic favorability of electron transfer from $*Ru^{II}_{phot}$ to Cu^{II}_{cat} center.

Upon photoexcitation, $*Ru^{II}_{phot}$ was oxidized to Ru^{III}_{phot}, which subsequently oxidized the sulfide substrate. Simultaneously, the reduced Cu^{I}_{cat} facilitated O_2 activation, generating an active Cu^{II}–O_2 adduct, thereby regenerating the Ru^{II}_{phot}-Cu^{II}_{cat} dyad. The formation of intermediate species was monitored through emission spectroscopy and visual inspection under UV light. Initially, the dyad exhibited weak luminescence, which intensified upon UV irradiation, suggesting the formation of the reduced Ru^{III}_{phot}-Cu^{I}_{cat} species characterized by the d^{10} electronic configuration of the Cu(I) ion. Subsequent exposure to air resulted in luminescence quenching, attributed to the generation of the active Ru^{II}_{phot}-Cu^{II}_{cat} (O_2) complex. This hetero-dinuclear complex demonstrated remarkable catalytic performance in the selective aerobic oxidation of sulfides under blue LED irradiation in CH_3CN/H_2O (8: 2, v/v), yielding sulfoxides without the formation of sulfones. The system exhibited

high selectivity and an exceptional turnover number (TON) of up to 32,000 for various sulfide substrates.

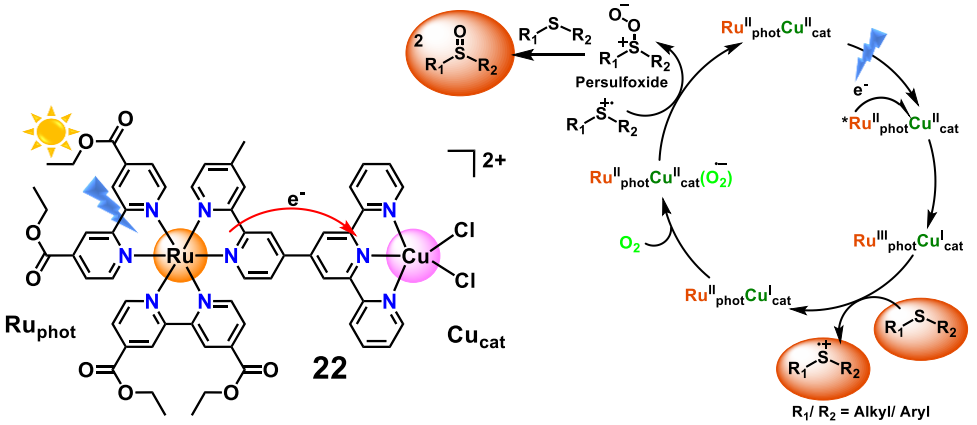

Fig. 1.22. Proposed catalytic mechanism for photocatalytic oxidation of organic substrates using hetero-dinuclear complex **22** with proposed catalytic mechanism (Chao and Zhao, 2017).

In a recent study (2023), Hamelin and co-workers (Klein et al., 2023) reported **23,** a Ru^{II}_{phot}-Cu^{II}_{cat} hetero-dinuclear dyad incorporating a 2,5-dimethylphenylene spacer unit (**Fig. 1.23**). Electrochemical investigations revealed a quasi-reversible redox couple attributed to the $Cu^{II/I}$ transition at –0.19 V and a reversible oxidation wave at 0.91 V corresponding to the $Ru^{III/II}$ couple. UV-Vis spectroscopic analysis showed a characteristic Ru^{II}-based MLCT band at 450 nm, along with ligand-centered π→π* transitions in the UV region. The isolated Ru^{II}_{phot} fragment exhibited strong luminescence with an average excited-state lifetime of 950 ns. However, upon covalent attachment of the Cu^{II}_{cat} moiety, a significant reduction (~35%) in emission intensity and lifetime was observed, indicating effective PeT between the two metal centers. For catalytic evaluation, 4-bromothioanisole was employed as a representative substrate under blue LED illumination (λ = 450 nm) in the presence of TEOA as a sacrificial electron donor and O_2 atmosphere in CH_3CN. The system demonstrated excellent catalytic efficiency, achieving up to 98% conversion. Moreover, the dyad exhibited broad substrate scope, with electron-donating substituents enhancing oxidation efficiency, up to 100% in the case of the -OMe

group. In contrast, substrates bearing strong electron-withdrawing groups, such as -NO_2, showed comparatively reduced conversion.

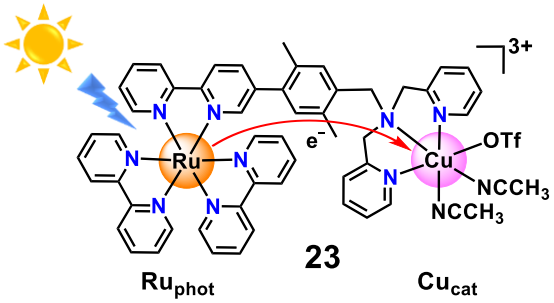

Fig. 1.23. Photocatalytic oxidation of various organic sulfides using hetero-dinuclear complex **23** under aerobic conditions (Klein et al., 2023).

Following the pioneering work by Gray's group on photosensitizer-Cytochrome P450 systems (Ener et al., 2010; Wilker et al., 1999), numerous studies have demonstrated the potential of hetero-dinuclear Ru^{II}_{phot}-Fe^{II}_{cat} dyads for photoconversion of organic substrates. In 2015, Herrero *et* al. (Herrero et al., 2015) introduced **24** a Ru-Fe photosensitizer-catalyst assembly, designed to mimic Fe-based metalloenzymes capable of oxidizing organic substrates through the photogeneration of high-valent iron-oxo species (**Fig. 1.24**). UV-Vis spectroscopic analysis of dyad **24** revealed a characteristic Ru^{II}-based MLCT absorption band around 450 nm, accompanied by a shoulder near 400 nm attributed to an Fe_{cat}-based MLCT transition. Electrochemical measurements identified a Ru^{III}/Ru^{II} redox couple at +1.26 V, while the Fe^{III}/Fe^{II} redox couples were recorded at +0.97 V (**24**-CH_3CN), +0.60 V (**24**-Cl), and +0.50 V (**24**-OH_2), indicating a sufficient thermodynamic driving force for electron transfer from Fe^{II}_{cat} to photo-generated Ru^{III}_{phot} during catalysis. The luminescence intensity and quantum yield of dyad **24** were significantly reduced compared to the isolated $[Ru(bpy)_3]^{2+}$ fragment, consistent with PeT from the excited state of the photosensitizer to the low-lying excited state of the Fe_{cat} moiety.

Upon light irradiation, the photogenerated Fe^{IV}_{cat}=O species facilitated the oxidation of triphenylphosphine in acetate buffer, yielding triphenylphosphine oxide, as confirmed by gas chromatography. Using

$[Co(NH_3)_5Cl]^{2+}$ as a sacrificial oxidant, the system achieved a turnover number (TON) of 3.2 with a catalytic efficiency of 20%.

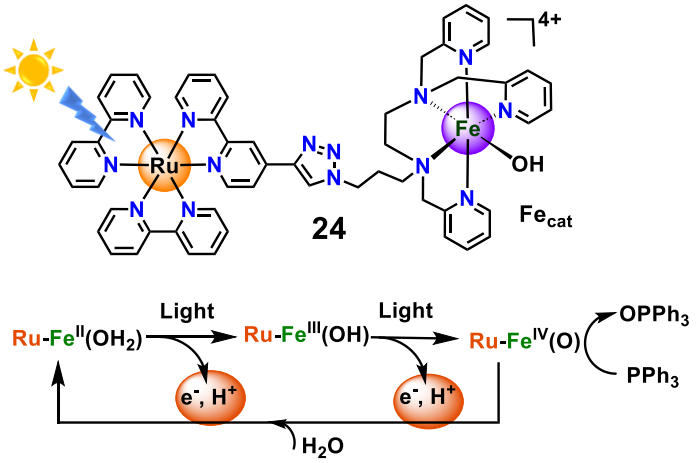

Fig. 1.24. Photocatalytic oxidation of triphenylphosphine (PPh_3) using hetero-dinuclear complex **24** with proposed catalytic mechanism (Herrero et al., 2015).

In 2021, our group (Singh et al., 2021) reported **25** a hetero-dinuclear Ru^{II}_{phot}-Fe^{III}_{cat} dyad, $[(bpy)_2Ru(imptp)Fe(Cl)]^{3+}$, where Himptp denotes *N*-[[6-(1H-imidazo[4,5-*f*][1,10]phena nthrolin-2-yl)pyridin-2-yl]methyl]-(pyridin-2-yl)-*N*-(pyridin-2-ylmethyl)methanamine (**Fig. 1.25**). UV-Vis absorption spectrum of dyad **25** exhibited two major bands at 360 nm and 460 nm, corresponding to MLCT transitions from both metal centers. The band near 460 nm was attributed to a typical Ru(II)-centered $d\pi(Ru) \rightarrow \pi^*(bpy)$ transition, while the absorption around 360 nm matched that of the individual Fe^{III}_{cat} unit (i.e., $[Fe^{III}(TPA)Cl_2]$), arising from a $d\pi(Fe) \rightarrow \pi^*(pyridine)$ transition. The free Ru^{II}_{phot} complex exhibited strong luminescence centered at 614 nm upon excitation at 468 nm. However, significant quenching of this emission was observed in dyad **25**, indicative of PeT from the excited Ru^{II}_{phot} to the Fe^{III}_{cat} center. Electrochemical studies supported this PET behavior: dyad **25** displayed a quasi-reversible oxidation wave for the $Ru^{II/III}$ couple at +1.26 V vs. SCE, and a redox wave near +0.56 V assigned to the $Fe^{III/II}$ couple. These potentials confirmed a thermodynamically favorable electron transfer from $*Ru^{II}_{phot}$ to Fe^{III}, leading to the formation of Ru^{III}_{phot}-Fe^{II}_{cat} species. The regeneration of the Ru^{II}_{phot} center was facilitated by the sacrificial electron donor TEOA. Under

blue LED irradiation, the dyad catalyzed the selective oxidation of various organic substrates, including alkanes and alkenes, with high alcohol selectivity. Notably, the covalently linked dyad system demonstrated superior catalytic performance compared to the corresponding bimolecular mixture of Ru^{II}_{phot} and Fe^{III}_{cat}. The proposed mechanism involves PET from $*Ru^{II}_{phot}$ to the Fe center, followed by O_2 coordination at the Fe site to generate a high-valent Fe^{IV}cat=O species capable of substrate oxidation.

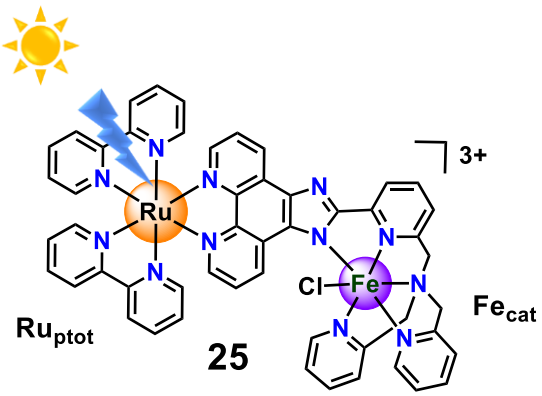

Fig. 1.25. Photocatalytic oxidation of various alkanes using hetero-dinuclear complex **25** with proposed catalytic mechanism (Singh et al., 2021).

Overall, this thesis explores the versatile roles of photosensitizers in luminescence sensing and photoredox catalysis. Their tunable photophysical properties, redox activity, and excited-state dynamics make them indispensable tools for both sensitive analyte detection and driving light-induced redox transformations. Through structural design and mechanistic understanding, photosensitizers can be effectively tailored to enhance performance across diverse light-driven chemical applications.

1.6. Research Gaps

i. Conventional analytical techniques such as atomic absorption spectroscopy, ICP-MS, and electrochemical methods often require costly instrumentation, elaborate sample preparation, and time-consuming protocols.

ii. Most reported organic photosensitizers suffer from low luminescence quantum yields and limited photostability, restricting their practical utility.

iii. Optical sensing of analytes in fully aqueous media remains a significant challenge, with most systems relying on organic solvents or mixed solvent environments.

iv. Solid-state optical sensing platforms for small-molecule detection are relatively underexplored.

v. Many catalytic organic transformations still depend on harsh redox reagents, limiting sustainability and functional group tolerance.

vi. A large proportion of reported photocatalytic systems rely on UV light sources, highlighting the need for more visible-light-active photocatalysts for organic transformations.

1.7. Objectives of the Thesis

1. Design and development of synthetic molecular photosensitizers.
2. Investigation of their photophysical and redox properties using UV-Vis, Fluorescence, and electrochemical studies
3. Luminescence sensing of small analytes such as cations and anions.
4. Catalytic applications of newly developed molecular photosensitizers for different organic transformations.

CHAPTER 2

MATERIALS, METHODS AND INSTRUMENTAION

This chapter provides a comprehensive overview of the chemicals, solvents, and materials used in the research, detailing their sources and specifications. It outlines the synthetic methodologies employed for compound preparation, emphasizing reaction conditions and step-by-step procedures. Furthermore, it delves into the advanced analytical techniques utilized for characterizing synthesized compounds and nanomaterials, including spectroscopic, spectrometric, and diffraction methods. Special focus is given to the principles, instrumentation, and applications of these techniques, ensuring precise structural and compositional analysis.

2.1. Materials

All the solvents and chemicals were procured from commercial sources with a reagent-grade quality. 2-naphthaldehyde, 2,2-(thiobis)ethylamine, 4-(2-bromoethoxy)benzaldehyde, 2-(2′-pyridyl)benzimidazole, K_2CO_3, $NaBH_4$, sodium borohydride, sodium bicarbonate, potassium bromide (KBr), ammonium acetate (NH_4OAc), sodium sulphate (Na_2SO_4), di-(2-picolyl)amine (DPA), 1,10-phenanthroline, and triethanolamine were obtained from Sigma Aldrich and Alfa Aesar and were utilized without any further purification. Several solvents have been utilized in experimental procedures such as acetonitrile, ethanol, methanol, dichloromethane, ethyl acetate, diethyl ether. The stock solutions of metal ions have been prepared before performing the experiments with chloride or nitrate salts of Al^{3+}, Zn^{2+}, Ag^{+}, Cd^{2+}, Cu^{2+}, Co^{2+}, Hg^{2+}, Ni^{2+}, Pb^{2+}, Fe^{2+}, Ca^{2+} and Na^{+} ions. The stock solutions of various anions were prepared immediately before carrying out the sensing experiments using tetrabutylammonium (TBA) or potassium salts of F^{-}, Cl^{-}, Br^{-}, I^{-}, $H_2PO_4^{-}$, CN^{-}, AcO^{-}, ClO_4^{-}, ClO_2^{-}, S^{2-}, NO_2^{-}, NO_3^{-}, $S_2O_3^{2-}$, SCN^{-}, PO_4^{3-}, AsO_2^{-}, and SO_4^{2-} ions.

1,10-Phenanthroline-5,6-dione and cis-$Ru(bpy)_2Cl_2$ have been synthesized according to a previously reported method. The majority of the synthetic procedures were carried out under an inert nitrogen atmosphere using the Schlenk line technique. All solvents were meticulously purified and dried before use. Reaction solvents were removed under reduced pressure with the aid of a rotary evaporator, and every solvent employed in the reactions and workup processes was distilled and dried to maintain high purity standards.

2.2. Methods

2.2.1. Calculation of limit of detection (LoD) and binding constant (K_b)

The LoD for analytes was determined using the formula LoD = 3σ/S, derived from emission titration data. Here, σ represents the standard deviation obtained from 10 blank emission measurements, while S corresponds to the slope of the calibration curve.

K_b of the probe for target analyte has been determined by Benesi-Hildebrand equation.

$$1/(F-F_0) = 1/(F_{max}-F_0) + 1/(F_{max}-F_0)(1/K_b)(1/[A]) \quad (1)$$

where A represents the target analyte. F_{max} denotes the fluorescence intensity of the probe when the analyte is present at its saturation point, F_0 is the fluorescence intensity of the probe in the absence of the analyte, and F corresponds to the fluorescence intensity of the probe at any intermediate concentration of the target metal ions or anions. The K_b value can be calculated from the slope of the linear plot obtained by graphing $1/(F - F_0)$ against 1/[A].

2.2.2. Calculation of emission quantum yield (Φ_{em})

The fluorescence quantum yields of the probes were measured using the slope method, reference dissolved in solvent. The procedure involves preparing solutions of the probe and reference at different concentrations, the absorbance was kept low and maintained at a fixed excitation wavelength. The quantum yield was calculated using the following equation:

$$\boldsymbol{\phi_X} = \phi_{std} \times \frac{Grad_x}{Grad_{std}} \times \frac{\eta_x^2}{\eta_{std}^2}$$

Φ_{ref} is the quantum yield of the reference (anthracene), $Grad_x$ and $Grad_{std}$ are the slopes of the emission intensity versus absorbance plots for the probe and reference, respectively. η_x and η_{std} are the refractive indices of the solvents used for the probe and reference, respectively.

2.2.3. Low-cost detection methods: Paper strips and colorimetric assay

For the test strip sensing experiments, Whatman filter paper strips were initially soaked in a stock solution of the probe and left to air-dry. Once dried, the treated strips were individually placed in beakers containing aqueous solutions of different metal ions. Visual changes in the strips were monitored under both UV and visible light, allowing for the detection and differentiation of metal ions based on their distinct colorimetric responses. This approach offers a straightforward, quick, and economical method for real-time metal ion sensing, where the observed fluorescence or color change acts as a clear visual indicator of the presence and concentration of specific ions.

2.2.4. Cell culture and imaging

The cell lines were maintained in DMEM-HG (Dulbecco's Modified Eagle's Medium with high glucose), enriched with 10% heat-inactivated fetal bovine serum (FBS). Cells were plated at a density of 0.05×10^6 cells per well in a 24-well plate and incubated at 37°C in a 5% CO_2 atmosphere for 24 hours. After incubation, the cells were treated with different concentrations of the probe for 4 hours, followed by a gentle wash with PBS buffer. Cells incubated with the probe at a specific concentration were subsequently exposed to varying concentrations of metal ions/anions for 2-3 hours, after which they were rinsed with PBS to eliminate any unbound metal ions. Cell imaging was conducted using an inverted fluorescence microscope (EVOS FLOID, Thermo Fisher, USA), with images captured in green, blue, and red fluorescence channels. This methodology allows for the visualization and evaluation of the probe's interaction with metal ions within live cells.

2.2.5. Analysis in real samples

The practical utility of the probes has been evaluated in real water samples, soil sample and Digene gastric tablets. In general, for the soil sample,

0.5 mg was mixed thoroughly with 10 mL of CH_3CN and centrifuged at 5000 rpm for 30 minutes. The mixture was then filtered using Whatman Grade 1 filter paper. The gastric tablet was finely powdered, sonicated, and soaked overnight in a CH_3CN solution, followed by filtration through filter paper. The filtered solution was diluted to a final volume of 50 mL. Both the soil and gastric tablet samples were spiked with known concentrations of metal ions/anions and combined with the probe solution. After a 10-minute incubation, the fluorescence spectra were recorded and compared against a calibration curve. This approach confirmed the probe's effectiveness in detecting metal ions in complex environmental and pharmaceutical samples.

2.3. Characterization Techniques

2.3.1. Melting point

The melting points of the synthesized compounds were determined using an electrically heated melting point apparatus. The samples were sealed in glass capillaries with one end closed before measurement. The melting points were recorded with an accuracy of ±2°C and reported accordingly.

2.3.2. Nuclear magnetic resonance (NMR) spectroscopy

NMR spectroscopy was extensively utilized for the characterization of synthesized compounds and monitoring reaction progress. The specific instrument used was JNM ECX-500 NMR Spectrometer. Operating at 500 MHz for ^{1}H and ^{13}C NMR spectral studies, this spectrometer was also employed to establish the mechanism between applied probe and target analyte. This high-precision instrument provided detailed spectral data, crucial for the structural and compositional analysis of the synthesized compounds and complexes.

2.3.3. Single crystal X-ray diffraction

X-ray diffraction data was collected using a Rigaku Oxford diffractometer equipped with graphite-monochromated Mo-Kα radiation (λ = 0.71073 Å). Data processing was performed using *CrysAlisPro* software, incorporating a multi-scan absorption correction to enhance accuracy and reliability. The crystal structure was solved using the direct method, followed

by full-matrix least-squares refinement against F^2 using the SHELXT software package. These procedures enabled the precise determination of molecular geometry, bond lengths, bond angles, and overall crystal structure, contributing to the comprehensive characterization of the synthesized compounds.

2.3.4. Fourier transform infrared (FT-IR) spectroscopy

FT-IR spectra were recorded using a Shimadzu IR Spirit spectrometer in the range of 4000-400 cm^{-1} with KBr pellets.

2.3.5. Photoluminescence study

Photoluminescence studies were meaured at ambient temperature using a PerkinElmer LS45 spectrophotometer. This technique was utilized to examine the photoluminescent properties of the synthesized compounds, including their emission spectra and intensity across different wavelengths.

2.3.6. UV-visible absorption spectroscopy

UV-visible absorption spectra of the synthesized materials were recorded at ambient temperature using a Shimadzu UV-240 spectrophotometer with a 1.0 cm path length quartz cuvette. This analysis offered key insights into the electronic transitions and optical properties of the compounds.

2.3.7. Time-resolved fluorescence (TRF) study

Photoluminescence lifetimes were determined using an FLS920 fluorescence lifetime and steady-state spectrophotometer, equipped with a 500 kHz light source.

2.3.8. Electrospray ionization mass spectrometry (ESI-MS)

ESI-MS analysis was performed using an Agilent Waters Q-TOF Premier-HAB213 mass spectrometer. Acetonitrile and methanol were used as solvents for sample preparation. This technique facilitated the determination of molecular weight, fragmentation patterns, and structural insights of the synthesized compounds.

CHAPTER 3

ORGANIC PROBES FOR LUMINESCENT DETECTION OF HEAVY METAL IONS

3.1. State of the Art

Metal ions have a huge impact on human life due to their crucial roles in various biological, environmental and industrial processes (Alam et al., 2021; Li et al., 2022; Pak et al., 2021; Qiao et al., 2021; Xu et al., 2022; Zhou et al., 2017). They have become a part of our day-to-day life; however, the overuse/mishandling of metal ions lead to the serious contamination to our ecological system that may be detrimental to human health and other living organisms (Mao et al., 2020; Park et al., 2020; Petitjean et al., 2021; Shen et al., 2022; Wan et al., 2021). For instance, Zn^{2+}, a bio-relevant metal ion, is involved in various biological processes such as cell division, gene transcription, bio-catalysis, signal transmission and matrix metalloproteinase regulation (Kindermann et al., 2005; Lu et al., 2022). But, excess intake of Zn^{2+} can suppress the absorption of Fe and/or Cu content in humans leading to various physiological disorders. Indeed, Zn^{2+} deficiency has been linked to many neurodegenerative issues e.g., diabetes, ischemic-stroke, Parkinson's disease, epilepsy, infantile-diarrhea and Alzheimer's disease (Bush, 2003; Livingstone, 2015; Ma et al., 2014). On the other hand, aluminium (Al) is the most abundant metal in the earth's crust and the third most abundant element in the lithosphere after oxygen and silicon (He et al., 2019; Singh et al., 2013). Despite being a non-essential element to humans, it is widely used in water treatment, cooking-ware, pharmaceuticals, food additive, packaging industry and alloys manufactures (Gui et al., 2015; Han et al., 2012; Krewski et al., 2007; Lee et al., 2014). Due to its large-scale usage, Al has been listed as a food pollutant by WHO, and thus, the daily intake of Al has been set as 3-10 mg per day (Li et al., 2021). Its ionic form (i.e., Al^{3+}) is found highly toxic to fishes as well as

plants (Qin et al., 2015; Sparling and Lowe, 1996). In humans, Al^{3+} causes softening of bones and atrophy as it interferes with calcium absorption. Furthermore, other health issues such as Alzheimer's disease, Parkinson's disease and dialysis encephalopathy have been linked to an excess intake of Al^{3+} ions (Fasman, 1996; Nayak, 2002; Shen et al., 2023; Xu et al., 2021).

So far, many conventional methods including ICP-MS, AAS, ESI-MS, HPLC and electrochemical analyses have been well employed for the quantification of metal ions. Nonetheless, such techniques may suffer from several issues such as tedious sample preparation methods, longer detection time, and sometimes the requirement of large quantity of sample which collectively makes them difficult to be employed for real-time analysis (Frankowski et al., 2010; Karuppiah et al., 2022; Wang et al., 2019). On the contrary, the optical (fluorometric and colorimetric) detection methods are emerging as viable alternative due to their operational convenience, low-cost, high selectivity and fast response toward target ions (Guo et al., 2021; Singha et al., 2019). Optical probes have been extensively applied in chemistry, medicines, life sciences, environmental and other fields. In recent years, fluorescent probes have seen gradual development and advancement in good efficiency, microscopic and real-time analysis (Krämer et al., 2022a; Wu et al., 2017).

Though a great number of fluorescent probes have been developed for monitoring of Al^{3+} and Zn^{2+} ions *in-vitro* and *in-vivo* (Mohanty et al., 2022; Roy, 2021; Wang et al., 2021), several Al^{3+}-responsive probes suffer from the tedious and laborious multi-step synthetic routes (Boonmee et al., 2018; Liu et al., 2018; Wang et al., 2023). Consequently, the sensors having structural simplicity are increasingly being developed and still are on high demand. In this context, Schiff base compounds with imine (>C=N–) functionality have gained tremendous attention of researchers (Han et al., 2012; Jana et al., 2012). Some advantageous features such as synthetic ease, good stability, strong metal ion binding ability, and insensitivity toward air and moisture enable them to act as viable candidates for sensing of metal ions (Berhanu et al., 2019; Liao et al., 2013). More importantly, the electronic, structural, and optical properties of

Schiff base derived fluorescent probes can simply be tailored *via* suitable modifications of any of their substrates (either amine or carbonyl moiety). Upon metal ion binding, Schiff bases demonstrate a signature 'turn-on' fluorescence behavior due to the selective inhibition of >C=N- isomerization (Das et al., 2018; Liu et al., 2018). This provides an opportunity to modulate the absorption and emission wavelengths by incorporating an appropriate fluorophore in the molecular scaffold of the Schiff-bases. The naphthalene unit is one of the most efficient fluorophores employed for the development of fluorescent Schiff base probes. In fine, due to their promising optical and structural characteristics, the fluorescent probes containing naphthalene moiety along with imine functionality have emerged as the gold standards over the past few years in the field of metal ion sensing (Das and Goswami, 2017; Kang et al., 2017; Li et al., 2021). Notably, several reports are available for the simultaneous detection of Al^{3+} and Zn^{2+} in different solvents using Schiff base fluorescent probes (Alam et al., 2016; Cao et al., 2014; Chiou et al., 2020; Fan et al., 2014). However, only a few probes exhibit simultaneous detection of Al^{3+} and Zn^{2+} in same solvent system (Hazra et al., 2018; Roy et al., 2019; Tang et al., 2016).

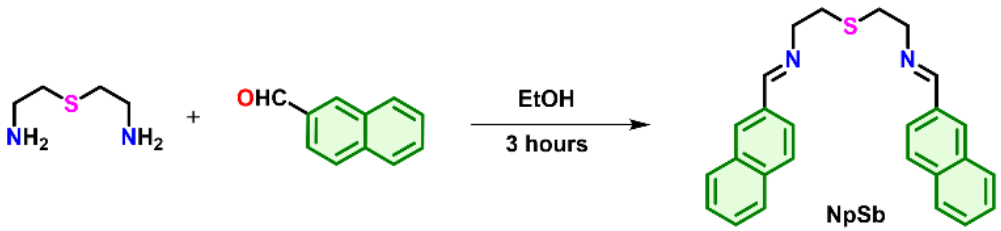

Scheme 3.1. Synthetic route to prepare Schiff base probe **NpSb**.

In this effort, we shed light on a fluorescent Schiff base probe (**NpSb**) derived *via* one-step condensation reaction between 2-naphthaldehyde and 2,2'-thiobis(ethylamine) (**Scheme 3.1**). The naphthalene core acts as the fluorophore unit while the S- and N-imine atoms coordinate to the respective target metal ions, accompanied by distinctive fluorescence changes. Due to their promising optical and structural characteristics, the fluorescent probes containing naphthalene moiety along with imine functionality have emerged as the gold standards over the past few years in the field of metal ion sensing. The coordination behavior and binding mode of **NpSb** toward Al^{3+} and Zn^{2+} ions

have been scrutinized using UV-Vis, fluorescence, ^{1}H NMR and ESI-MS studies which were further corroborated by DFT analyses.

3.2. Experimental Section

3.2.1. Synthesis of probe NpSb

A batch of 2-naphthaldehyde (0.2 mmol, 0.031 g) was dissolved in 20 mL ethanol, and 2,2-thiobis(ethylamine) (0.1 mmol, 0.012 g) was added to it. The solution was stirred for 3 hours to give **NpSb** *via* a simple one-step condensation reaction between the substrates. The obtained white precipitate was filtered out and dried in air to give a white solid (0.036 g) of **NpSb** (Yield *ca.* 92%). FT-IR (KBr disk): 3440, 3049, 2870, 1631 ($\nu_{>C=N}$), 1372, 1124, 966, 836, 744 cm^{-1}. UV-Vis (CH_2Cl_2): λ_{max}/nm (ε/M^{-1} cm^{-1}) = 241 (1.22 × 10^5), 249 (1.17 × 10^5) and 283 (3.29 × 10^4). ^{1}H NMR ($CDCl_3$, 500 MHz), δ (ppm): 8.93 (s, 2H, -C<u>H</u>=N-), 8.89 (m, 2H), 7.89 (m, 6H), 7.59-7.48 (m, 6H), 3.98 (t, 4H, -C<u>H</u>$_2$-N-), 3.07 (t, 4H, -C<u>H</u>$_2$-S<). ^{13}C NMR ($CDCl_3$, 500 MHz), δ (ppm): 161.88, 133.84, 131.50, 131.33, 131.13, 128.80, 128.64, 127.19, 126.07, 125.47, 124.31, 115.00, 62.54, 33.55.

3.2.2. X-Ray crystallography

Probe **NpSb** was dissolved in dichloromethane-methanol (9:1, *v/v*), and was crystallized in a glass vial at room temperature *via* slow evaporation method. Appropriate single crystals were selected under the microscope and mounted with Paratone Oil on a Cryoloop. X-ray data has been collected at 150 K on RIGAKU Super Nova diffractometer using monochromatic Cu-Kα radiation (λ = 1.5416Å) (CrysAlis, 2009). Lorentz polarization as well as the absorption corrections have been applied with Bruker SAINT and SADABS softwares (Bruker and Saint, 2008; Sheldrick, 2002). The solution of crystal structure was performed by direct method and refined using full-matrix least squares on F^2 for all the reflections using SHELXTL (Sheldrick, 2000). Non-hydrogen atoms were refined anisotropically. All hydrogen atoms were refined isotropically and accordingly generated at the calculated positions considering riding models.

3.2.3. Absorption and emission spectra

Probe **NpSb** displayed a low solubility in pure water, and therefore, the fluorescence and UV-Vis experiments have been conducted in organic-aqueous (CH_3CN: H_2O = 4:1; *v/v*) solvent mixture. The emission spectrum was measured from 320 nm to 540 nm where the excitation wavelength (λ_{ex}) was fixed at 300 nm. The stock solutions of NpSb (2.0×10^{-5} M) and assorted metal ions (10^{-2} M) were prepared in CH_3CN and distilled water, respectively. For UV-Vis and fluorescence titration experiments, the aqueous stock solutions of metal ions were further diluted and gradually added with the help of a micropipette.

3.2.4. Detection of Al^{3+}/Zn^{2+} ions in real samples

Tap water, distilled water and soil samples have been utilized as the real specimens to validate the practical applicability of **NpSb**. Tap water and distilled water samples were used without any pre-treatment; however, the soil samples (0.5 mg in 5 mL milli-Q water) were centrifuged at 5000 rpm for 20 minutes to get rid of any large particles followed by two-step filtration. After that, acetonitrile was added to obtain a H_2O-CH_3CN (4:1 v/v) solvent mixture. The probe **NpSb** (5.0 mM) was added to the H_2O-CH_3CN samples and then Al^{3+}/Zn^{2+} ions (0-15.0 mM) were added.

3.2.5. Test paper strips experiments

The test strips experiments were carried out by immersing the filter paper strips (Whatman Grade-1) into CH_3CN solution of **NpSb** (50 mM). The test strips were then taken out and dried in open air. After that, the treated strips were kept into the solutions of various metal ions (*ca*. 10^{-2} M) to eventually observe the visual changes under UV as well as visible light illumination.

3.3. Results and Discussion

3.3.1. Syntheses and characterization of NpSb

Schiff base **NpSb** was facilely synthesized by the treatment of 2-naphthaldehyde with 2,2-thiobis(ethylamine) for 2-3 hours in anhydrous ethanol, as shown in **Scheme 3.1**. **NpSb** was found stable at room temperature and exhibited good solubility in most of the organic solvents as well as in the

organic-water (4:1) solvent mixture. The structure of **NpSb** was confirmed with the help of $^{1}H/^{13}C$ NMR, ESI-MS and SC-XRD analyses. ^{1}H NMR study of **NpSb** clearly exhibited all the expected resonances in aliphatic as well as aromatic regions (**Fig. A1**, Annexure-I). A sharp singlet near 8.91 ppm was assigned to the proton of -CH=N– functionality. Two triplets centred at 3.98 ppm and 3.08 ppm were ascribed to the methylene protons of $–CH_2–N=$ and $–CH_2$-S- groups, respectively. In ^{13}C NMR spectra of **NpSb**, the signal near 162.0 ppm corresponds to the carbon atom of imine group while the peaks at 62.54 ppm and 33.55 ppm have been assigned to the methylene groups (**Fig. A2**). Infrared (IR) spectrum of the probe **NpSb** exhibited a vibrational frequency near 2950 cm^{-1} which could be assigned to the methylene $–CH_2$ groups. A strong band at 1631 cm^{-1} was attributed to the vibrations of imine group (**Fig. A3**). Furthermore, the ESI-MS analysis of **NpSb** yielded an exact mass of 397.1736 which corresponds to the protonated molecular ion [**NpSb** + $H]^{+}$ species. The experimental value coincides well with the theoretical value of 397.17 (**Fig. A4**).

Finally, the crystal structure of **NpSb** was depicted using SC-XRD analysis. The ORTEP diagram of **NpSb** with atom labelling is displayed in **Fig. 3.1**. **NpSb** crystallizes in monoclinic system having space group of -P2yn. The crystallographic data and its relevant refinement parameters have been provided in whereas the selected bond parameters are listed in Table A2. Both intra- as well as intermolecular H-bonding interactions were visible in the molecular structure of **NpSb** stabilizing the conformation. The intramolecular H-bonding interactions occur between C(2)–H(1) of the naphthyl ring and the imine-N atom whereas intermolecular hydrogen bonds, N(1)–H(9)···C(1) formed between the thiobis-CH_2 and the imine N atoms of the two adjacent probe molecules.

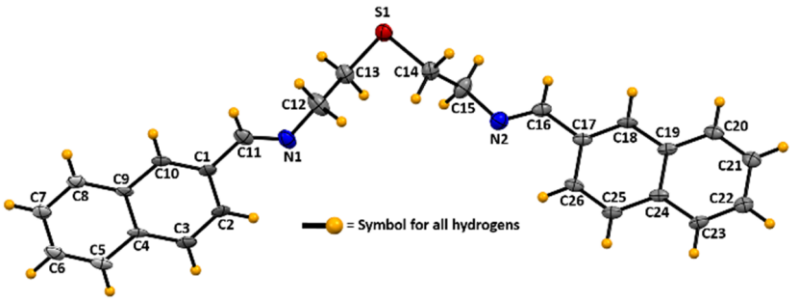

Fig. 3.1. ORTEP diagram for probe **NpSb**.

3.3.2. Selectivity of NpSb for Al^{3+} and Zn^{2+} ions

UV-Vis and fluorescence studies were employed to investigate the metal ion sensing ability of **NpSb** in CH_3CN-H_2O (4:1, v/v) in the presence of assorted metal ions such as Al^{3+}, Zn^{2+}, Ag^{+}, Cd^{2+}, Cu^{2+}, Co^{2+}, Hg^{2+}, Ni^{2+}, Pb^{2+}, Fe^{2+}, Ca^{2+} and Na^{+} ions. UV-Vis spectrum of **NpSb** revealed two strong absorptions near 241 nm ($\varepsilon = 1.22 \times 10^5\ M^{-1}cm^{-1}$) and 249 nm ($\varepsilon = 1.17 \times 10^5\ M^{-1}cm^{-1}$) along with one moderate absorption peak centered at 283 nm ($\varepsilon = 3.29 \times 10^4\ M^{-1}cm^{-1}$) (**Fig. 3.2**). Upon addition of Al^{3+}, the peaks at 241 nm and 249 nm declined to merge into one peak, and simultaneously, the band at 283 nm diminished. The spectral change was accompanied by three new bands observed at 248, 265 nm and 311 nm. Furthermore, a low intensity absorption appeared in the range of 350-380 nm upon successive addition of Al^{3+} ions. Four clear isosbestic points at 215 nm, 255 nm, 273 nm and 291 nm suggested the formation of a new species between **NpSb** and Al^{3+} ion. On the contrary, the addition of Zn^{2+} to **NpSb** resulted only in a slight decrease in the absorption intensity of the spectra (**Fig. A5**). The spectral changes in **NpSb** were also accompanied by an obvious color change from colorless to pale green in the case of Al^{3+} ion.

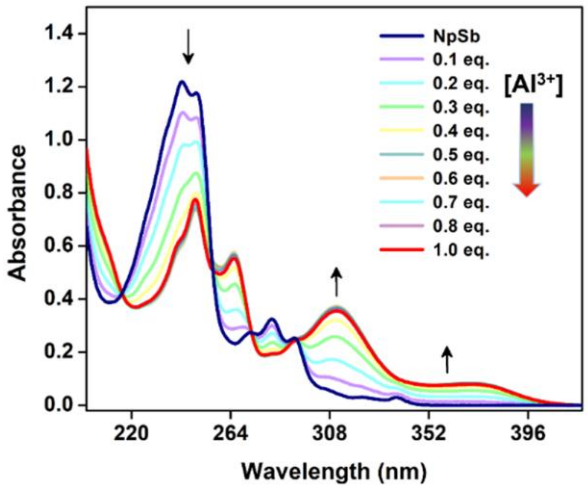

Fig. 3.2. UV-Vis spectral changes for **NpSb** (1.0×10^{-5} M) in CH_3CN-H_2O solution (4:1, v/v) after successive addition of Al^{3+} ions (0-1.0 equiv,).

In fluorescence study, **NpSb** exhibited negligible fluorescence emission (due to >C=N- isomerization) when excited at 300 nm in CH_3CN-H_2O solution (4:1, *v/v*). Upon addition of different metal ions, only Zn^{2+} and Al^{3+} induced obvious emission changes while other metal ions did not show apparent changes in the fluorescence emission of **NpSb**. The Stokes shift of the emission band for Zn^{2+} and Al^{3+} detection was observed to be 108 nm and 161 nm, respectively.

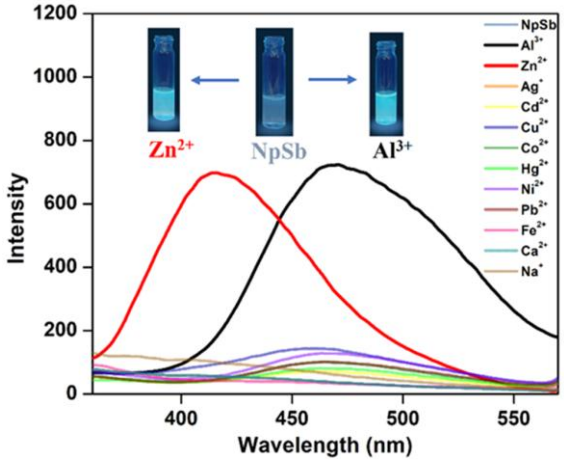

Fig. 3.3. Emission spectral changes for **NpSb** (1.0×10^{-6} M) in CH_3CN-H_2O (4:1, v/v) in the presence of various metal ions (λ_{ex} = 300 nm).

As shown in **Fig. 3.3**, Zn^{2+} and Al^{3+} could easily be distinguished from the distinctive emission features as remarkable fluorescence enhancement

centered at 416 nm and 469 nm was obtained after the addition of Zn^{2+} and Al^{3+}, respectively. The stock solutions of metal ions were diluted to 10^{-6} M, and the fluorescence titration experiments were carried out *via* sequential addition of Al^{3+}/Zn^{2+} ions. Almost non-fluorescent **NpSb** exhibited a significant emission enhancement when treated with Al^{3+}/Zn^{2+} ions. Furthermore, the emission quantum yield (Φ_{em}) of **NpSb** (i.e., 0.00944) increased to 0.0271 and 0.0275 for Al^{3+} and Zn^{2+}, respectively. At nearly 1.0 equiv. of Zn^{2+}/Al^{3+}, the fluorescence enhancement attained saturation indicating a 1:1 stoichiometry for both the ions (**Fig. 3.4**). On the basis of stoichiometry analysis and Benesi-Hildebrand plot, the binding constants for Al^{3+} and Zn^{2+} were determined as 1.18×10^6 M^{-1} and 3.5×10^5 M^{-1}, respectively (**Figs. A6 and A7**). Furthermore, the limit of detection (LoD) values for Al^{3+} and Zn^{2+} have been depicted as 38.0 nM and 43.0 nM, respectively (**Figs. A8 and A9)**. The LoD value was found comparable to the works reported earlier.

The selective response of probe **NpSb** towards Zn^{2+} and Al^{3+} ions was further assessed in the presence of different competing cationic species. The emission titration experiments for Zn^{2+} and Al^{3+} were performed in the presence of 10 equiv of other metal ions. As displayed in **Figs. A10 and A11**, no remarkable interference could be realized in **NpSb**-Al^{3+} solution. **NpSb** was then treated with Zn^{2+} in the presence of other assorted metal ions (10 equiv). The solution of **NpSb**-Zn^{2+} exhibited negligible emission variations in presence of other cations except Al^{3+} while Cu^{2+} led to a slight variation in fluorescence intensity. We have also recorded the relative fluorescence Intensity of **NpSb** with Al^{3+} and Zn^{2+} in CH_3CN-H_2O (4:1, v/v) solution (**Fig. A12**).

In comparison to **NpSb**-Zn^{2+}, the formation of more stable **NpSb**-Al^{3+} complex could be ascribed to the higher affinity of Al^{3+} for **NpSb** having NNS donor sites. The performance of our probe was also compared with the previously reported works and the sensing parameters have been summarized in **Table 3.1**.

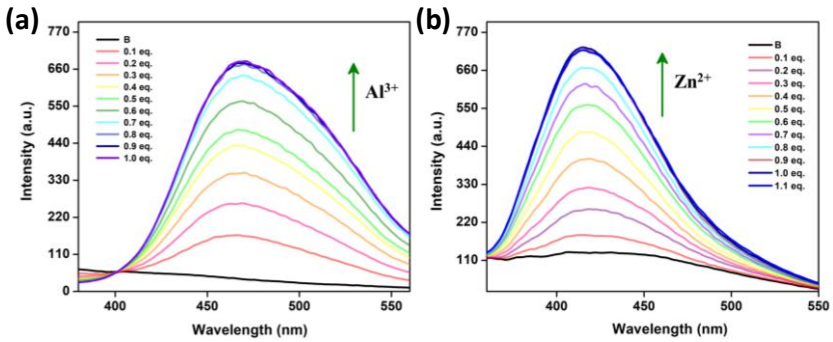

Fig. 3.4. Emission spectral changes for **NpSb** (1.0×10^{-6} M) in CH_3CN-H_2O (4:1, v/v) in the presence of different concentrations of (a) Al^{3+} and (b) Zn^{2+} ions (λ_{ex} = 300 nm).

3.3.3. Binding mechanism studies

The binding mechanism between probe **NpSb** and Al^{3+}/Zn^{2+} was determined with the help of Job's plot, NMR, and ESI-MS analyses. Job's plot revealed a binding stoichiometry of 1:1 for the detection of Al^{3+} and Zn^{2+} ions (**Figs. A13 and A14**). ESI-mass spectrometry is another direct analysis to investigate the binding mode between **NpSb** and the target metal ion. In the positive mode, *m/z* peaks at 531.05 and 595.06 were attributed to [**NpSb** + Al^{3+} + $3Cl^-$ + H^+]$^+$ and [**NpSb** + Zn^{2+} + Cl^-]$^+$, respectively (**Figs. 3.5a and 3.5b**). A 1:1 complex formation between **NpSb** and Al^{3+}/Zn^{2+} has been observed in mass analysis. The binding mechanism was further investigated by ^{1}H NMR titration with Zn^{2+} ions. In comparison to free probe, the singlet for imine protons displayed a slightly downfield shift upon gradual addition of Zn^{2+} (0 to 1.0 equiv) that corresponds to the coordination of Zn^{2+} to **NpSb** *via* imine-N atoms (**Fig. A15**). In fine, the fluorescence enhancement event could be ascribed to formation of stable complexes between **NpSb** and Zn^{2+}/Al^{3+}, resulting in the CHEF (chelation-enhanced fluorescence) effect *via* imine N atoms and (thiobis)ethylamine-S chelating the metal ions. Notably, the binding of Zn^{2+}/Al^{3+} to **NpSb** inhibits the >C=N- isomerization, and meanwhile the NNS binding to Zn^{2+}/Al^{3+} prevents PET event, both of them become conducive to the fluorescence enhancement of **NpSb**.

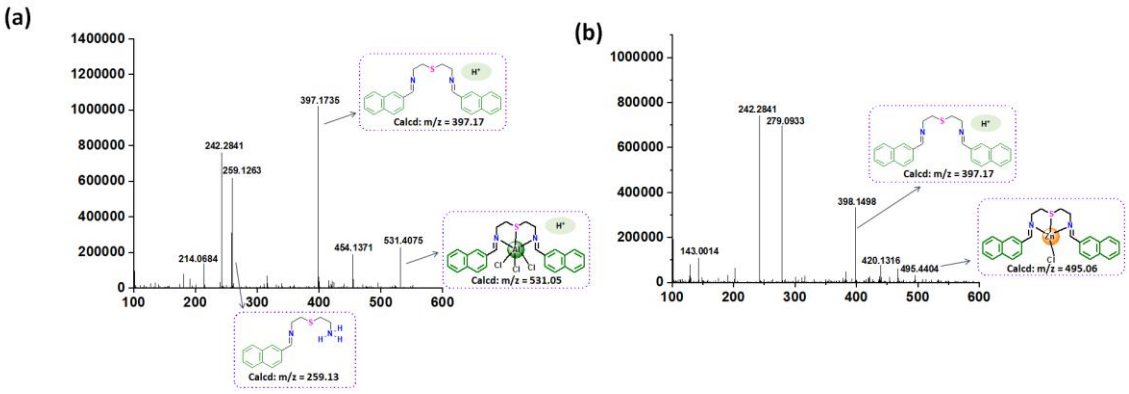

Fig. 3.5. ESI-MS analysis of **NpSb** in methanol after addition of 2.0 equiv of (a) Al^{3+} and (b) Zn^{2+} ions.

The binding mechanism was further investigated by the DFT studies using Gaussian 09 program at B3LYP level with the LANL2DZ basis set for Al/Zn and 6-31G+(d,p) basis set for other atoms. The optimized structures and the resultant frontier molecular orbitals (i.e., HOMO and LUMO) of the free and chelated states are shown in **Fig. 3.6**. The metal ions chelated to S and imine nitrogen atoms of **NpSb**. The bond parameters of the optimized geometries were found consistent with the data reported earlier (Prabha et al., 2021) (for **NpSb**-Al^{3+}: Al-N1 = 1.92393 Å, Al-N2 = 1.88076 Å and Al–S = 2.36840 Å; for **NpSb**-Zn^{2+}: Zn-N1 = 2.00158 Å, Zn-N2 = 1.97738 Å and Zn–S = 2.47775 Å). The energy band gaps (i.e., ΔE) between HOMO and LUMO of **NpSb**, **NpSb**-Al^{3+} and **NpSb**-Zn^{2+} were depicted as 4.36 eV, 1.66 eV and 2.98 eV, respectively, which indicated that the electronic and photophysical properties of **NpSb** are remarkably influenced upon binding with Al^{3+}/Zn^{2+} ions. The lowering in energy gaps of frontier molecular orbitals after complexation indicated the red-shift absorptions which further correlated well with the experimental data. Notably, the HOMO and LUMO of both **NpSb**-Al^{3+} and **NpSb**-Zn^{2+} were better stabilized than those of free **NpSb**. Based on the results obtained from the Job's plot, ESI-MS analysis and DFT calculations, the coordination modes of **NpSb**-Al^{3+}/Zn^{2+} have been proposed in **Scheme 3.2**.

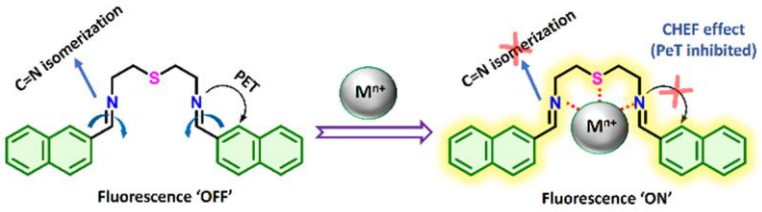

Scheme 3.2. Proposed binding mode of **NpSb** with Zn^{2+} and Al^{3+} ions.

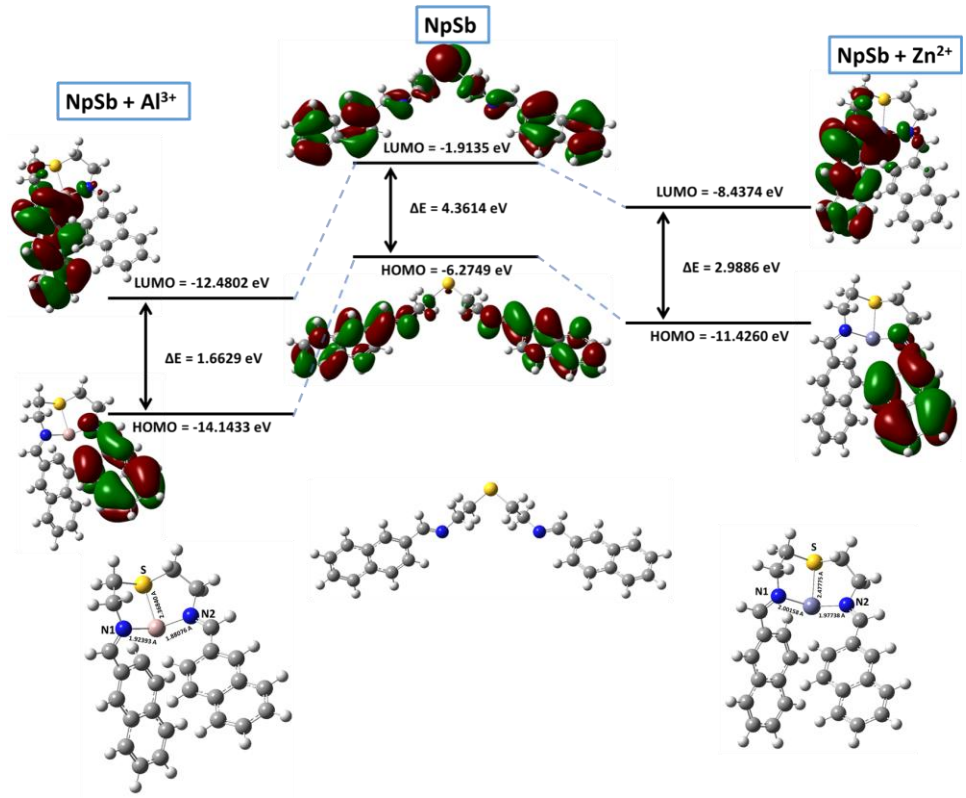

Fig. 3.6. DFT calculations of free probe **NpSb** and after its treatment with Al^{3+} and Zn^{2+} ions and their HOMO–LUMO energy levels.

3.3.4. Reversibility studies and logic gate behaviors

Reversibility is an important factor for the optimum functioning of a chemosensor. In case of Al^{3+} ion, NaF was used to remove Al^{3+} to achieve the reversibility (**Fig. 3.8a**). Al^{3+} ion enhances the fluorescence of **NpSb**; however, the addition of fluoride (F^-) ion restored the original fluorescence, and the reversibility cycles were generated for the successive addition of Al^{3+} and F– ions. Similarly, EDTA was used to remove Zn^{2+} ion to achieve the original probe (**Fig. 3.8b**). The reversibility experiments clearly suggested that the probe **NpSb** could be recycled upto three cycles (**Figs. A17 and A18**). As NaF and

EDTA can be used to attain the reversibility by removing Al^{3+} and Zn^{2+} ions; the logic circuits and the truth tables for probe **NpSb** have been constructed for the detection of Al^{3+} (IN 1 = Al^{3+} and IN 2 = F^{-}) and Zn^{2+} (IN 1 = Zn^{2+} and IN 2 = EDTA) ions. The threshold emission value was fixed at 400 nm (OUT) for both Al^{3+} and Zn^{2+} ions (**Figs. 3.8c-3.8d**). The emission above and below these threshold values were allocated as "ON" and "OFF" for "on" and "off" output signals, respectively. The simplest symbolic representation of Al^{3+}–F^{-} (**Fig. 3.8c**, blue-colored truth table and logic gate) and Zn^{2+}–EDTA (**Fig. 3.8d**, green-colored truth table and logic gate) systems provided an INHIBIT logic gate. Wherein Al^{3+} or Zn^{2+} input line goes into a single-input OR gate and F^{-} or EDTA input line goes into NOT gate while output from the NOT gate goes into the OR gate (Kumar et al., 2017; Kumar et al., 2017). Finally, the output of OR gate is the fluorescence intensity of the probe.

3.3.5. Applications in real samples and test strips

The practical applicability of **NpSb** was investigated in real samples such as tap water, distilled water and soil samples to for monitoring of Zn^{2+}/Al^{3+} ions. The soil samples were first centrifuged and then filtered to remove any large particles whereas tap and distilled water samples were used without any pre-treatment. Probe **NpSb** (5.0 μM) was then added to the H_2O-CH_3CN solution (4:1, v/v) of real samples. The resultant samples were treated with different concentrations of Al^{3+}/Zn^{2+} ions (0-15.0 μM). A significant fluorescence enhancement could be observed in the samples spiked with Al^{3+} with relatively less remarkable changes in case of Zn^{2+} ions. The results clearly exhibited the high selectivity of probe toward Al^{3+} ions. Notably, the emission band was found blue-shifted (453 nm) in highly aqueous medium (H_2O:CH_3CN; 4:1, v/v) as compared to the one observed in pure organic or a 1:4 mixture of H_2O:CH_3CN (v/v) (469 nm) (**Fig. A18**). The probe also exhibited good recoveries in the range of 93 to 107% (**Table A3**).

We have also performed the low-cost colorimetric and paper strips methods for the detection of Al^{3+} and Zn^{2+} ions. For better colour visualization, a highly concentrated (~10^{-2} M) solution of metal ions was added to the solution of probe **NpSb** in different glass vials. Amongst the various metal ions studied,

only Al^{3+} and Zn^{2+} exhibited fluorescence enhancement under UV light illumination (**Fig. 3.7a**); however, only nominal changes could be realized in visible light. The test paper strips (Whatman filter paper-grade 1) were dipped in the solution of probe **NpSb** and then air dried. These dried strips were then dipped into the concentrated stock solutions of various metal ions. Under UV light illumination, a 'turn-on' fluorescence response was observed in presence of both Al^{3+} and Zn^{2+} ions (**Fig. 3.7b**).

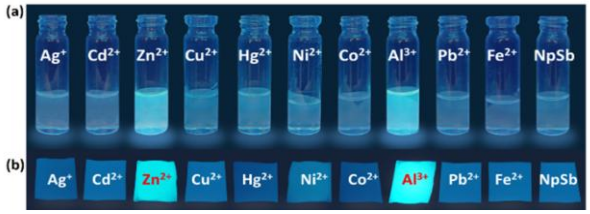

Fig. 3.7. Photographs of fluorescent changes in probe **NpSb** upon addition of 3.0 equiv of various metal ions under UV light (λ_{max}= 365 nm) (a) in solution and (b) on filter paper strips.

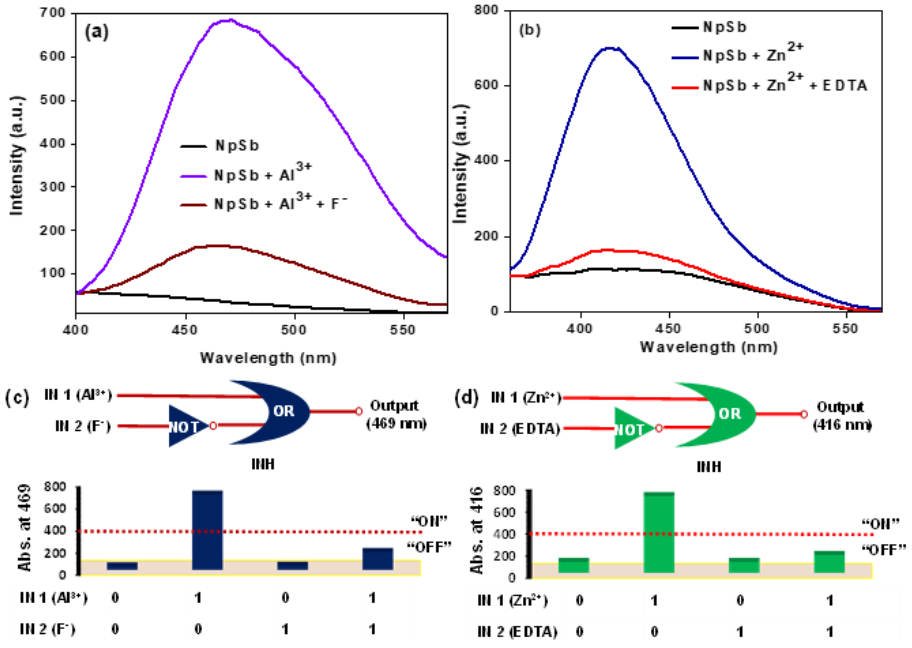

Fig. 3.8. Reversibility studies for probe **NpSb** by (a) F^- ion for the detection of Al^{3+} and (b) EDTA for the detection of Zn^{2+} ion. Emission outputs and corresponding two-input combinational logic circuit of **NpSb** in presence of chemical inputs viz; (c) IN 1 = Al^{3+} and IN 2 = F^- (blue bars, 469 nm) and (d) IN 1 = Zn^{2+} and IN 2 = EDTA (green bars, 416 nm).

Table 3.1. Comparison of probe **NpSb** with previously related probes.

S.No	Structure of Probe	Target cation	LoD (μM)	Binding constant (M^{-1})	Application	Fluorescence response	Ref
1.	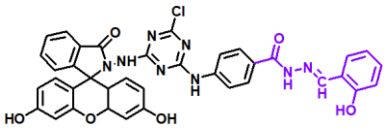	Al^{3+} Zn^{2+}	0.053 0.079	1.5×10^5 6.0×10^5	Industrial wastewater; Live cell imaging	Turn-on Turn-on	(Zhao et al., 2020)
2.	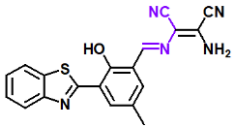	Al^{3+} Zn^{2+}	7.06 2.98	1.32×10^7 1.92×10^4	Live cell imaging	Turn-on Turn-on	(Li et al., 2021)
3	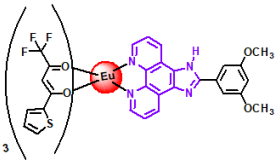	Al^{3+} Zn^{2+}	0.588 0.076	6.92×10^3 1.73×10^5	Lake water; Tap water	Ratiometric	(Song et al., 2021)
4.	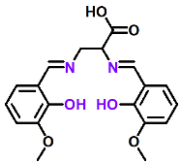	Al^{3+} Zn^{2+}	0.0018 0.0076	5.83×10^4 7.71×10^4	Live cell imaging; Test paper strips	Turn-on Turn-on	(Theetharappan et al., 2021)
5.	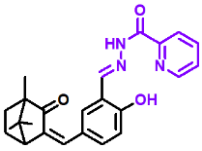	Al^{3+} Zn^{2+}	0.012 0.014	3.77×10^4 6.58×10^4	Live cell imaging; Test paper strips; Distilled water; Tap water; Lake water	Turn-on Turn-on	(Gong et al., 2022)
6.	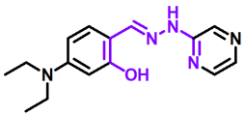	Al^{3+} Zn^{2+}	0.233 0.168	2.03×10^4 1.15×10^4	Cotton swabs; Potable water; Drug sample	Turn-on Turn-on	(Liu et al., 2022)
7.	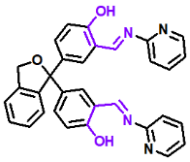	Al^{3+} Zn^{2+}	0.085 0.188	2.01×10^4 6.84×10^4	Live cell imaging	Turn-on Turn-on	(Samanta et al., 2022)
8.	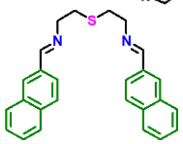	**Al^{3+}** **Zn^{2+}**	**0.038** **0.043**	**1.18×10^6** **3.5×10^5**	**Test paper strip; Distilled water; Tap water; Soil samples**	**Turn-on Turn-on**	**This work**

3.4. Conclusions

In summary, a Schiff base probe **NpSb** containing NSN chelate and naphthalene unit as fluorophore has been synthesized to detect Al^{3+} and Zn^{2+} ions. The probe acted as 'turn-on' sensor via emission at different wavelengths for Al^{3+} (469 nm) and Zn^{2+} (416 nm). The probe displayed an excellent detection limit of 38.0 nM for Al^{3+} and 43.0 nM for Zn^{2+} ions. **NpSb** was able to detect Al^{3+}/Zn^{2+} even in the presence of other interfering metal ions. The reason for the 'turn-on' response was the inhibition of PET process and >C=N- isomerization upon chelation of metal ions with **NpSb**. The metal ion binding mechanism was strongly supported by ESI-MS and DFT analysis. NaF and EDTA could be used to achieve reversibility by removing Al^{3+} and Zn^{2+} ions from the adduct **NpSb**-Al^{3+}/Zn^{2+}. Corresponding logic circuits and truth tables have been developed. For practical applications, test paper strips-based experiments were also performed which could easily detect Al^{3+} and Zn^{2+} ions.

CHAPTER 4

MODIFICATION OF ORGANIC PROBES FOR ANION SENSING

4.1. State of the Art

Perchlorate ion (ClO_4^-) can naturally occur from different environmental sources including photochemical reactions between ozone and chlorine and volcanic eruptions (Furdui et al., 2018; Kang et al., 2008; Ye et al., 2012). Beside this, anthropogenic activities significantly contribute towards increasing concentration of perchlorate ions in environment (Cao et al., 2019; Kumarathilaka et al., 2016). Though perchlorate salts are widely employed in various industrial and metallurgical processes, excessive usage has adversely impacted both environment as well as human health (Dou et al., 2024; Niziński et al., 2021; Pleus and Corey, 2018). Notably, perchlorate-based explosives have been involved in more than 60% of worldwide explosive incidents over the proceeding years, as reported by the United State Bomb Data Center (Watson, 2018).

Perchlorate ions often present in soil and water sources post fireworks, structural fires, and industrial discharge end up on domestic water supply (Kounaves et al., 2010; Kucharzyk et al., 2009; Kumar, 2020; Steinmaus, 2016). Additionally, a subsequent leakage of perchlorate ions from industrially produced wastewater to domestic water is unavoidable. It is of interest to note that the charge and ionic radius of perchlorate ion is similar to the iodide ion, and therefore, it can inhibit thyroid uptake in humans and can also cause brain injury, iodine deficiency, and goiter (Lewandowski et al., 2015; Zhang et al., 2010). Moreover, a high level of perchlorate in the urine is also associated with diabetes mellitus (Liu et al., 2017). In recent years, the World Health Organization (WHO) has set the intake limit of perchlorate in drinking water to be lower than 70.0 µg/L per day (EPA US, 2009). Therefore, there is an urgent

need to develop a rapid, convenient, and inexpensive detection method for perchlorate ions in biological and environmental settings.

In this context, various conventional strategies including AAS, HPLC, ICP-MS, reflection X-ray fluorescence analysis (XRF), and attenuate total reflectance chromatography have been well established to detect trace levels of perchlorate ions (Batjoens et al., 1993; Hatzistavros and Kallithrakas-Kontos, 2011; Sahana et al., 2013; Weiss and Stanbury, 1972). However, these methods require heavy and expensive instrumentation, time consuming processes and well controlled experimental conditions with skilled professionals (Goswami et al., 2023; Manna et al., 2022; Xiong et al., 2022). Over the preceding years, optical sensors have emerged as a promising alternative in the field of anion sensing due to their high selectivity and sensitivity, low-cost instrumentation, ease of handling, good detection limit together with on-site detection capabilities (Guo et al., 2021; Pal et al., 2021; Singha et al., 2019).

It is worth mentioning that the detection of anions is comparatively challenging than their counterpart cations and other small neutral analytes. The fact lies behind their lesser charge to size ratio and related solvation effect which make electrostatic interactions between the probe and analyte less effective (Chang et al., 2015; Hein and Beer, 2022; Naithani et al., 2023a; Naithani et al., 2024). Even among anions, perchlorate detection is more elusive due to its high mobility and weak coordination behavior (Brown and Gu, 2006; Tielrooij et al., 2010). Therefore, a judicious design of molecular frameworks is required to develop efficient optical sensors for recognition of perchlorate ions.

So far, only a few reports are available demonstrating perchlorate ion detection using fluorescent probes, and many of them suffer from structural complexities. They are mainly based on costly transition metals (such as platinum and iridium) (Chao and Zhang, 2017; Su et al., 2021; Taylor et al., 2010), lanthanides (such as europium) (Sagami et al., 2017), and MOFs. More importantly, a majority of these sensors show ‘turn-off’ behavior in presence of perchlorate ion (Kumar et al., 2012; Sagami et al., 2017; Tohora et al., 2023). Since ‘turn-off’ behavior can be triggered by multiple factors, it is relatively less preferred compared to ‘turn-on’ responsive sensors. Therefore, the

development of structurally simple ‘turn-on’ sensors for perchlorate recognition is highly demanded especially for environmental and health monitoring.

Herein, we report a pyridyl-benzimidazole fluorophore based luminescent probe **RSB1** (**Scheme 4.1**) to detect perchlorate in the semi-aqueous media (CH_3CN-H_2O; 4:1, v/v) with an appreciable detection limit of 0.121 μM. The architecture of the probe has been designed to equip the receptor pocket (anion binding cavity) with multi-point hydrogen bonding sites, consisting of two -N-H and cooperative adjacent aryl-C-H hydrogen bonds. This probe could be successfully employed to trace perchlorate in real samples such as tap water, distilled water, and soil samples.

4.2. Experimental Section

4.2.1. Synthesis of compound 1

First, 4-(2-bromoethoxy)benzaldehyde was synthesized following the literature procedure which was then used for the synthesis of compound **1** (Santra et al., 2015). A 5.0 mL DMF solution of 2-(2′-pyridyl)benzimidazole (2.0 mmol, 0.4 g) was taken in a double-neck round bottom flask (50 mL) under inert atmosphere. A batch of 6.0 mmol of K_2CO_3 (0.82 g) was then added, and the reaction mixture was heated at 90°C for 15 minutes. To the above mixture, 2.0 mmol (0.46 g) of 4-(2-bromoethoxy)benzaldehyde with 2-3 mL DMF was added using an airtight syringe. The color of the reaction mixture changed to pale yellow from white. The reaction mixture was then refluxed at 140°C for 48 hours while maintaining an inert atmosphere. Subsequently, the hot reaction mixture was poured into a 1 L beaker containing 500 mL ice-cold distilled water. The white precipitate of obtained compound (**1**) was collected by filtration and drying in air. Yield 0.51 g, 75%. Anal. Calcd. for $C_{21}H_{17}N_3O_2$: C, 73.45; H, 4.99; N, 12.24. Found: C, 73.32; H, 5.20; N, 12.38. ^{1}H NMR [500 MHz, $CDCl_3$, TMS, δ (ppm)]: 9.84 (s, 1H), 8.67 (d, 1H), 8.46 (d, 1H), 7.89-7.83 (m, 2H), 7.76 (d, 2H), 7.61 (d, 1H), 7.40-7.31 (m, 3H), 6.91 (d, 2H), 5.22 (t, 2H), 4.61 (t, 2H) (**Fig. A19**).

4.2.2. Synthesis of probe RSB1

A 1:2 molar ratio of 2,2'-thiobis(ethylamine) (0.3 mmol, 0.07 g) and compound **1** (0.3 mmol, 0.15 g) was taken in 20 mL methanol, and the reaction mixture was stirred at room temperature for 2 hours. Thereafter, 3.0 mmol of $NaBH_4$ was added to the above mixture, and the stirring was continued for next 40 hours to obtain the target compound **RSB1**. The resulting precipitate was filtered out and dried in air (Yield 92%). Anal. Calcd. for $C_{46}H_{46}N_8O_2S$: C, 71.29; H, 5.98; N, 14.46. Found: C, 70.98; H, 5.76; N, 13.86. ^{1}H NMR [(500 MHz, $CDCl_3$, TMS, δ (ppm)]: 8.65 (d, 2H), 8.42 (d, 2H), 7.83 (m, 4H), 7.59 (d, 2H), 7.36-7.29 (m, 6H), 7.13 (d, 4H), 6.74 (d, 4H), 5.15 (t, 4H), 4.78 (s, 2H, broad), 4.44 (t, 4H), 3.66 (s, 4H), 2.73 (t, 4H), 2.63 (t, 4H). ^{13}C NMR (500 MHz, $CDCl_3$): δ 157.54, 150.43, 149.88, 148.63, 142.48, 137.15, 136.94, 132.05, 129.36, 124.70, 123.84, 123.54, 122.80, 120.01, 114.39, 110.75, 67.27, 52.69, 47.67, 44.97, 31.98. IR (KBr disk): 3282 ($\nu_{N\text{-}H}$), 2944, 2828 (ν_{CH2}), 1635, 1603, 1502, 1446, 1254 ($\nu_{C\text{-}O\text{-}}$), 1035, 820, 746 and 619 cm^{-1}. ESI-MS: (positive, CH_3OH): *m/z* Calcd. for $[M+H^+]^+$ 775.3543, Found 775.3522; *m/2z* Calcd. for $[M+2H^+]^{2+}$ 388.1810, Found 388.1780.

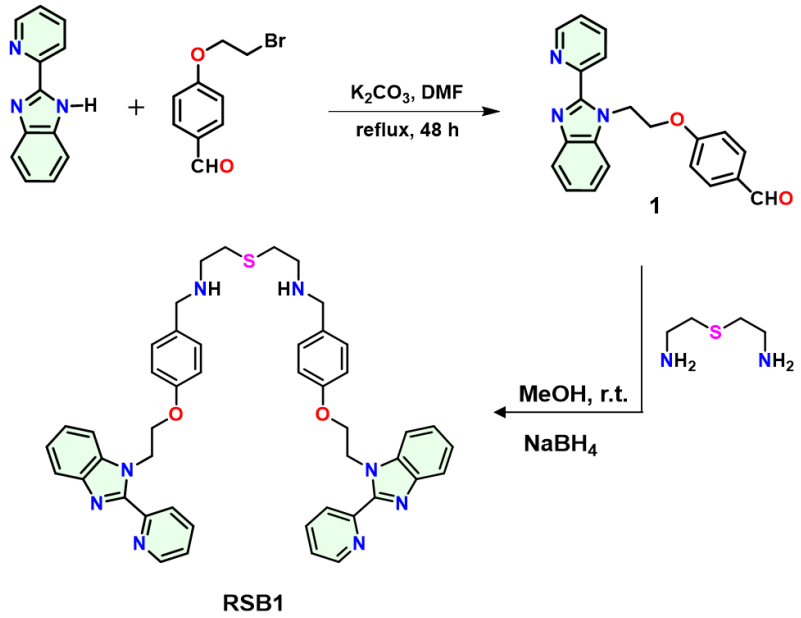

Scheme 4.1. Synthetic route to prepare the probe **RSB1**.

4.2.3. Absorption and emission spectra

The probe **RSB1** was sparingly soluble in water, and thus, UV-Vis and fluorescence-based experiments have been conducted in semi-aqueous medium (CH_3CN-H_2O; 4:1, *v/v*). The spectral data after the addition of an anion was recorded instantly.

4.3. Results and Discussion

Compound **RSB1** was synthesized by the treatment of 2,2'-thiobis(ethylamine) and compound **1** in the presence of $NaBH_4$ as a reducing agent (**Scheme 4.1**). **RSB1** was found to be stable at ambient temperature and displayed good to excellent solubility in common organic solvents as well as in the organic-water (4:1) solvent system. This probe has been characterized by using standard spectroscopic/analytic techniques such as FT-IR, NMR, UV-Vis, fluorescence, ESI-mass and elemental analysis.

^{1}H NMR spectrum of the probe was recorded in $CDCl_3$ solution. Two triplets at 2.63 ppm and 2.73 ppm have been assigned to the methylene (>CH_2) protons adjacent to each other in the cavity of thiobis(ethylamine) moiety. Another set of two triplets observed at 4.44 ppm and 5.15 ppm could be ascribed to the methylene protons bridging pyridyl benzimidazole unit and the oxygen atom, respectively (**Fig. A20**). The presence of methylene protons between N-H unit and benzene ring was evidenced by the resonance observed near 3.66 ppm. All the aromatic protons resonated between 6.70-8.70 ppm while a broad singlet near 4.8 ppm corresponded to two N-H protons. ^{13}C NMR spectrum of **RSB1** revealed two clear signals near 67.27 ppm and 52. 69 ppm corresponding to the carbon atoms of -O-CH_2- and -N-CH_2- groups directly linked to pyridyl benzimidazole moiety. In addition, all the aromatic carbon atoms appeared between 157.0-110.0 ppm while the carbon atoms of -N-CH_2- and -S-CH_2- available with thiobis(ethylamine) moiety were found at 44.97 ppm and 31.98 ppm, respectively (**Fig. A21**).

FT-IR spectrum of **RSB1** (**Fig. A22**) exhibited a modest intensity band near 3282 cm^{-1} which could be attributed to the N-H stretching frequency. The vibrational band for methylene >CH_2 group was found near 2828 cm^{-1}. An

intense peak near 1254 cm^{-1} was assigned to the C-O stretching frequency of the ethereal moiety. Moreover, the peaks around 746 cm^{-1} and 619 cm^{-1} represented out-of-plane -C-H bending vibrations of phenyl group. ESI-mass spectrum of **RSB1** revealed an exact mass of 775.3522 (*m/z*) and 388.1780 attributed to the molecular ion [**RSB1**+H]$^{+}$ and [**RSB1**+2H]$^{2+}$ species in positive ion mode (**Fig. A23**). The absorption and emission spectra of the probe were measured in CH_3CN: H_2O (4:1, v/v) solution. The absorption spectra exhibited a broad moderate intensity absorption peak near 307 nm (ε = 45348 M^{-1} cm^{-1}) that could be attributed to π -π* transitions (Kırpık et al., 2020; Tzeng et al., 2011). The probe **RSB1** (1.2×10^{-6} M) exhibited an emission band at 363 nm in semi-aqueous mixture when excited at 300 nm (**Fig. 4.1(a)**).

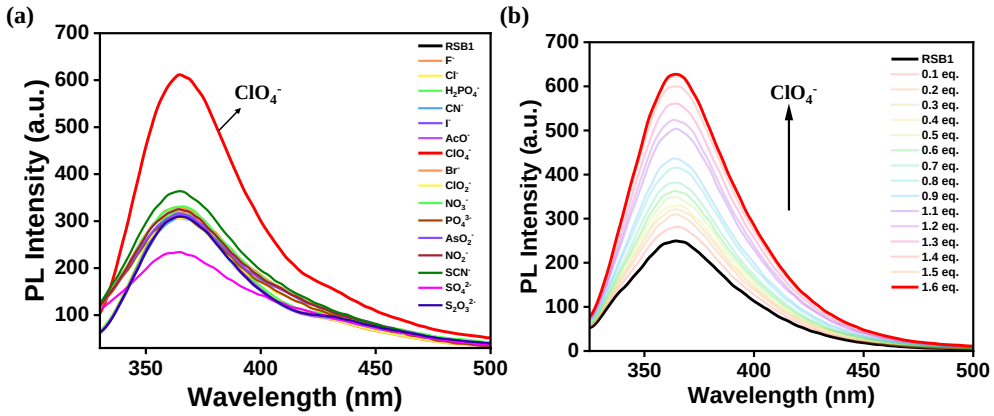

Fig. 4.1. (a) Fluorescence spectral changes for **RSB1** (1.2×10^{-6} M) in CH_3CN-H_2O mixture (4:1, v/v) with various anions (λ_{ex} = 300 nm) and (b) Emission titration of **RSB1** with variable concentrations of ClO_4^- ion in CH_3CN-H_2O (4:1, v/v) mixture. The stock solutions of anions were prepared using tetrabutylammonium or potassium salts.

The anion sensing ability of the probe **RSB1** was investigated using fluorescence spectral studies. A remarkable fluorescence enhancement at 363 nm could be noticed upon addition of 6.0 equiv. of perchlorate ions while other anions (such as F^- , Cl^-, Br^- , I^-, $H_2PO_4^-$, CN^-, AcO^-, ClO_4^-, ClO_2^-, S^{2-}, NO_2^-, NO_3^-, $S_2O_3^{2-}$, SCN^-, PO_4^{3-}, AsO_2^-, and SO_4^{2-}) produced nominal changes showcasing a selective turn-on response of **RSB1** towards ClO_4^- in semi-aqueous medium (**Fig. 4.1(a)**).

Furthermore, emission titration experiments have been carried out to better grasp the anion sensing mechanism of the probe (**Fig. 4.1(b)**). The emission spectra of **RSB1** have been recorded upon successive addition of perchlorate ions (0-1.6 equiv). A good linear response (R^2 ~0.99) could be realized over a wide concentration range of ClO_4^- ions, as shown in **Fig. 4.2**. The fluorescence titration study clearly indicated that the 'turn-on' response followed Stern-Volmer relation $F/F_0 = 1+ k_{sv}[ClO_4^-]$, where F and F_0 represent the fluorescence intensity of **RSB1** in presence and absence of ClO_4^- ion. The LoD for ClO_4^- was estimated to be ~0.12 μM which is significantly lower than the permissible intake limit in drinking water as set by U.S. EPA. Thus, the as developed probe has considerable potential to be utilized in real life sensing applications. Temperature variations can significantly impact hydrogen bonding interactions; and thus, parallel experiments were conducted at 40°C for comparison purpose. Interestingly, the probe maintained a strong response to perchlorate ions even at this moderately elevated temperature, displaying minimal impact on its sensing ability. At 40°C, the probe exhibited a slightly higher LoD of 0.15 μM and a modestly lower binding constant of 2.1×10^5 M^{-1} (**Fig. A24**). The analyte response time study of the probe indicated that the enhancement in fluorescence intensity reached saturation within *ca*. 45 minutes (**Fig. A25a**). The response of **RSB1** to ClO_4^- ions was also studied across a pH range of 2.0 to 12.0 using buffer solutions (**Fig. A25b**). The free probe showed slightly higher fluorescence at acidic pH levels (2.0-4.0). Upon adding perchlorate ions to the **RSB1** solution, a significant fluorescence enhancement was observed, particularly in the pH range of 2.0-8.0, covering both acidic and neutral conditions. In contrast, under basic conditions, the presence of OH^- ions compete with perchlorate ions, resulting in minimal emission changes. These results highlight the probe's excellent ability to detect ClO_4^- in acidic and neutral media, indicating its potential for real-world applications.

The selectivity of the probe **RSB1** was further tested in the presence of different competing anionic species (such as F^-, Cl^-, Br^-, I^-, $H_2PO_4^-$, CN^-, AcO^-, ClO_4^-, ClO_2^-, S^{2-}, NO_2^-, NO_3^-, $S_2O_3^{2-}$, SCN^-, PO_4^{3-}, AsO_2^-, and SO_4^{2-}). As shown in (**Fig. A26**), the perchlorate selectivity of the probe was barely

affected by other competing ions including I^-. However, fluoride and cyanide ions showed slight quenching effect. This could be attributed to the strong hydrogen affinity of these ions towards the N-H donor site available in the receptor pocket of **RSB1**.

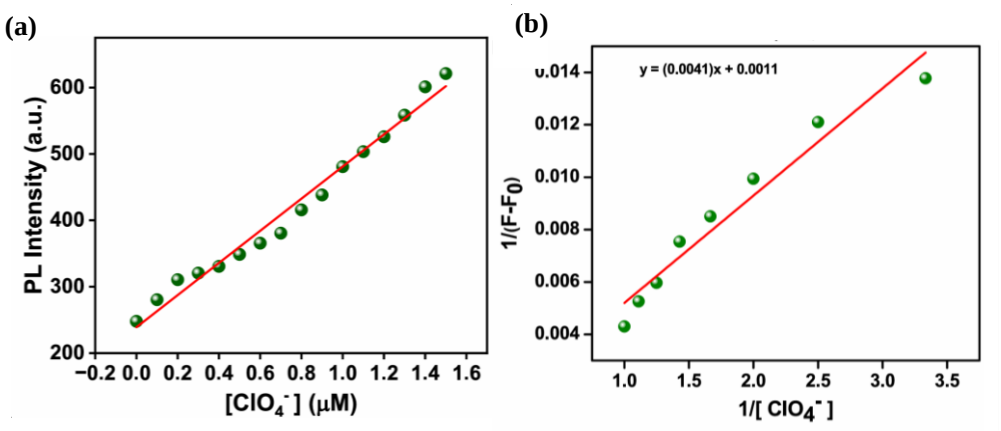

Fig. 4.2. (a) Plot for fluorescence intensity of **RSB1** (1.2 μM) versus [ClO_4^-] (λ_{em} = 363 nm) along with the linear fit for LoD calculation and (b) Plot for 1/(F-F_0) with the linear fit for the calculation of binding constant using B-H plot in CH_3CN-H_2O mixture (4:1, v/v) (λ_{ex} = 300 nm).

Additionally, the sensing experiments towards ClO_4^- have been tested in tetrahydrofuran (THF) and dichloromethane (CH_2Cl_2) and dimethylsulfoxide (DMSO) solutions (**Fig. A27**). In THF, the probe showed minimal response to ClO_4^- ions, while significant fluorescence was observed in CH_2Cl_2. This difference can be attributed to the stronger H-bond accepting ability of THF, which competes with ClO_4^- for binding to the N-H groups in the probe's cavity, thereby inhibiting perchlorate-induced fluorescence. Furthermore, UV-Vis spectroscopy was employed to assess the anion sensing ability of **RSB1**; however, the addition of 6.0 equiv of different anions produced negligible changes in the electronic absorption spectrum of **RSB1** (**Fig. A28**).

4.3.1. Anion binding mechanism

The graph plotted between the double reciprocal of 1/Δ(F)I and (1/[ClO_4^-]) was used to calculate the binding constant with the help of slope and intercept (**Fig. 4.2(b)**). The binding constant was calculated to be 2.6×10^5 M^{-1}. Job's plot analysis clearly revealed a 1:1 binding stoichiometry for **RSB1**-

ClO_4^- adduct (**Fig. A29**). Both the size of the receptor pocket as well as the acidity of N-H groups combinedly create an ideal cavity in **RSB1** for perchlorate ion binding.

To further investigate the sensing mechanism, Density Functional Theory (DFT) calculations have been performed for **RSB1** and **RSB1**-ClO_4^- species. The geometry optimizations were carried out using the B3LYP level with 6-311G++(d,p) basis set. **Fig. 4.3(a)** clearly presents the anion binding C-shape cavity in the optimized structure of **RSB1**. The optimization of adduct **RSB1**-ClO_4^- exhibited slight conformational changes, and as expected, ClO_4^- anchored in this cavity *via* multi-point H-bonding interactions involving the N-H groups of the receptor (**Fig. 4.3(b)**). The selected bond distances between O atoms of perchlorate ion and H atoms of N-H groups (O1-H1 1.99438 Å and O2-H2 1.92015 Å) suggested substantial hydrogen bonding interactions existing between the probe and the analyte. The proximity of C-H proton H3 of bridged phenyl ring to perchlorate (O4-H3 2.38831 Å) also suggested some C-H/ anion…pi interactions (Desiraju, 1991; Grabowski, 2011). As shown in **Fig. A30**, the HOMO of the free probe **RSB1** is mainly localized over the thiobis(ethylamine) group. After photoexcitation, the electron density is completely transferred to one pyridyl-benzimidazole moiety leading to the strong PET process. This results in a weak fluorescence response in free probe, more likely due to a non-radiative decay of the excite-state. Unlike free **RSB1**, the HOMO is found localized only over one pyridyl-benzimidazole moiety in case of **RSB1**-ClO_4^- while a modest charge transfer could be noticed in case of its LUMO. This is most likely due to the possible inhibition of PET process leading to an enhanced fluorescence upon ClO_4^- addition. Furthermore, the hydrogen bonding between the N-H units and perchlorate ion enhances the structural rigidity of the probe which may also contribute to the enhanced fluorescence in adduct **RSB1**-ClO_4^-.

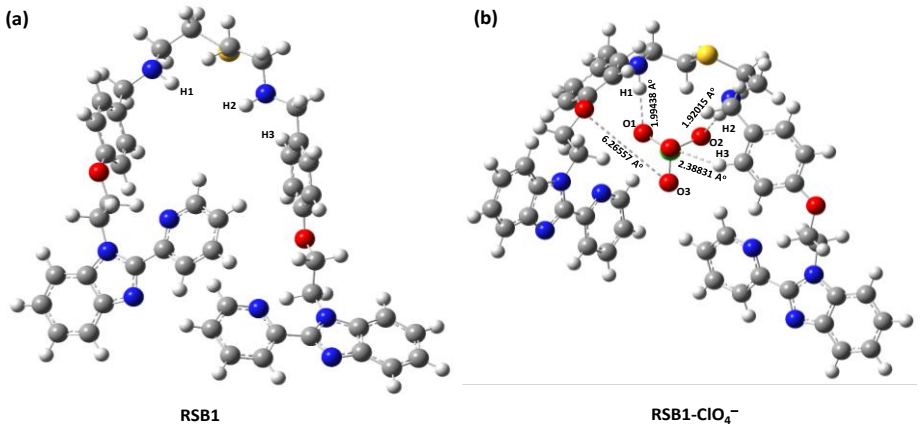

Fig 4.3. DFT optimized geometries of (a) probe **RSB1** and (b) its perchlorate adduct RSB1-ClO_4^-.

^{1}H NMR study of probe **RSB1** revealed the presence of N-H protons resonating near 4.60 ppm. Upon successive addition of ClO_4^- (0-1.0 eq.), the broad peak of the N-H protons declined and then fully disappeared indicating the existence of hydrogen bonding interaction followed by deprotonation process. Furthermore, other aromatic protons were found to be slightly shifted down-field or up-field upon interaction with perchlorate ion (**Fig. A31**). Based upon these studies, a plausible mode of perchlorate binding has been provided in **Scheme 4.2**.

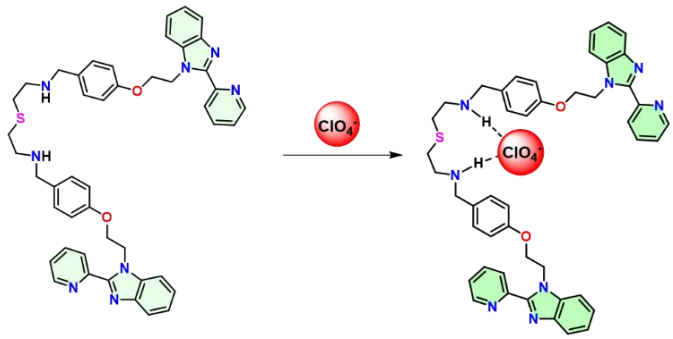

Scheme 4.2. Proposed binding mode of **RSB1** with ClO_4^- ion.

4.3.2 Solvent effect on the fluorescence behavior of probe

Emission spectroscopy was further employed to study the influence of various solvents on the emission behavior of **RSB1**. As can be seen in **Fig. 4.4**,

the fluorescence intensity of **RSB1** at 363 nm remarkably enhanced in tetrahydrofuran (THF) while a complete quenching response could be noticed in case of acetone. This data reveals that probe **RSB1** may act as a 'turn-on' sensor for THF and a 'turn-off' sensor for acetone when dissolved into a solvent giving moderate fluorescent intensity (such as DMF, DMSO, DCM, ACN and methanol). Due to a significant quenching response towards acetone, fluorescent titration studies were carried out targeting acetone as an analyte using DMF as solvent.

The fluorescence intensity of **RSB1** at 363 nm displayed gradual quenching upon successive addition of acetone to the probe's solution. This quenching behavior may be attributed to the competitive absorption of acetone (200–300 nm) with the excitation wavelength (λ_{ex} 300 nm) which indicated the existence of IFE (inner filter effect) or FRET process.

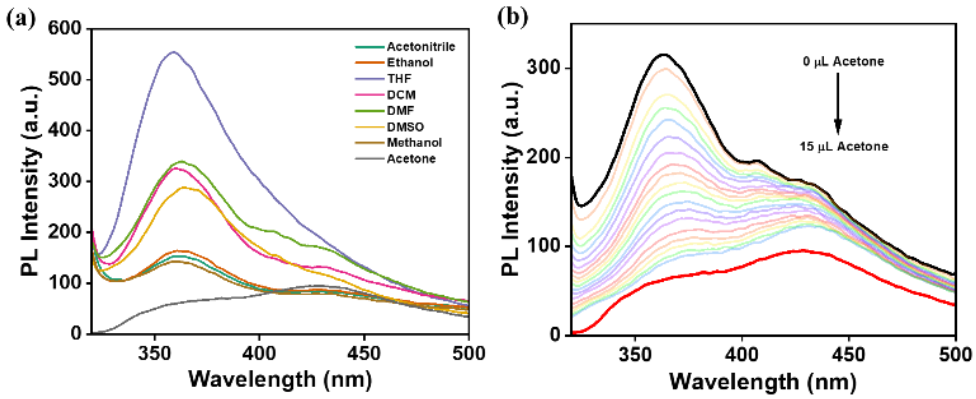

Fig 4.4. Fluorescence spectral changes of **RSB1** (5.0×10^{-7} M) with different solvents (λ_{ex} = 300 nm) and (b) Fluorescence spectra of **RSB1** (5.0×10^{-7} M) in DMF in the presence of varying concentrations of acetone.

4.3.3. Real sample analysis

The practical utility of the probe **RSB1** to trace ClO_4^- ion was determined in real samples such as soil, tap water and distilled water samples. Water samples were directly spiked with known concentration of perchlorate ions; however, the soil samples were first sonicated followed by filtration to remove any earthy impurities and then perchlorate spiked. The standard

solutions were then titrated against the probe's solution to estimate the perchlorate concentration *via* fluorescent calibration curve. The progressive addition of an individual sample resulted in the fluorescence intensity enhancement of the probe at 363 nm. Furthermore, **RSB1** exhibited an appreciable recovery value from 90% to 105% suggesting that this sensory system can be potentially used for real practical applications (Table 4.1). The reason for possible deviation in recovery values is due to the interferrence from diverse analytes present in real samples . The sensing performance of our probe has been compared with some previously reported perchlorate-responsive probes (Table A4). It is worth mentioning here that majority of the previous perchlorate sensors often rely on costly transition metals, lanthanides or MOFs, and tend to exhibit 'turn-off' responses with substantial interference from iodide ion. In contrast, **RSB1** is structurally simple, featuring a binding cavity especially optimized for multi-point hydrogen bonding, with an ultimate goal to enhance perchlorate ion selectivity and to minimize iodide interference. **RSB1** also achieves a comparable or lower LoD than previously reported probes and shows consistent response to perchlorate ions across various pH levels.

Table 4.1 Determination of ClO_4^- ion with various perchlorate-spiked real water and soil samples.

Sample	**ClO_4^- Added (μM)**	**ClO_4^- Calcd. (μM)**	**% Recovery**
Water samples			
Distilled water	0.4	0.38	95.0
Tap water1	0.8	0.77	96.25
Tap water2	1.0	1.04	104
Soil samples			
Sample 1	0.4	0.39	97.5
Sample 2	0.8	0.82	102.5
Sample 3	1.0	0.97	97

4.4. Conclusions

In summary, we have developed a pyridyl-benzimidazole based probe **RSB1** for selective 'turn-on' fluorescent detection of perchlorate (ClO_4^-) ion over other potentially competing anions in semi-aqueous media (CH_3CN-H_2O; 4:1, *v/v*). A 1:1 binding stoichiometry for **RSB1**-ClO_4^- has been thoroughly investigated by means of Job's plot, ^1H NMR, and DFT analyses. Theoretical calculations clearly revealed that the receptor unit of **RSB1** possesses a C-shape cavity to anchor ClO_4^- with multi-point hydrogen-bonding sites. The LoD value has been depicted as 0.121 µM with a binding constant of 2.6×10^5 M^{-1}. Sensing studies in different solvents suggested that the probe **RSB1** exhibited remarkable fluorescence enhancement in tetrahydrofuran while a quenching response could be noticed in pure acetone. The potential practical applications of this probe have been demonstrated *via* perchlorate monitoring in real-world samples including soil, tap water and distilled water samples.

CHAPTER 5

INORGANIC PROBE FOR ANION SENSING IN AQUEOUS MEDIUM: A RU(II) PHOTOSENSITIZER

5.1. State of the Art

The development of compounds that can selectively detect anions is on high demand as they play a significant role in numerous biological, environmental, industrial, and chemical processes (Gale and Caltagirone, 2018; Junaid et al., 2022; Manna et al., 2022; Wu et al., 2020). However, this is quite challenging due to the varied shapes, sizes, and high solvation features of anions (Alreja and Kaur, 2016b; Chang et al., 2015). Among the various anions, CN^- is of singular relevance as it is an extremely toxic inorganic anion that results into detrimental effects on aquatic ecosystems and human health. Indeed, it is fatal in small concentrations, and can be easily absorbed by cutaneous, respiratory as well as digestive pathways (Malahom et al., 2022, 2023; Pengpumkiat et al., 2020). For instance, cyanide ion interrupts aerobic respiration by inhibiting the cytochrome *c* oxidase; it hinders the production of ATP (i.e., adenosine triphosphate) from cells with a dysfunction of the electron transport chain (Manoj et al., 2020). Consequently, the WHO has set the maximum permissible limit for cyanide as 1.9 µM in drinking water. Despite its high toxicity, cyanide-based compounds are widely used in various fields such as electroplating, artificial-plastic and gum industries, X-ray film recovery, gold-silver leaching, as well as in the development of diverse range of organic chemicals, pharmaceuticals, and polymers (Basri et al., 2022; Guo et al., 2019; Pal et al., 2021; F. Wang et al., 2014; Z. Xu et al., 2010). Cyanide contamination and poisoning may result from many sources including industrial exposures, structural fires, medical exposures (e.g., sodium nitroprusside), and some foods (e.g., lima beans and almonds) (Graham and Traylor, 2022). Accidental discharge and the subsequent leakage of CN^- from industrially produced

wastewater into the domestic water is quite inevitable. *In fine*, water arose as the key medium of biological and environmental systems accountable for major trafficking of the cyanide contamination. Accordingly, it becomes critical to specifically design sensors that can be directly used for CN^- detection in pure water instead of other organic solvent systems. Among the various conventional detection methods such as chromatography, spectrophotometry, flow injection and electrochemical analysis (Hein et al., 2020a; Randviir and Banks, 2015; Xiong et al., 2022), the optical (luminescent and/or chromogenic) sensors are emerging as viable alternatives for anion detection due to their archetypal simplicity, satisfying selectivity, high sensitivity, on-site detection, and instant response time (Chan et al., 2012; Goswami et al., 2023; Guo et al., 2021; Li, Hou, et al., 2023; Li, Zeng, et al., 2023; Park et al., 2020; Singha et al., 2019).

In recent years, several cyanide-responsive optical sensors having different recognition units (e.g., amide, benzyl, urea, thiourea, fluoroacetophenone, imidazolium, indolium, borane, boronic acid, oxazine, coumarin and hydrazone derivatives) have been reported (Kumar et al., 2010; Li et al., 2019; Murugesan et al., 2018; Nie et al., 2014; Thanayupong et al., 2017; Yilmaz et al., 2022b). So far, two major approaches have been typically employed to design a CN^- responsive optical probe. The most common is the chemodosimeter (or reaction-based) sensing approach in which CN^- attacks an electrophilic >C=O (aldehyde or ketone) group or binds with a metal centre to elicit an obvious change in absorption/emission spectra of the sensing probe (Pati, 2016; Paul et al., 2022; Tigreros and Portilla, 2022). However, such sensors commonly function in either organic or organic-aqueous solvent systems; *a contrario*, detection of this non-innocent ion in 100% aqueous medium is rather challenging and less explored. The reason lies notably behind the high solvation of CN^- in water depressing the extent of carbonyl-CN^- interaction. Such a drawback limits the applications of these cyanide-responsive chemodosimeters in real-life samples (Karmakar et al., 2016).

The second approach combines an anion binding site with luminophores (or signalling unit) through a π-conjugated spacer. Conventionally, a CN^- ion interacts with binding site, often *via* H-bonding (hydrogen-bonding), and

triggers the detectable optical spectral changes in the probe (Goswami et al., 2013; Jo et al., 2013; Wang et al., 2014; Yang et al., 2014). The latter has been essentially used to recognize acetate (OAc^-) and halide ions; however, the H-bonded cyanide-responsive probes, particularly functioning under physiological conditions, are still less explored (Kaushik et al., 2016; Udhayakumari, 2018). This is due to the fact that cyanide ion often loses its charge at physiological pH through involvement in protonation equilibria; and thus, it exhibits less affinity toward weak H-bonding donors (Ma and Dasgupta, 2010). Nonetheless, as compared to F^- and OAc^- ions, CN^- acts as a stronger base in water. These observations cohesively hint that the acidic character of H-bonding donors plays an important role in selective detection of CN^- among other competing anions (e.g., F^- and OAc^-) in water (Mo et al., 2012). Besides, our group highlighted in a recent study the significance of imidazo-phenanthroline based luminescent probes having the N-H functionality as the key site for anion binding and recognition (Naithani et al., 2023a); the anion binding affinity of such probes could easily be tuned by adjusting the acidic character of N-H site. The stronger acidity of the latter results into stronger binding of anions. Indeed, recent development in this field has revealed that the probes having multipoint H-bonding may lead to high anion affinity, ultimately enabling the CN^- probes to tolerate an extensive amount of water from the solvent (Mo et al., 2012).

In this context, ruthenium(II)-polypyridyl based luminescent probes are receiving wide attention due notably to their excellent photophysical properties, large stokes shift, appreciable water solubility, long excited-state lifetime and visible light emission/excitation (Kumar et al., 2021; Kumar et al., 2022; Lee and Lo, 2022). Resultantly, several mono- and bi-metallic Ru(II) probes have been reported for the detection of cyanide *via* both binding and reaction-based approaches (Alreja and Kaur, 2016b; Khatua et al., 2012; Li et al., 2014; Maity et al., 2015; Mardanya et al., 2015; Mo et al., 2012; Pal et al., 2020; Obali, 2020a; Zhu et al., 2020). Though significant achievements have been obtained for optical cyanide sensing, some disadvantages including sensor's reversibility and lack of efficiency with higher LoD in protic media cannot be ignored. In addition, many of such sensors suffer from complicated multi-step synthetic

procedures, poor solubility and low analyte selectivity in water. Therefore, the development of simple architectures, cost-effective, highly selective/sensitive cyanide-responsive probes is essential and remains a challenge.

In this endeavour, we demonstrate an easily synthesizable Ru(II)-based optical probe (**Ru-1**) derived from 2-(pyridin-2-yl)-1*H*-benzo[*d*]imidazole ligand for the selective detection of CN^- ion particularly in water (**Scheme 5.1**). Probe **Ru-1** has been prepared earlier (Haga and Tanaka, 1979; Yi et al., 2003); however, to the best of our knowledge, it was never used for anion sensing purpose. Thus, we anticipately and rationally hypothesized that the sensing ability of **Ru-1** would be more pronounced in comparison to previously reported systems because the N-H group is in relative proximity of the metal centre in **Ru-1**; as a result, the N-H proton of the imidazole moiety becomes substantially acidic due to the strong electron pull of Ru(II) centre. Beyond the selective detection of CN^- in aqueous media, probe **Ru-1** has also been employed in organic as well as in aqueous-organic media to recognise other anions further defining the versatility of the probe; hence, it could detect F^-, AcO^-, and CN^- ions in acetonitrile solution *via* H-bonding interaction. The effect of water content on the selectivity of this probe for various anions has also been scrutinized in this report. About the applied potential, the CN^- recognition ability of probe **Ru-1** was purposely tested in water-based real samples such as living cells, drinking water, tap water, and in soil samples. Beyond, this probe proved to be of relevance to detect F^- and AcO^- ions in fluoride-containing toothpaste/mouthwash and commercial vinegar samples, respectively, in semi-aqueous (CH_3CN-H_2O) solutions.

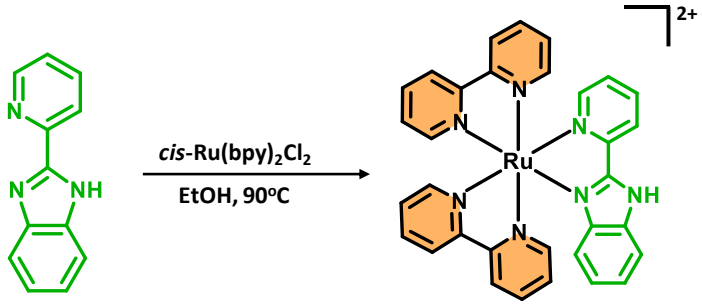

Scheme 5.1. Synthesis of Ru(II)-based luminescent probe **Ru-1**.

5.2. Experimental Section

5.2.1. Synthesis of Ru-1

Complex **Ru-1** has been synthesized according to the literature procedure. Briefly, a batch of 0.1 mmol *cis*-$Ru(bpy)_2Cl_2$, 0.1 mmol 2-(pyridin-2-yl)-1*H*-benzo[*d*]imidazole, and 20 mL ethanol were added to a 50 mL three-neck round bottom flask. The reaction mixture was refluxed at 90°C for 10-12 h under inert atmosphere. The color of the solution turned red orange. The complex was precipitated out by addition of a saturated aqueous solution of sodium hexafluorophosphate ($NaPF_6$) and then collected using vacuum filtration. Ultimately, complex **Ru-1** has been purified using silica-gel column chromatography with CH_3CN as eluent followed by recrystallization from CH_3CN-MeOH (1:1, v/v) mixture. (Yield: 88 %). Anal. Calcd. for $C_{32}H_{25}F_{12}N_7P_2$: C, 42.77; H, 2.78 and N, 10.91. Found: C, 42.72; H, 2.85 and N, 10.76. FT-IR (KBr disk): 3360, 3064, 1615, 1462, 1240, 962, 838, 760 and 550 cm^{-1}. UV-Vis (H_2O): λ_{max}/nm = 285 nm and 460 nm. ESI-MS (positive, CH_3CN): *m/z* Calcd. for $[M–H–PF_6]^+$ = 608.11, Found = 608.1110; *m/2z* Calcd. for $[M–2PF_6]^{2+}$ = 304.56, Found = 304.5589.

5.2.2. Spectroscopic titrations

The sensing behavior of probe **Ru-1** for different anions was investigated in water and in CH_3CN (10 μM) solution. The stock solutions of anions (1.0 mM) were prepared just before performing the sensing experiments using tetrabutylammonium or potassium salts of $F^–$, $Cl^–$, $Br^–$, $H_2PO_4^–$, $CN^–$, $I^–$, $AcO^–$, $NO_3^–$, $SO_3^{2–}$, $S^{2–}$, $SO_4^{2–}$ and $NO_2^–$ ions. Quartz cuvettes of 1.0 cm path length and 3.0 mL volume were used for all the UV-Vis measurements. For a typical UV-Vis titration, 200 mL aliquot of a given anion (1.0 mM) was added to 2.9 mL solution of the probe (10 μM). For emission titration experiment, 200 mL aliquot of a given anion (1.0 mM) was added to 2.9 mL solution of the probe (1.0 μM), and the excitation wavelength (λ_{ex}) was fixed at 460 nm maintaining the excitation slit width as 5.0 mm.

5.2.3. Detection of $F^-/AcO^-/CN^-$ ions in real samples

The response of probe **Ru-1** was demonstrated against some real samples such as tap water, distilled water and commercially available vinegar, mouthwash and toothpaste samples. The toothpaste, and mouthwash samples were prepared by dissolving 40 mg of the commercial sample in 5.0 mL CH_3CN by vigorously mixing and followed by sonication.

5.2.4. Test paper strips experiments

The low-cost test paper strips experiments were carried out by immersing the finely cut-shaped Whatman filter paper strips into an aqueous solution of **Ru-1** (50 μM). The test strips were then taken out and air-dried. After that, the treated strips were kept into the solutions of various selected anions (*ca*. 10^{-2} M) to eventually observe the visual changes under UV as well as visible light illumination.

5.2.5. DFT calculations

The DFT calculations have been performed for probe **Ru-1** and its deprotonated form (i.e., **Ru-1-dp**) without symmetry constraints by using Gaussian 09W program. The geometries of the complexes have been derived by the help of semi-empirical PM3 level for the molecular frameworks. Moreover, the analytical vibrational frequency was calculated using the long-range corrected (LC) hybrid density functional with empirical distribution correction (GD3B) by calculating ZPE at 273.15 K T and 1.0 atm pressure. The structures were optimized using B3LYP theory with 6-311G++(d,p) basis set for the C, N, and O atom and LANL2DZ basis set for Ru centre with effective core potential. The numerical simulation was performed using a superfine grid.

5.3. Results and Discussion

Probe **Ru-1** has been synthesized following the procedure reported earlier [45,46], and notably characterized by UV-Vis, fluorescence, FT-IR, ESI-MS, and elemental analyses. UV-Vis studies clearly revealed the characteristic Ru(II)-bpy centred bands at 285 nm ($\pi \rightarrow \pi^*$; ligand centred) and 460 nm ($d\pi_{Ru} \rightarrow \pi^*_{bpy}$; MLCT) (**Fig. 5.1(a)**) while the emission maximum for **Ru-1** was

observed at 625 nm in pure water (**Fig. 5.1(b)**). In CH_3CN solution, the absorption and emission maxima appeared at 457 nm and 622 nm, respectively (**Figs. A32 and A33**). The peaks in ESI-MS at 304.5589 and 608.1110 have been attributed to the original (*m/2z*) and deprotonated (*m/z*) molecular ion peaks (**Fig. A34**).

5.3.1. Sensing behavior of Ru-1 in aqueous media

The development of highly water-soluble and luminescent probes remains the need of modern-day-research for their practical utility and successful implementation into real-life samples. Both UV-Vis and emission spectral studies have been employed to assess its sensing ability toward various anions of relevance in 100% aqueous medium. A 10 μM solution of **Ru-1** was prepared in deionised water and was tested against various selected anions (such as F^-, Cl^-, Br^-, $H_2PO_4^-$, I^-, CN^-, AcO^-, NO_3^-, SO_3^{2-}, S^{2-}, SO_4^{2-} and NO_2^-). As expected, complex **Ru-1** served as a highly selective sensor for CN^- ion in water amongst the pool of tested anions. The progressive addition of CN^- (0-9 equiv) resulted in a pronounced red-shift in the MLCT band of **Ru-1** from 460 to 487 nm which was accompanied with three isosbestic points at 324 nm, 402 nm, and 477 nm (**Fig. 5.1(a)**).

The clear isosbestic points suggested the stoichiometric generation of some new species from **Ru-1** upon interaction with CN^- ion. Comparatively, other anions including the competing F^- and AcO^- failed to produce any such changes. These results were further corroborated by emission titration experiments. As shown in **Fig. 5.1(b)**, the luminescence intensity of **Ru-1** at 625 nm underwent substantial quenching solely in case of CN^- ion (9.0 equiv) over other anions (λ_{ex} = 460 nm).

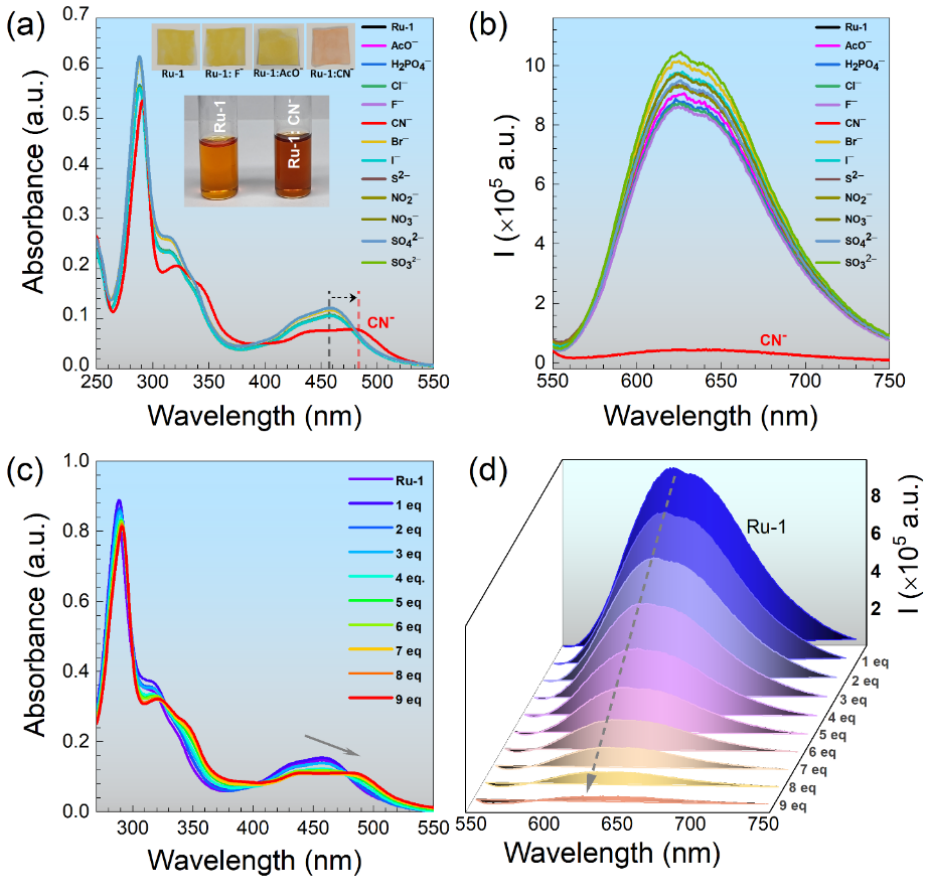

Fig. 5.1. (a-b) UV-Vis and emission spectra of the probe **Ru-1** (*ca.* 10.0 μM) with various anions in water (in Fig. 5.1(a), the spectral signature of several anions is typically overlapping with that of the probe, only distinct spectral change can be noticed in case of CN^- ion); (c-d) UV-Vis and emission spectral variations in **Ru-1** at different concentrations of cyanide ion (0-9.0 equiv). Inset: Color changes in aqueous solution and on paper strips that occur when **Ru-1** was treated with CN^- ions.

Interestingly, **Ru-1** also acted as a colorimetric probe for CN^- as the original red-orange color of **Ru-1** turned red-brown in presence of CN^- ions (inset of **Fig. 5.1(a)**). Job's plot analysis indicated a 1:1 binding stoichiometry for **Ru-1**···CN^- adduct formation (**Fig. A35**). The limit of detection for CN^- has been depicted as 12.8. nM (**Fig. 5.2**) which is remarkably lower than the maximum CN^- contaminant level in the drinking water scaled by U.S. EPA (Kaushik et al., 2016; Xu et al., 2010). To further rationalize the latter, a

systematic comparison of the sensing parameters with previously reported CN^--responsive Ru(II)-based luminescent probes has been recapped (see **Table 5.1**). The comparison clearly suggests that the relative proximity of imidazole ring with Ru(II) results into an improved LoD value; however, the binding constant was found relatively comparable ranging from 10^5 to 10^6 M^{-1} in majority of the cases. Notably, the CN^- addition induced more pronounced MLCT shift in **Ru-1** as compared to the probes integrated with other ligand scaffolds.

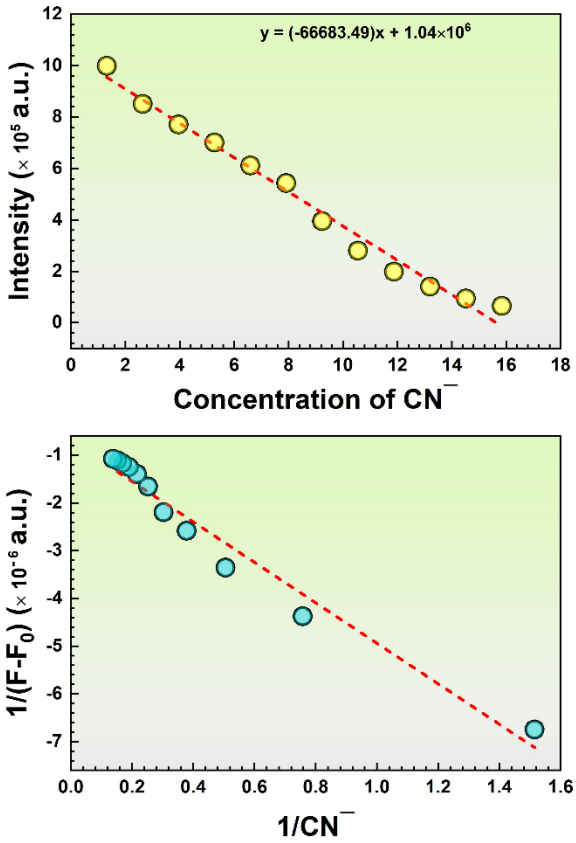

Fig. 5.2. Emission intensity of **Ru-1** at 625 nm *vs*. concentration of CN^- ion, with binding constant calculated from a 1:1 binding model.

5.3.2. Sensing behavior of Ru-1 in acetonitrile solution

The anion sensing ability of **Ru-1** was also investigated in CH_3CN solution (**Figs. A36-A40**). A 10 µM solution of **Ru-1** was titrated against 6.0 equiv of anionic species including F^-, Cl^-, Br^-, $H_2PO_4^-$, CN^-, I^-, AcO^-, NO_3^-, SO_3^{2-}, SO_4^{2-} and NO_2^- ions. The MLCT band of **Ru-1** markedly red-shifted (from 457 nm to 497 nm) in the presence of F^-, AcO^- and CN^- ions while other

anions displayed almost negligible changes (**Fig. A36(a)**). The extent of red-shift in acetonitrile (i.e., 40 nm) was more than that observed in water (i.e., 27 nm). Similar to aqueous medium, the absorption changes were associated with three clean isosbestic points at 322 nm, 411 nm and 474 nm. Probe **Ru-1** emitted near 624 nm in CH_3CN when excitation wavelength was 460 nm. The luminescence intensity exhibited a complete quenching upon the addition of F^-, CN^-, AcO^- and $H_2PO_4^-$ (6.0 equiv) with no remarkable changes in the presence of other investigated anions (**Fig. A36(b)**). These results clearly revealed that **Ru-1** could be utilized to detect F^-, CN^-, AcO^- and $H_2PO_4^-$ ions in CH_3CN solution. Interestingly, in CH_3CN, the limit of detection LoD was found relatively better (1.30 nM) for CN^- ion when compared with that in aqueous medium (12.8 nM), most likely due to some hydration of cyanide ion in water. Moreover, the LoD values for F^- and AcO^- were depicted as 2.26 nM and 1.90 nM, respectively, in CH_3CN solution.

The reason behind the anion-induced luminescence quenching of **Ru-1** both in water and CH_3CN may be attributed to the strong hydrogen bonding interaction between the selected anions (A^-) and the N–H functionality of the 2-(pyridin-2-yl)-1*H*-benzo[*d*]imidazole ligand leading to N–H···A^- incipient. At higher concentration of A^-, the N–H bond may further stretch to eventually split due to proton transfer process i.e., initially hydrogen bonding is formed by anions followed by the deprotonation of the N–H group. The red-shift in MLCT band has been ascribed to the increased electron density on the imidazole moiety that concomitantly strengthens both σ-donation from imidazole-N toward Ru(II) and π-backdonation from Ru(II) toward ligands. This promotes the charge transfer process between the Ru(II) and the bpy ($d\pi \longrightarrow \pi^*$) moieties. On the other hand, the quenching in the emission band was due to the PET (photoinduced electron transfer) effect arising from the deprotonated benzimidazole to the ^{3}MLCT state of the luminescent complex. Furthermore, it was very difficult to distinguish between F^-, AcO^- and CN^- in acetonitrile solutions as they all exhibit similar changes in the UV-Vis and emission spectra.

Distinctly, we also performed the interference experiments in water in the presence of other competing anions. No change in the luminescence of **Ru-**

1 could be realized when treated with competing anions such as F^- and AcO^- ions even at their high concentrations (upto 10 equiv); however, as soon as a small concentration of CN^- was added, the emission band was completely quenched (**Fig. 5.3**). Hence, the response of **Ru-1** for CN^- was found unaffected by the presence of other assorted anions, indicating a high selectivity of **Ru-1** for CN^- in aqueous medium. Besides, the probe exhibited reversibility in water in the presence of acetic acid; indeed, the dark-red colored solution of **Ru-1**---- CN^- faded, and the original emission/absorption spectra of the probe **Ru-1** restored due to the protonation process induced by acetic acid.

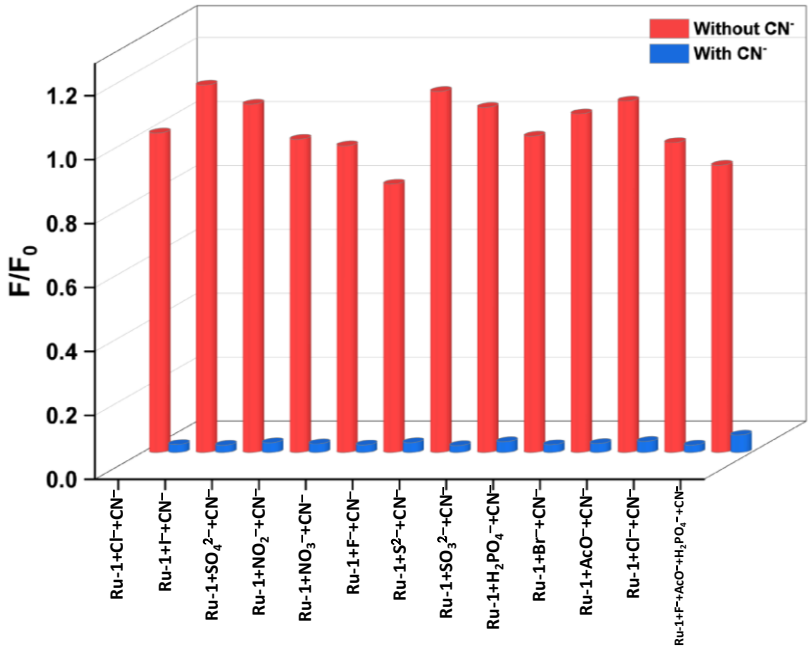

Fig. 5.3. Relative fluorescent response of probe **Ru-1** for CN^- with 10 equiv. of other anions in water.

5.3.3. Effect of water content

For its practical usage, the changes in UV-Vis spectra of probe **Ru-1** for F^- and CN^- ions were evaluated and monitored in different mixtures of CH_3CN-H_2O (80/20, 50/50 and 35/65; v/v), and the results were compared with the data observed in pure CH_3CN solution. In pure CH_3CN, nearly 1.2 equiv of either F^- or CN^- completed the binding reaction with a red-shift in the MLCT band from 457 nm to 497 nm. On the other hand, in 20% aqueous solution (CH_3CN-H_2O, 80/20, v/v), the addition of 3.0 equiv of both the anions was required to exhibit

a similar change (**Fig. A41(a)**). In 50% aqueous solution, *ca.* 20.0 equiv of F^- was required to complete the reaction while the amount used for CN^- was 6.0 equiv (**Fig. A41(b)**). Further increase into water content (i.e., 65% aqueous solution) resulted into remarkable changes as the reaction was incomplete even after addition of 50 equiv of F^- ions; however, 8.0 equiv CN^- led to the completion of the reaction (**Fig. A41(c)**). Therefore, the concentration of water is an important parameter for selectivity, and sensitivity of probe **Ru-1**.

Fundamentally, the high selectivity of probe **Ru-1** for CN^- in water may be attributed to a relatively lower hydration value of CN^- ($\Delta G_{cyanide}$ = -295 KJ/mol) as compared to the other anions ($\Delta G_{fluoride}$ = -465 KJ/mol, $\Delta G_{acetate}$ = -365 KJ/mol) (Karmakar et al., 2016; Marcus, 1991; Mo et al., 2012). The other anions basically preferred to be hydrated and did not form any hydrogen bond with the N-H of the imidazole moiety in **Ru-1**. Moreover, CN^- has a larger pKa value (9.0 for HCN) which indicates that it acts as stronger base in water when compared to AcOH (pKa 4.75) and HF (pKa 3.17) that can easily extract a proton. As a result, the high selectivity towards CN^- makes this probe a powerful candidate for the detection of CN^- ion in real aqueous samples.

The photosensitivity of probe **Ru-1** has been investigated with the help of absorption and emission spectral analyses in aqueous medium. Upon irradiation of **Ru-1** with UV and visible light at different time intervals up to 2 hours, the negligible spectral changes could be noticed which clearly indicated the photostable behaviour of our probe (**Fig. A42 and A43**).

5.3.4. Time-resolved fluorescence study

Luminescence lifetime experiments have also been performed to corroborate the CN^- sensing mechanism. The time resolved emission spectrum of free probe (i.e., **Ru-1**) exhibited a mono-exponential decay, and the emission lifetime was calculated to be 166.9 ns in water. The gradual addition of F^- and AcO^- displayed no change in its lifetime (**Fig. A44**); however, the addition of CN^- induced a quenching in the average lifetime from 134 ns to 115 ns (**Fig. 5.4**).

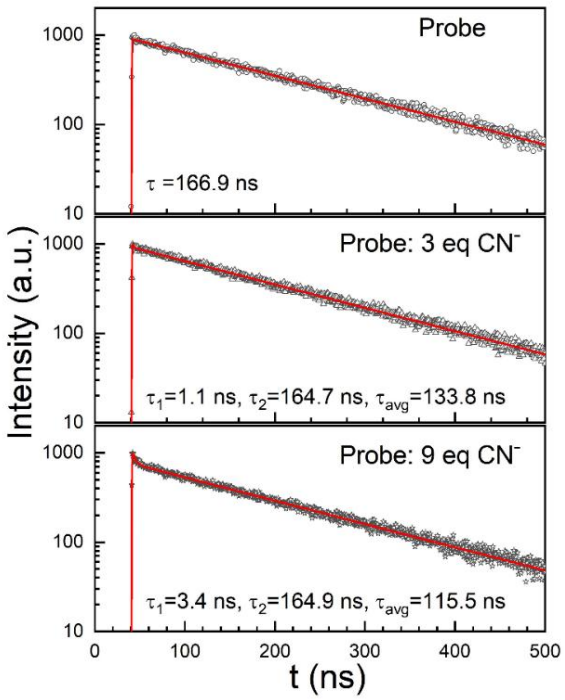

Fig. 5.4. TRF spectra of **Ru-1** with different concentrations of CN^- ions. Decay curves were fitted to a biexponential model for the probe in the presence of CN^- ions. For 3 equiv. CN^-: τ_1 = 1.1 ns (α_1=0.1563) and τ_2 = 164.7 ns (α_2=0.6719); for 9 equiv. CN^-: τ_1=3.4 ns (α_1=0.2449) and τ_2 = 164.9 ns (α_2=0.5544). α_1 and α_2 represent the relative contribution of each lifetime component to the total emission.

Notably, unlike the other competing anions, the introduction of CN^- resulted in a bi-exponential decay profile. The concurrent existence of more than one species, each with distinct lifetime, may result in a bi-exponential decay. The rational assumption is that the CN^- ion deprotonates the N-H group making the emission lifetime shorter than the free probe and results in the luminescence quenching. Hence, the observed bi-exponential decay profile might be attributed to the existence of probe **Ru-1** in two states i.e., protonated (i.e., original probe **Ru-1**) and deprotonated (referred as **Ru-1-dp**) having different lifetimes. It is worth noting that the change in lifetime is consistent with the probe's steady-state behavior.

5.3.5. Detection of anions in real samples

To further assess its practical relevance and applied potential, the sensing ability of **Ru-1** for CN^- was exploited in real water and food sources such as drinking water, tap water, apple seeds and sprouting potatoes. The water

samples were spiked with varied concentrations of CN^- ions. The detection was monitored by recording the UV-Vis spectral changes. The addition of aqueous sample spiked with CN^- ion to probe's solution induced a red-shift in the MLCT absorption of probe **Ru-1** together with a color change of solution from orange to red-brown (shown in **Fig. 5.5**). The cyanide concentration in the spiked water sample could be determined with excellent recovery values (**Tables A5 and A6**). On the other hand, the luminescence intensity of **Ru-1** declined immediately upon addition of cyanide containing tap water sample to probe **Ru-1** (**Fig. A45 (a)).**

The food samples have been prepared following the procedure reported earlier (Bhaskar and Sarveswari, 2019; Sun et al., 2018). Apple seeds and sprouting potatoes were crushed and soaked in 50 mL water for a day. The samples were then filtered, washed with NaOH solution and double distilled to adjust to a pH of 7.0. As shown in **Fig. A45(b)**, a significant luminescence quenching in could be noticed upon the addition of the cyanide containing food samples to the aqueous solution of the probe **Ru-1**. These results confirmed that **Ru-1** acts a simple, fast and efficient CN^- sensor that can be utilized to detect cyanide in various real samples.

Distinctly, to investigate the versatility of probe **Ru-1**, we have used commercially available vinegar (for OAc^-) and mouthwash/toothpaste (for F^-) samples. The addition of one drop of either mouthwash or vinegar sample to **Ru-1** led to an instant color change in probe's solution (visible to the naked eye). The OAc^-/F^- sensing ability of **Ru-1** into commercially available mouthwash and vinegar samples was also supported by slightly red-shifted MLCT band at 460 nm in UV-Vis spectra (**Fig. 5.5**). For sensing of fluoride ion, the sample was prepared by dissolving 40 mg of toothpaste/mouthwash in 5.0 mL CH_3CN with the help of sonication followed by the centrifugation. The sample solution (30 μL) was then added to the aqueous solution of **Ru-1** (10 μL) and the changes were monitored using UV-Vis analysis. A remarkable luminescence quenching in **Ru-1** could also be observed upon the addition of the mouthwash and vinegar samples to the acetonitrile solution of probe **Ru-1** (**Fig. A45**).

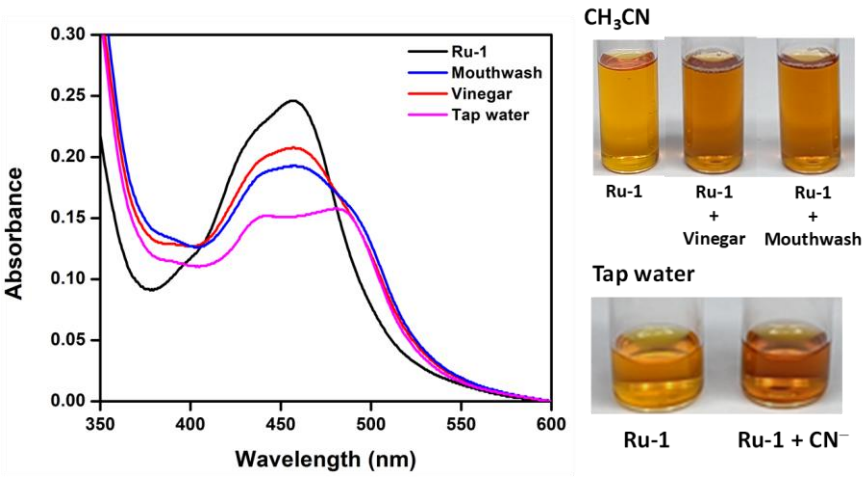

Fig. 5.5. Response of probe **Ru-1** for different real samples. (a) Detection of OAc^- in commercially available vinegar (red-line); F^- in mouthwash (blue-line) and CN^- in cyanide-spiked tap water (pink-line) using UV-Vis spectra.

5.3.6. Low-cost test strips experiments

In order to further apply our probe in everyday life applications, we have developed the test strips by soaking the finely cut-shaped filter paper (Whatman Grade) strips in aqueous solution of probe **Ru-1** (*ca.* 10^{-3} M) followed by the drying in open air. A significant color change from light yellow to red could be observed when the test strips were treated with CN^- ions and visualised under visible light illumination. These results clearly suggested that this probe can be applied to recognise cyanide traces in real samples (inset of **Fig. 5.1(a)**).

5.3.7. Cell imaging study

The probe **Ru-1** was also investigated for biological application such as cell imaging in human breast cancer MCF-7 cell lines. Upon incubation with variable concentration of **Ru-1** (20-60 μM), the cell lines displayed bright red fluorescence as seen in **Fig. 5.6(a)**. The successive addition of cyanide ions induced significant quenching of luminescence when treated with cells containing 40 μM of probe **Ru-1** (**Fig. 5.6(b)**). These results were in consistence with the *in vitro* studies and indicated that the probe **Ru-1** can be utilized for imaging of CN^- in biological settings.

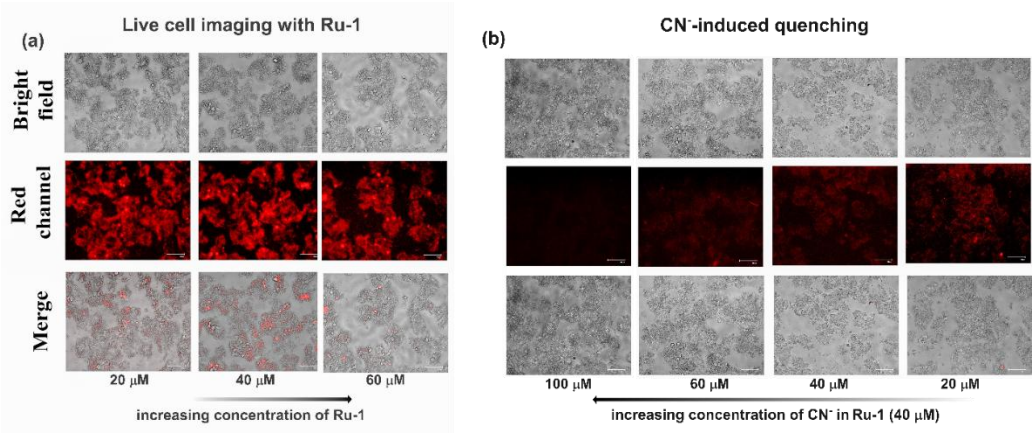

Fig. 5.6. Confocal luminescence imaging of human breast cancer MCF-7 cell lines. (a) Cell lines incubated with variable concentrations (20-60 μM) of only probe **Ru-1** and (b) incubation of cell lines with progressive addition of CN^- ions (20-100 μM) in presence of 40 μM **Ru-1**.

5.3.8. Mechanism for anion binding

The outcomes of the experimental findings indicate explicitly that the probe **Ru-1** interacts strongly with CN^- ion in pure aqueous medium. In CH_3CN, it acts as a sensor for CN^-, F^- and AcO^- ions but with less selectivity. It is probable that the N-H proton of imidazole unit interacts with the target anion (X^-) to afford an incipient N-H···X bond, and the presence of excess X^- induced further N-H bond stretching eventually leading to the splitting and concomitant transfer of the N-H proton (as shown in **Scheme 5.2**). Furthermore, a very similar spectral profile of **Ru-1** in presence of hydroxyl anion (OH^-) with that of CN^-, F^- and AcO^- clearly suggests the ultimate deprotonation of N-H proton of coordinated pyridyl-benzimidazole ligand in **Ru-1** (**Figs. A46 and A47**).

The deprotonation event results in a red shift of the MLCT band along with luminescence quenching. The increased electron density on the imidazole moiety strengthens both σ-donation from imidazole-N toward Ru(II) as well as π-backdonation from Ru(II) toward ligands. This promotes the charge transfer process between Ru(II) centre and the bpy ($d\pi \longrightarrow \pi^*$) units. On the other hand, the luminescence quenching may be attributed to the PET effect arising from the deprotonated imidazole moiety to the photoexcited Ru(II) in **Ru-1**. Furthermore, TRF studies suggested the sensing mechanism was due to the

eventual deprotonation of the N-H group by the cyanide ion which results in two distinct species and therefore a biexponential curve was observed.

Density functional theory (DFT) calculations have also been carried out to support the anion binding mechanism. A distorted octahedral geometry around Ru(II) centre is evident in complex **Ru-1** and its deprotonated form i.e., **Ru-1-dp**. The $Ru(bpy)_2$ unit is coordinated by the two N atoms of the pyridyl benzimidazole moiety. The related optimized structures of probe **Ru-1** and **Ru-1-dp** are presented in **Fig. 5.7(a)**.

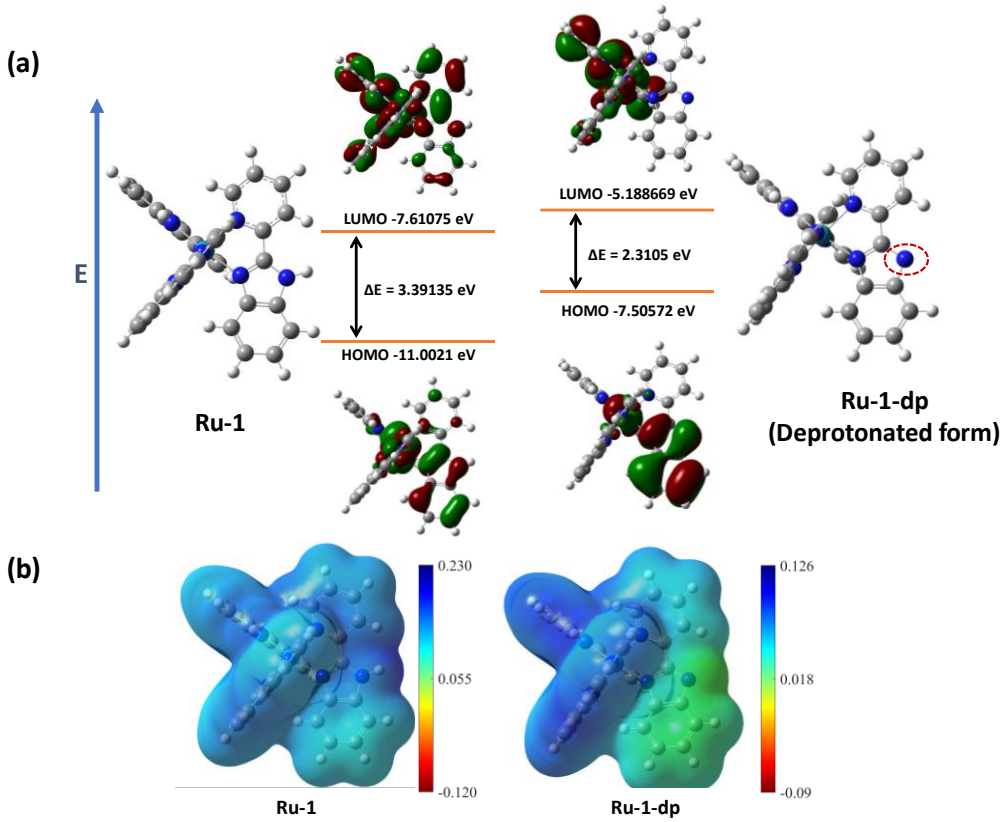

Fig. 5.7. (a) DFT studies of probe **Ru-1** and its deprotonated form **Ru-1-dp** and (b) the electrostatic potential (ESP) map of the probe **Ru-1** and its deprotonated form **Ru-1-dp** on isodensity surface in ground state within the range of -0.120 (red) to + 0.230 (blue) for **Ru-1** and -0.09 (red) to +0.126 (blue) for **Ru-1-dp**.

The HOMO (i.e., highest occupied molecular orbital) of **Ru-1** was primarily composed of Ru-character with a very small contribution from the benzimidazole group of the pyridyl-benzimidazole ligand. On the other hand, its LUMO (i.e., lowest unoccupied molecular orbital) was equally localized over

all three ligands. In the deprotonated form **Ru-1-dp**, the HOMO mainly consisted of the benzimidazole unit with a significant decrease in Ru contribution; however, its LUMO was mainly bpy centred. These data suggested an increased delocalization of negative charge over the benzimidazole group after deprotonation in **Ru-1-dp**. The energy gap between the frontier molecular orbitals in complex **Ru-1** was depicted to be 3.39 eV that was reduced to 2.31 eV after deprotonation process (**Fig. 5.7(a)**). The lowering in the energy gap between HOMO and LUMO of **Ru-1-dp** agreed well with the red-shifted MLCT absorption in the UV-Vis spectrum due to **Ru-1**···CN^- interaction (*vide supra*). The calculated ground state Ru-N_{bpy} bond lengths in **Ru-1** and **Ru-1-dp** were found close to each other ranging from 2.08-2.09 Å (**Table A7** and **Fig. A48**). Notably, the Ru-$N_{imidazole}$ bond length reduced markedly from 2.10 Å to 2.07 Å after deprotonation. This shortening in the bond length may be ascribed to the increased synergic effect between the metal centre and nitrogen atom of the imidazole unit. The electrostatic potential (ESP) was also mapped for better visualization of the distribution of electronic charge density and its reorganization after deprotonation. The different color corresponds to the different electron density; basically, the dark blue color represents electropositive area while the bluish-green area corresponds to the electron rich site. The ESP analysis clearly revealed an increased electronic density on the benzimidazole moiety after deprotonation of **Ru-1** (**Fig. 5.7(b)**). The proposed mechanism for sensing is shown in **Scheme 5.2**.

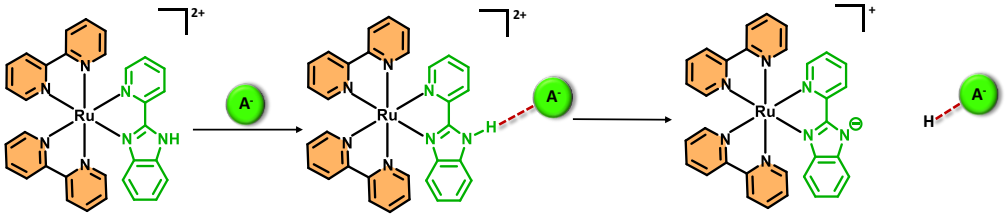

Scheme 5.2. Probable binding mode of anions (A^-) with probe **Ru-1** (A^- = F^-, AcO^-, and CN^- ions).

Table 5.1. Different mono and binuclear Ru(II)-based optical probes employed for the detection of CN^- ion.

S.No.	Probe	LoD (nM)	Real sample	Solvent	Ref.
(a) Reaction-based probes					
1.	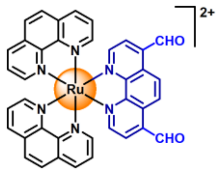	180	-	CH_3CN	(Khatua et al., 2012)
2.	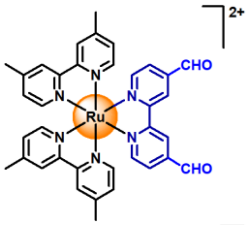	-	-	CH_3CN	(Li et al., 2014)
3.	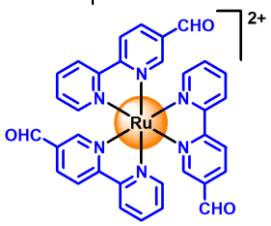	700	-	CH_3CN/H_2O (4:6)	(Zhu et al., 2020)
(b) Binding-based probes					
4.	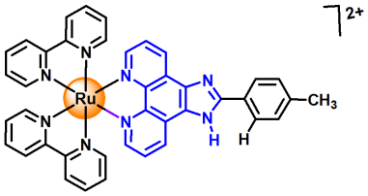	10^5	-	H_2O	(Mo et al., 2012)
5.	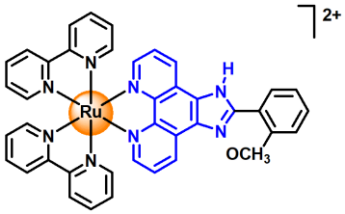	300	-	CH_3CN	(Alreja and Kaur, 2016b)

6.	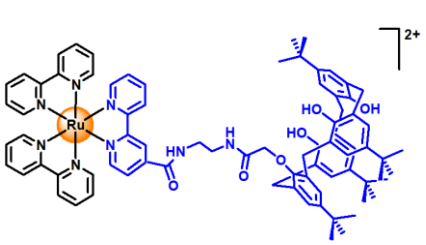	70			(Maity et al., 2015)
7.	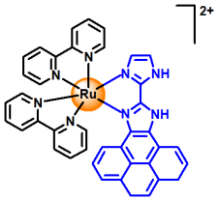	11.2	Solid state	H_2O	(Mardanya et al., 2015)
8.	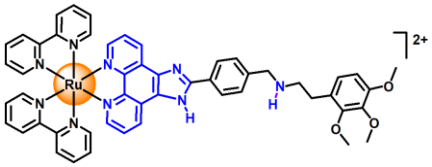	330	-	H_2O	(Obali 2020a)
9	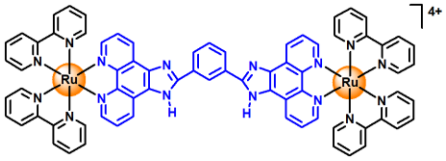	5000	-	H_2O	(Mo et al., 2012)
10	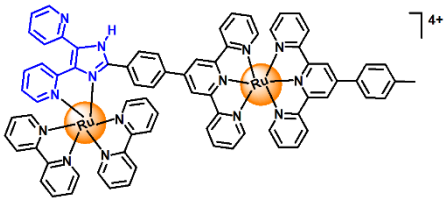	10	Paper Strip	H_2O	(Bar et al., 2017)
11	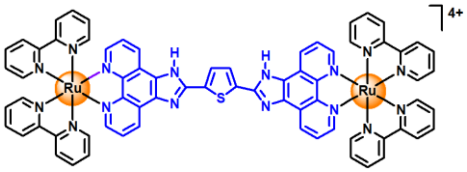	31		H_2O	(Pal et al., 2020)
This work	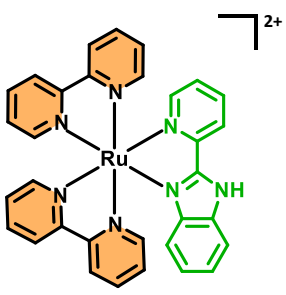	12.8	Paper strip, Tap water, Distilled water, Live cell imaging	H_2O	

5.4. Conclusions

In summary, a cyanide-responsive probe with high selectivity in pure water *via* H-bonding interaction has been presented. In probe **Ru-1**, the direct coordination of imidazole moiety with metal centre leads to an enhanced acidity of N−H proton which is an important parameter to define the selectivity of **Ru-1** toward CN- ion in water. Furthermore, this probe has been exploited to assess the CN^--induced emission lifetime changes in aqueous medium. The 1:1 anion binding stoichiometry has been established by Job's plot and DFT analyses. The live cell imaging assessment clearly revealed the successful imaging of CN^- ions in MCF-7 cell lines. Thus, the probe **Ru-1** holds promising application prospects cyanide species analytical field, providing overall a new strategy for the future development of luminescent anion-responsive sensors.

CHAPTER 6

PHOTOINDUCED CATALYSIS USING PHOTOSENSITIZER-CATALYST SYSTEM

6.1. State of the Art

In modern day research, economically and environmentally compatible synthetic routes are gaining growing attention (Mariotti et al., 2020; Shrivastava et al., 2025). Consequently, the green chemistry notion has emerged to endorse the mild chemical reaction conditions that include the use of non-polluting reagents, visible light as a major energy source, and water or O_2 as O atom and/or electron source(s) (Rana et al., 2022; Sharma et al., 2020). In this context, chemical oxidation reactions for diverse panel of organic substrates would benefit from remarkable improvements. Sulfoxidation and epoxidation reactions are on high demand in organic chemistry as the resultant products i.e., sulfoxides and epoxides are key scaffolds in biological, natural and pharmaceutical science (Caron et al., 2006; Moschona et al., 2020; Song et al., 2025). To access these functionalities, transition-metal catalyzed sulfoxidation and epoxidation reactions are the most common and efficient strategy, however, these processes require harsh oxidants such as H_2O_2 (Adams et al., 2025; Srour et al., 2013). These harsh oxidizing agents have several demerits such as they often show poor catalytic selectivity, may lead to uncontrolled oxidation reactions and are not sustainable and eco-friendly (Goyal et al., 2022; Saravanan et al., 2022). Conversely, in biological world, several metalloenzymes based on different 3d series metals such as Cu/Fe/Mn utilize O_2 as green, viable and cheap oxygen atom source for different oxidation reactions (Cho et al., 2004; Mezzaroba et al., 2019; Rosenzweig and Sazinsky, 2006). Generally, in these metalloenzymes, the activation of dioxygen occurs at active metal centre by a two-electron reduction of the O_2 to form the peroxo state and subsequent O-O bond cleavage. In case of metalloenzymes containing two metal centres in their active sites, one of the metal ions acts as an electron donor, however, in

mononuclear metalloenzymes, an external electron donor is required (Valdez et al., 2014; Vallee and Williams, 1968). Several mononuclear metalloenzymes of iron such as Cytochrome P450 and copper (peptidylglycine α-hydroxylating monooxygenase (PHM), dopamine β-monooxygenase (DβM), tyramine β-monooxygenase (TβM), etc.) have been identified till date, which effectively and selectively oxidize several compounds (Klinman, 2006; Kunishita et al., 2012; MacPherson and Murphy, 2007; Nebert and Russell, 2002).

Inspiring from these metalloenzymes, several research groups have tried to mimic their active sites in the form of different metal complexes (or synthetic models). Although Fe and Mn based complexes are most explored in this field, Cu(I)/O_2 chemistry is gaining increasing attention (Bryliakov and Talsi, 2014). Like their natural metalloenzymes, the catalytic cycle in the artificial copper systems is maintained by the presence of a reducing co-factor in close proximity, that allows a regeneration of the active Cu(I) species from the final inactive Cu(II) state. Unlike the biological world, the requirement of costly electron donors such as NADP(H) made the use of such catalytic systems fetter at large scale (O'Reilly et al., 2011).

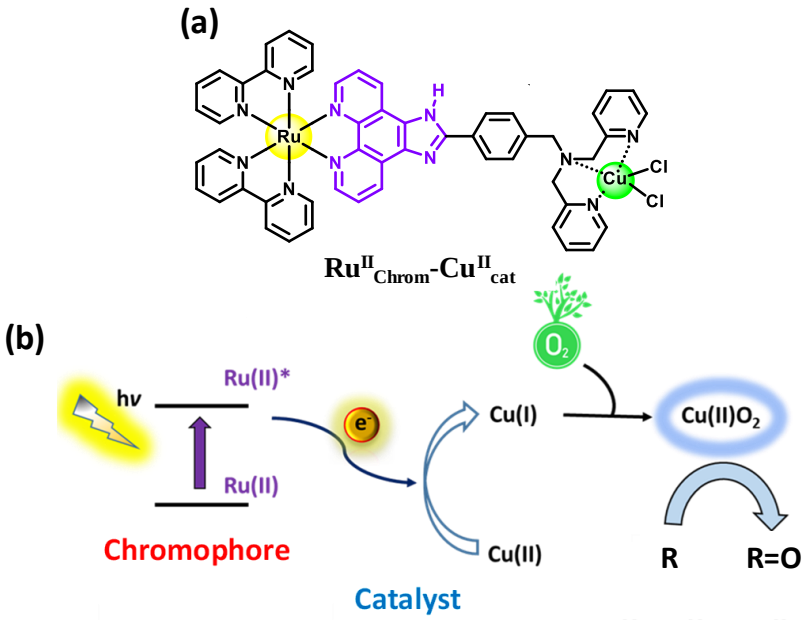

Scheme. 6.1. (a) Chemical structure of $\mathbf{Ru^{II}_{chrom}}$–$\mathbf{Cu^{II}_{cat}}$ dyad and (b) graphical representation of electron flow and sulfoxidation reaction catalyzed by $\mathbf{Ru^{II}_{chrom}}$–$\mathbf{Cu^{II}_{cat}}$ under visible light illumination.

An alternative and increasingly promising strategy in photoinduced catalysis involves the integration of chromophores with catalytic metal centres to form light-responsive systems (Castellano, 2015; Mulfort and Utschig, 2016). In such assemblies, the chromophore functions as a visible light-activated electron donor, effectively acting as a photoreductant that channels electrons to the catalytic metal center. Specifically, in copper-based systems, these chromophores mimic biological reduction cofactors by supplying electrons to the Cu(II) centre, thereby enabling catalytic activity under light irradiation (Reiser, 2016).

Recent studies have demonstrated both unimolecular and bimolecular assemblies of chromophores and catalytic centres for driving oxidation reactions using molecular oxygen as the sole oxidant [87]. Among these, unimolecular constructs have shown superior efficiency compared to their bimolecular counterparts. This enhanced performance is largely attributed to the covalent linkage between chromophore and catalytic site, which promotes efficient and directed intramolecular electron transfer, crucial for sustaining catalytic turnover under light irradiation (Chauhan et al., 2025; Kumar et al., 2022).

An elegant study by Hamelin and co-workers described the first Ru(II)-Cu(II) dyad system capable of photoinduced activation of dioxygen for oxidation reactions (Iali et al., 2015). To date, only three such Ru(II)-Cu(II) dyads have been reported in the literature, highlighting the novelty and underexplored nature of this design strategy (Chao and Zhao, 2017; Iali et al., 2015; Klein et al., 2023). In a recent advancement, our group introduced a Ru(II)-Fe(III) heterobimetallic dyad, capable of facilitating C-H oxidation *via* visible light-driven O_2 activation, thereby expanding the scope of such photoredox-active systems (Singh et al., 2021).

All these investigations prompted us to develop a novel heterobimetallic complex abbreviated as $\mathbf{Ru^{II}_{chrom}\text{-}Cu^{II}_{cat}}$ which incorporates a Ru(II) photosensitizer and a Cu(II) catalytic centre, bridged through an imidazo[4,5-*f*][1,10]phenanthroline ligand (**Scheme 6.1(a)**). Upon visible light irradiation,

the Ru(II) chromophore becomes photoexcited and transfers an electron to the adjacent Cu(II) center, generating a transient Ru(II)-Cu(I) species (**Scheme 6.1(b)**). The rigid and π-conjugated nature of the bridging ligand ensures strong electronic communication and minimizes the distance between the redox-active centers, thereby promoting rapid and directional electron transfer.

Subsequent exposure of this photogenerated Ru(II)-Cu(I) intermediate to dioxygen results in the formation of a reactive Ru(II)-Cu(II)–O_2 adduct, which acts as the key oxidant in substrate transformations. We have successfully demonstrated the catalytic potential of this dyad in a range of high-impact oxidation reactions, showcasing its utility as a green and efficient photocatalyst for selective oxygenation processes.

6.2. Experimental Section

6.2.1. Synthesis of ligand bpmpip

A solution containing 1,10-phenanthroline-5,6-dione (0.52 g, 2.5 mmol) and ammonium acetate (NH_4OAc, 5.8 g, 75 mmol) was prepared in hot glacial acetic acid (30 mL) under nitrogen atmosphere without light. Subsequently, bpmp-CHO (A) (0.79 g, 2.5 mmol) was added to the reaction mixture, which was then refluxed at 80°C for 2-3 hours. After completion, the reaction mixture was cooled in an ice bath and neutralized to pH 7 using 1 M NaOH. A light-brown precipitate of the crude product formed was collected by filtration, washed thoroughly with distilled water, and dried under vacuum. The crude compound was purified by silica gel column chromatography using a mixture of dichloromethane and methanol (9:1, *v/v*). The solution was concentrated to a small volume, followed by the addition of diethyl ether to induce precipitation. The resulting solid was isolated and dried to afford a yellow powder of bpmpip. Yield: 0.92 g, 72%. ^{1}H NMR (500 MHz, DMSO-d_6, TMS, δ in ppm): 13.88 (s, 1H, NH-imidazole), 8.96 (s, 4H), 8.53 (s, 2H), 8.04 (d, 2H), 7.66 (t, 2H), 7.53 (d, 3H), 7.27-7.32 (m, 3H), 7.17 (t, 2H), 3.78 (s, 4H, -CH_2-pyridine), 3.59 (s, 2H, -CH_2-phenyl).

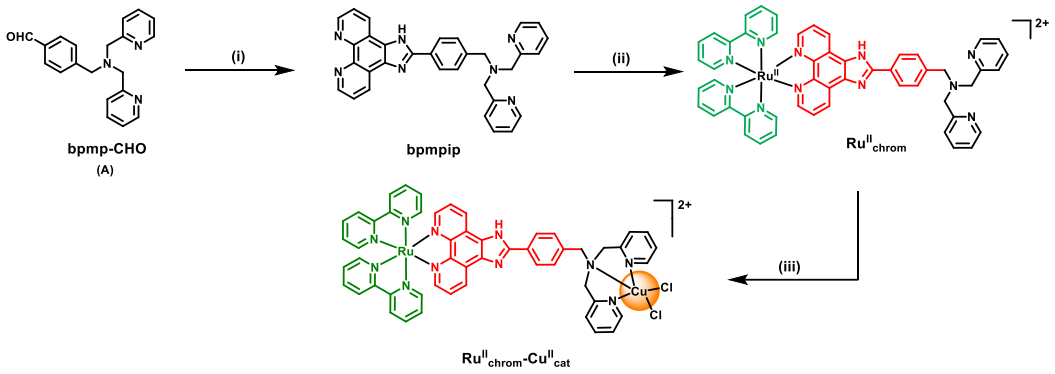

Scheme 6.2. Synthesis of dyad $\mathbf{Ru^{II}_{chrom}\text{-}Cu^{II}_{cat}}$. (i) 1,10-phenanthroline-5,6-dione, NH_4OAc, AcOH, 70-80ºC, 3h; (ii) *cis*-$Ru(bpy)_2Cl_2$, EtOH–H_2O (1:1), reflux, 12 h; (iii) anhydrous $CuCl_2$, CH_3CN, 2 h.

6.2.2 Synthesis of photosensitizer ($\mathbf{Ru^{II}_{chrom}}$)

A degassed ethanol-water solution (25 mL) containing *cis*-$Ru(bpy)_2Cl_2$ (0.1 mmol) and bpmpip (0.1 mmol) was refluxed for 10-12 hours under inert atmosphere. During the reaction, the solution color changed to red-orange, indicating complex formation. The resulting complex was precipitated by the addition of saturated $NaPF_6$ aqueous solution and later collected by vacuum filtration. Purification was carried out *via* column chromatography over basic alumina, employing a solvent mixture of acetonitrile and 20% aqueous KNO_3 (8:1, *v/v*). The collected fractions were concentrated, followed by anion exchange with $NaPF_6$ to yield the final complex ($\mathbf{Ru^{II}_{chrom}}$). The product was recrystallized from a mixture of acetonitrile and diethyl ether, weighing 0.084 g of the compound in 69% yield. Anal. Calcd. for $C_{52}H_{41}F_{12}N_{11}P_2Ru$: C, 51.58; H, 3.41; N, 12.72. Found: C, 51.82; H, 3.66; N, 12.76. ^{1}H NMR (500 MHz, DMSO-d_6, TMS, δ in ppm): 15.34 (s, 1H, NH-imidazole), 8.88 (dd, 6H), 8.50 (m, 4H), 8.21 (t, 3H), 8.10 (t, 3H), 7.80-7.89 (m, 5H), 7.59-7.64 (m, 9H), 7.34 (t, 2H), 7.27 (t, 2H), 3.77 (s, 4H, -CH_2-pyridine), 3.74 (s, 2H, -CH_2-phenyl). ESI-MS (positive, in H_2O): *m/z* = 1212.19 $[(Ru\text{-}L) + H^+]^+$ $(M + H)^+$, *m/z* = 1066.22 $[(Ru\text{-}L) - PF_6^-]^+$ $(M - PF_6^-)^+$, *m/z* = 920.21 and *m/z* = 460.62 $[(Ru\text{-}L) - 2PF_6^-]^{2+}$ $(M - 2PF_6^-)^{2+}$.

6.2.3 Synthesis of Ru^{II}_{chrom}-Cu^{II}_{cat} dyad

The heterobimetallic **Ru^{II}_{chrom}-Cu^{II}_{cat}** dyad was synthesized *via* a straightforward coordination protocol. A solution of **Ru^{II}_{chrom}** (0.1 mmol) was prepared in 15 mL of dry acetonitrile under an inert nitrogen atmosphere. To this solution, anhydrous $CuCl_2$ (0.12 mmol) was added directly as a solid. The reaction mixture was stirred at room temperature for 2 hours to ensure complete coordination between the Cu^{II} centre and the available donor sites of the Ru^{II} complex. Upon completion, the reaction mixture was transferred to a 50 mL round-bottom flask, and the solvent was removed under reduced pressure. The resulting residue was then dissolved in a minimal volume of methanol (3-4 mL). To this solution, a saturated aqueous solution of $NaPF_6$ was added dropwise with constant stirring, resulting in the precipitation of the target heterobimetallic complex as a solid. The precipitate was collected by filtration, washed with cold water and diethyl ether, and dried under vacuum to yield the pure **Ru^{II}_{chrom}-Cu^{II}_{cat}** dyad.

6.3. Results and Discussion

The synthesis of the bridging ligand was accomplished *via* the condensation of 1,10-phenanthroline-5,6-dione with *bpmp*-CHO in refluxing glacial acetic acid in the presence of excess ammonium acetate. This reaction afforded the desired imidazo-functionalized ligand in good yield. Subsequently, the Ru^{II}-based chromophore **Ru^{II}_{chrom}** was synthesized through a stoichiometric reaction between *cis*-$Ru(bpy)_2Cl_2$ and the imidazole-containing ligand (bpmpip) in a mixed ethanol-water solvent system. The structural integrity of the complex was confirmed by ^1H NMR analysis and ESI-MS spectrometry. ^1H NMR spectrum of **Ru^{II}_{chrom}** recorded in $(CD_3)_2SO$ at room temperature exhibited all expected signals corresponding to the bpmpip and bpy ligands. A distinctive downfield resonance at 15.34 ppm was attributed to the -NH proton of the imidazole ring, indicating successful cyclization. Additionally, two singlets at 3.74 and 3.77 ppm were assigned to the methylene protons of the phenyl-CH_2 and pyridine-CH_2 moieties, respectively. Electrospray ionization mass spectrometry (ESI-MS) further confirmed the structure of **Ru^{II}_{chrom}**. A

prominent peak at *m/z* = 460.6249 (calcd. 460.63) corresponded to the doubly charged species [$\mathbf{Ru^{II}_{chrom}}$ − $2PF_6^-$]$^{2+}$. Additional peaks at *m/z* = 1212.1860 (calcd. 1212.20) and 1066.2244 (calcd. 1066.22) were assigned to the protonated molecular ion [$\mathbf{Ru^{II}_{chrom}}$ + H^+]$^+$ and the singly charged species [$\mathbf{Ru^{II}_{chrom}}$ − PF_6^-]$^+$, respectively.

To construct the heterobimetallic dyad, $\mathbf{Ru^{II}_{chrom}}$ was treated with anhydrous $CuCl_2$ in dry acetonitrile under stirring. The resulting complex $\mathbf{Ru^{II}_{chrom}}$-$\mathbf{Cu^{II}_{cat}}$ was characterized by ESI-MS analysis. The spectrum revealed multiple peaks: *m/z* = 1055.0886 (calcd. 1055.13), 583.0478 (calcd. 583.06), and 509.0615 (calcd. 509.58), corresponding to the species [$\mathbf{Ru^{II}_{chrom}}$ − $2PF_6^-$ + Cu^{2+} + $2Cl^-$]$^{2+}$, [$\mathbf{Ru^{II}_{chrom}}$ − PF_6^- + Cu^{2+} + Cl^-]$^{2+}$, and [$\mathbf{Ru^{II}_{chrom}}$ − $2PF_6^-$ + Cu^{2+} + Cl^-]$^{3+}$, respectively. These mass signals collectively support the successful formation of a covalently linked $\mathbf{Ru^{II}_{chrom}}$-$\mathbf{Cu^{II}_{cat}}$ heterobimetallic complex.

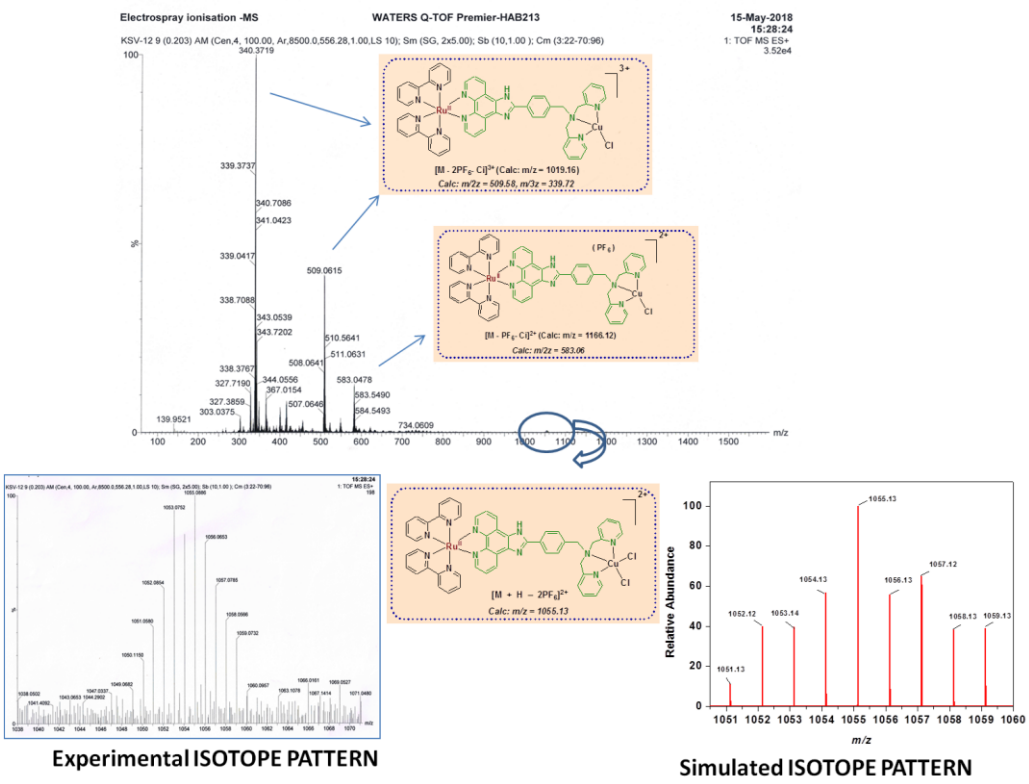

Fig. 6.1. ESI-MS analysis of $\mathbf{Ru^{II}_{chrom}}$-$\mathbf{Cu^{II}_{cat}}$ in acetonitrile-water at room temperature (Arora et al., 2019).

The molecular structure of the **Ru^{II}_{chrom}** was elucidated by single-crystal X-ray diffraction analysis (**Fig. 6.2(b)**). Relevant crystallographic data and selected bond parameters are summarized in **Tables 6.1 and 6.2**, respectively. The crystal structure reveals that the Ru(II) center adopts a distorted octahedral geometry, coordinated by the nitrogen atoms of the phenanthroline moiety. Notably, the nitrogen donors from the dipicolylamine (DPA) end of the ligand remain uncoordinated. The Ru-N bond lengths fall within the range of 2.044(4)-2.059(4) Å, while the trans N-Ru-N bond angles lie between 172.60(17)° and 174.70(15)°, supporting a slightly distorted but predominantly octahedral coordination environment around the Ru(II) center. These bond metrics are in excellent agreement with values reported for similar ruthenium complexes, confirming the structural integrity and coordination behavior of the ligand framework.

Table 6.1. Crystallographic data for **$[Ru^{II}_{chrom}](PF_6)_2$**.

Sum formula	$C_{52}H_{30}F_{12}N_{11}OP_2Ru$
Formula weight ($gmol^{-1}$)	1215.88
Color	Red orange
Space group	P1 21/c 1
Temperature/K	293(2)
λ (Å) (Mo-Kα)	1.54184
Crystal system	Monoclinic
a (Å)	29.9852(13)
b (Å)	10.6407(3)
c (Å)	16.2765(6)
α(˚)	90
β (˚)	96.481(4)
γ (˚)	90
V ($Å^3$)	5160.1(3)
Z	4
ρ_{calc}(gcm^{-3})	1.565
Crystal size (mm)	0.11 x 0.06 x 0.04
F(000)	2436.0
Index ranges	$35 < h < -35$ $8 < k < -12$ $17 < l < -19$
GOF on F^2	1.033
$R1^a$ [$I > 2\sigma(I)$]	0.0630

*R*1[all data]	0.0897
*wR*2[b] [$I > 2\sigma(I)$]	0.1662
*wR*2 [all data]	0.1934

[a]$R1 = \Sigma||F_o|-|F_c||/\Sigma|F_o|$; [b]$wR2=|\Sigma w(|F_o|^2- |F_c|^2)|/\Sigma|w(F_o^2)^2|^{1/2}$

Table 6.2. Selected bond lengths [Å] and angles [°] in the single crystal of **$[Ru^{II}_{chrom}](PF_6)_2$**.

Bond Lengths (Å)	
Ru-N1	2.059(4)
Ru-N2	2.057(4)
Ru-N3	2.049(4)
Ru-N4	2.054(4)
Ru-N5	2.044(4)
Ru-N6	2.054(4)
Bond Angles (º)	
N5-Ru1-N3	172.60(17)
N2-Ru1-N4	173.22(16)
N6-Ru1-N1	174.70(15)
N5-Ru1-N2	90.07(17)

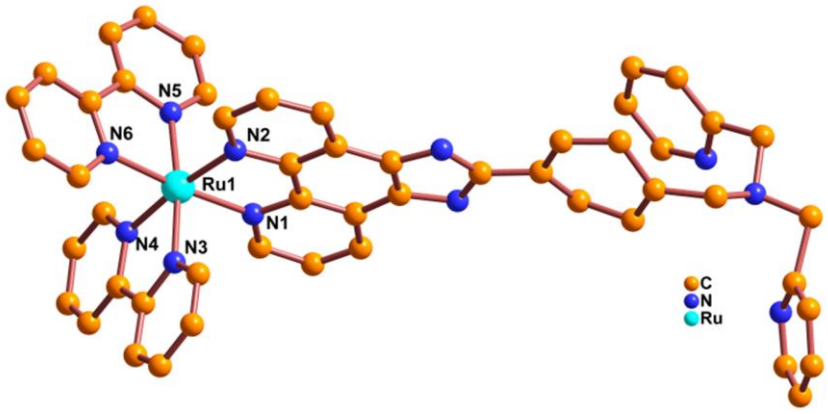

Fig. 6.2. Crystal structure of photosensitizer **Ru^{II}_{chrom}** (Arora et al., 2019).

The photophysical behavior of **Ru^{II}_{chrom}** was examined in acetonitrile solution at room temperature (**Fig. 6.3**). A strong absorption band was observed in the range of 280-300 nm assigned to ligand-centered π–π* transitions. Additionally, a characteristic moderate-intensity band was observed between

450-460 nm, attributed to the metal-to-ligand charge transfer (MLCT) transitions. The covalent linking of the $\mathbf{Cu^{II}_{cat}}$ moiety with the $\mathbf{Ru^{II}_{chrom}}$ unit did not lead to substantial alteration in the spectral band, aside from the appearance of a very weak, broad d–d transition in the 600-700 nm region.

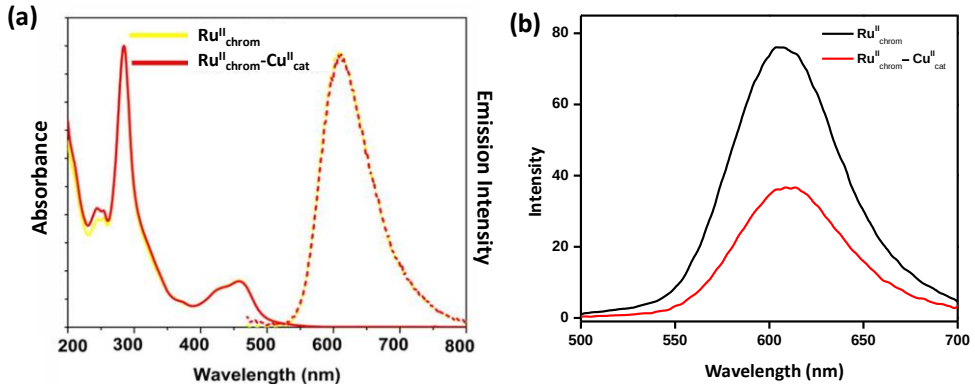

Fig. 6.3. (a) Normalized absorption and luminescence spectra of $\mathbf{Ru^{II}_{chrom}}$ and $\mathbf{Ru^{II}_{chrom}}$-$\mathbf{Cu^{II}_{cat}}$ (b) Luminescence spectra of $\mathbf{Ru^{II}_{chrom}}$ and $\mathbf{Ru^{II}_{chrom}}$-$\mathbf{Cu^{II}_{cat}}$.

The luminescence behavior of the complexes was investigated in CH_3CN upon excitation at 460 nm (**Fig. 6.3**). The $\mathbf{Ru^{II}_{chrom}}$ fragment exhibited an emission maximum at 615 nm and incorporation of the catalytic moiety in the complex framework led to significant quenching of the emission band and a notable decrease in quantum yield. This quenching effect can be attributed to photoinduced electron transfer from the excited state of photosensitizer to the low-lying excited-state of Cu_{cat} moiety, a phenomenon previously reported in similar Ru-Cu polypyridyl dyads and heterobimetallic complexes

Furthermore, the emission decay of $\mathbf{Ru^{II}_{chrom}}$ followed a mono-exponential profile with a lifetime of 0.43 µs, characteristic of radiative deactivation from the ^{3}MLCT excited state. In contrast, coordination with the catalytic unit produced a bi-exponential decay, featuring a short-lived component of 0.02 µs and a longer component of 0.40 µs, resulting in a markedly reduced average lifetime of 0.04 µs. This pronounced quenching strongly supports intramolecular photoinduced electron transfer from the chromophore to the catalytic center (**Fig. 6.4**). Given that (i) the energy transfer between the triplet excited state of Ru and the singlet ground state of the Cu moiety is spin-forbidden, and (ii) the Cu subunit exhibits a weak extinction coefficient, energy

transfer is possible but likely plays only a minor role in excited-state deactivation. Accordingly, the short-lived component is attributed to PET-induced quenching of the ^{3}MLCT state.

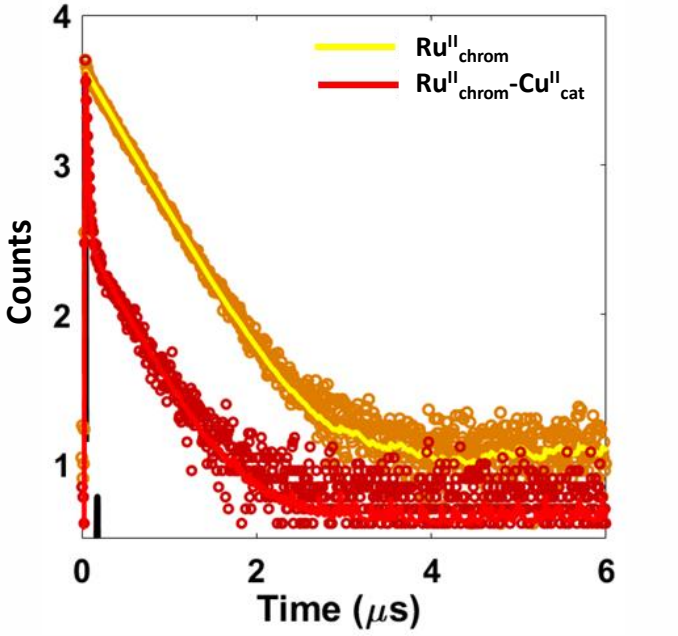

Sample	α_1	τ_1 (μS)	α_2	τ_2 (μS)	τ_{avg}	χ
Ru^{II}_{chrom}	–	–	1.00	0.43	0.43	1.61
Ru^{II}_{chrom}-Cu^{II}_{cat}	0.96	0.02	0.04	0.40	0.04	1.79

Fig. 6.4. TRF studies of **Ru^{II}_{chrom}** and **Ru^{II}_{chrom}-Cu^{II}_{cat}**.

Photocatalytic experiments were conducted under blue light-emitting diode (LED) irradiation, which were selected to match the MLCT absorption band of the photosensitizer unit. Triphenylphosphine (PPh_3) was employed as the model substrate for optimizing reaction conditions. In a sealed glass vial, substrate solution (500 µL of 0.2 M PPh_3 in CH_3CN, 100 µmol, 100 equiv.) and triethanolamine (1000 µL of 0.2 M in CH_3CN, 200 µmol, 200 equiv.) were introduced. The air in the vial was subsequently purged with O_2, followed by the addition of the catalyst solution (250 µL of 4 mM in CH_3CN, 1 µmol, 1 equiv.). The reaction mixture was stirred continuously and irradiated over a period of 24 hours. Gas chromatography with flame ionization detection (GC-FID) analysis showed an exceptional ~99% conversion of PPh_3 to

triphenylphosphine oxide (PPh_3=O), which was further supported by ^{31}P NMR spectroscopy (**Fig. 6.5**).

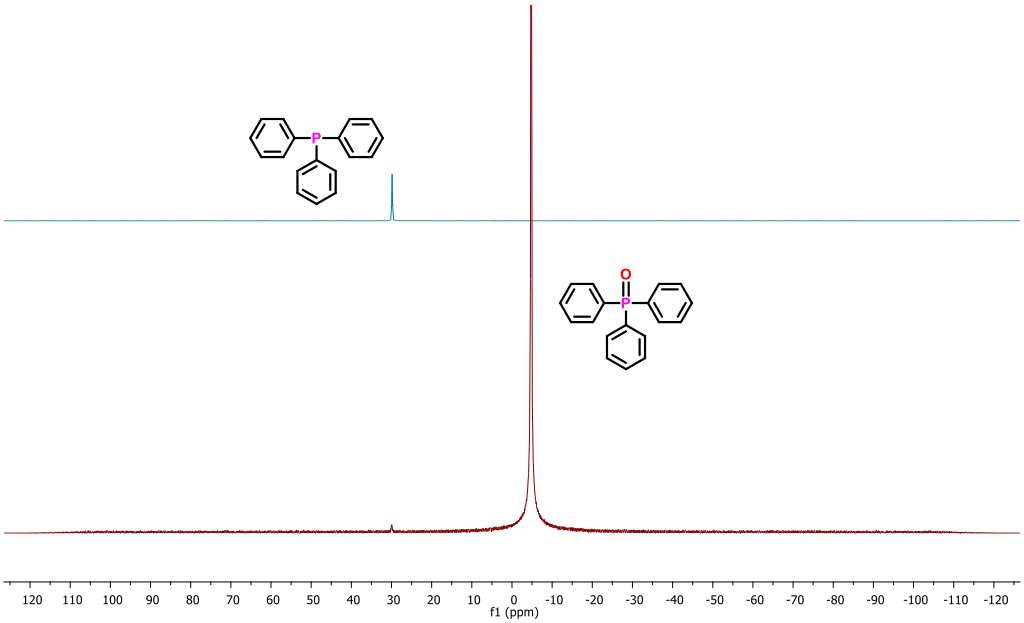

Fig. 6.5. ^{31}P NMR spectra of substrate (PPh_3) and product (PPh_3=O).

Table 6.3. Photocatalytic PPh_3 oxygenation under different conditions.

S.No	Complex	e^- donor	Subs:Cat:SA	Light	Solvent	Conversion
1	$\mathbf{Ru^{II}_{chrom}\text{-}Cu^{II}_{cat}}$	TEOA	100:1:200	Off	CH_3CN (O_2)	-
2	$\mathbf{Ru^{II}_{chrom}\text{-}Cu^{II}_{cat}}$	TEOA	100:1:200	On	CH_3CN (O_2)	~99%
3	$\mathbf{Ru^{II}_{chrom}\text{-}Cu^{II}_{cat}}$	TEOA	100:1:200	On	CH_3CN (Air)	48%
4	$\mathbf{Ru^{II}_{chrom}}$	TEOA				24%
6	$\mathbf{Cu^{II}_{cat}}$	ascorbate	100:1:200	On	CH_3CN (O_2)	-
7	$\mathbf{Ru^{II}_{chrom}}$ + $\mathbf{Cu^{II}_{cat}}$	TEOA	100:1:200	On	CH_3CN (O_2)	52%

Several control experiments have been carried out to optimize the photocatalytic conditions. Poor or no substrate oxidation was observed in the absence of light, catalyst, or molecular oxygen, confirming their vital roles in the reaction. The presence of triethanolamine (TEOA) was also found to be critical, as its absence resulted in significantly reduced catalytic efficiency. Additional experiments using a bimolecular mixture of $\mathbf{Ru^{II}_{chrom}}$ and $\mathbf{Cu^{II}_{cat}}$ fragments (photosensitizer and catalytic units were added separately) demonstrated markedly lower activity compared to the covalently linked

Ru^{II}_{chrom}-Cu^{II}_{cat} dyad. This observation indicates intramolecular electron transfer was much more efficient than intermolecular electron transfer. Furthermore, when excess ascorbate was introduced into the reaction system, no oxidized products were detected, further supporting the necessity of electron transfer processes to the Cu^{II}_{cat} unit as an important prerequisite for effective catalysis. Following the successful oxidation of triphenylphosphine, the substrate scope was extended to include sulfoxidation reactions involving anisole and 4-bromothioanisole. The conversion of these substrates into oxidized products was confirmed by GC-MS studies.

Table 6.4. Photocatalytic oxidation of substrates.

S.No	Substrate	Product	Subs: Cat: SA	Light	Solvent	Conversion
1	PPh_3	PPh_3=O	100:1:200	On	CH_3CN (O_2)	~99%
2	$CH_3C_6H_5S$	$CH_3C_6H_5S$=O	100:1:200	On	CH_3CN (O_2)	~97%
3	$CH_3C_6H_4BrS$	$CH_3C_6H_4BrS$=O	100:1:200	On	CH_3CN (O_2)	~98%

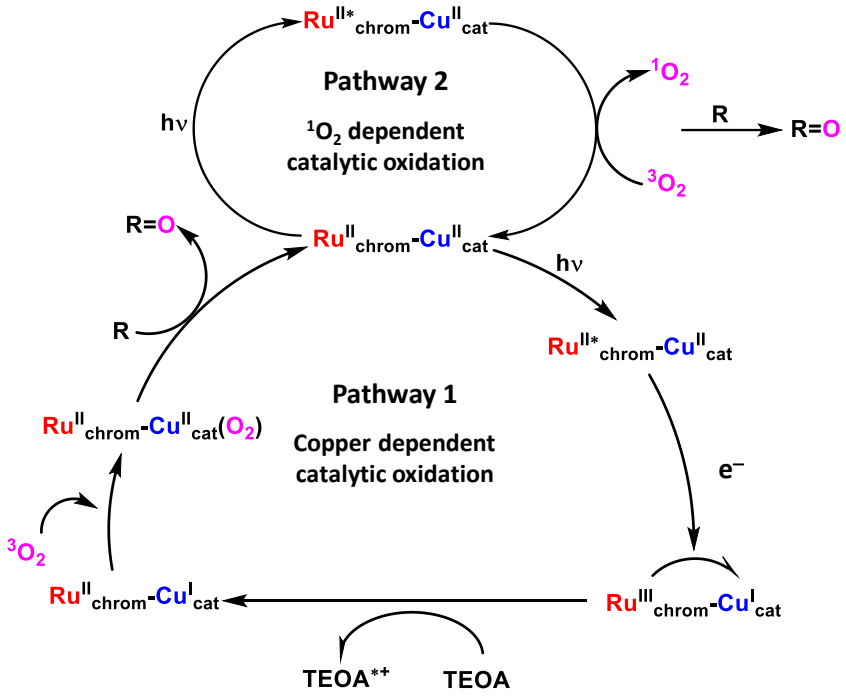

Scheme. 6.3. Possible mechanistic pathways for photo-assisted substrate oxidation *via* Ru^{II}_{chrom}-Cu^{II}_{cat} dyad.

Based on prior studies, two mechanistic pathways have been proposed for the photocatalytic oxidation of sulfides facilitated by the $\mathbf{Ru^{II}_{chrom}}$-$\mathbf{Cu^{II}_{cat}}$ dyad. Pathway-1 is $^1O_2$ dependent catalytic oxidation or copper independent pathway. In this mechanism, the dyad absorbs a photon and goes to its excited state, $\mathbf{Ru^{II*}_{chrom}}$-$\mathbf{Cu^{II}_{cat}}$. This excited state transfers its energy to molecular oxygen, generating singlet oxygen ($^1O_2$), which subsequently oxidizes the sulfide substrate. However, this pathway seems to play a minimal role, as evidenced by the significantly reduced conversion rates observed in the absence of TEOA. Another probable pathway is 'Cu-dependent catalytic oxidation' in which the mechanism involves a photoinduced electron transfer process. Upon absorbing a photon, the dyad reaches its excited state, $\mathbf{Ru^{II*}_{chrom}}$-$\mathbf{Cu^{II}_{cat}}$, which facilitates an intramolecular electron transfer from the $\mathbf{Ru^{II*}_{chrom}}$ to the $\mathbf{Cu^{II}_{cat}}$ resulting in the formation of $\mathbf{Ru^{III}_{chrom}}$-$\mathbf{Cu^{I}_{cat}}$. The reduced $\mathbf{Cu^{I}_{cat}}$ center then activates molecular oxygen, forming a $\mathbf{Cu^{II}_{cat}}$–(O_2) adduct that is primarily responsible for oxidizing the sulfide substrate. Simultaneously, the $\mathbf{Ru^{II}_{phot}}$ is subsequently regenerated by the help of TEOA, completing the catalytic cycle.

6.4. Conclusions

In conclusion, we report successful synthesis and characterization of heterobimetallic $\mathbf{Ru^{II}_{chrom}}$-$\mathbf{Cu^{II}_{cat}}$ dyad and demonstrates its efficient photoinduced electron transfer behavior. The covalent linkage between the $\mathbf{Ru^{II}_{chrom}}$ and $\mathbf{Cu^{II}_{cat}}$ facilitates effective electron communication, enabling key oxidative transformations under visible light. The observed quenching in luminescence, reduction in quantum yield, and significant lifetime changes further confirm the electron transfer from $\mathbf{Ru^{II}_{chrom}}$ to $\mathbf{Cu^{II}_{cat}}$. The dyad was further utilized for photocatalytic substrate oxidation and mechanistic pathways were further discussed.

SUMMARY AND FUTURE PERSPECTIVES

This thesis presents the development of novel luminophores for the highly selective detection of metal ions and anions, with an emphasis on structurally simple designs that allow for easy synthesis and purification. Preference has been given to "turn-on" sensors due to their superior reliability compared to quenching-based sensors. Among the targeted analytes, the detection of Al^{3+}, Zn^{2+}, ClO_4^- and CN^- ions has been prioritized due to their significant environmental and biological implications. Additionally, the thesis explores photocatalytic applications using newly developed Ru-based photosensitizers for the oxidation of small organic substrates. The findings from this research have been published in prestigious journals, as listed below:

1. **Sudhanshu Naithani**, Tapas Goswami, Franck Thetiot, Sushil Kumar "Imidazo[4,5-*f*][1,10]phenanthroline based luminescent probes for anion recognition: Recent achievements and challenges" ***Coord. Chem. Rev.*** **2023**, 475, 214894.
2. **Sudhanshu Naithani**, Nidhi Goswami, Sain Singh, Vikas Yadav, Sanjay Kumar, Pramod Kumar, Amit Kumar, Tapas Goswami, Sushil Kumar "Turn-on detection of Al^{3+} and Zn^{2+} ions by NSN donors probe: Reversibility, logic gates and DFT calculations" ***Anal. Methods*** **2023**, *15*, 6021–6030.
3. **Sudhanshu Naithani**, Franck Thetiot, Vikas Yadav, Saakshi Saini, Partha Roy, Samar Layek, Tapas Goswami, Sushil Kumar "A pyridyl-benzimidazole based ruthenium(II) complex as optical sensor: Targeted cyanide detection and live cell imaging applications" ***J. Photochem. Photobiol. A: Chem.*** **2024**, *453*, 115610.
4. **Sudhanshu Naithani**, Ritesh Dubey, Tapas Goswami, Franck Thetiot, Sushil Kumar "Optical detection strategies for Ni(II) ion using metal-organic chemosensors: From molecular design to environmental applications" ***Dalton Trans.*** **2024**, *53*, 17409-17428.
5. **Sudhanshu Naithani**, Heena, Pooja Sharma, Samar Layek, Franck Thetiot, Tapas Goswami, Sushil Kumar "Nanoparticles and quantum dots as emerging optical sensing platforms for Ni(II) detection: Recent approaches and perspectives" ***Coord. Chem. Rev.*** **2025**, *524*, 216331.

6. **Sudhanshu Naithani**, Nidhi Goswami, Vikas Yadav, Jimmy Mangalam, Tapas Goswami, Sushil Kumar **"**Selective turn-on luminescent recognition of perchlorate ion using pyridyl-benzimidazole based probe" ***Luminescence*** **2024**, *40,* e70087.
7. **Sudhanshu Naithani**, Pramod Kumar, Ritesh Dubey, Franck Thetiot, Samar Layek, Tapas Goswami, Sushil Kumar "Design principles for metal-organic receptors targeting optical recognition of Pd(II) in environmental and biological matrices" ***J. Mater. Chem. C.*** **2025**, *13,* 11562-11585.

The structure of this thesis has been divided into six chapters:

Chapter 1 introduces different types of optical sensors, fluorescent/colorimetric probes, and molecular photocatalysts along with existing research gaps, and the primary objectives of this work.

Chapter 2 details the materials, methods, and analytical techniques used in sensor development, metal ion detection, cell imaging, and probe characterization.

Chapter 3 describes the synthesis and application of a Schiff base probe (**NpSb**) for selective detection of Al^{3+} and Zn^{2+} ions. The incorporated thio-bis moiety offers an efficient coordination site for metal ions, facilitating strong and selective binding. The probe exhibited a "turn-on" fluorescence response at 469 nm for Al^{3+} and 416 nm for Zn^{2+} (excited at 300 nm), with detection limits of 38.0 nM and 43.0 nM, respectively. The sensing mechanism was validated through ESI-MS and DFT analysis, and the reversibility of the binding has been demonstrated using NaF and EDTA. Practical applications were confirmed *via* real sample testing in tap water, distilled water, and soil, with successful fluorescence visualization on filter paper test strips.

Chapter 4 focuses on the development of a pyridyl-benzimidazole based luminescent probe (**RSB1**) for the selective detection of ClO_4^- ions in a semi-aqueous system (CH_3CN-H_2O, 4:1, *v/v*). The probe was rationally designed by incorporating an N–H functionality into the thio-bis core to enhance its selectivity toward a specific anion. The probe exhibited strong fluorescence enhancement with a detection limit of 0.121 μM and a

binding constant of 2.6×10^5 M^{-1}. Job's plot, NMR, and DFT studies confirmed a 1:1 binding stoichiometry, revealing a C-shaped cavity that anchors ClO_4^- through multiple hydrogen bonds. **RSB1** was successfully tested in real-world samples, including soil, tap water, and distilled water.

Chapter 5 demonstrates a Ru(II)-based probe (**Ru-1**) for highly selective CN^- detection in pure water. The short distance between the imidazole moiety and **Ru-1** enhances the acidity of the N-H proton, enabling strong H-bonding interactions with CN^-. The 1:1 binding stoichiometry was confirmed by Job's plot and DFT studies. Live cell imaging demonstrated successful CN^- detection in MCF-7 cell lines, indicating promising applications in biological and analytical fields.

Chapter 6 presents a chromophore-catalyst system ($\mathbf{Ru^{II}_{phot}}$–$\mathbf{Cu^{II}_{cat}}$) for reductive O_2 activation. The system serves as an efficient photocatalyst for substrate oxidation reactions and outperforms conventional bimolecular catalytic mixtures. Ongoing efforts are focused on optimizing excited-state properties through ligand modifications and exploring more potent oxidation catalysts for applied photocatalysis.

This thesis contributes significantly to the advancement of luminescent probes and photocatalytic systems for industrial, environmental and biological applications. The newly developed optical sensors provide highly selective and sensitive detection of metal ions (Al^{3+} and Zn^{2+}) and anions (ClO_4^- and CN^-) with excellent practical applicability in real sample analysis. Their mechanisms were thoroughly investigated using spectroscopic and computational methods, confirming robust and reversible interactions with target analytes. Additionally, the introduction of a heterobimetallic chromophore-catalyst system for organic substrate oxidation presents a novel approach to visible-light-driven photocatalysis.

Though the current work validates the potential of these systems, future studies will focus on improving sensor stability, extending their applicability to biological systems, and further optimizing photocatalytic efficiency. These advancements will contribute to the development of

next-generation molecular probes and catalysts for real-world environmental and biomedical applications.

Future prospects in anion/cation sensing using molecular photosensitizers

I. **Real time and biological monitoring:**
Molecular photosensitizers offer dynamic, real-time detection of biologically and environmentally relevant ions and can aid in studying enzymatic or cellular processes.

II. **Theranostic potential:**
Their dual diagnostic and therapeutic ability enables integration into theranostic systems, including applications like chelation therapy for metal ion detoxification.

III. **Material and solid-state integration:**
Embedding these probes in polymers, films, or nanoparticles enhances stability, selectivity, and sensitivity- supporting analyte detection and removal in complex or solid-state environments.

IV. **AI/ML augmentation:**
Incorporating artificial intelligence and machine learning can refine selectivity and enable simultaneous multi-analyte sensing in complex matrices.

V. **Portable and smartphone-based devices:**
Development of smartphone-compatible or portable sensor devices can provide cost-effective, accessible tools for on-site and point-of-care diagnostics.

Future prospects in molecular photocatalysis

I. **Scale-up *via* continuous flow chemistry:**
Integration of photocatalysis into continuous flow reactors allows industrial-scale application by offering enhanced light penetration, controlled reaction conditions, improved mass transfer, energy efficiency, and safer handling of reactive intermediates.

II. **Tunable photosensitizer and catalytic units for diverse transformations:**

Expanding beyond Ru- and Ir-based systems, the development of Cu(I), Ni(II), Mo, and Mn-based photosensitizers and catalysts opens avenues for activating small molecules like CO_2, N_2, and CH_4, paving the way for greener and more diverse chemical transformations.

III. **Photoinduced Cu(I) catalysis for click reactions:**

The in-situ generation of Cu(I) *via* PeT offers a light-driven pathway for efficient click chemistry under mild and selective conditions, suitable for biomolecule labeling and polymer modification.

IV. **Immobilization for heterogeneous photocatalysis:**

Anchoring molecular photocatalysts onto solid supports (e.g., MOFs, COFs, silica, graphene) enhances stability, reusability, and facilitates integration into devices, particularly for solar fuel generation and environmental remediation.

V. **Sacrificial agent free photocatalysis:**

Emphasis is shifting toward designing self-sustained redox systems that operate without sacrificial agents, improving atom economy, minimizing waste, and advancing green and sustainable photocatalytic cycles.

ANNEXURE-I

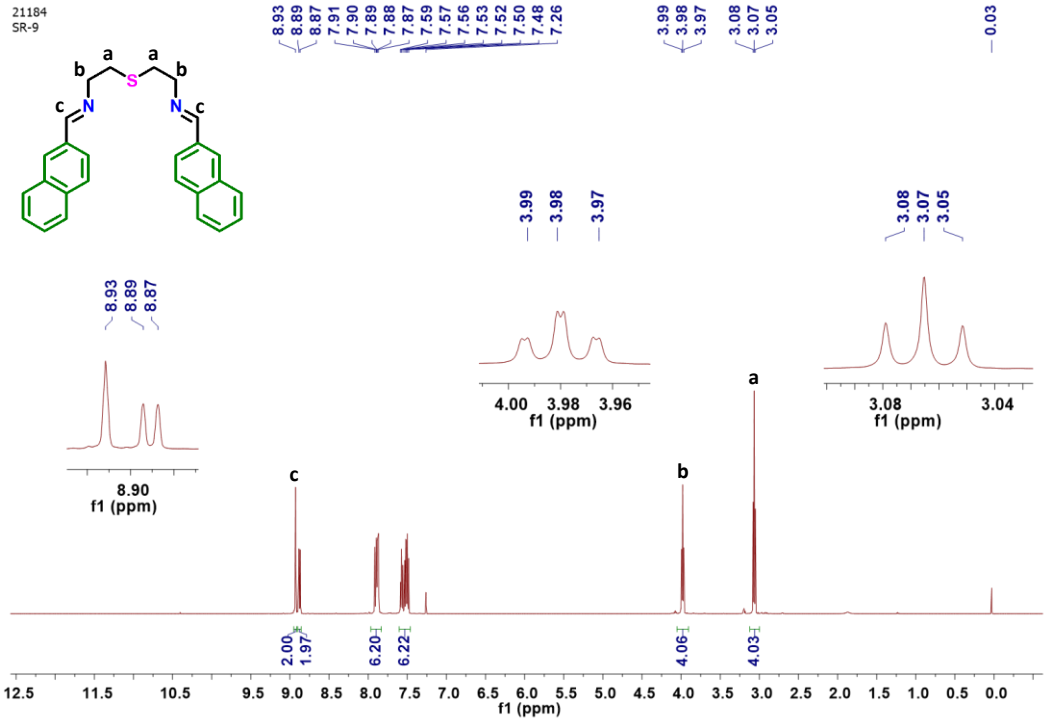

Fig. A1. ^{1}H NMR spectrum of **NpSb** in $CDCl_3$ at room temperature. ^{1}H NMR ($CDCl_3$, 500 MHz, TMS), δ (ppm): 8.93 (s, 2H, -C<u>H</u>=N-), 8.89 (m, 2H), 7.89 (m, 6H), 7.59-7.48 (m, 6H), 3.98 (t, 4H, -C<u>H</u>$_2$-N-), 3.07 (t, 4H, -C<u>H</u>$_2$-S<).

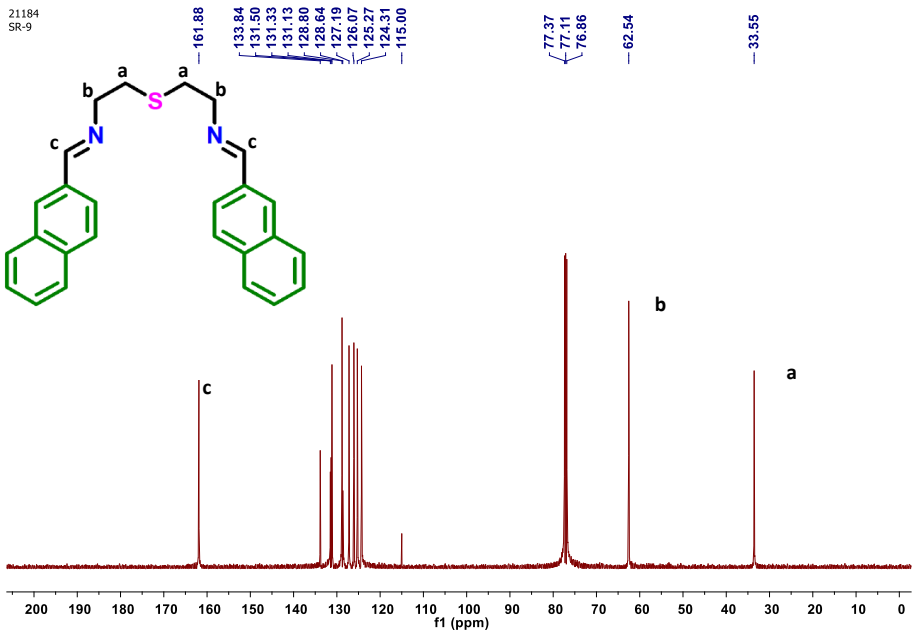

Fig. A2. ^{13}C NMR spectrum of **NpSb** in $CDCl_3$ at room temperature. ^{13}C NMR ($CDCl_3$, 500 MHz), δ (ppm): 161.88, 133.84, 131.50, 131.33, 131.13, 128.80, 128.64, 127.19, 126.07, 125.47, 124.31, 115.00, 62.54, 33.55.

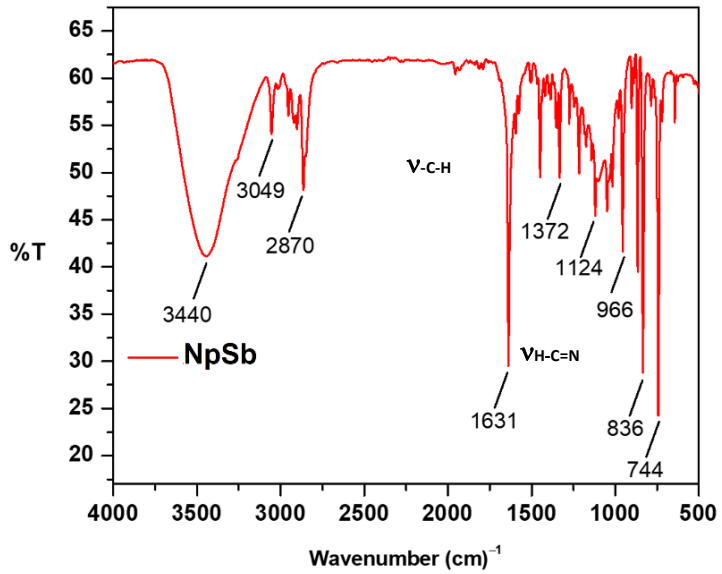

Fig. A3. FT-IR spectrum of **NpSb**. IR data (KBr disk, cm^{-1}): 3440, 3049, 2870 ,1631 ($\nu_{C=N}$), 1372, 1124, 966, 836, 744.

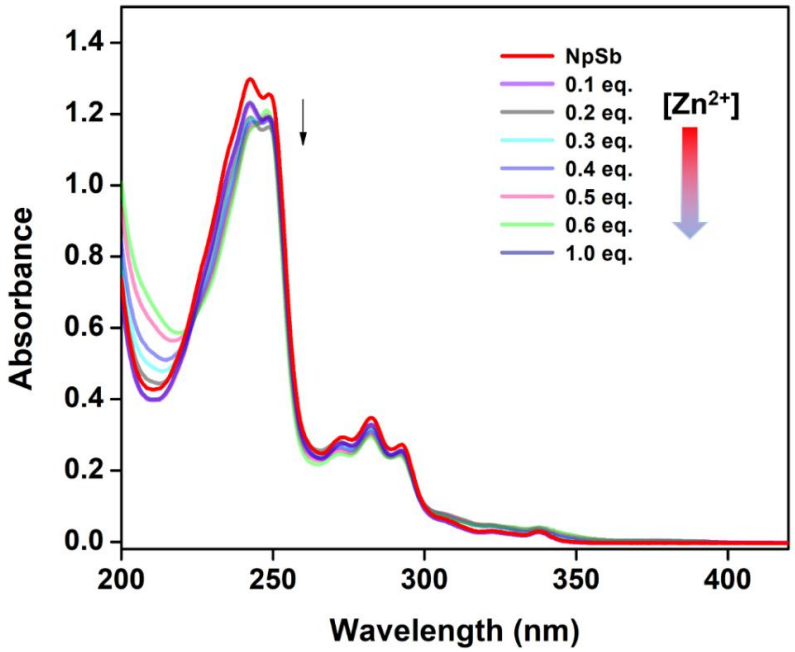

Fig. A4. UV-Vis spectral changes for **NpSb** (1.0×10^{-5} M) in CH_3CN-H_2O (4:1, v/v) after successive addition of Zn^{2+} ions (0-1.0 equiv.).

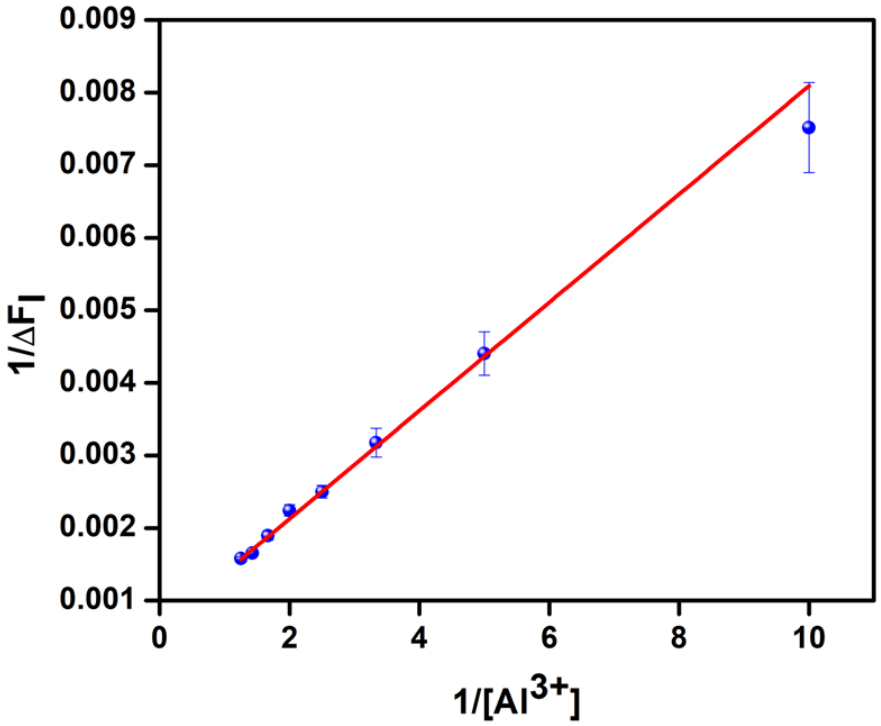

Fig. A5. Determination of binding constant of **NpSb** (10^{-6} M) for Al^{3+} in CH_3CN-H_2O (4:1, v/v) by employing Benesi-Hildebrand plots from fluorescence spectroscopy (λ_{ex} =300 nm).

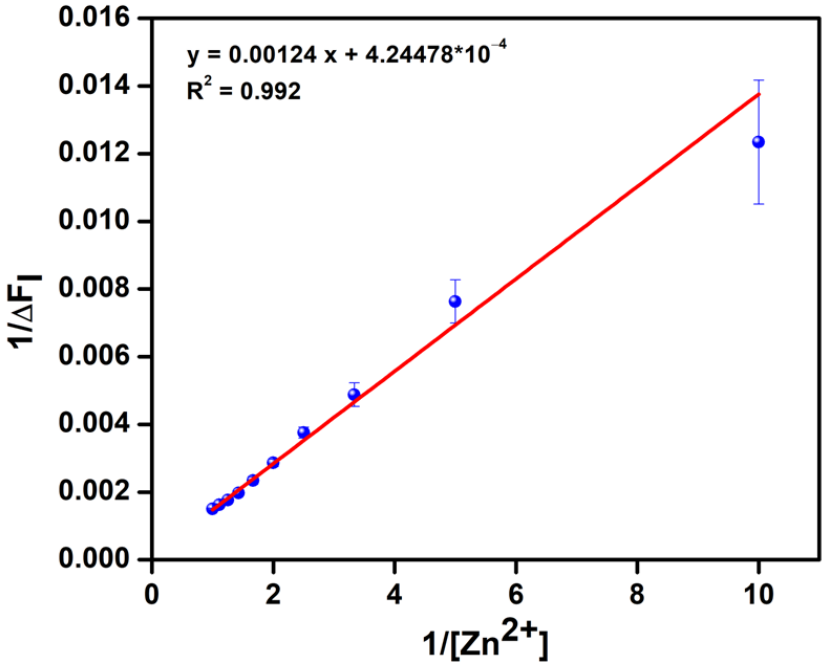

Fig. A6. Determination of binding constant of **NpSb** (10^{-6} M) for Zn^{2+} in CH_3CN-H_2O (4:1, v/v) by employing Benesi-Hildebrand plots from fluorescence spectroscopy (λ_{ex} =300 nm).

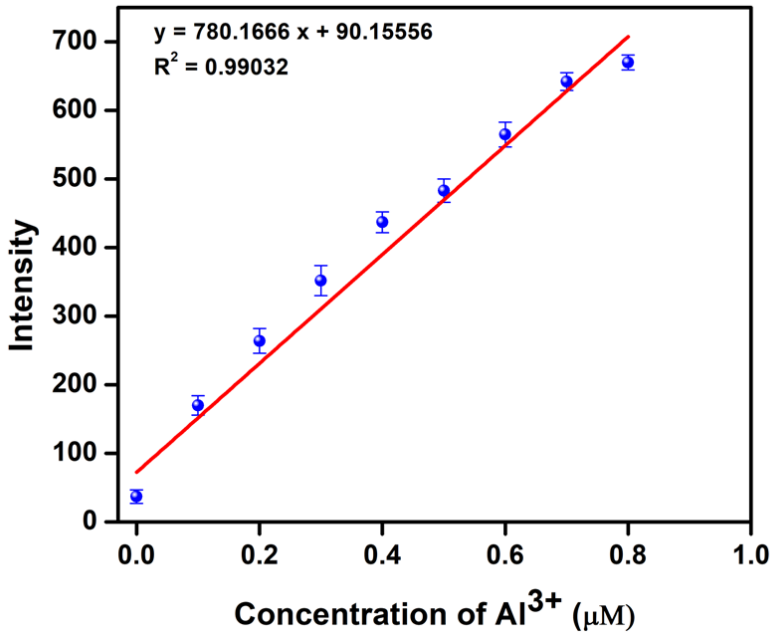

Fig. A7. Linear curves of the emission intensity of **NpSb** (10^{-6} M) with Al^{3+} for the determination of LoD in CH_3CN-H_2O (4:1, v/v) using fluorescence spectroscopy (λ_{ex} =300 nm).

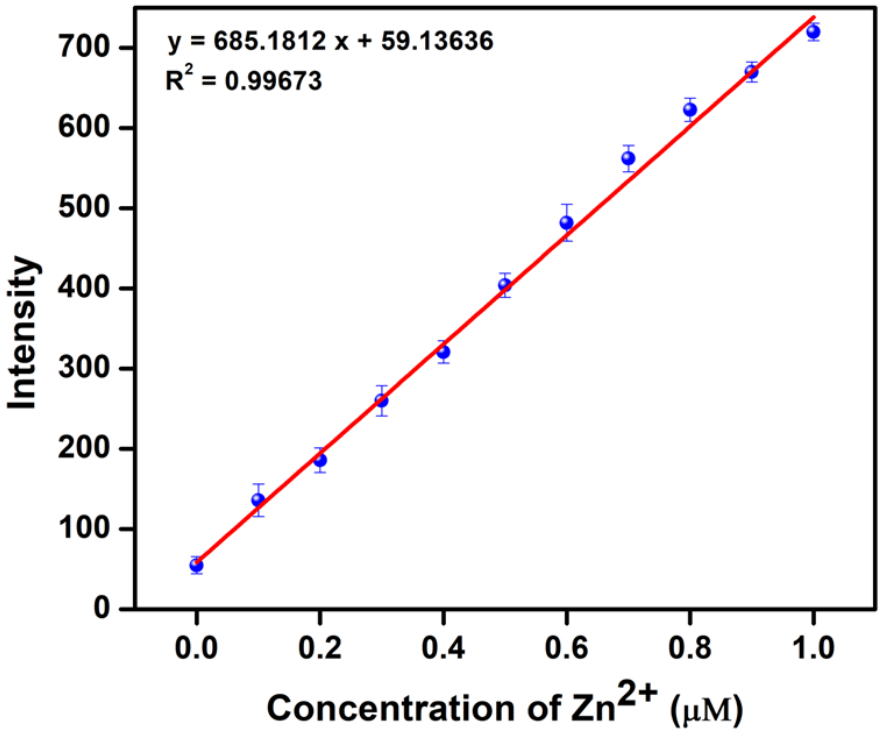

Fig. A8. Linear curves of the emission intensity of **NpSb** (10^{-6} M) with Zn^{2+} for the determination of LoD in CH_3CN-H_2O (4:1, v/v) using fluorescence spectroscopy (λ_{ex} =300 nm).

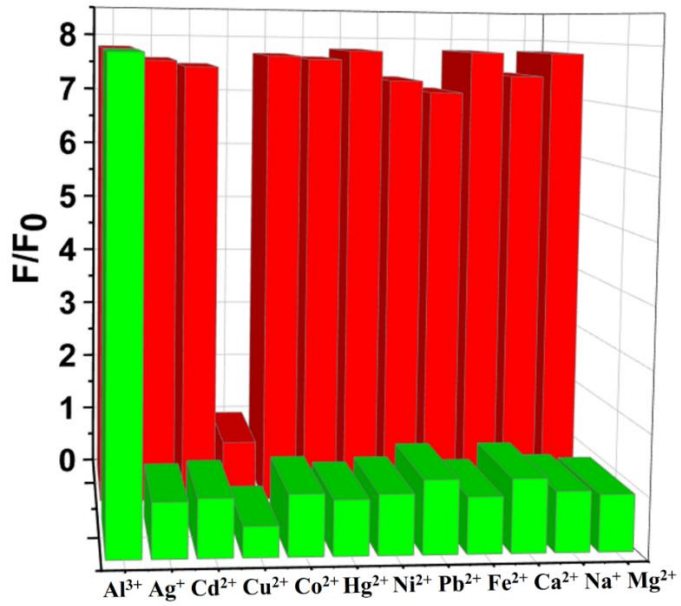

Fig. A9. Relative fluorescence Intensity of **NpSb** (10^{-6} M) with Al^{3+} in the presence of 10 equiv. of other cations in CH_3CN-H_2O (4:1, v/v) (λ_{ex} =300 nm).

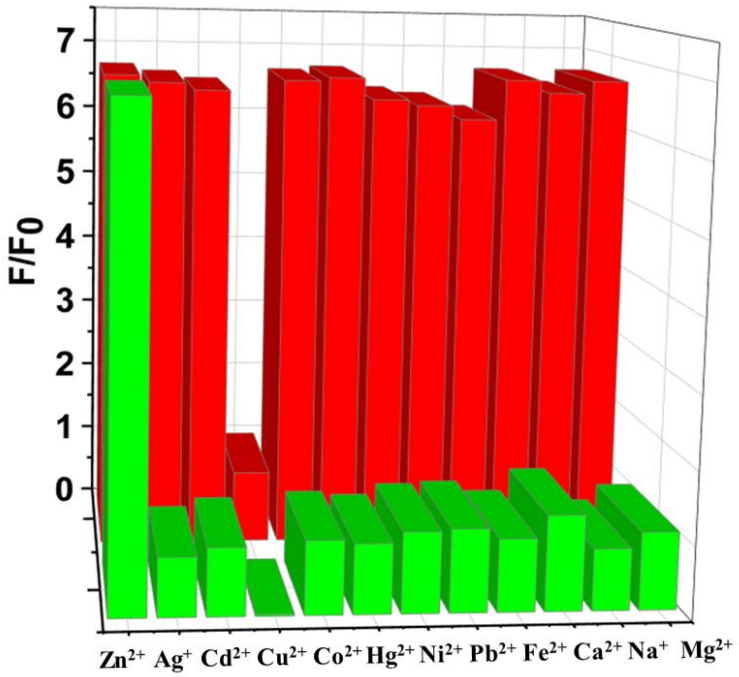

Fig. A10. Relative fluorescence intensity of **NpSb** (10^{-6} M) with Zn^{2+} in the presence of 10 equiv. of other cations in CH_3CN-H_2O (4:1, v/v) solution (λ_{ex} =300 nm).

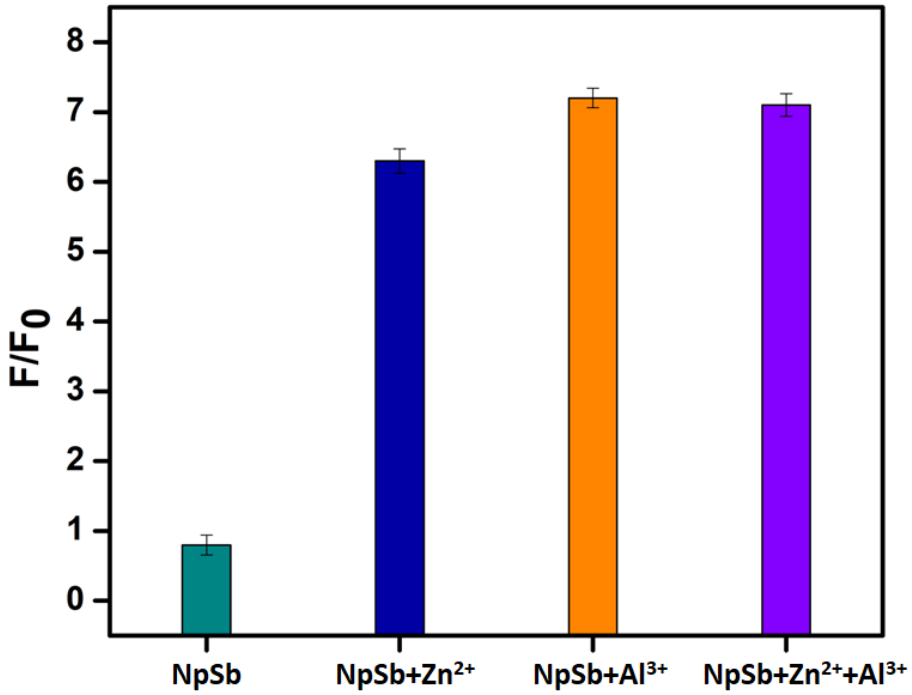

Fig. A11. Relative fluorescence Intensity of **NpSb** (10^{-6} M) with Al^{3+} and Zn^{2+} in CH_3CN-H_2O (4:1, v/v) solution (λ_{ex} =300 nm).

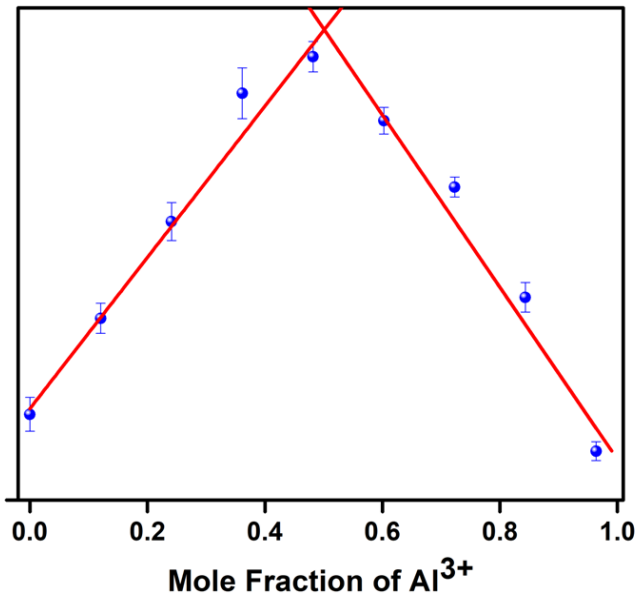

Fig. A12. Job's plot analyses for **NpSb** (10^{-6} M) *vs*. Al^{3+} in CH_3CN-H_2O (4:1, v/v).

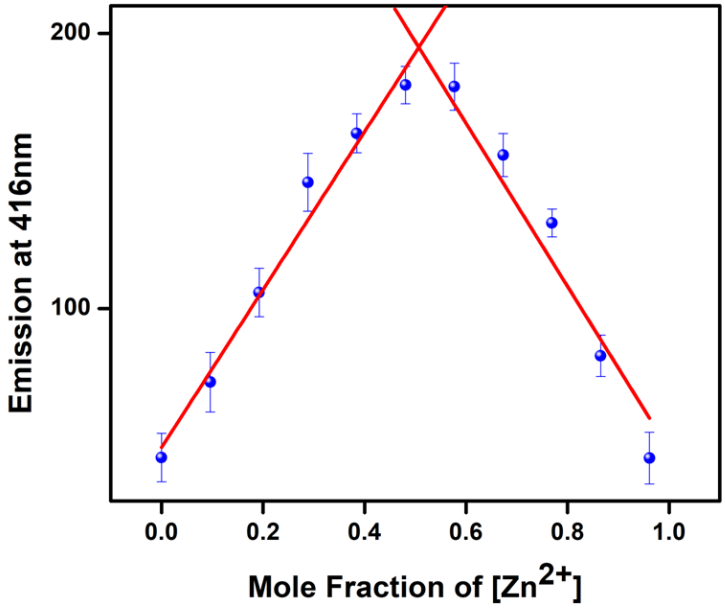

Fig. A13. Job's plot analyses for **NpSb** (10^{-6} M) *vs*. Zn^{2+} in CH_3CN-H_2O (4:1, v/v).

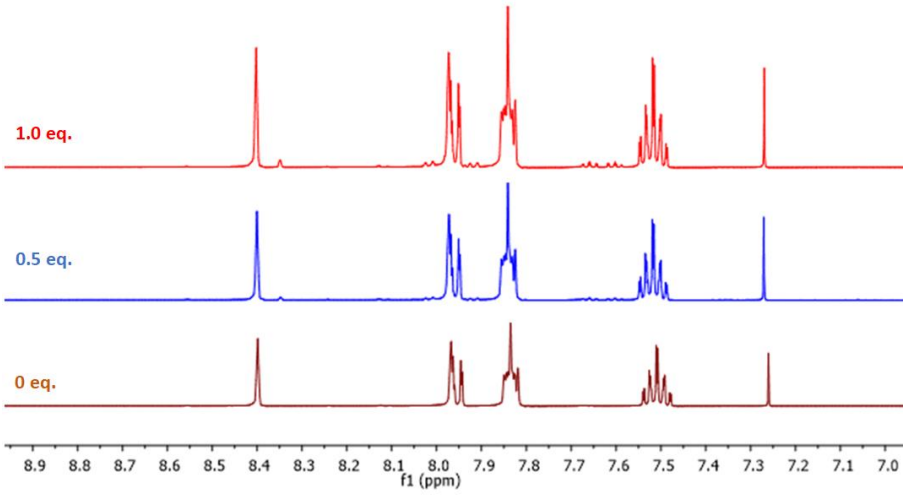

Fig. A14.[1]H NMR titration for **NpSb** with Zn^{2+} ions.

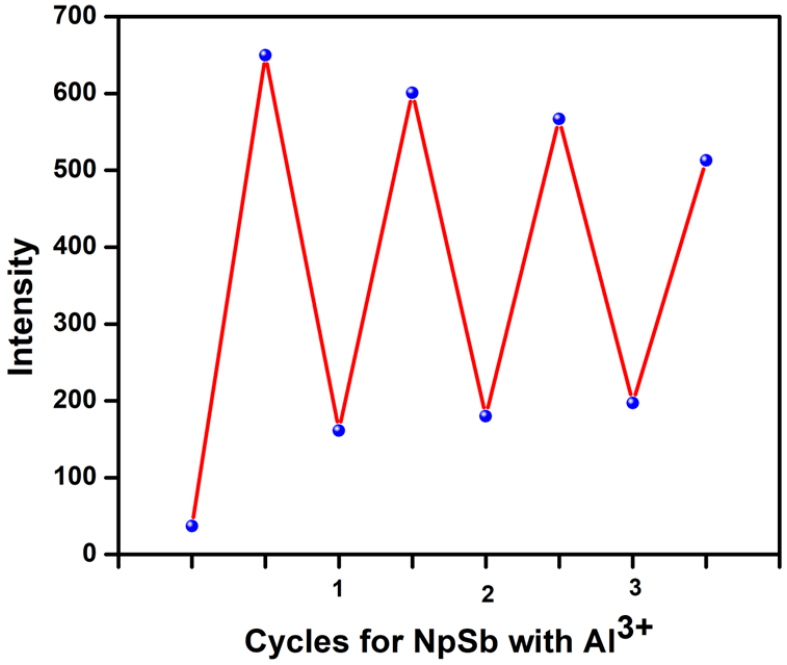

Fig. A15. Number of cycles of probe **NpSb** (10^{-6} M) with Al^{3+} ions in CH_3CN-H_2O (4:1, v/v) (λ_{ex} =300 nm).

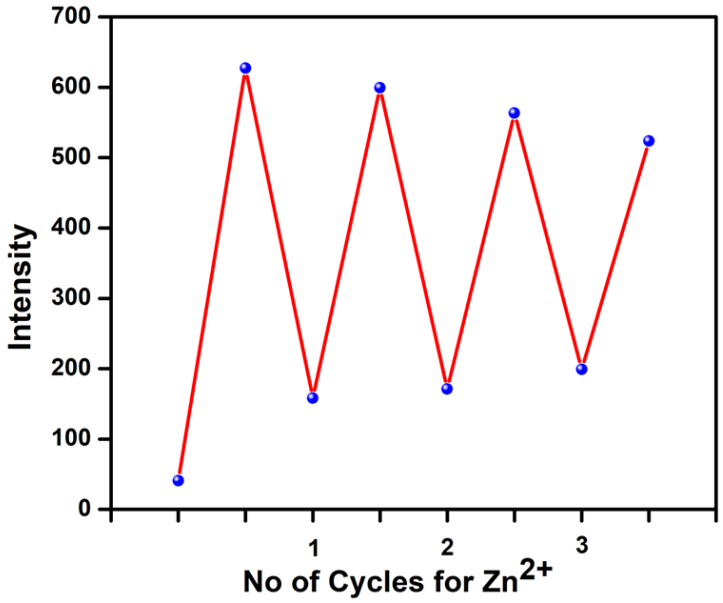

Fig. A16. Number of cycles of probe **NpSb** (10^{-6} M) with Zn^{2+} ions in in CH_3CN-H_2O (4:1, v/v) (λ_{ex} =300 nm).

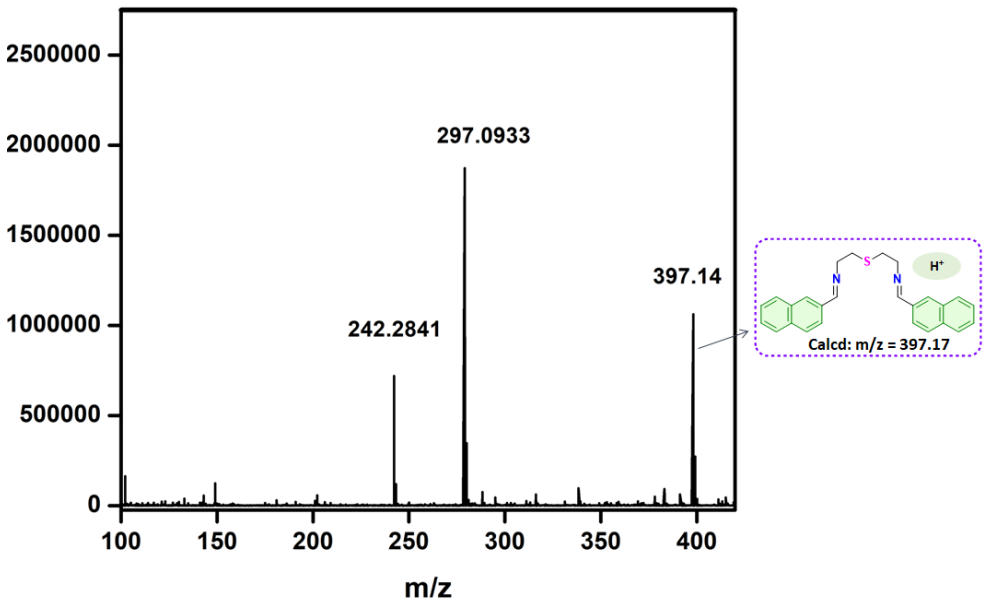

Fig. A17. ESI-MS analysis of probe **NpSb**.

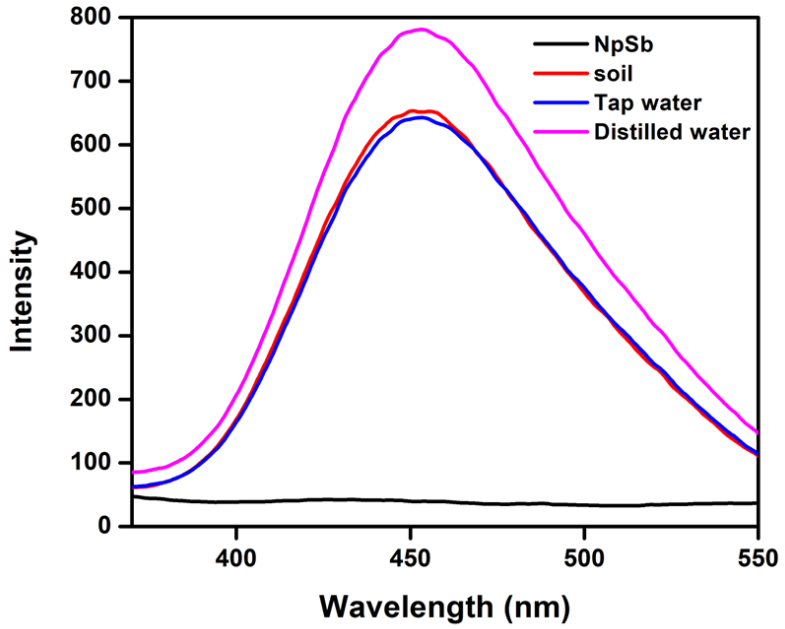

Fig. A18. Interaction of probe **NpSb** (10^{-6} M) with Al^{3+}-spiked real samples (λ_{ex} =300 nm).

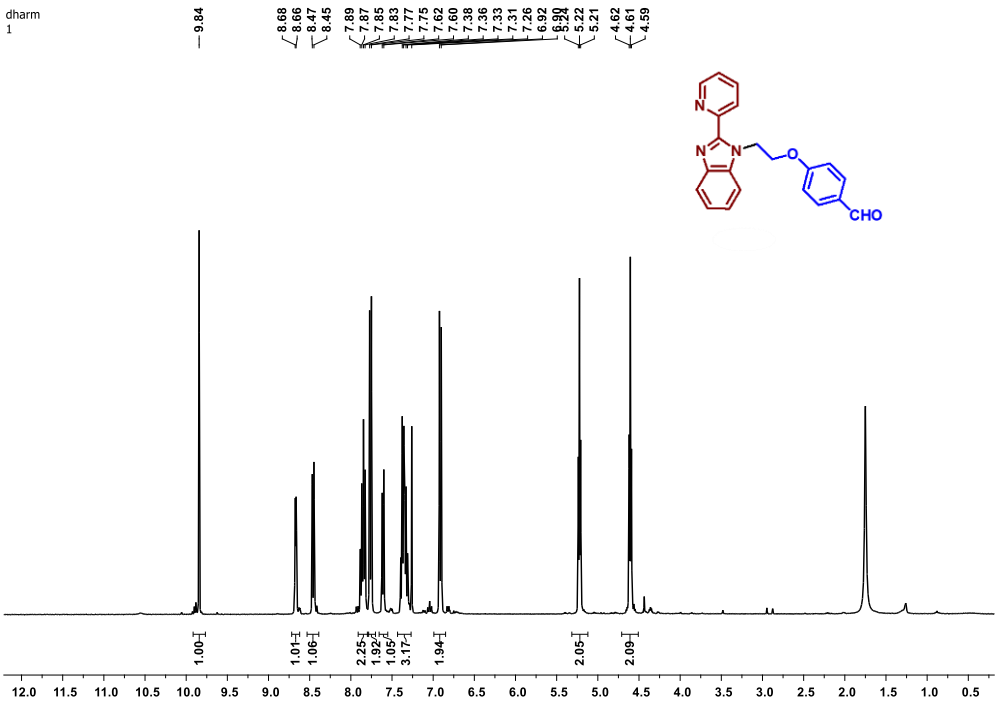

Fig. A19. ^{1}H NMR spectrum of compound **1** in $CDCl_3$ at room temperature. ^{1}H NMR [(500 MHz, $CDCl_3$, TMS, δ (ppm)]: 9.84 (s, 1H), 8.67 (d, 1H), 8.46 (d, 1H), 7.89-7.83 (m, 2H), 7.76 (d, 2H), 7.61 (d, 1H), 7.40-7.31 (m, 3H), 6.91 (d, 2H), 5.22 (t, 2H), 4.61 (t, 2H).

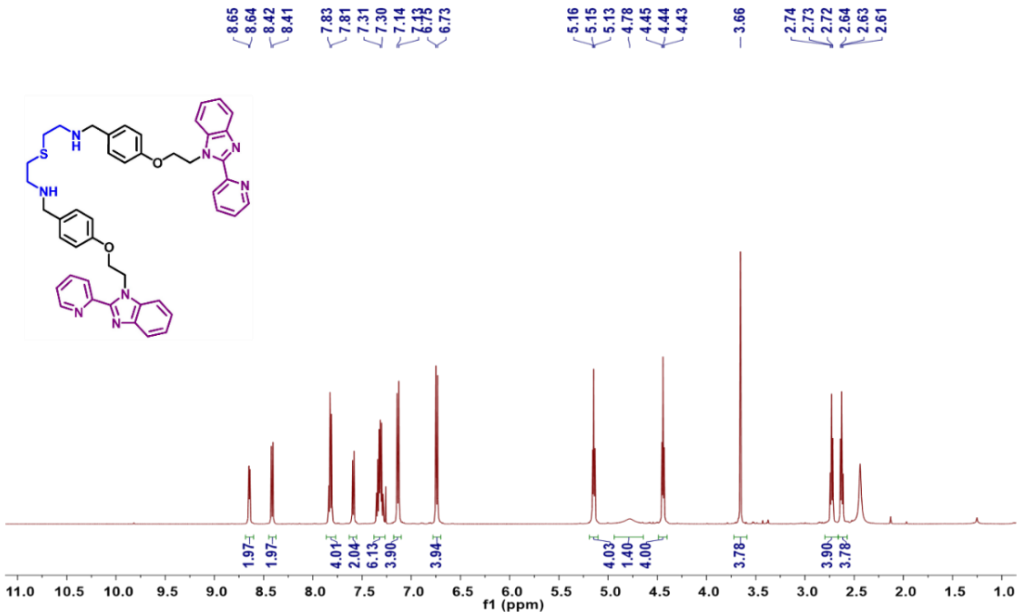

Fig. A20. ^{1}H NMR spectrum of probe **RSB1** in $CDCl_3$ solution. ^{1}H NMR [(500 MHz, $CDCl_3$, TMS, δ (ppm)]: 8.65 (d, 2H), 8.42 (d, 2H), 7.83 (m, 4H), 7.59 (d, 2H), 7.36-7.29 (m, 6H), 7.13 (d, 4H), 6.74 (d, 4H), 5.15 (t, 4H), 4.78 (s, 2H, broad), 4.44 (t, 4H), 3.66 (s, 4H), 2.73 (t, 4H), 2.63 (t, 4H).

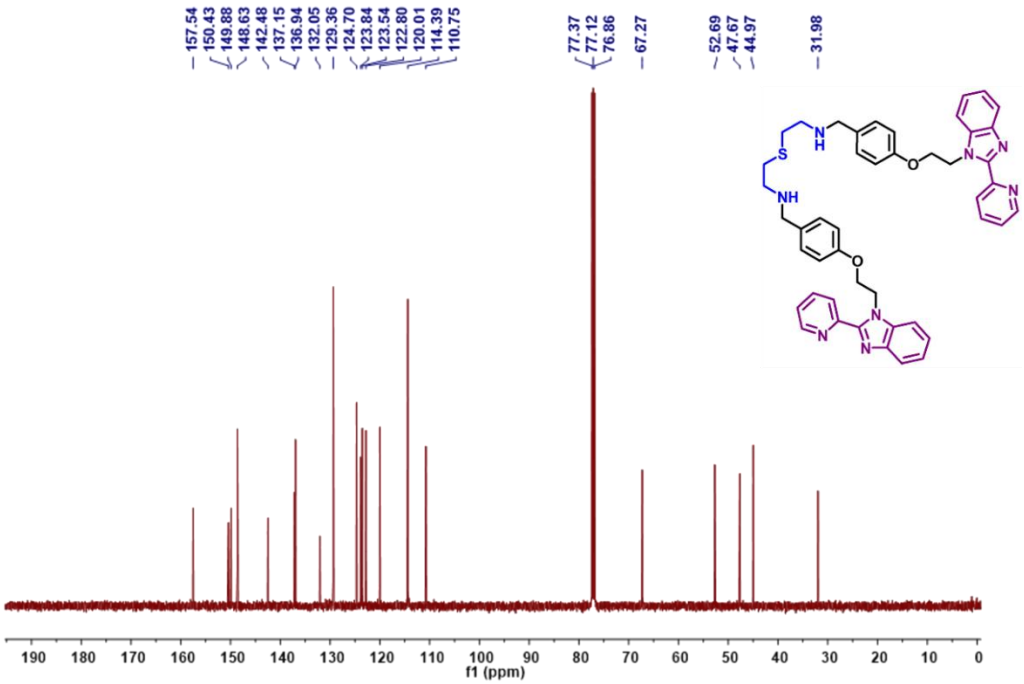

Fig. A21. ^{13}C NMR spectrum of **RSB1** in $CDCl_3$ solution. ^{13}C NMR [(500 MHz, $CDCl_3$, TMS, δ (ppm)]: 157.54, 150.43, 149.88, 148.63, 142.48, 137.15, 136.94, 132.05, 129.36, 124.70, 123.84, 123.54, 122.80, 120.01, 114.39, 110.75, 67.27, 52.69, 47.67, 44.97, 31.98.

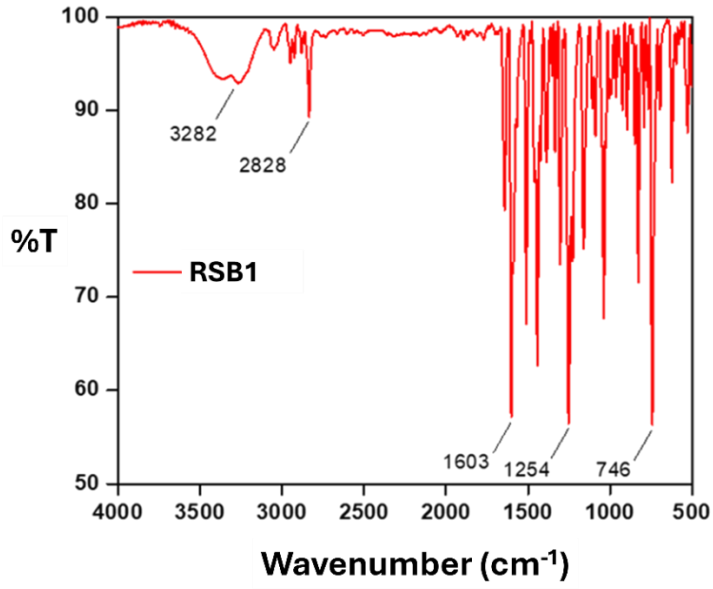

Fig. A22. IR spectrum of the probe **RSB1**. IR (KBr disk): 3282 (ν_{N-H}), 2944, 2828 (ν_{CH2}), 1635, 1603, 1502, 1446, 1254 (ν_{C-O-}), 1035, 820, 746 and 619 cm^{-1}.

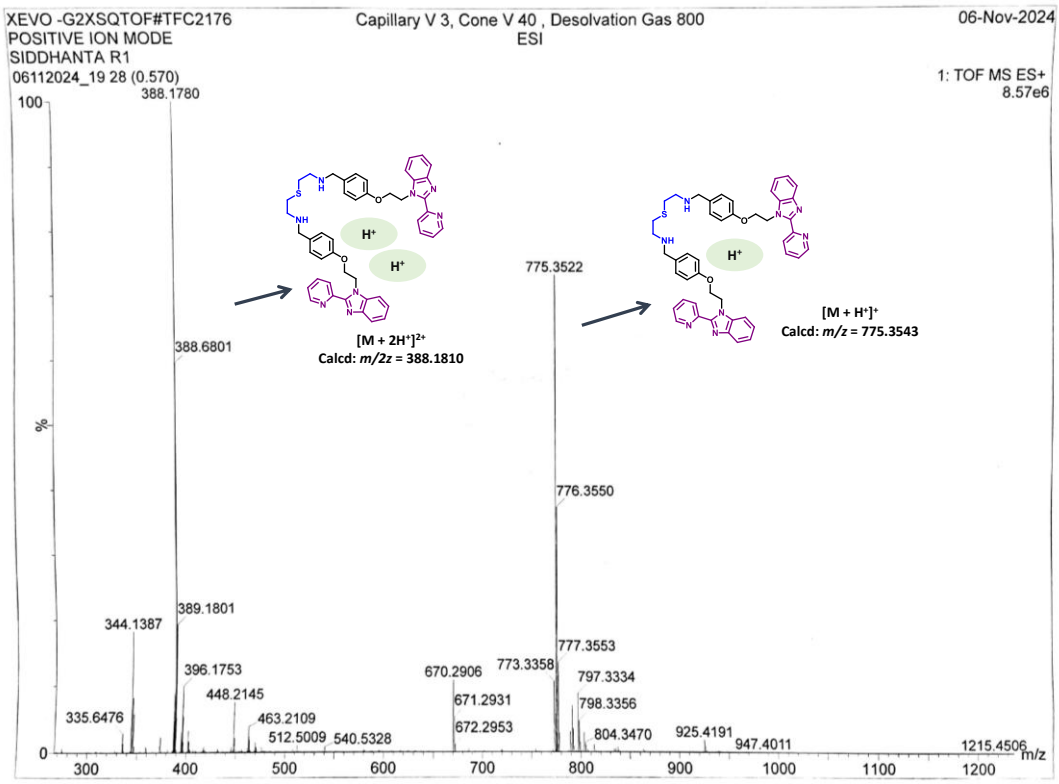

Fig. A23. ESI-MS analysis of **RSB1** in methanol.

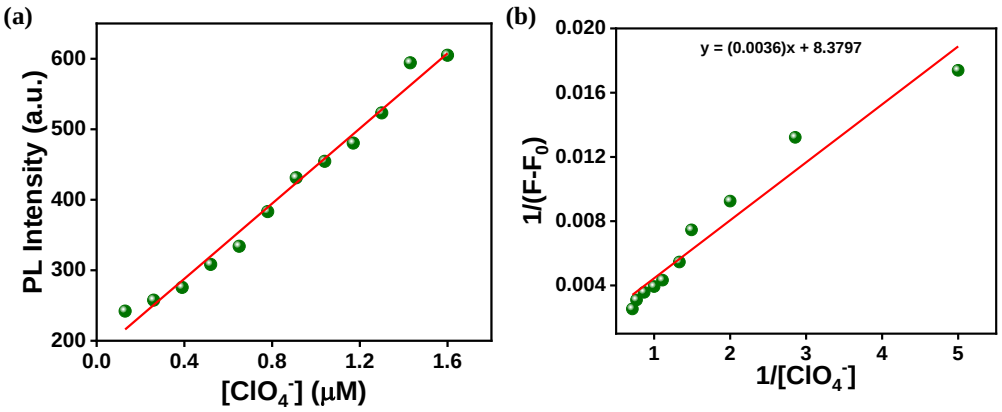

Fig. A24. (a) LoD and (b) binding constant of probe **RSB1** (1.2 μM) with ClO_4^- ion at 40°C in CH_3CN-H_2O mixture (4:1, v/v) (λ_{ex} = 300 nm).

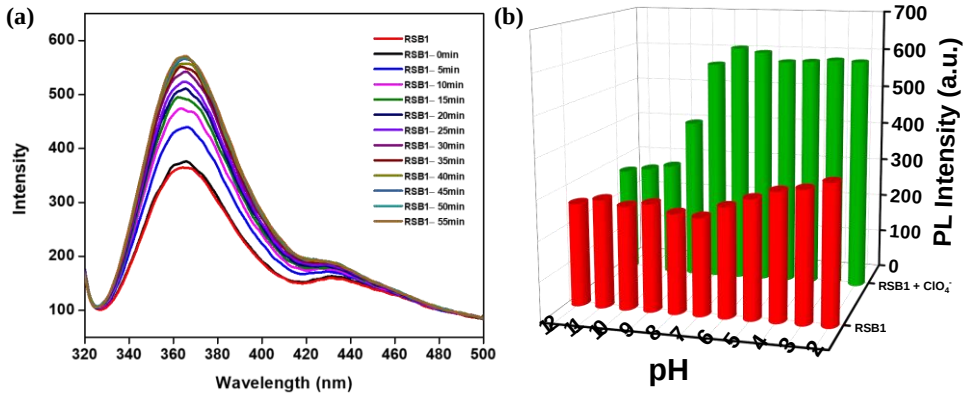

Fig. A25. (a) Response time of probe **RSB1** (1.2 μM) with ClO_4^- ion and (b) effect of pH on the detection of ClO_4^- using **RSB1** in CH_3CN-H_2O mixture (4:1, v/v) (λ_{ex} = 300 nm).

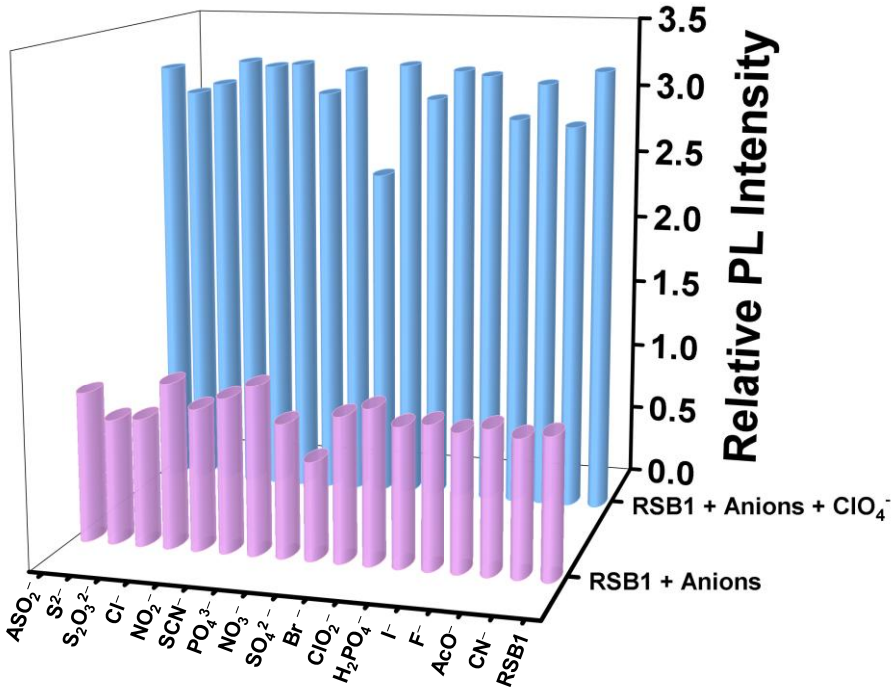

Fig. A26. Relative fluorescent intensity enhancement of **RSB1** (1.2 μM) with perchlorate in the presence of different interfering anions in CH_3CN-H_2O mixture (4:1, v/v) (λ_{ex} = 300 nm).

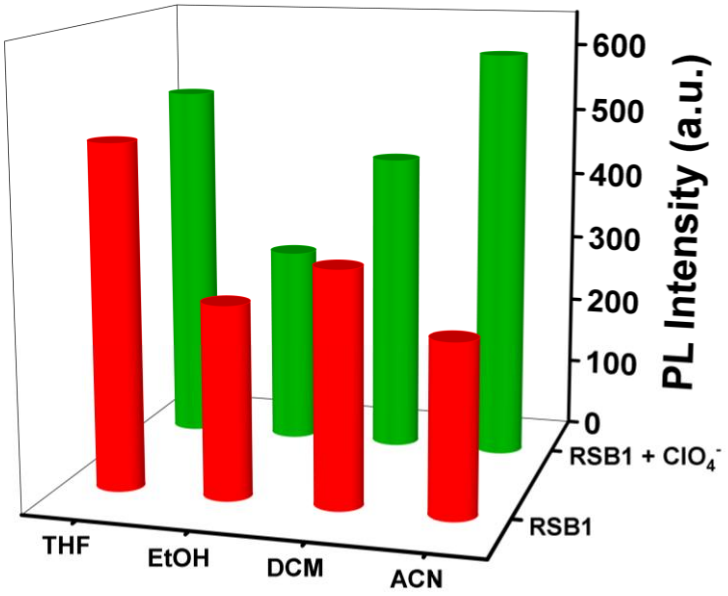

Fig. A27. Sensing performance of probe **RSB1** (1.2 μM) towards ClO_4^- ions in different organic solvents.

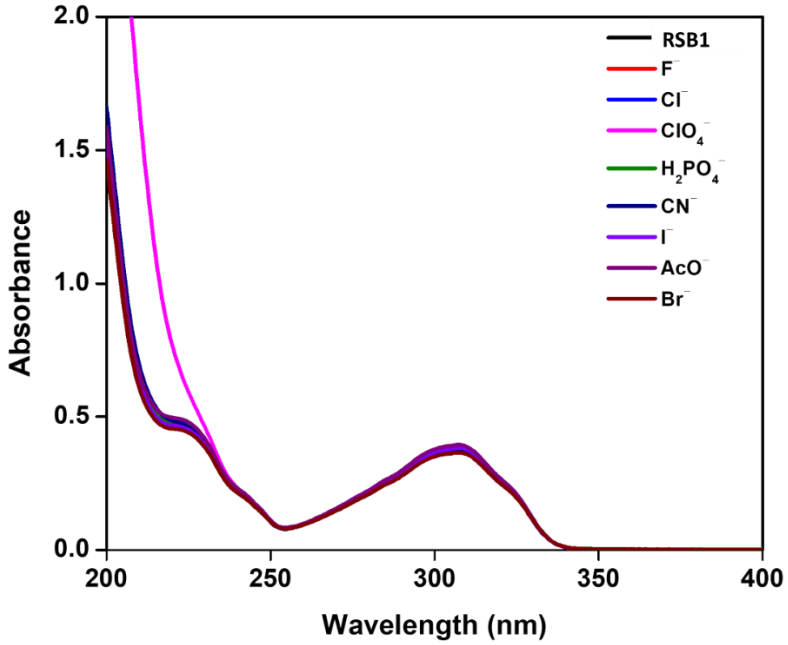

Fig. A28. UV-Vis spectra of **RSB1** (8.6×10^{-6} M) in CH_3CN-H_2O (4:1, v/v) mixture in the presence of various anions.

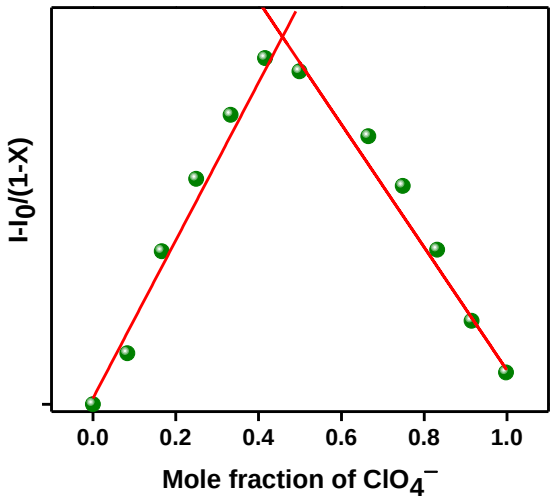

Fig. A29. Job's plot analysis for **RSB1** (1.2 μM) versus ClO_4^- ions in CH_3CN-H_2O (4:1, v/v) mixture. The data has been obtained from fluorescence titration profile.

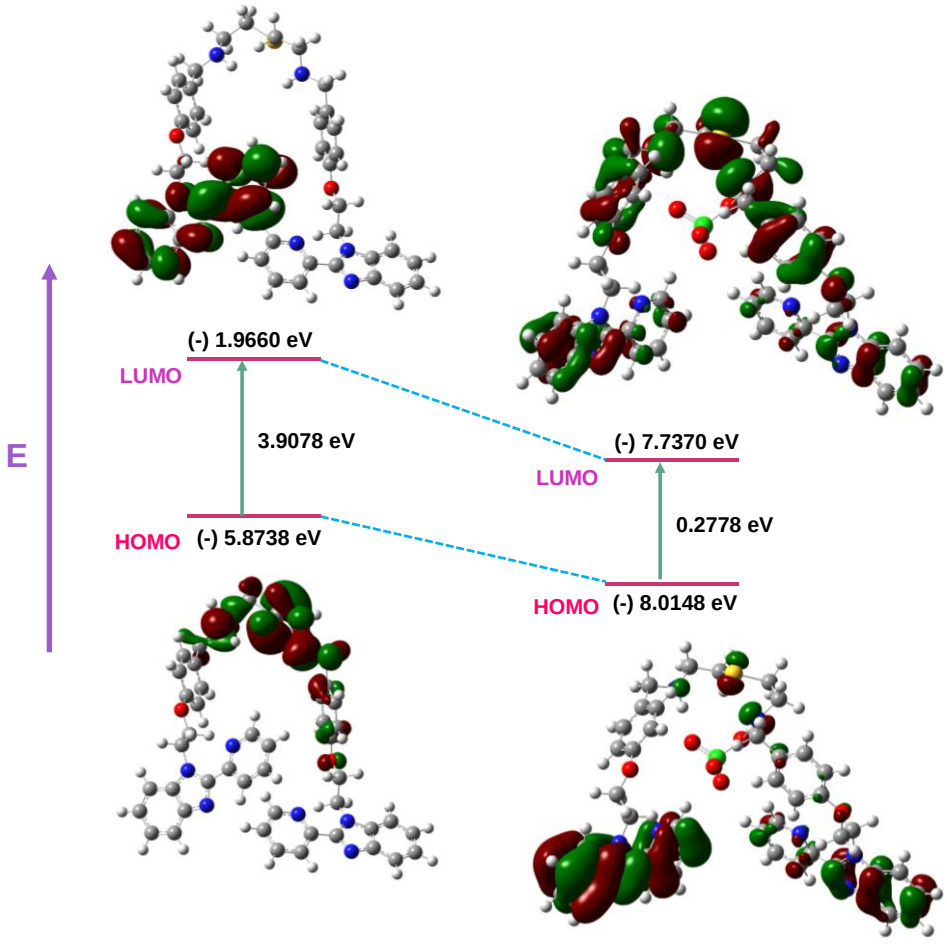

Fig. A30. HOMO and LUMO of optimized probe **RSB1** and adduct **RSB1**-ClO_4^-.

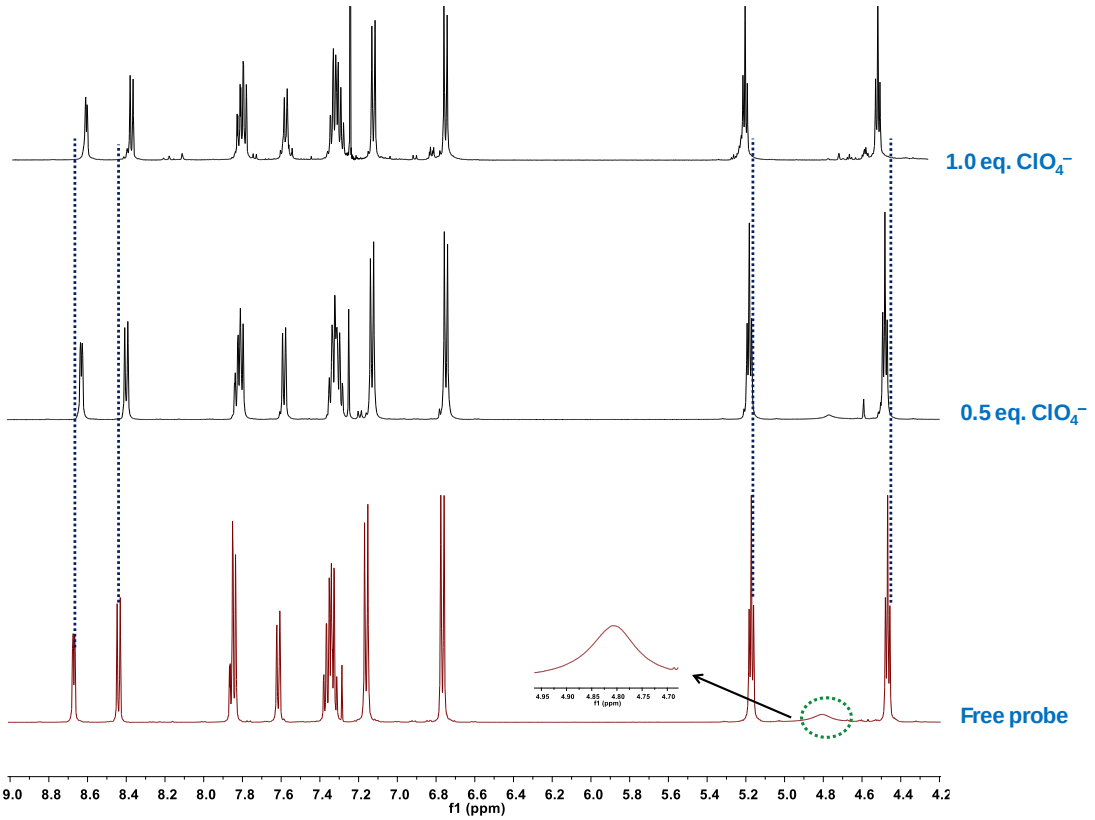

Fig. A31. ^{1}H NMR titration of **RSB1** with varied concentrations of ClO_4^- ions (0-1.0 equiv.) at room temperature.

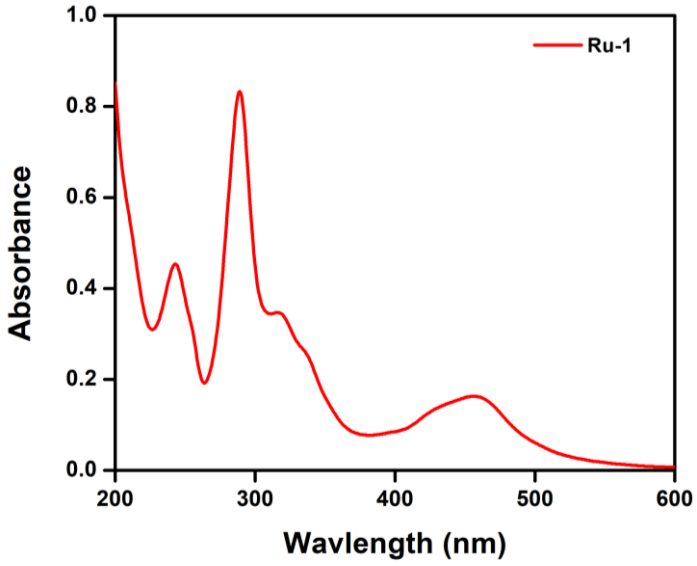

Fig. A32. UV-Vis spectrum of **Ru-1** (10.0 μM) in CH_3CN solution at room temperature.

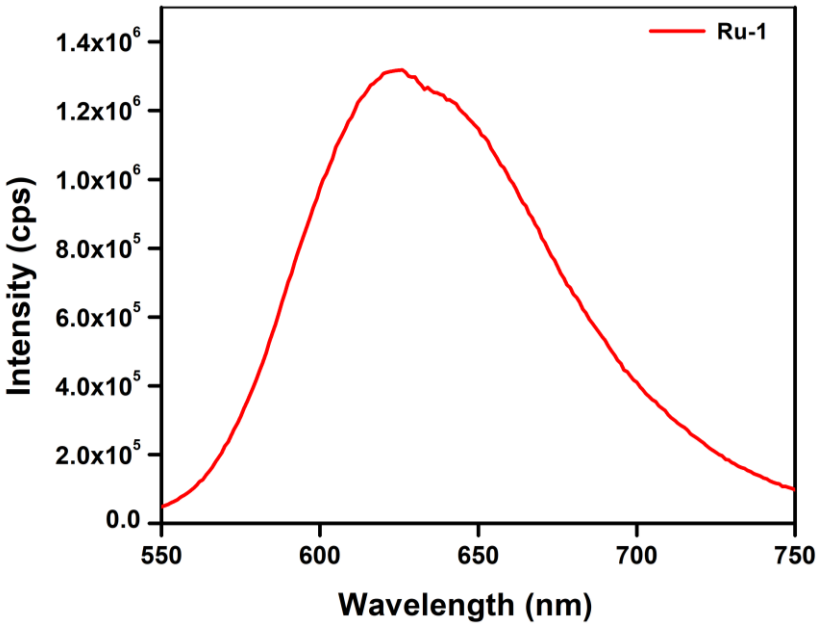

Fig. A33. Emission spectrum of **Ru-1** (10.0 μM) in CH_3CN solution at room temperature (λ_{ex} = 460 nm).

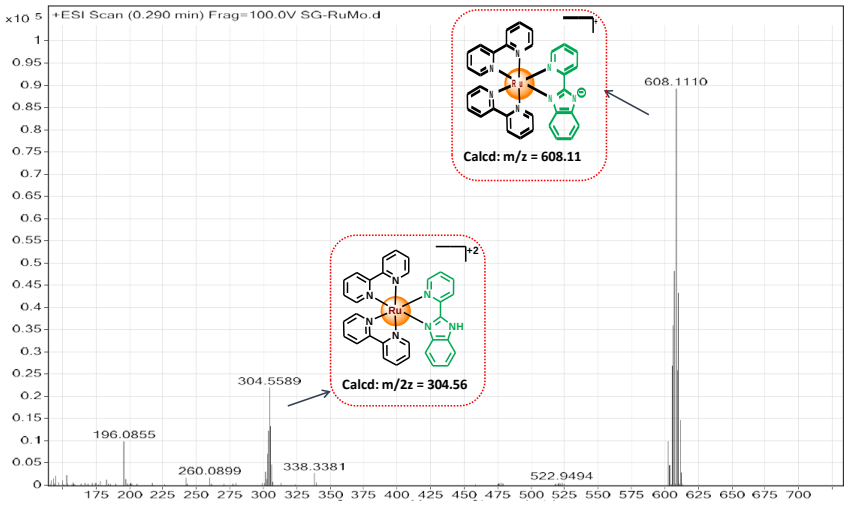

Fig. A34. ESI-mass analysis of **Ru-1** in CH_3CN solution at room temperature.

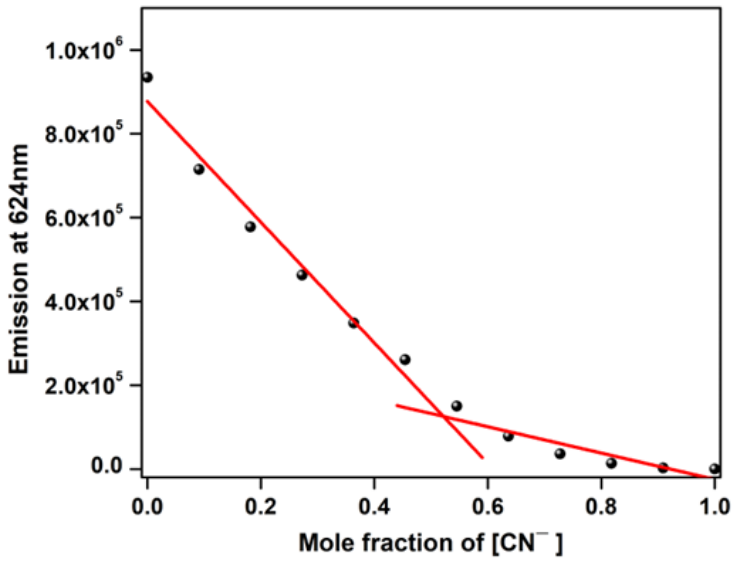

Fig. A35. Job's plot analysis for **Ru-1** with CN^- in water (λ_{ex} = 460 nm)..

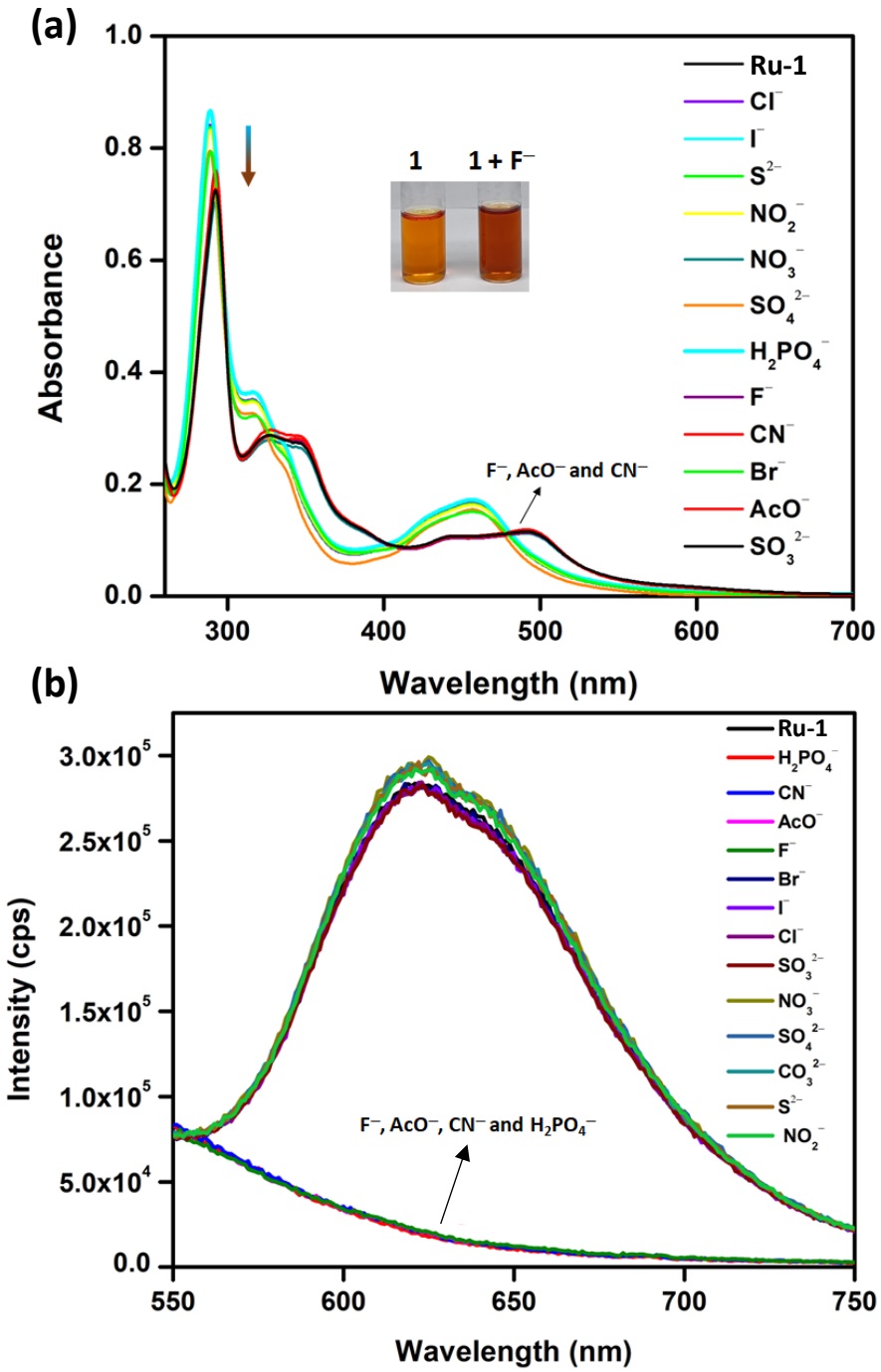

Fig. A36. (a) UV-Vis and (b) emission spectra of probe **Ru-1** with various anions in CH_3CN solutions (λ_{ex} = 460 nm).

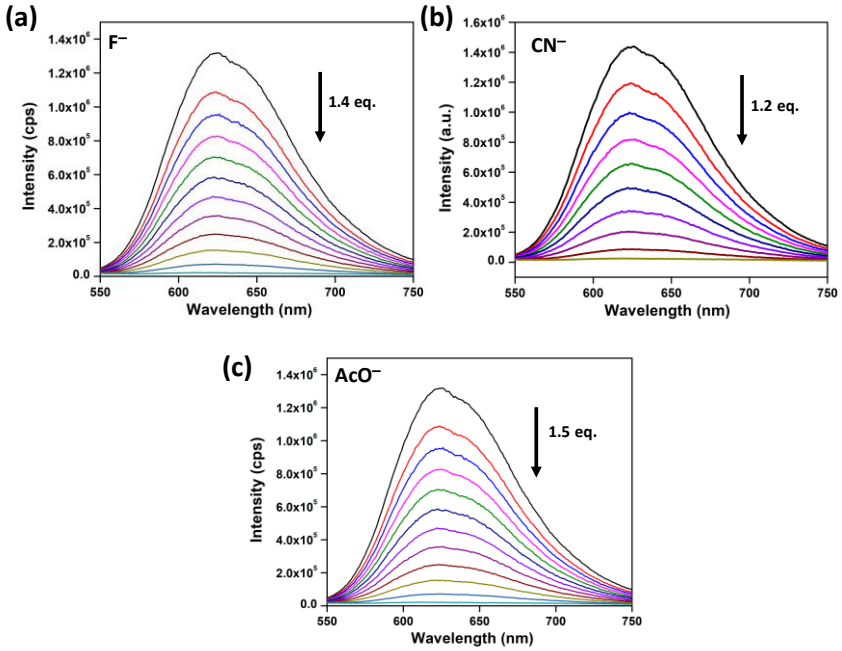

Fig. A37. Emission titration profiles of **Ru-1** (~2.0 μM) in the presence of various concentrations of (a) F^-; (b) CN^- and (c) AcO^- in CH_3CN solutions (λ_{ex} = 460 nm).

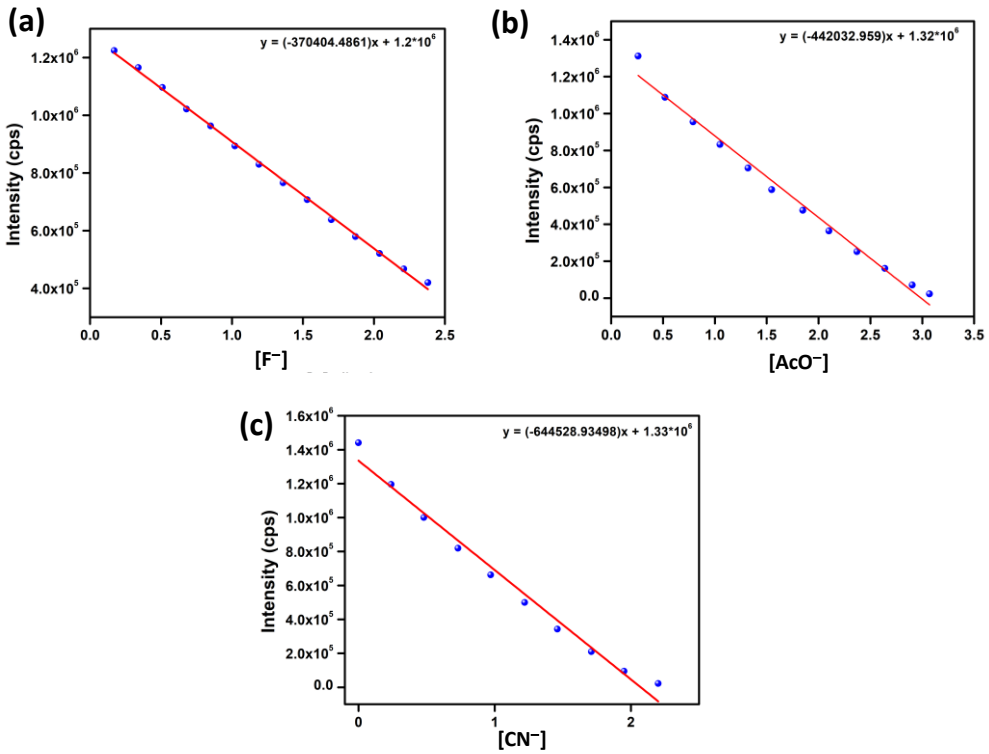

Fig. A38. Linear curves of the emission intensity of **Ru-1** (~2.0 μM) with (a) F^-; (b) AcO^- and (c) CN^- for the determination of LoD in CH_3CN solutions using fluorescence spectroscopy (λ_{ex} = 460 nm).

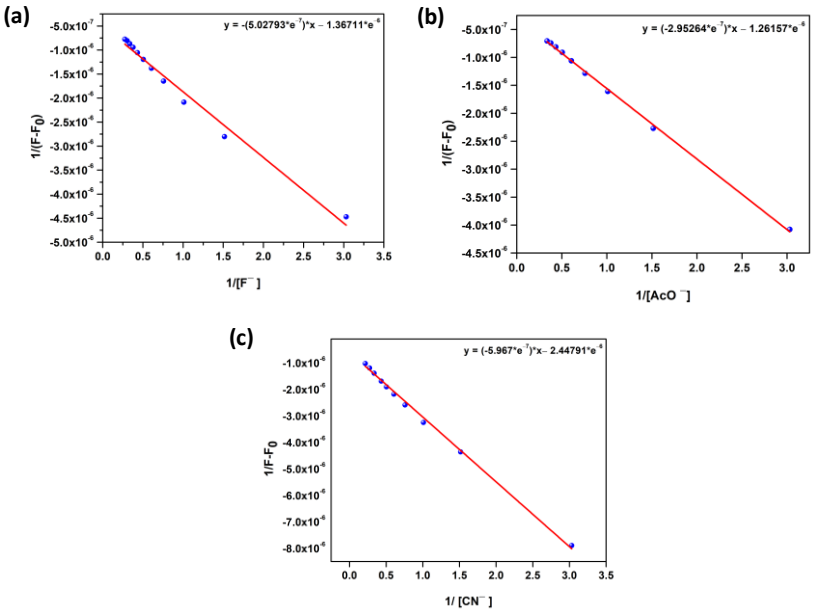

Fig. A39. Benesi-Hildebrand plots of **Ru-1** (~2.0 µM) with various anions (F^-, AcO^-, and CN^-) for the determination of binding constant values in CH_3CN solutions (λ_{ex} = 460 nm).

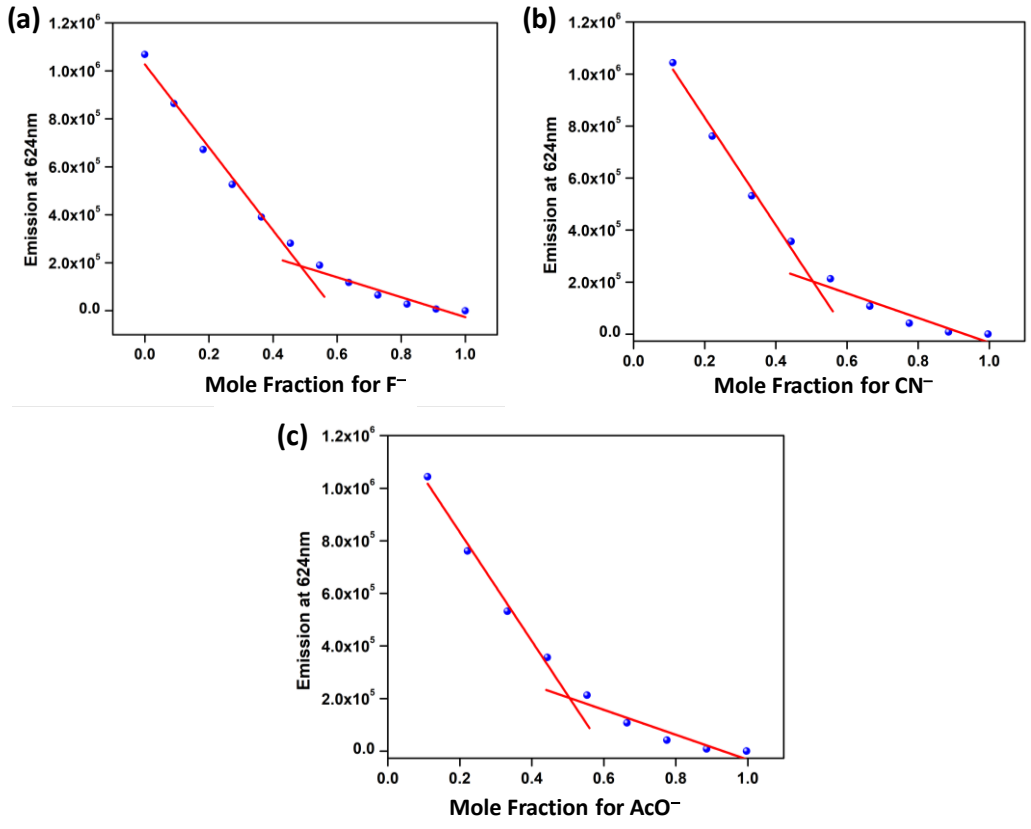

Fig. A40. Job's plot analyses for **Ru-1** (~2.0 µM) with various anions (F^-, AcO^- and CN^- ions) in CH_3CN solutions (λ_{ex} = 460 nm).

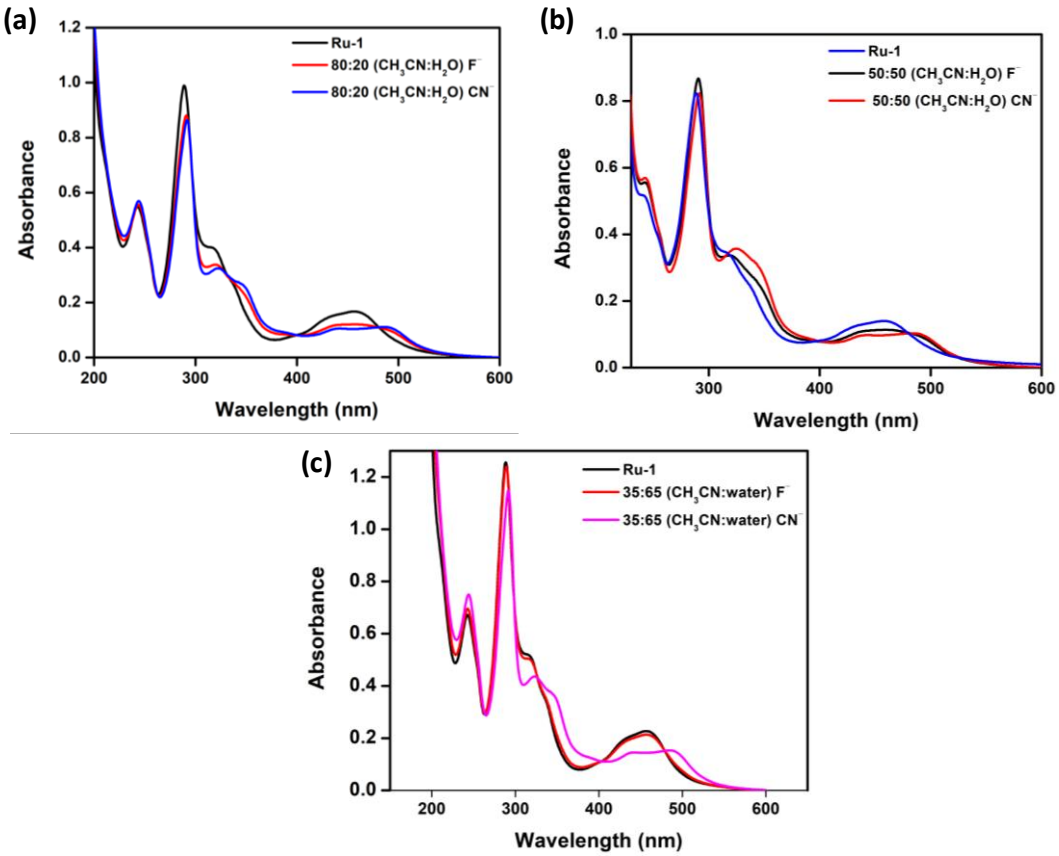

Fig. A41. UV-Vis spectral changes of **Ru-1** with (a) 3.0 equiv. of F^- and CN^- ions in CH_3CN: H_2O mixture (80: 20, v/v); (b) with 20.0 equiv. of F^- and 6.0 equiv. of CN^- ions in CH_3CN: H_2O mixture (50: 50, *v/v*); and (c) with 50.0 equiv. of F^- ions and 8.0 equiv. of CN^- in CH_3CN: H_2O mixture (35: 65, *v/v*).

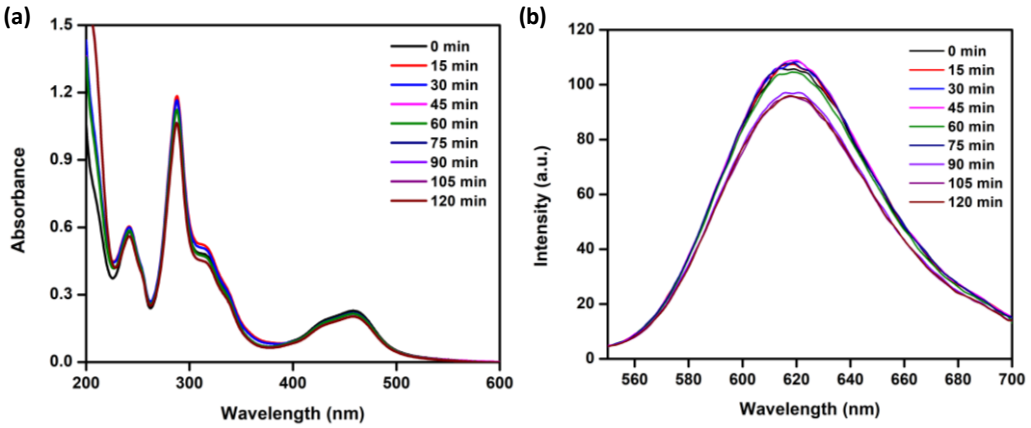

Fig. A42. (a) UV-Vis of **Ru-1** and (b) emission spectra of **Ru-1** upon irradiation with 365nm light.

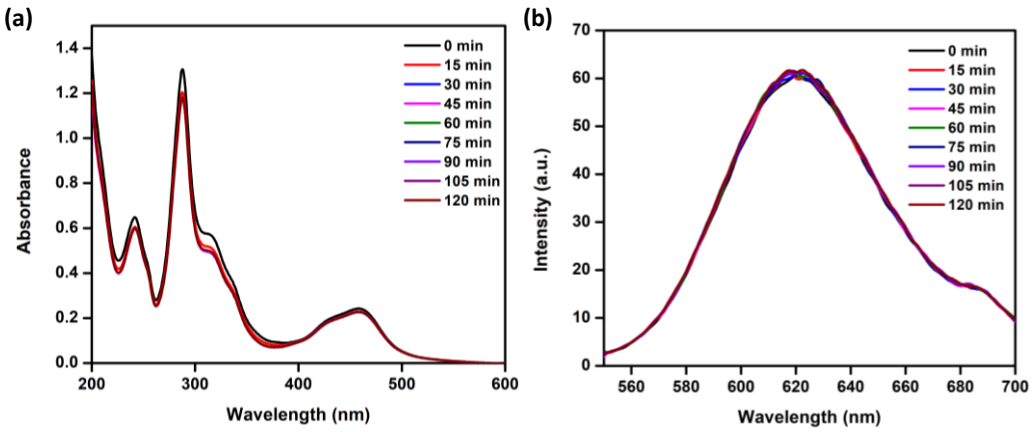

Fig. A43. (a) UV-Vis of **Ru-1** and (b) emission spectra of **Ru-1** upon irradiation with visible light.

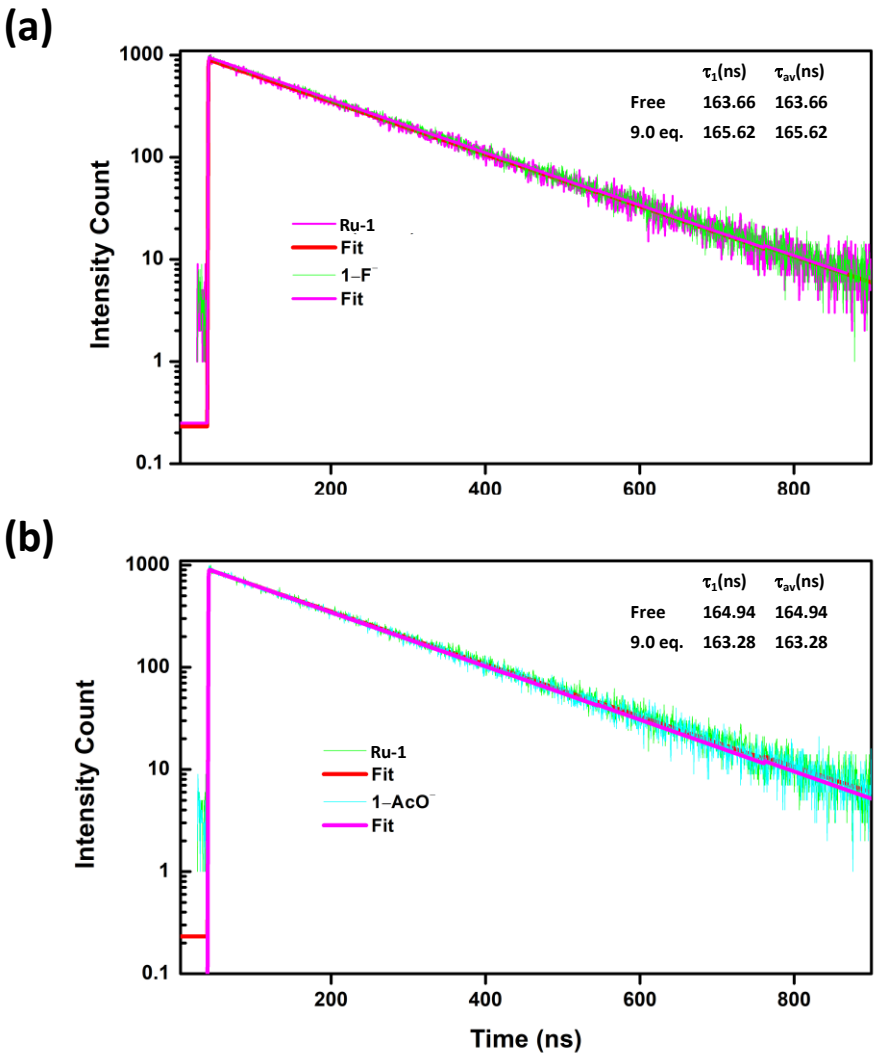

Fig. A44. Lifetime changes of **Ru-1** with (a) F^- in H_2O; and (b) AcO^- in H_2O.

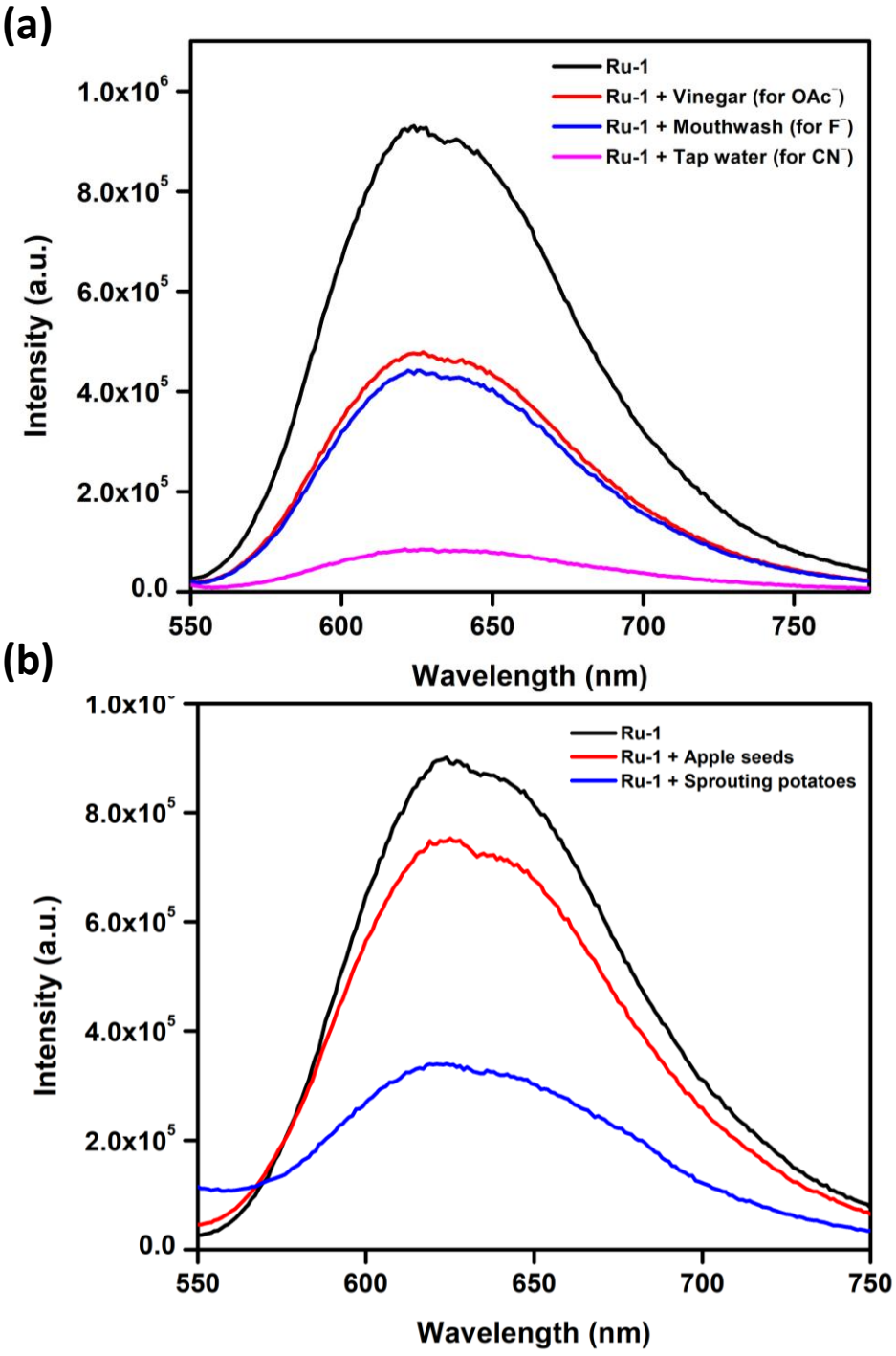

Fig. A45. (a) Luminescence-based detection of OAc^- in commercially available vinegar (red-line); F^- in mouthwash (blue-line) and CN^- in cyanide-spiked tap water (pink-line) and (b) luminescence-based detection of CN^- in food samples including apple seeds and sprouting potatoes.

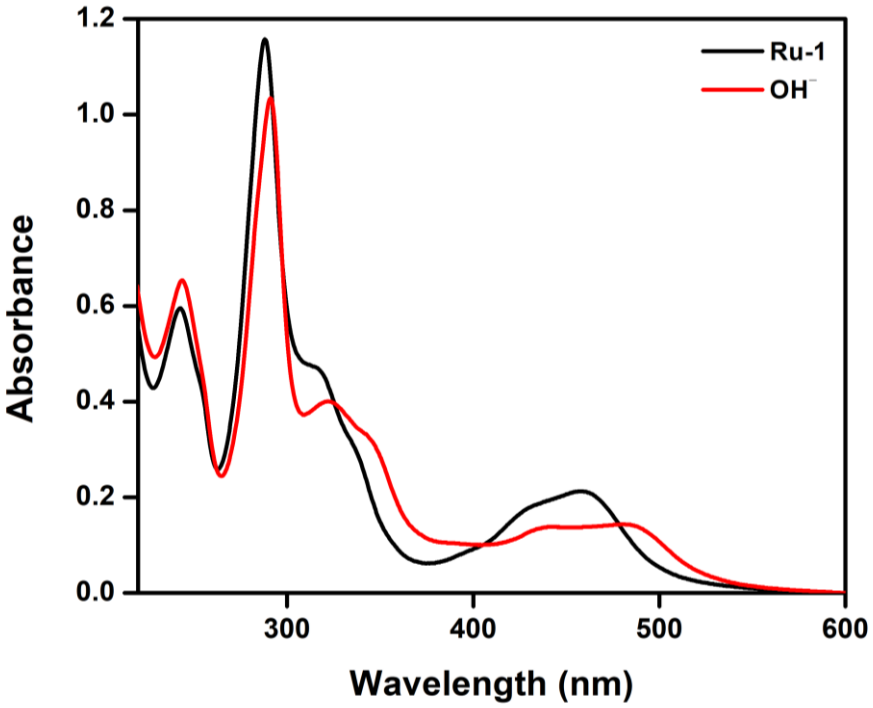

Fig. A46. UV-Vis spectral variations in **Ru-1** with 9.0 equiv. of OH^- in H_2O.

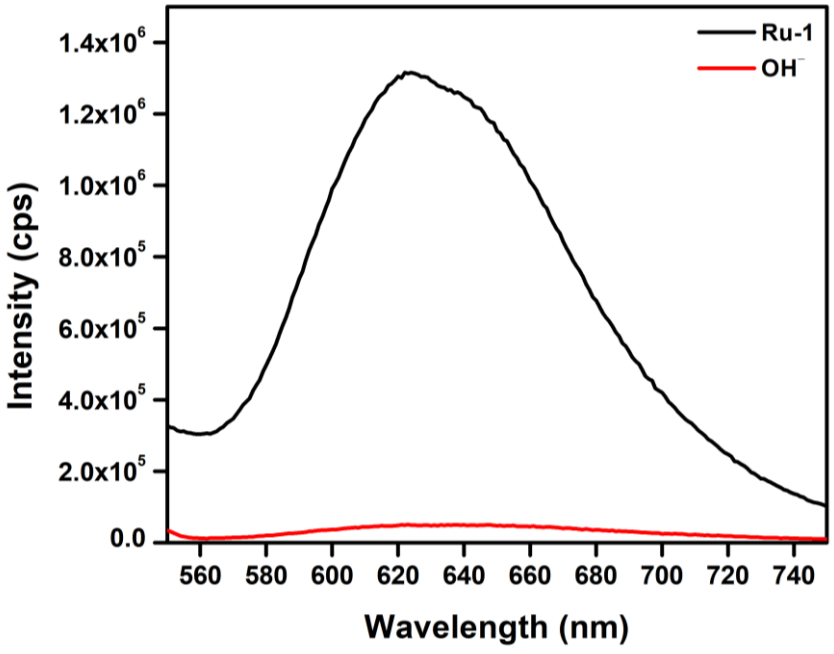

Fig. A47. Emission spectral variations in **Ru-1** with 9.0 equiv. of OH^- in H_2O.

Table A1. Crystallographic data for **NpSb**.

Formula	$C_{26}H_{24}N_2S$
Formula weight ($gmol^{-1}$)	396.53
Space group (hall)	-P 2yn
Temperature/K	150(2)
λ (Å) (Cu-Kα)	1.54184
Crystal system	monoclinic
a (Å)	5.7751(6)
b (Å)	46.275(3)
c (Å)	7.7780(8)
α(°)	90
β (°)	90.655(10)
γ (°)	90
V ($Å^3$)	2078.5(3)
Z	4
ρ_{calc}(gcm^{-3})	1.267
Crystal size (mm)	0.18 × 0.15 × 0.10
F(000)	840
Index ranges	-7 <*h*<7
	-56 <*k*< 56
	-9<*l*< 9
Reflns/ para/ restraints.	3889/263/407
GOF on F^2	1.119
$R1^a$ [$I > 2\sigma(I)$]	0.1178
*R*1[all data]	0.1694
$wR2^b$ [$I > 2\sigma(I)$]	0.3025
*wR*2 [all data]	0.3474

$^a R1 = \Sigma||Fo|-|Fc||/\Sigma|Fo|$; $^b wR2 = |\Sigma w(|Fo|^2 - |Fc|^2)|/\Sigma|w(Fo)^2|^{1/2}$

Table A2. Selected bond lengths [Å] and angles [°] in the single crystals of **NpSb**.

Bond Length (Å)		**Bond Angle (°)**	
S(1)–C(13)	1.784(10)	C(13)–S(1)–C(14)	101.7(5)
S(1) –C(14)	1.803(9)	C(12)–C(13)–S(1)	112.6(7)
C(13)–C(12)	1.510(13)	C(15)–C(14)–S(1)	112.6(6)
C(14)–C(15)	1.510(13)	C(15)–N(2)–C(16)	116.1(8)
C(12)–N(1)	1.477(12)	C(11)–N(1)–C(12)	116.0(10)
C(15)–N(2)	1.478(11)		
C(11)–N(1)	1.263(12)		
C(16)–N(2)	1.257(11)		

Table A3. Detection of Al^{3+} in real sample.

Tap water			
	Al^{3+} added (μM)	**Al^{3+} calculated (μm)**	**% Recovery**
	0.3	0.28	93.3
	0.8	0.77	96.2
Distilled water			
	0.3	0.29	96.6
	0.8	0.83	103.7
Soil sample			
	0.3	0.31	103.3
	0.8	0.81	98.7

Table A4. Comparison of sensing parameters of probe **RSB1** with some previously reported works.

S. No.	**Probe**	**LoD (nm)**	**Real Sample**	**Solvent**	**Mechanism**
1.	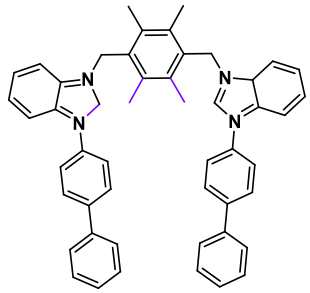	100	Tap water	HEPES buffer	Cavity recognition
2.	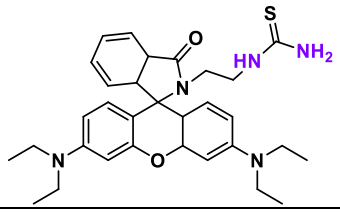	100	Live cell imaging	CH_3CN-H_2O (4:1)	H-bonding
3.	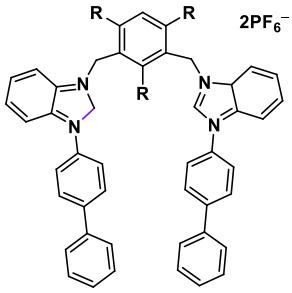	0.01	Test paper strip	HEPES buffer with 2% DMSO	Aggregation/ Disaggregation mechanism
4.	Eu-based complex	-	-	H_2O	Anion displacement

5.	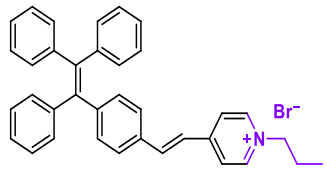	380	-	DMSO-Water	Ionic interaction, Van Der Waals interaction
6.	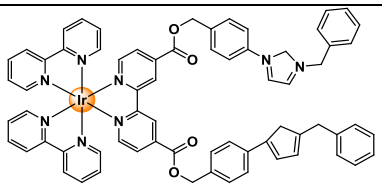	960	Live cell imaging	Water	Aggregation Induced Emission
7.	Zr-based MOF	1440	-	EtOH	H-bonding interaction
8.	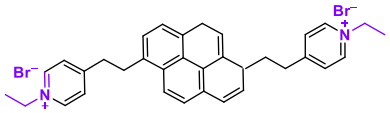	1162	-	MeOH	Ionic interaction
9.	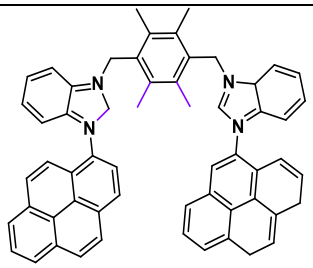	651		CH_3CN-H_2O	Cavity recognition, H-bonding interaction, charge transfer
10.	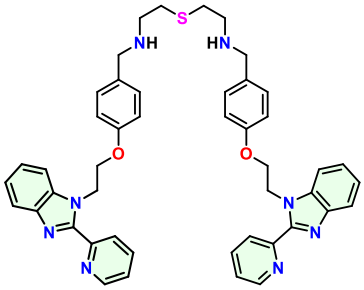	121	Distilled water, Tap water, Soil Sample	CH_3CN-H_2O	Cavity recognition, H-bonding interaction

Table A5. Determination of CN^- in tap water and distilled water using UV-Vis spectra.

Real Sample	CN^- added (µM)	CN^- detected (µM)	% Recovery	Relative Standard Deviation (n=3)
Tap water	25	24.833	99.33	3.3%
	50	47.168	94.93	2.1%
	75	74.136	98.84	2.8%
Drinking water	25	24.982	99.92	2.6%
	50	51.327	102.65	3.2%
	75	76.542	102.05	2.7%

Table A6. Determination of CN^- in tap water and distilled water using emission spectra.

Real Sample	CN^- added (µM)	CN^- detected (µM)	% Recovery	Relative Standard Deviation (n=3)
Tap water	4	4.132	102.5	3.4%
	8	8.041	94.93	2.8%
	14	13.99	98.84	2.8%
Drinking water	4	3.981	99.92	3.1%
	8	8.135	102.65	2.9%
	14	14.376	102.05	2.3%

Table A7. Comparison of bond parameters obtained after optimization of complexes.

	Ru-1	**Ru-1-dp**
Ru-N1	2.12268 Å	2.12368 Å
Ru-N2	2.10093 Å	2.07064 Å
Ru-N12	2.08626 Å	2.07731
Ru-N11	2.08856 Å	2.09513 Å
Ru-N21	2.09133 Å	2.07716 Å
Ru-N22	2.08237 Å	2.07393 Å
N1-Ru-N2	77.69134	78.42661
N11-Ru-N12	78.37640	78.22489
N11-Ru-N22	78.36175	78.46931

References

Adams, H. K., Kadarauch, M., Hodson, N. J., Lit, A. R. and Phipps, R. J. (2025). Design Approaches That Utilize Ionic Interactions to Control Selectivity in Transition Metal Catalysis. Chemical Reviews, Vol. 125. No. 5, pp. 2846–2907.

Afrin, A. and Swamy, P.C.A. (2023). Novel Schiff base derivatives for the detection of one-to-multi metal ions and tracking the live cell imaging. Coordination Chemistry Reviews, Vol. 494. pp. 215327.

Al-Abadleh, H. A., Al-Hosney, H. A. and Grassian, V. H. (2005). Oxide and carbonate surfaces as environmental interfaces: the importance of water in surface composition and surface reactivity. Journal of Molecular Catalysis A: Chemical, Vol. 228. No. 1, pp. 47–54.

Alam, P., Leung, N. L. C., Zhang, J., Kwok, R. T. K., Lam, J. W. Y. and Tang, B. Z. (2021). AIE-based luminescence probes for metal ion detection. Coordination Chemistry Reviews, Vol. 429. pp. 213693.

Alam, R., Mistri, T., Bhowmick, R., Katarkar, A., Chaudhuri, K. and Ali, M. (2016). ESIPT blocked CHEF based differential dual sensor for Zn2+ and Al3+in a pseudo-aqueous medium with intracellular bio-imaging applications and computational studies. RSC Advances, Vol. 6. No. 2, pp. 1268–1278.

Alreja, P. and Kaur, N. (2016a). Establishing the anion recognition correlation of the 2-(2-methoxyphenyl)-1H-imidazo [4, 5-f][1,10] phenanthroline and its Ru(bipy)22+ complex via fluorimetry. Journal of Luminescence, Vol. 179. pp. 372–377.

Amaro-Gahete, J., Pavliuk, M. V, Tian, H., Esquivel, D., Romero-Salguero, F. J. and Ott, S. (2021). Catalytic systems mimicking the [FeFe]-hydrogenase active site for visible-light-driven hydrogen production. Coordination Chemistry Reviews, Vol. 448. pp. 214172.

Amiard, J. C., Amiard-Triquet, C., Berthet, B. and Metayer, C. (1987). Comparative study of the patterns of bioaccumulation of essential (Cu, Zn) and non-essential (Cd, Pb) trace metals in various estuarine and coastal organisms. Journal of Experimental Marine Biology and Ecology, Vol.

106. No. 1, pp. 73–89.

Angerani, S. and Winssinger, N. (2019). Visible Light Photoredox Catalysis Using Ruthenium Complexes in Chemical Biology. Chemistry – A European Journal, Vol. 25. No. 27, pp. 6661–6672.

Arcudi, F., Đorđević, L., Schweitzer, N., Stupp, S. I. and Weiss, E. A. (2022). Selective visible-light photocatalysis of acetylene to ethylene using a cobalt molecular catalyst and water as a proton source. Nature Chemistry, Vol. 14. No. 9, pp. 1007–1012.

Arias-Rotondo, D. M. and McCusker, J. K. (2016). The photophysics of photoredox catalysis: A roadmap for catalyst design. Chemical Society Reviews, Vol. 45. No. 21, pp. 5803–5820.

Arienzo, M. and Capasso, R. (2000). Analysis of Metal Cations and Inorganic Anions in Olive Oil Mill Waste Waters by Atomic Absorption Spectroscopy and Ion Chromatography. Detection of Metals Bound Mainly to the Organic Polymeric Fraction. Journal of Agricultural and Food Chemistry, Vol. 48. No. 4, pp. 1405–1410.

Arora, A., Kaushal, J., Kumar, A., Kumar, P. and Kumar, S. (2019). Ruthenium(II)-Polypyridyl-Based Sensor Bearing a DPA Unit for Selective Detection of Cu(II) Ion in Aqueous Medium. ChemistrySelect, Vol. 4. No. 20, pp. 6140–6147.

Ateia, M., Wei, H. and Andreescu, S. (2024). Sensors for Emerging Water Contaminants: Overcoming Roadblocks to Innovation. Environmental Science & Technology, Vol. 58. No. 6, pp. 2636–2651.

Balas, C. (2009). Review of biomedical optical imaging—a powerful, non-invasive, non-ionizing technology for improving in vivo diagnosis. Measurement Science and Technology, Vol. 20. No. 10, pp. 104020.

Bao, X., Yu, J. and Zhou, Y. (2009). Selective colorimetric sensing for F^- by a cleft-shaped anion receptor containing amide and hydroxyl as recognition units. Sensors and Actuators B: Chemical, Vol. 140. No. 2, pp. 467–472.

Bar, M., Maity, D., Das, K. and Baitalik, S. (2017). Asymmetric bimetallic ruthenium(II) complexes selectively sense cyanide in water through significant modulation of their ground and excited state properties. Sensors

and Actuators, B: Chemical, Vol. 251, pp. 208–223.

Basri, R., Ahmed, N., Khalid, M., Khan, M. U., Abdullah, M., Syed, A., Elgorban, A. M., Al-Rejaie, S. S., Braga, A. A. C. and Shafiq, Z. (2022). Quinoline based thiosemicarbazones as colorimetric chemosensors for fluoride and cyanide ions and DFT studies. Scientific Reports, Vol. 12. No. 1, pp. 1–19.

Batjoens, P., De Brabander, H. F. and T'Kindt, L. (1993). Ion chromatographic determination of perchlorate in cattle urine. Analytica Chimica Acta, Vol. 275. No. 1, pp. 335–340.

Beer, P. D. and Gale, P. A. (2001). Anion Recognition and Sensing: The State of the Art and Future Perspectives. Angewandte Chemie International Edition, Vol. 40. No. 3, pp. 486–516.

Berend, K., Van Hulsteijn, L. H. and Gans, R. O. B. (2012). Chloride: The queen of electrolytes? European Journal of Internal Medicine, Vol. 23. No.3, pp. 203–211.

Berezin, M. Y. and Achilefu, S. (2010). Fluorescence Lifetime Measurements and Biological Imaging. Chemical Reviews, Vol. 110. No.5, pp. 2641–2684.

Berhanu, A. L., Gaurav, Mohiuddin, I., Malik, A. K., Aulakh, J. S., Kumar, V. and Kim, K.-H. (2019). A review of the applications of Schiff bases as optical chemical sensors. TrAC Trends in Analytical Chemistry, Vol. 116. pp. 74–91.

Bhaskar, R., Mageswari, N., Sankar, D. and Vinoth Kumar, G. G. (2022). Fluorescence chemosensor for fluoride ion using quinoline-derived probe: Molecular logic gate application. Materials Letters, Vol. 327. pp. 133040.

Bhaskar, R. and Sarveswari, S. (2019). Colorimetric sensor for real-time detection of cyanide ion in water and food samples. Inorganic Chemistry Communications, Vol. 102. pp. 83–89.

Bodman, S. E. and Butler, S. J. (2021). Advances in anion binding and sensing using luminescent lanthanide complexes. Chemical Science, Vol. 12. No. 8, pp. 2716–2734.).

Boonmee, C., Promarak, V., Tuntulani, T. and Ngeontae, W. (2018).

Cysteamine-capped copper nanoclusters as a highly selective turn-on fluorescent assay for the detection of aluminum ions. Talanta, Vol. 178. pp. 796–804.

Broering, E. P., Truong, P. T., Gale, E. M. and Harrop, T. C. (2013). Synthetic analogues of nickel superoxide dismutase: A new role for nickel in biology. Biochemistry, Vol. 52. No. 1, pp. 4–18.

Brown, G. M. and Gu, B. (2006). The Chemistry of Perchlorate in the Environment BT - Perchlorate: Environmental Occurrence, Interactions and Treatment (pp. 17–47). Springer US.

Bruker, A. and Saint, A. X. S. (2008). Inc., Madison, WI, 2004 (b) GM Sheldrick. Acta Crystallogr., Sect. A: Fundam. Crystallogr, Vol. 64. pp. 112.

Bryliakov, K. P. and Talsi, E. P. (2014). Active sites and mechanisms of bioinspired oxidation with H2O2, catalyzed by non-heme Fe and related Mn complexes. Coordination Chemistry Reviews, Vol. 276. pp. 73–96.

Bush, A. I. (2003). The metallobiology of Alzheimer's disease. Trends in Neurosciences, Vol. 26. No. 4, pp. 207–214.

Busschaert, N., Caltagirone, C., Van Rossom, W. and Gale, P. A. (2015). Applications of Supramolecular Anion Recognition. Chemical Reviews, Vol. 115. No. 15, pp. 8038–8155.

Butler, S. J. and Parker, D. (2013). Anion binding in water at lanthanide centres: From structure and selectivity to signalling and sensing. Chemical Society Reviews, Vol. 42. No.4, pp. 1652–1666.

Butt, M. A., Mateos, X. and Piramidowicz, R. (2024). Photonics sensors: A perspective on current advancements, emerging challenges, and potential solutions. Physics Letters A, Vol. 516. pp. 129633.

Cao, F., Jaunat, J., Sturchio, N., Cancès, B., Morvan, X., Devos, A., Barbin, V. and Ollivier, P. (2019). Worldwide occurrence and origin of perchlorate ion in waters: A review. Science of The Total Environment, Vol. 661. pp. 737–749.

Cao, W., Zheng, X. J., Sun, J. P., Wong, W. T., Fang, D. C., Zhang, J. X. and Jin, L. P. (2014). A highly selective chemosensor for Al(III) and Zn(II) and

its coordination with metal ions. Inorganic Chemistry, Vol. 53. No.6, pp. 3012–3021.

Caricato, M., Coluccini, C., Vander Griend, D. A., Forni, A. and Pasini, D. (2013). From red to blue shift: switching the binding affinity from the acceptor to the donor end by increasing the π-bridge in push–pull chromophores with coordinative ends. New Journal of Chemistry, Vol. 37. No. 9, pp. 2792–2799.

Caron, S., Dugger, R. W., Ruggeri, S. G., Ragan, J. A. and Brown Ripin, D. H. (2006). Large-scale oxidations in the pharmaceutical industry. Chemical Reviews, Vol. 106. No. 7, pp. 2943–2989.

Carreira-Barral, I., Rodríguez-Blas, T., Platas-Iglesias, C., de Blas, A. and Esteban-Gómez, D. (2014). Cooperative Anion Recognition in Copper(II) and Zinc(II) Complexes with a Ditopic Tripodal Ligand Containing a Urea Group. Inorganic Chemistry, Vol. 53. No. 5, pp. 2554–2568.

Castellano, F. N. (2015). Altering Molecular Photophysics by Merging Organic and Inorganic Chromophores. Accounts of Chemical Research, Vol. 48. No. 3, pp. 828–839.

Cerfontaine, S., Wehlin, S. A. M., Elias, B. and Troian-Gautier, L. (2020). Photostable Polynuclear Ruthenium(II) Photosensitizers Competent for Dehalogenation Photoredox Catalysis at 590 nm. Journal of the American Chemical Society, Vol. 142. No. 12, pp. 5549–5555.

Chan, J., Dodani, S. C. and Chang, C. J. (2012). Reaction-based small-molecule fluorescent probes for chemoselective bioimaging. Nature Chemistry, Vol. 4. No. 12, pp. 973–984.

Chang, B., Chen, J., Bao, J., Sun, T. and Cheng, Z. (2023). Molecularly Engineered Room-Temperature Phosphorescence for Biomedical Application: From the Visible toward Second Near-Infrared Window. Chemical Reviews, Vol. 123. No. 24, pp. 13966–14037.

Chang, K.-C., Sun, S.-S., Odago, M. O. and Lees, A. J. (2015). Anion recognition and sensing by transition-metal complexes with polarized NH recognition motifs. Coordination Chemistry Reviews, Vol. 284. pp. 111–123.

Chao, D. and Fu, W.-F. (2013). Facile synthesis of a ruthenium assembly and its application for light-driven oxidation of alcohols in water. Chemical Communications, Vol. 49. No. 37, pp. 3872–3874.

Chao, D. and Zhang, Y. (2017). A water–soluble cationic Ir(III) complex for turn–on sensing of ClO4− based on aggregation–induced emission. Sensors and Actuators, B: Chemical, Vol. 245. pp. 599–604.

Chao, D. and Zhao, M. (2017). Robust Cooperative Photo-oxidation of Sulfides without Sacrificial Reagent under Air Using a Dinuclear RuII–CuII Assembly. ChemSusChem, Vol. 10. No. 17, pp. 3358–3362.

Chauhan, A., Singh, S., Singh, A. K., Singh, A. K., Kumar, S., Yadav, R. K., Singh, A. P., Tripathi, U. N. and Kumar, M. (2025). Photocatalytic oxidation of various organic substrates using multinuclear Ru(II)-polypyridyl complexes. Coordination Chemistry Reviews, Vol. 525, pp. 216344.

Chen, C. and Fang, C. (2020). Devising Efficient Red-Shifting Strategies for Bioimaging: A Generalizable Donor-Acceptor Fluorophore Prototype. Chemistry – An Asian Journal, Vol. 15. No. 10, pp. 1514–1523.

Chen, M., Burn, P. L. and Shaw, P. E. (2023). Luminescence-based detection and identification of illicit drugs. Physical Chemistry Chemical Physics, Vol. 25. No. 19, pp. 13244–13259.

Chen, P., Wang, J., Xue, Y., Wang, C., Sun, W., Yu, J. and Guo, H. (2024). From challenge to opportunity: Revolutionizing the monitoring of emerging contaminants in water with advanced sensors. Water Research, Vol. 265. pp. 122297.

Chiou, Y. R., Chen, J. H., Hu, C. H. and Wu, A. T. (2020). A new fluorescence turn-on sensor for the distinct detection of Zn2+ and Al3+: Experimental and density functional theory study. Inorganica Chimica Acta, Vol. 502, pp. 119295.

Cho, P., Mattisson, T. and Lyngfelt, A. (2004). Comparison of iron-, nickel-, copper- and manganese-based oxygen carriers for chemical-looping combustion. Fuel, Vol. 83. No. 9, pp. 1215–1225.

Chopra, T., Sasan, S., Devi, L., Parkesh, R. and Kapoor, K. K. (2022). A

comprehensive review on recent advances in copper sensors. Coordination Chemistry Reviews, Vol. 470, pp. 214704.

Chua, M. H., Chin, K. L. O., Loh, X. J., Zhu, Q. and Xu, J. (2023). Aggregation-Induced Emission-Active Nanostructures: Beyond Biomedical Applications. ACS Nano, Vol. 17. No. 3, pp.1845–1878.

Chua, M. H., Hui, B. Y. K., Chin, K. L. O., Zhu, Q., Liu, X. and Xu, J. (2023). Recent advances in aggregation-induced emission (AIE)-based chemosensors for the detection of organic small molecules. Materials Chemistry Frontiers, Vol. 7. No. 22, pp. 5561–5660.

Collin, M. S., Venkatraman, S. K., Vijayakumar, N., Kanimozhi, V., Arbaaz, S. M., Stacey, R. G. S., Anusha, J., Choudhary, R., Lvov, V., Tovar, G. I., Senatov, F., Koppala, S. and Swamiappan, S. (2022). Bioaccumulation of lead (Pb) and its effects on human: A review. Journal of Hazardous Materials Advances, Vol. 7, pp. 100094.

Company, A., Sabenya, G., González-Béjar, M., Gómez, L., Clémancey, M., Blondin, G., Jasniewski, A. J., Puri, M., Browne, W. R., Latour, J. M., Que, L., Costas, M., Pérez-Prieto, J. and Lloret-Fillol, J. (2014). Triggering the generation of an iron(IV)-oxo compound and its reactivity toward sulfides by RuII photocatalysis. Journal of the American Chemical Society, Vol. 136. No. 12, pp. 4624–4633.

CrysAlis, P. R. O. (2009). Oxford Diffraction Ltd. Yarnton, England.

Cui, C., Shi, Y., Li, J. and Cheng, T. (2024). Photochemistry and photophysics of metal-metal bonded dinuclear transition metal complexes. Coordination Chemistry Reviews, Vol. 516, pp. 215984.

Czarnik, A. W. (1993). Fluorescent chemosensors for ion and molecule recognition. ACS Publications.

Czarnik, A. W. (1994). Chemical communication in water using fluorescent chemosensors. Accounts of Chemical Research, Vol. 27. No. 10, pp. 302–308.

Daly, B., Ling, J. and De Silva, A. P. (2015). Current developments in fluorescent PET (photoinduced electron transfer) sensors and switches. Chemical Society Reviews, Vol. 44. No. 13, pp. 4203–4211.

Das, A. K. and Goswami, S. (2017). 2-Hydroxy-1-naphthaldehyde: A versatile building block for the development of sensors in supramolecular chemistry and molecular recognition. Sensors and Actuators B: Chemical, Vol. 245. pp. 1062–1125.

Das, B., Dey, S., Maiti, G. P., Bhattacharjee, A., Dhara, A. and Jana, A. (2018). Hydrazinopyrimidine derived novel Al3+ chemosensor: Molecular logic gate and biological applications. New Journal of Chemistry, Vol. 42. No. 12, pp. 9424–9435.

de Castro, C. S., Cova, T. F. G. G., Pais, A. C. C., Pinheiro, D., Nuñez, C., Lodeiro, C. and Seixas de Melo, J. S. (2016). Probing metal cations with two new Schiff base bischromophoric pyrene based chemosensors: Synthesis, photophysics and interactions patterns. Dyes and Pigments, Vol. 134. pp. 601–612.

de Silva, A. P., Moody, T. S. and Wright, G. D. (2009). Fluorescent PET (Photoinduced Electron Transfer) sensors as potent analytical tools. Analyst, Vol. 134. No. 12, pp. 2385–2393.

Deng, W., Feng, W., Li, Y. and Bao, H. (2018). Merging Visible-Light Photocatalysis and Transition-Metal Catalysis in Three-Component Alkyl-Fluorination of Olefins with a Fluoride Ion. Organic Letters, Vol. 20. No. 14, pp. 4245–4249.

Desiraju, G. R. (1991). The C-H.cntdot..cntdot..cntdot.O hydrogen bond in crystals: what is it? Accounts of Chemical Research, Vol. 24. No. 10, pp. 290–296.

Desiraju, G. R. (2011). A bond by any other name. Angewandte Chemie - International Edition, Vol. 50. No. 1, pp. 52–59.

Dou, D., He, M., Liu, J., Xiao, S., Gao, F., An, W. and Qi, L. (2024). Occurrence, distribution characteristics and exposure assessment of perchlorate in the environment in China. Journal of Hazardous Materials, Vol. 474, pp. 134805.

Du, Y. and Dong, S. (2017). Nucleic Acid Biosensors: Recent Advances and Perspectives. Analytical Chemistry, Vol. 89. No. 1, pp. 189–215.

Ducrot, A. B., Coulson, B. A., Perutz, R. N. and Duhme-Klair, A.-K. (2016).

Light-Induced Activation of a Molybdenum Oxotransferase Model within a Ru(II)–Mo(VI) Dyad. Inorganic Chemistry, Vol. 55. No. 24, pp. 12583–12594.

Elgrishi, N., Chambers, M. B., Wang, X. and Fontecave, M. (2017). Molecular polypyridine-based metal complexes as catalysts for the reduction of CO2. Chemical Society Reviews, Vol. 46. No. 3, pp. 761–796.

Ener, M. E., Lee, Y.-T., Winkler, J. R., Gray, H. B. and Cheruzel, L. (2010). Photooxidation of cytochrome P450-BM3. Proceedings of the National Academy of Sciences, Vol. 107. No. 44, pp. 18783–18786.

EPA US. (2009). US EPA.

Evangelista, E., de Jesus, I. S., Pauli, F. P., de Souza, A. S., Borges, A. de A., Gomes, M. V. S. F., Ferreira, V. F., da Silva, F. de C., Melo, M. A. and Forezi, L. da S. M. (2025). Recent Advances in the Application of Coumarins as Photosensitizers for the Construction of a Dye-Sensitized Solar Cell. ACS Omega, Vol. 10. No. 14, pp. 13726–13748.

Fan, L., Qin, J. C., Li, T. R., Wang, B. D. and Yang, Z. Y. (2014). A novel rhodamine chromone-based “off-On” chemosensor for the differential detection of Al(III) and Zn(II) in aqueous solutions. Sensors and Actuators, B: Chemical, Vol. 203. pp. 550–556.

Fasman, G. D. (1996). Aluminum and Alzheimer’s disease: Model studies. Coordination Chemistry Reviews, Vol. 149. pp. 125–165.

Feng, G., Zhang, G.-Q. and Ding, D. (2020). Design of superior phototheranostic agents guided by Jablonski diagrams. Chemical Society Reviews, Vol. 49. No. 22, pp. 8179–8234.

Fillaut, J.-L. (2024). Ruthenium (II) polypyridyl complexes as two-photon absorbers and sensitizers: Design, structure-properties relationships and applications. Coordination Chemistry Reviews, Vol. 518. pp. 216050.

Frankowski, M., Zioła-Frankowska, A. and Siepak, J. (2010). New method for speciation analysis of aluminium fluoride complexes by HPLC-FAAS hyphenated technique. Talanta, Vol. 80. No. 5, pp. 2120–2126.

Fukuzumi, S., Kishi, T., Kotani, H., Lee, Y. M. and Nam, W. (2011). Highly efficient photocatalytic oxygenation reactions using water as an oxygen

source. Nature Chemistry, Vol. 3. No. 1, pp. 38–41.

Furdui, V. I., Zheng, J. and Furdui, A. (2018). Anthropogenic Perchlorate Increases since 1980 in the Canadian High Arctic. Environmental Science & Technology, Vol. 52. No. 3, pp. 972–981.

Gale, P. A. and Caltagirone, C. (2015). Anion sensing by small molecules and molecular ensembles. Chemical Society Reviews, Vol. 44. No. 13, pp. 4212–4227.

Gale, P. A. and Caltagirone, C. (2018). Fluorescent and colorimetric sensors for anionic species. Coordination Chemistry Reviews, Vol. 354. pp. 2–27.

Geng, H., Zhong, Q.-Z., Li, J., Lin, Z., Cui, J., Caruso, F. and Hao, J. (2022). Metal Ion-Directed Functional Metal–Phenolic Materials. Chemical Reviews, Vol. 122. No. 13, pp. 11432–11473.

Ghosh, I., Shaikh, R. S. and König, B. (2017). Sensitization-Initiated Electron Transfer for Photoredox Catalysis. Angewandte Chemie International Edition, Vol. 56. No. 29, pp. 8544–8549.

Gong, S., Zhang, Y., Qin, A., Li, M., Gao, Y., Zhang, C., ... & Wang, S. (2022). A novel AIE-active camphor-based fluorescent probe for simultaneous detection of Al 3+ and Zn2+ at dual channels in living cells and zebrafish. Analyst, Vol. 147, No. 1, pp. 87-100.

Goshisht, M. K., Patra, G. K. and Tripathi, N. (2022). Fluorescent Schiff base sensors as a versatile tool for metal ion detection: strategies, mechanistic insights, and applications. Materials Advances, Vol. 3, No. 6, pp. 2612–2669.

Goshisht, M. K. and Tripathi, N. (2021). Fluorescence-based sensors as an emerging tool for anion detection: mechanism, sensory materials and applications. Journal of Materials Chemistry C, Vol. 9. No. 31, pp. 9820–9850.

Goswami, N., Naithani, S., Goswami, T., Kumar, P. and Kumar, S. (2024). A quinoline derived Schiff base as highly selective ‘turn-on’ probe for fluorogenic recognition of Al3+ ion. Spectrochimica Acta - Part A: Molecular and Biomolecular Spectroscopy, Vol. 310. pp. 123971

Goswami, N., Naithani, S., Mangalam, J., Goswami, T., Dubey, R., Kumar, P.,

Kumar, P. and Kumar, S. (2023). Fluorescent and chromogenic organic probes to detect group 10 metal ions: design strategies and sensing applications. Dalton Transactions, Vol. 52. No. 41, pp. 14704–14732.

Goswami, S., Manna, A., Paul, S., Das, A. K., Aich, K. and Nandi, P. K. (2013). Resonance-assisted hydrogen bonding induced nucleophilic addition to hamper ESIPT: Ratiometric detection of cyanide in aqueous media. Chemical Communications, Vol. 49. No. 28, pp. 2912–2914.

Gotico, P., Tran, T. T., Baron, A., Vauzeilles, B., Lefumeux, C., Ha-Thi, M. H., Pino, T., Halime, Z., Quaranta, A., Leibl, W. and Aukauloo, A. (2021). Tracking Charge Accumulation in a Functional Triazole-Linked Ruthenium-Rhenium Dyad Towards Photocatalytic Carbon Dioxide Reduction. ChemPhotoChem, Vol. 5. No. 7, pp. 654–664.

Goyal, R., Singh, O., Agrawal, A., Samanta, C. and Sarkar, B. (2022). Advantages and limitations of catalytic oxidation with hydrogen peroxide: from bulk chemicals to lab scale process. Catalysis Reviews, Vol. 64. No. 2, pp. 229–285.

Grabowski, S. J. (2011). What Is the Covalency of Hydrogen Bonding? Chemical Reviews, Vol. 111. No. 4, pp. 2597–2625.

Graham, J. and Traylor, J. (2022). Cyanide Toxicity. StatPearls Publishing, Treasure Island (FL). http://europepmc.org/abstract/MED/29939573

Gui, S., Huang, Y., Hu, F., Jin, Y., Zhang, G., Yan, L., Zhang, D. and Zhao, R. (2015). Fluorescence turn-on chemosensor for highly selective and sensitive detection and bioimaging of al3+ in living cells based on ion-induced aggregation. Analytical Chemistry, Vol. 87. No. 3, pp. 1470–1474.

Guo, C., Sedgwick, A. C., Hirao, T. and Sessler, J. L. (2021). Supramolecular fluorescent sensors: An historical overview and update. Coordination Chemistry Reviews, Vol. 427. pp. 213560.

Guo, Z., Hu, T., Sun, T., Li, T., Chi, H. and Niu, Q. (2019). A colorimetric and fluorometric oligothiophene-indenedione-based sensor for rapid and highly sensitive detection of cyanide in real samples and bioimaging in living cells. Dyes and Pigments, Vol. 163. pp. 667–674.

Haga, M. and Tanaka, T. (1979). Synthesis and properties of mixed-ligand ruthenium (II) complexes containing 2-(2-pyridyl)-benzimidazole and related ligands. Chemistry Letters, Vol. 8. No. 7, pp. 863–864.

Hagfeldt, A., Boschloo, G., Sun, L., Kloo, L. and Pettersson, H. (2010). Dye-Sensitized Solar Cells. Chemical Reviews, Vol. 110. No. 11, pp. 6595–6663.

Han, L.-J., Kong, Y.-J., Xu, Y.-Y. and Huang, M.-M. (2021). A Zn-based coordination compound for fluorescence detection of Fe3+, Cu2+, Ni2+ and CrO42− ions. Polyhedron, Vol. 193. pp. 114868.

Han, T., Feng, X., Tong, B., Shi, J., Chen, L., Zhi, J. and Dong, Y. (2012). A novel “turn-on” fluorescent chemosensor for the selective detection of Al3+ based on aggregation-induced emission. Chemical Communications, Vol. 48. No. 3, pp. 416–418.

Hatsis, P. and Lucy, C. A. (2002). Ultra-fast HPLC separation of common anions using a monolithic stationary phase. Analyst, Vol. 127. No. 4, pp. 451–454.

Hatzistavros, V. S. and Kallithrakas-Kontos, N. G. (2011). Determination of Trace Perchlorate Concentrations by Anion-Selective Membranes and Total Reflection X-ray Fluorescence Analysis. Analytical Chemistry, Vol. 83. No. 9, pp. 3386–3391.

Hazra, A., Roy, A., Mukherjee, A., Maiti, G. P. and Roy, P. (2018). Remarkable difference in Al3+ and Zn2+ sensing properties of quinoline based isomers. Dalton Transactions, Vol. 47. No. 39, pp. 13972–13989.

He, H., Li, Y. and He, L. F. (2019). Aluminum toxicity and tolerance in Solanaceae plants. South African Journal of Botany, Vol. 123. No. 1, pp. 23–29.

Hein, R. and Beer, P. D. (2022). Halogen bonding and chalcogen bonding mediated sensing. Chemical Science, Vol. 13. No. 24, pp. 7098–7125.

Hein, R., Beer, P. D. and Davis, J. J. (2020a). Electrochemical Anion Sensing: Supramolecular Approaches [Review-article]. Chemical Reviews, Vol. 120. No. 3, pp. 1888–1935.

Hein, R., Beer, P. D. and Davis, J. J. (2020b). Electrochemical Anion Sensing:

Supramolecular Approaches. Chemical Reviews, Vol. 120. No. 3, pp. 1888–1935.

Herrero, C., Quaranta, A., Sircoglou, M., Sénéchal-David, K., Baron, A., Marín, I. M., Buron, C., Baltaze, J. P., Leibl, W., Aukauloo, A. and Banse, F. (2015). Successive light-induced two electron transfers in a Ru-Fe supramolecular assembly: From Ru-Fe(ii)-OH2 to Ru-Fe(iv)-oxo. Chemical Science, Vol. 6. No. 4, pp. 2323–2327.

Hishimone, P. N., Hamukwaya, E. and Uahengo, V. (2021). The C2-Symmetry Colorimetric Dye Based on a Thiosemicarbazone Derivative and its Cadmium Complex for Detecting Heavy Metal Cations (Ni2+, Co2+, Cd2+, and Cu2+) Collectively, in DMF. Journal of Fluorescence, Vol. 31. No. 4, pp. 999–1008.

Ho, T.-L. (1975). Hard soft acids bases (HSAB) principle and organic chemistry. Chemical Reviews, Vol. 75. No. 1, pp. 1–20.

Hojjati-Najafabadi, A., Mansoorianfar, M., Liang, T., Shahin, K. and Karimi-Maleh, H. (2022). A review on magnetic sensors for monitoring of hazardous pollutants in water resources. Science of The Total Environment, Vol. 824. pp. 153844.

Hu, Y., Liu, Y., Kim, G., Jun, E. J., Swamy, K. M. K., Kim, Y., Kim, S.-J. and Yoon, J. (2015). Pyrene based fluorescent probes for detecting endogenous zinc ions in live cells. Dyes and Pigments, Vol. 113. pp. 372–377.

Iali, W., Lanoe, P., Torelli, S., Jouvenot, D., Loiseau, F., Lebrun, C., Hamelin, O. and Ménage, S. (2015). A Ruthenium(II)–Copper(II) Dyad for the Photocatalytic Oxygenation of Organic Substrates Mediated by Dioxygen Activation. Angewandte Chemie, Vol. 127. No. 29, pp. 8535–8539.

Iwamura, M., Takeuchi, S. and Tahara, T. (2007). Real-Time Observation of the Photoinduced Structural Change of Bis(2,9-dimethyl-1,10-phenanthroline)copper(I) by Femtosecond Fluorescence Spectroscopy: A Realistic Potential Curve of the Jahn−Teller Distortion. Journal of the American Chemical Society, Vol. 129. No. 16, pp. 5248–5256.

Jalal, A. H., Alam, F., Roychoudhury, S., Umasankar, Y., Pala, N. and Bhansali, S. (2018). Prospects and Challenges of Volatile Organic Compound

Sensors in Human Healthcare. ACS Sensors, Vol. 3. No. 7, pp. 1246–1263.

Jameson, D. M. (2025). Introduction to fluorescence. CRC press.

Jana, S., Dalapati, S., Alam, M. A. and Guchhait, N. (2012). Spectroscopic, colorimetric and theoretical investigation of Salicylidene hydrazine based reduced Schiff base and its application towards biologically important anions. Spectrochimica Acta - Part A: Molecular and Biomolecular Spectroscopy, Vol. 92. pp. 131–136.

Jiang, G., Liu, H., Liu, H., Ke, G., Ren, T., Xiong, B., Zhang, X. and Yuan, L. (2024). Chemical approaches to optimize the properties of organic fluorophores for imaging and sensing. Angewandte Chemie, Vol. 136. No. 11, pp. e202315217.

Jo, J., Olasz, A., Chen, C. H. and Lee, D. (2013). Interdigitated hydrogen bonds: Electrophile activation for covalent capture and fluorescence turn-on detection of cyanide. Journal of the American Chemical Society, Vol. 135 No. 9, pp. 3620–3632.

Junaid, H. M., Batool, M., Harun, F. W., Akhter, M. S. and Shabbir, N. (2022). Naked Eye Chemosensing of Anions by Schiff Bases. Critical Reviews in Analytical Chemistry, Vol. 52. No. 3, pp. 463–480.

Kalita, D., Radaram, B., Brooks, B., Kannam, P. P. and Zhao, X. (2011). Photocatalytic oxidation of hydrocarbons in water by ruthenium complexes. ChemCatChem, Vol. 3. No. 3, pp. 571–573.

Kang, J. H., Lee, S. Y., Ahn, H. M. and Kim, C. (2017). A novel colorimetric chemosensor for the sequential detection of Ni2+ and CN− in aqueous solution. Sensors and Actuators B: Chemical, Vol. 242. pp. 25–34.

Kang, L., Liu, Y.-T., Li, N.-N., Dang, Q.-X., Xing, Z.-Y., Li, J.-L. and Zhang, Y. (2017). A schiff-base receptor based naphthalimide derivative: Highly selective and colorimetric fluorescent turn-on sensor for Al3+. Journal of Luminescence, Vol. 186. pp. 48–52.

Kang, N., Jackson, W. A., Dasgupta, P. K. and Anderson, T. A. (2008). Perchlorate production by ozone oxidation of chloride in aqueous and dry systems. Science of The Total Environment, Vol. 405. No. 1, pp. 301–309.

Kärkäs, M. D., Verho, O., Johnston, E. V. and Åkermark, B. (2014). Artificial photosynthesis: Molecular systems for catalytic water oxidation. Chemical Reviews, Vol. 114. No. 24, pp. 11863–12001.

Karmakar, S., Mardanya, S., Maity, D. and Baitalik, S. (2016). Polypyridyl-imidazole based Os(II) complex as optical chemosensor for anions and cations and multi-readout molecular logic gates and memory device: Experimental and DFT/TDDFT study. Sensors and Actuators, B: Chemical, Vol. 226. pp. 388–402.

Karuppiah, K., Muniyasamy, H., Nelson, M., Selvaraj, M., Sepperumal, M. and Ayyanar, S. (2022). A novel indolehydrazone appended salicyaldehyde platform for detection of multianalytes (Al3+, Zn2+ and F- ions): Live cell imaging. Inorganic Chemistry Communications, Vol. 135. pp. 109080.

Kashyap, S., Singh, R. and Singh, U. P. (2020). Inorganic and organic anion sensing by azole family members. Coordination Chemistry Reviews, Vol. 417. pp. 213369.

Kaur, A., Kaur, P. and Ahuja, S. (2020). Förster resonance energy transfer (FRET) and applications thereof. Analytical Methods, Vol. 12. No. 46, pp. 5532–5550.

Kaur, P. and Singh, K. (2023). Analyte Detection: A Decade of Progress in the Development of Optical/Fluorescent Sensing Probes. The Chemical Record, Vol. 23. No.1, pp. e202200184.

Kaushik, R., Ghosh, A., Singh, A., Gupta, P., Mittal, A. and Jose, D. A. (2016). Selective Detection of Cyanide in Water and Biological Samples by an Off-the-Shelf Compound. ACS Sensors, Vol. 1. No. 10, pp. 1265–1271

Khanmohammadi, H. and Rezaeian, K. (2014). A catalyst-free approach to a novel imidazo [4,5-f][1,10] phenanthroline ligand and its corresponding ruthenium(ii) complex: Insights into their applications in colorimetric anion sensing. New Journal of Chemistry, Vol. 38. No. 11, pp. 5536–5543.

Khatua, S., Samanta, D., Bats, J. W. and Schmittel, M. (2012). Rapid and highly sensitive dual-channel detection of cyanide by bis-heteroleptic ruthenium(II) complexes. Inorganic Chemistry, Vol. 51. No. 13, pp. 7075–7086.

Kim, D., Dang, V. Q. and Teets, T. S. (2024). Improved transition metal photosensitizers to drive advances in photocatalysis. Chemical Science, Vol. 15. No. 1, pp. 77–94.

Kim, Y. S., Park, G. J., Lee, J. J., Lee, S. Y., Lee, S. Y. and Kim, C. (2015). Multiple target chemosensor: a fluorescent sensor for Zn(ii) and Al(iii) and a chromogenic sensor for Fe(ii) and Fe(iii). RSC Advances, Vol. 5. No. 15, pp. 11229–11239.

Kindermann, B., Döring, F., Budczies, J. and Daniel, H. (2005). Zinc-sensitive genes as potential new target genes of the metal transcription factor-1 (MTF-1). Biochemistry and Cell Biology, Vol. 83. No.2, pp 221–229.

Kırpık, H., Kose, M. and Ballı, J. N. (2020). Tridentate benzimidazole ligand and its metal complexes: Synthesis, characterization, photo physical and sensor properties. Applied Organometallic Chemistry, Vol. 34. No. 12, pp. 1–11.

Klein, J., Girardon, A., Moreno-Betancourt, A., Loiseau, F., Jouvenot, D., Pécaut, J., Hamelin, O. and Torelli, S. (2023). Covalent Association of a Ruthenium-Based Chromophore and a Copper Catalyst: A Synergy for Sulfides Photo-oxidation. European Journal of Inorganic Chemistry, Vol. 26. No. 36, pp. e202300397.

Klinman, J. P. (2006). The copper-enzyme family of dopamine β-monooxygenase and peptidylglycine α-hydroxylating monooxygenase: Resolving the chemical pathway for substrate hydroxylation. Journal of Biological Chemistry, Vol. 281, No. 6, pp. 3013–3016.

Knör, G. and Monkowius, U. (2011). Photosensitization and photocatalysis in bioinorganic, bio-organometallic and biomimetic systems. Advances in Inorganic chemistry, Vol. 63. pp. 235–289.

Kolanowski, J. L., Liu, F. and New, E. J. (2018). Fluorescent probes for the simultaneous detection of multiple analytes in biology. Chemical Society Reviews, Vol. 47. No. 1, pp. 195–208.

Kounaves, S. P., Stroble, S. T., Anderson, R. M., Moore, Q., Catling, D. C., Douglas, S., McKay, C. P., Ming, D. W., Smith, P. H., Tamppari, L. K. and Zent, A. P. (2010). Discovery of Natural Perchlorate in the Antarctic

Dry Valleys and Its Global Implications. Environmental Science & Technology, Vol. 44. No. 7, pp. 2360–2364.

Krämer, J., Kang, R., Grimm, L. M., De Cola, L., Picchetti, P. and Biedermann, F. (2022). Molecular Probes, Chemosensors, and Nanosensors for Optical Detection of Biorelevant Molecules and Ions in Aqueous Media and Biofluids. Chemical Reviews, Vol. 122. No. 3, pp. 3459–3636.

Krewski, D., Yokel, R. A., Nieboer, E., Borchelt, D., Cohen, J., Harry, J., Kacew, S., Lindsay, J., Mahfouz, A. M. and Rondeau, V. (2007). Human health risk assessment for aluminium, aluminium oxide, and aluminium hydroxide. Journal of Toxicology and Environmental Health - Part B: Critical Reviews, Vol. 10. pp. 1-169.

Krishna Deepak, R. N. V. and Sankararamakrishnan, R. (2016). N-H···N Hydrogen Bonds Involving Histidine Imidazole Nitrogen Atoms: A New Structural Role for Histidine Residues in Proteins. Biochemistry, Vol. 55. No. 27, pp. 3774–3783.

Kubik, S. (2010). Anion recognition in water. Chemical Society Reviews, Vol. 39. No. 10, pp. 3648–3663.

Kucharzyk, K. H., Crawford, R. L., Cosens, B. and Hess, T. F. (2009). Development of drinking water standards for perchlorate in the United States. Journal of Environmental Management, Vol. 91. No. 2, pp. 303–310.

Kumar, A., Chhatwal, M., Singh, A. K., Singh, V. and Trivedi, M. (2014). A fast and selective probe for monitoring Pd2+ in aqueous medium via the dual-optical readout. Chemical Communications, Vol. 50. No. 62, pp. 8488–8490.

Kumar, M. (2020). Runoff from firework manufacturing as major perchlorate source in the surface waters around Diwali in Ahmedabad, India. Journal of Environmental Management, Vol. 273. pp. 111091.

Kumar, P., Kumar, V. and Gupta, R. (2017). Selective fluorescent turn-off sensing of Pd2+ ion: applications as paper strips, polystyrene films, and in cell imaging. RSC Advances, Vol. 7. No. 13, pp. 7734–7741.

Kumar, R., Kumar, S., Singh, P., Hundal, G., Hundal, M. S. and Kumar, S.

(2012). A fluorescent chemosensor for detection of perchlorate ions in water. Analyst, Vol. 137. No. 21, pp. 4913–4916.

Kumar, R., Sandhu, S., Singh, P. and Kumar, S. (2016). Water dispersed fluorescent organic aggregates for the picomolar detection of ClO4- in water, soil and blood serum and the attogram detection of ClO4- in the solid state by a contact mode method. Journal of Materials Chemistry C, Vol. 4. No. 31, pp. 7420–7429.

Kumar, R., Singh, B., Gahlyan, P., Kumar, R. and Pani, B. (2023). Recent developments on the colorimetric and fluorometric detection of 3d block metal ions using Schiff base probes. Journal of Molecular Structure, Vol. 1289. pp. 135859.

Kumar, S., Singh, S., Kumar, A. and Kumar, P. (2021). Recognition, mechanistic investigation and applications for the detection of biorelevant Cu2+/Fe2+/Fe3+ions by ruthenium(ii)-polypyridyl based fluorescent sensors. Dalton Transactions, Vol. 50. No. 8, pp. 2705–2721.

Kumar, S., Singh, S., Kumar, A., Murthy, K. S. R. and Singh, A. K. (2022). pH-Responsive luminescence sensing, photoredox catalysis and photodynamic applications of ruthenium (II) photosensitizers bearing imidazo [4, 5-f][1, 10] phenanthroline scaffolds. Coordination Chemistry Reviews, Vol. 452. pp. 214272.

Kumar, V., Kaushik, M. P., Srivastava, A. K., Pratap, A., Thiruvenkatam, V. and Row, T. N. G. (2010). Thiourea based novel chromogenic sensor for selective detection of fluoride and cyanide anions in organic and aqueous media. Analytica Chimica Acta, Vol. 663. No. 1, pp. 77–84.

Kumar, V., Kumar, P. and Gupta, R. (2017). Fluorescent detection of multiple ions by two related chemosensors: structural elucidations and logic gate applications. RSC Advances, Vol. 7. No. 37, pp. 23127–23135.

Kumarathilaka, P., Oze, C., Indraratne, S. P. and Vithanage, M. (2016). Perchlorate as an emerging contaminant in soil, water and food. Chemosphere, Vol. 150. pp. 667–677.

Kunishita, A., Ertem, M. Z., Okubo, Y., Tano, T., Sugimoto, H., Ohkubo, K., Fujieda, N., Fukuzumi, S., Cramer, C. J. and Itoh, S. (2012). Active site

models for the CuA site of peptidylglycine α-hydroxylating monooxygenase and dopamine β-monooxygenase. Inorganic Chemistry, Vol. 51. No. 17, pp. 9465–9480.

Kwon, N., Hong, J., Kim, G., Jun, E. J. and Yoon, J. (2020). Control strategy of displacement processes to sense biothiols via fluorescent changes. Dyes and Pigments, Vol. 173. pp. 107871.

Lan, M., Zhao, S., Liu, W., Lee, C.-S., Zhang, W. and Wang, P. (2019). Photosensitizers for Photodynamic Therapy. Advanced Healthcare Materials, Vol. 8. No. 13, pp. 1900132.

Lang, X., Zhao, J. and Chen, X. (2016). Cooperative photoredox catalysis. Chemical Society Reviews, Vol. 45. No. 11, pp. 3026–3038.

Lechner, V. M., Nappi, M., Deneny, P. J., Folliet, S., Chu, J. C. K. and Gaunt, M. J. (2022). Visible-Light-Mediated Modification and Manipulation of Biomacromolecules. Chemical Reviews, Vol. 122. No. 2, pp. 1752–1829.

Lee, L. C.-C. and Lo, K. K.-W. (2022). Strategic Design of Luminescent Rhenium(I), Ruthenium(II), and Iridium(III) Complexes as Activity-Based Probes for Bioimaging and Biosensing. Chemistry – An Asian Journal, Vol. 17. No. 22, pp. e202200840.

Lee, M. H., Kim, J. S. and Sessler, J. L. (2015). Small molecule-based ratiometric fluorescence probes for cations, anions, and biomolecules. Chemical Society Reviews, Vol. 44. No. 13, pp. 4185–4191.

Lee, S. Y., Yang, M. and Kim, C. (2018). A dual target chemosensor for the fluorometric detection of In3+ and colorimetric detection of Fe3+. Spectrochimica Acta Part A: Molecular and Biomolecular Spectroscopy, Vol. 205. pp. 622–629.

Lee, Y. J., Lim, C., Suh, H., Song, E. J. and Kim, C. (2014). A multifunctional sensor: Chromogenic sensing for Mn2+ and fluorescent sensing for Zn2+ and Al3+. Sensors and Actuators, B: Chemical, Vol. 201. pp. 535–544.

Lewandowski, T. A., Peterson, M. K. and Charnley, G. (2015). Iodine supplementation and drinking-water perchlorate mitigation. Food and Chemical Toxicology, Vol. 80. pp. 261–270.

Li, J., Xu, B.-S., Xinglong-Zhang, Zhao, L.-L., Yi, S.-Z. and Li, B.-N. (2025).

Recent Advances in Smart Sensing Based on Excited-State Intramolecular Proton-Transfer (ESIPT)-Inspired Emitters. Asian Journal of Organic Chemistry, Vol. 14. No. 2, pp. e202400572.

Li, L., Wang, J., Xu, S., Li, C. and Dong, B. (2022). Recent progress in fluorescent probes for metal ion detection. Frontiers in Chemistry, 10, 875241. p.

Li, M. J., Lin, Z., Chen, X. and Chen, G. (2014). Colorimetric and luminescent bifunctional Ru(ii) complexes for rapid and highly sensitive recognition of cyanide. Dalton Transactions, Vol. 43. No. 30, pp. 11745–11751.

Li, R.-Y., Wei, Z.-L., Wang, L., Zhang, Y. and Ru, J.-X. (2021). A new salamo-based fluorescence probe to visually detect aluminum(III) ion and bio-imaging in zebrafish. Microchemical Journal, Vol. 162. pp. 105720.

Li, Y.-L., Li, A.-J., Huang, S.-L., Vittal, J. J. and Yang, G.-Y. (2023). Polypyridyl Ru(ii) or cyclometalated Ir(iii) functionalized architectures for photocatalysis. Chemical Society Reviews, Vol. 52. No. 14, pp. 4725–4754.

Li, Y. and Zamble, D. B. (2009). Nickel homeostasis and nickel regulation: An overview. Chemical Reviews, Vol. 109. No. 10, pp. 4617–4643.

Li, Z., Dai, Y., Lu, Z., Pei, Y., Song, Y., Zhang, L. and Guo, H. (2019). A Photoswitchable Triple Chemosensor for Cyanide Anion Based on Dicyanovinyl-Functionalized Dithienylethene. European Journal of Organic Chemistry, Vol. 2019. No. 22, pp. 3614–3621.

Li, Z., Hou, J. T., Wang, S., Zhu, L., He, X. and Shen, J. (2022). Recent advances of luminescent sensors for iron and copper: Platforms, mechanisms, and bio-applications. Coordination Chemistry Reviews, Vol. 469. pp. 214695.

Li, Z., Hou, S., Zhang, H., Song, Q., Wang, S. and Guo, H. (2023). Recent advances in fluorescent and colorimetric sensing for volatile organic amines and biogenic amines in food. Advanced Agrochem, Vol. 2. No. 1, pp. 79–87.

Li, Z., Wang, J., Xiao, L., Wang, J. and Yan, H. (2021). A dual-response fluorescent probe for Al3+ and Zn2+ in aqueous medium based on

benzothiazole and its application in living cells. Inorganica Chimica Acta, Vol. 516. pp. 120147.

Li, Z., Zeng, X., Gao, C., Song, J., He, F., He, T., Guo, H. and Yin, J. (2023). Photoswitchable diarylethenes: From molecular structures to biological applications. Coordination Chemistry Reviews, Vol. 497. pp. 215451.

Liao, Z.-C., Yang, Z.-Y., Li, Y., Wang, B.-D. and Zhou, Q.-X. (2013). A simple structure fluorescent chemosensor for high selectivity and sensitivity of aluminum ions. Dyes and Pigments, Vol. 97. No. 1, pp. 124–128.

Lin, W., Li, J., Feng, H., Qi, F. and Huang, L. (2023). Recent Advances in Triplet–Triplet Annihilation Upconversion for Bioimaging and Biosensing. Journal of Analysis and Testing, Vol. 7. No. 4, pp. 327–344.

Liu, B., Zhuang, J. and Wei, G. (2020). Recent advances in the design of colorimetric sensors for environmental monitoring. Environmental Science: Nano, Vol. 7. No. 8, pp. 2195–2213.

Liu, G., Zong, G., Dhana, K., Hu, Y., Blount, B. C., Morel-Espinosa, M. and Sun, Q. (2017). Exposure to perchlorate, nitrate and thiocyanate, and prevalence of diabetes mellitus. International Journal of Epidemiology, Vol. 46. No.6, pp. 1913–1923.

Liu, H., Jiang, G., Ke, G., Ren, T.-B. and Yuan, L. (2024). Organic Fluorophores with Large Stokes Shift for Bioimaging and Biosensing. ChemPhotoChem, Vol. 8. No. 5, pp. e202300277.

Liu, H., Liu, T., Li, J., Zhang, Y., Li, J., Song, J., Qu, J. and Wong, W. Y. (2018). A simple Schiff base as dual-responsive fluorescent sensor for bioimaging recognition of Zn2+ and Al3+ in living cells. Journal of Materials Chemistry B, Vol. 6. No. 34, pp. 5435–5442.

Liu, J., Wang, X., Wang, J., Leung, C.-H. and Wang, W. (2023). Imaging mitochondrial palladium species in living cells with a NIR iridium(III) complex. Spectrochimica Acta Part A: Molecular and Biomolecular Spectroscopy, Vol. 288. pp.122188.

Liu, P., Li, W., Guo, S., Xu, D., Wang, M., Shi, J., Cai, Z., Tong, B. and Dong, Y. (2018). Application of a Novel “turn-on” Fluorescent Material to the Detection of Aluminum Ion in Blood Serum. ACS Applied Materials and

Interfaces, Vol. 10. No. 28, pp. 23667–23673.

Liu, Q. and Wu, L.-Z. (2017). Recent advances in visible-light-driven organic reactions. National Science Review, Vol. 4. No. 3, pp. 359–380.

Liu, Y., Wu, M., Zhao, J., Wang, Y., & Zhang, Y. (2022). A simple salicylaldehyde-bearing pyrazine as a turn-on fluorescent chemosensor for Al3+ and Zn2+ recognition and its applications. Rev. Anal. Chem., Vol. 41. No. 1, pp. 217-227.

Livingstone, C. (2015). Zinc: Physiology, deficiency, and parenteral nutrition. Nutrition in Clinical Practice, Vol. 30. No. 3, pp. 371–382.

LoPachin, R. M., Gavin, T., DeCaprio, A. and Barber, D. S. (2012). Application of the Hard and Soft, Acids and Bases (HSAB) Theory to Toxicant–Target Interactions. Chemical Research in Toxicology, Vol. 25. No. 2, pp. 239–251.

Lovell, J. F., Liu, T. W. B., Chen, J. and Zheng, G. (2010). Activatable photosensitizers for imaging and therapy. Chemical Reviews, Vol. 110. No. 5, pp. 2839–2857.

Lu, X., Wu, M., Wang, S., Qin, J. and Li, P. (2022). An AIE/PET-based fluorescent probe for Zn2+/Al3+ detection and its application in fluorescence-assisted diagnosis for prostate cancer. Dyes and Pigments, Vol. 203, pp. 110372.

Lv, J., Xie, J., Mohamed, A. G. A., Zhang, X., Feng, Y., Jiao, L., Zhou, E., Yuan, D. and Wang, Y. (2023). Solar utilization beyond photosynthesis. Nature Reviews Chemistry, Vol. 7. No. 2, pp. 91–105.

Ma, D. L., He, H. Z., Zhong, H. J., Lin, S., Chan, D. S. H., Wang, L., Lee, S. M. Y., Leung, C. H. and Wong, C. Y. (2014). Visualization of Zn2+ ions in live zebrafish using a luminescent iridium(III) chemosensor. ACS Applied Materials and Interfaces, Vol. 6. No. 16, pp. 14008–14015.

Ma, J. and Dasgupta, P. K. (2010). Recent developments in cyanide detection: A review. Analytica Chimica Acta, Vol. 673. No. 2, pp. 117–125.

MacPherson, I. S. and Murphy, M. E. P. (2007). Type-2 copper-containing enzymes. In Cellular and Molecular Life Sciences, Vol. 64, No. 22, pp. 2887–2899.

Maity, D., Vyas, G., Bhatt, M. and Paul, P. (2015). Detection of NaCN in aqueous media using a calixarene-based fluoroionophore containing ruthenium(ii)-bipyridine as the fluorogenic unit. RSC Advances, Vol. 5. No. 8, 6151–6159.

Malahom, N., Jarujamrus, P., Anutrasakda, W., Siripinyanond, A., Amatatongchai, M., Citterio, D. and Nacapricha, D. (2022). Ag3PO4/Ag nanocomposite for selective and sensitive cyanide determination in food samples through catalytical colorimetry using a paper-based test kit. Sensors and Actuators B: Chemical, Vol. 356. pp. 103351.

Malahom, N., Ma-In, T., Naksen, P., Anutrasakda, W., Amatatongchai, M., Citterio, D. and Jarujamrus, P. (2023). Nitrogen-Doped Graphene Quantum Dots as "Off-On" Fluorescent Probes in Paper-Based Test Kits for Selective Monitoring of Cyanide in Food. ACS Applied Nano Materials, Vol. 6. No. 13, pp. 11144–11153.

Mandal, T. N., Karmakar, A., Sharma, S. and Ghosh, S. K. (2018). Metal-Organic Frameworks (MOFs) as Functional Supramolecular Architectures for Anion Recognition and Sensing. Chemical Record, Vol. 18. No. 2, pp. 154–164.

Manna, A. S., Ghosh, S., Ghosh, T., Karchaudhuri, N., Das, S., Roy, A. and Maiti, D. K. (2025). Smart Luminescent Materials for Emerging Sensors: Fundamentals and Advances. Chemistry – An Asian Journal, Vol. 20. No. 6, pp. e202401328.

Manna, U., Das, G. and Hossain, M. A. (2022). Insights into the binding aspects of fluoride with neutral synthetic receptors. Coordination Chemistry Reviews, Vol. 455. pp. 214357.

Manoj, K. M., Ramasamy, S., Parashar, A., Gideon, D. A., Soman, V., Jacob, V. D. and Pakshirajan, K. (2020). Acute toxicity of cyanide in aerobic respiration: Theoretical and experimental support for murburn explanation. Biomolecular Concepts, Vol. 11. No. 1, pp. 32–56.

Mao, L., Liu, L., Yan, N., Li, F., Tao, H., Ye, H. and Wen, H. (2020). Factors controlling the accumulation and ecological risk of trace metal(loid)s in river sediments in agricultural field. Chemosphere, Vol. 243. pp. 125359.

Mao, S., Chang, J., Zhou, G. and Chen, J. (2015). Nanomaterial-enabled Rapid Detection of Water Contaminants. Small, Vol. 11. No. 40, pp. 5336–5359.

Marcus, Y. (1991). Thermodynamics of solvation of ions. Part 5.—Gibbs free energy of hydration at 298.15 K. Journal of the Chemical Society, Faraday Transactions, Vol. 87. No. 18, pp. 2995–2999.

Mardanya, S., Karmakar, S., Bar, M. and Baitalik, S. (2015). Pyrene-bIImidazole based Ru(II) and Os(II) complexes as highly efficient probes for the visible and near-infrared detection of cyanide in aqueous media. Dalton Transactions, Vol. 44. No. 48, pp. 21053–21072.

Mariotti, N., Bonomo, M., Fagiolari, L., Barbero, N., Gerbaldi, C., Bella, F. and Barolo, C. (2020). Recent advances in eco-friendly and cost-effective materials towards sustainable dye-sensitized solar cells. Green Chemistry, Vol. 22. No. 21, pp. 7168–7218.

Marzo, L., Pagire, S. K., Reiser, O. and König, B. (2018). Visible-Light Photocatalysis: Does It Make a Difference in Organic Synthesis? Angewandte Chemie - International Edition, Vol. 57. No. 32, pp. 10034–10072.

Mezzaroba, L., Alfieri, D. F., Colado Simão, A. N. and Vissoci Reiche, E. M. (2019). The role of zinc, copper, manganese and iron in neurodegenerative diseases. NeuroToxicology, Vol. 74. pp. 230–241.

Mo, H.-J., Shen, Y. and Ye, B.-H. (2012). Selective, Recognition of Cyanide Anion via Formation of Multipoint NH and Phenyl CH Hydrogen Bonding with Acyclic Ruthenium Bipyridine Imidazole Receptors in Water. Inorganic Chemistry, Vol. 51. No. 13, pp. 7174–7184.

Mohanty, P., Behura, R., Bhardwaj, V., Dash, P. P., Sahoo, S. K. and Jali, B. R. (2022). Recent advancement on chromo-fluorogenic sensing of aluminum(III) with Schiff bases. Trends in Environmental Analytical Chemistry, Vol. 34. pp. e00166.

Molina, P., Tárraga, A. and Otón, F. (2012). Imidazole derivatives: A comprehensive survey of their recognition properties. Organic & Biomolecular Chemistry, Vol. 10. No. 9, pp. 1711–1724.

Morimoto, T. and Ishitani, O. (2017). Modulation of the Photophysical,

Photochemical, and Electrochemical Properties of Re(I) Diimine Complexes by Interligand Interactions. Accounts of Chemical Research, Vol. 50. No. 11, pp. 2673–2683.

Moschona, F., Savvopoulou, I., Tsitopoulou, M., Tataraki, D. and Rassias, G. (2020). Epoxide syntheses and ring-opening reactions in drug development. Catalysts, Vol. 10. No. 10, pp. 1–65. pp.

Mu, M., Ke, X., Cheng, W., Li, J., Ji, C. and Yin, M. (2022). Perylenemonoimide-Based Colorimetric Probe with High Contrast for Naked-Eye Detection of Fluoride Ions. Analytical Chemistry, Vol. 94. No. 33, pp. 11470–11475.

Mühldorf, B., Lennert, U. and Wolf, R. (2020). Coupling photoredox and biomimetic catalysis for the visible-light-driven oxygenation of organic compounds. Chemical Photocatalysis, Vol. 4. No. 3, pp. 223–243.

Mulfort, K. L. and Utschig, L. M. (2016). Modular Homogeneous Chromophore-Catalyst Assemblies. Accounts of Chemical Research, Vol. 49. No. 5, pp. 835–843.

Mulrooney, S. B. and Hausinger, R. P. (2003). Nickel uptake and utilization by microorganisms. FEMS Microbiology Reviews, Vol. 27. pp. 239–261

Murugesan, K., Jeyasingh, V., Lakshminarayanan, S., Govindaraj, T. S., Paulraj, M. S., Narayanan, S. and Piramuthu, L. (2018). Electron-deficient tripodal amide based receptor: An exclusive turn-on fluorescent and colorimetric chemo sensor for cyanide ion. Spectrochimica Acta - Part A: Molecular and Biomolecular Spectroscopy, Vol. 198. pp. 309–314.

Naithani, S., Dubey, R., Goswami, T., Thetiot, F. and Kumar, S. (2024). Optical detection strategies for Ni(ii) ion using metal-organic chemosensors: from molecular design to environmental applications. Dalton Transactions, Vol. 53. No. 43, pp. 17409–17428.

Naithani, S., Goswami, T., Thetiot, F. and Kumar, S. (2023). Imidazo[4,5-f][1,10]phenanthroline based luminescent probes for anion recognition: Recent achievements and challenges. Coordination Chemistry Reviews, Vol. 475. pp. 214894.

Naithani, S., Kumar, P., Dubey, R., Thetiot, F., Layek, S., Goswami, T. and

Kumar, S. (2025). Design principles for metal–organic receptors targeting optical recognition of Pd(ii) in environmental matrices. Journal of Materials Chemistry C, Vol. 13. No. 23, pp. 11562–11585.

Naithani, S., Thetiot, F., Yadav, V., Saini, S., Roy, P., Layek, S., Goswami, T. and Kumar, S. (2024). A pyridyl-benzimidazole based ruthenium(II) complex as optical sensor: Targeted cyanide detection and live cell imaging applications. Journal of Photochemistry and Photobiology A: Chemistry, Vol. 453. pp. 115610.

Nayak, P. (2002). Aluminum: Impacts and disease. Environmental Research, Vol. 89. No. 2, pp. 101–115.

Nebert, D. W. and Russell, D. W. (2002). Clinical importance of the cytochromes P450. Lancet, Vol. 360. No. 9340, pp. 1155–1162.

Nestoros, E., Sharma, A., Kim, E., Kim, J. S. and Vendrell, M. (2025). Smart molecular designs and applications of activatable organic photosensitizers. Nature Reviews Chemistry, Vol. 9. No. 1, pp. 46–60.

Nie, H. M., Gong, C. Bin, Tang, Q., Ma, X. B. and Chow, C. F. (2014). Visual and reversible detection of cyanide ions in protic solvents by a novel colorimetric receptor. Dyes and Pigments, Vol. 106, pp. 74–80.

Ning, Y., Jin, G.-Q., Wang, M.-X., Gao, S. and Zhang, J.-L. (2022). Recent progress in metal-based molecular probes for optical bioimaging and biosensing. Current Opinion in Chemical Biology, Vol. 66, pp. 102097.

Niu, H., Liu, J., O'Connor, H. M., Gunnlaugsson, T., James, T. D. and Zhang, H. (2023). Photoinduced electron transfer (PeT) based fluorescent probes for cellular imaging and disease therapy. Chemical Society Reviews, Vol. 52. No. 7, pp. 2322–2357.

Niziński, P., Błażewicz, A., Kończyk, J. and Michalski, R. (2021). Perchlorate – properties, toxicity and human health effects: an updated review. Vol. 36. No. 2, pp. 199–222.

Nosaka, Y. and Nosaka, A. Y. (2017). Generation and Detection of Reactive Oxygen Species in Photocatalysis. Chemical Reviews, Vol. 117. No. 17, pp. 11302–11336.

Novaes, R. D., Mouro, V. G. S., Gonçalves, R. V, Mendonça, A. A. S., Santos,

E. C., Fialho, M. C. Q. and Machado-Neves, M. (2018). Aluminum: A potentially toxic metal with dose-dependent effects on cardiac bioaccumulation, mineral distribution, DNA oxidation and microstructural remodeling. Environmental Pollution, Vol. 242, pp. 814–826.

O'Connor, A. E., Gallagher, W. M. and Byrne, A. T. (2009). Porphyrin and Nonporphyrin Photosensitizers in Oncology: Preclinical and Clinical Advances in Photodynamic Therapy. Photochemistry and Photobiology, Vol. 85. No. 5, pp. 1053–1074.

O'Reilly, E., Köhler, V., Flitsch, S. L. and Turner, N. J. (2011). Cytochromes P450 as useful biocatalysts: addressing the limitations. Chemical Communications, Vol. 47. No.9, pp. 2490–2501.

Pak, Y. L., Wang, Y. and Xu, Q. (2021). Conjugated polymer based fluorescent probes for metal ions. Coordination Chemistry Reviews, Vol. 433. pp. 213745.

Pal, A., Karmakar, M., Bhatta, S. R. and Thakur, A. (2021). A detailed insight into anion sensing based on intramolecular charge transfer (ICT) mechanism: A comprehensive review of the years 2016 to 2021. Coordination Chemistry Reviews, Vol. 448. pp. 214167.

Pal, A., Bhatta, S. and Thakur, A. (2021). Recent advances in the development of ferrocene based electroactive small molecules for cation recognition: A comprehensive review of the years 2010–2020. Coordination Chemistry Reviews, Vol .431. pp. 213685.

Pal, P., Ganguly, T., Karmakar, S. and Baitalik, S. (2020). Anion- and solvent induced modulation of photophysical properties of a luminescent bimetallic Ru(II) complex: Experimental and TD-DFT study. Inorganica Chimica Acta, Vol. 502. pp. 119337.

Park, C. H. and Simmons, H. E. (1968). Macrobicyclic Amines. III. Encapsulation of Halide Ions by in,in-1,(k + 2)-Diazabicyclo[k.l.m]aIkane-ammonium Ions. Journal of the American Chemical Society, Vol. 90. No 9, pp. 2431–2432).

Park, S. H., Kwon, N., Lee, J. H., Yoon, J. and Shin, I. (2020). Synthetic ratiometric fluorescent probes for detection of ions. Chemical Society

Reviews, Vol. 49. No. 1, pp. 143–179.

Pati, P. B. (2016). Organic chemodosimeter for cyanide: A nucleophilic approach. Sensors and Actuators, B: Chemical, Vol. 222. pp. 374–390.

Patrick, S. C., Beer, P. D. and Davis, J. J. (2024). Solvent effects in anion recognition. Nature Reviews Chemistry, Vol. 8. Number 4, 256–276. pp.).

Paul, S., Das, R. and Banerjee, P. (2022). Recent endeavours in the development of organo chromo-fluorogenic probes towards the targeted detection of the toxic industrial pollutants Cu2+ and CN−: recognition to implementation in sensory device. Materials Chemistry Frontiers, Vol. 6. No. 18, pp. 2561–2595.

Pengpumkiat, S., Wu, Y., Sumantakul, S. and Remcho, V. T. (2020). A membrane-based disposable well-plate for cyanide detection incorporating a fluorescent chitosan-CdTe quantum dot. Analytical Sciences, Vol. 36. No. 2, pp. 193–199.

Petitjean, Q., Jacquin, L., Riem, L., Pitout, M., Perrault, A., Cousseau, M., Laffaille, P. and Jean, S. (2021). Intraspecific variability of responses to combined metal contamination and immune challenge among wild fish populations. Environmental Pollution, Vol. 272, pp. 116042.

Pham, T. C., Nguyen, V.-N., Choi, Y., Lee, S. and Yoon, J. (2021). Recent strategies to develop innovative photosensitizers for enhanced photodynamic therapy. Chemical Reviews, Vol. 121. No. 21, pp. 13454–13619.

Phungsripheng, S., Akita, M. and Inagaki, A. (2017). Substituent Effect of the Bridging Ligand in the Trinuclear Ru Complexes on Photocatalytic Oxygenation of a Sulfide and Alkenes. Inorganic Chemistry, Vol. 56. No. 21, pp. 12996–13006.

Pitre, S. P., McTiernan, C. D. and Scaiano, J. C. (2016). Understanding the Kinetics and Spectroscopy of Photoredox Catalysis and Transition-Metal-Free Alternatives. Accounts of Chemical Research, Vol. 49. No.6, pp. 1320–1330.

Pleus, R. C. and Corey, L. M. (2018). Environmental exposure to perchlorate: A review of toxicology and human health. Toxicology and Applied

Pharmacology, Vol. 358. pp. 102–109.

Prabha, D., Singh, D., Kumar, P. and Gupta, R. (2021). Selective Detection of Picric Acid and Pyrosulfate Ion by Nickel Complexes Offering a Hydrogen-Bonding-Based Cavity. Inorganic Chemistry, Vol. 60. No. 23), pp. 17889–17899.

Pramanik, R. (2025). A Review on Fluorescent Molecular Probes for Hg2+ Ion Detection: Mechanisms, Strategies, and Future Directions. ChemistrySelect, Vol. 10. No. 7, pp. e202404525.

Prier, C. K., Rankic, D. A. and MacMillan, D. W. C. (2013). Visible light photoredox catalysis with transition metal complexes: Applications in organic synthesis. Chemical Reviews, Vol. 113. No. 7, pp. 5322–5363.

Qiao, M., Ding, L. and Lv, F. (2021). Surfactant assemblies encapsulating fluorescent probes as selective and discriminative sensors for metal ions. Coordination Chemistry Reviews, Vol. 432. pp. 213696.

Qin, J. C., Fan, L., Li, T. R. and Yang, Z. Y. (2015). Recognition of Al3+ and Zn2+ using a single Schiff-base in aqueous media. Synthetic Metals, Vol. 199. pp. 179–186.

Quina, F. H. and Silva, G. T. M. (2021). The photophysics of photosensitization: A brief overview. Journal of Photochemistry and Photobiology, Vol. 7. pp. 100042.

Rainbow, P. S. and Luoma, S. N. (2011). Metal toxicity, uptake and bioaccumulation in aquatic invertebrates—Modelling zinc in crustaceans. Aquatic Toxicology, Vol. 105. No. 3, pp. 455–465.

Rana, P., Kaushik, B., Solanki, K., Saini, K. M. and Sharma, R. K. (2022). Development of heterogeneous photocatalysts via the covalent grafting of metal complexes on various solid supports. Chemical Communications, Vol. 58. No. 81, pp. 11354–11377.

Randviir, E. P. and Banks, C. E. (2015). The latest developments in quantifying cyanide and hydrogen cyanide. TrAC - Trends in Analytical Chemistry, Vol. 64. pp. 75–85.

Rasheed, S., Kanwal, T., Ahmad, N., Fatima, B., Najam-ul-Haq, M. and Hussain, D. (2024). Advances and challenges in portable optical

biosensors for onsite detection and point-of-care diagnostics. TrAC Trends in Analytical Chemistry, Vol. 173. pp. 117640.

Rathi, B. S., Kumar, P. S. and Vo, D.-V. N. (2021). Critical review on hazardous pollutants in water environment: Occurrence, monitoring, fate, removal technologies and risk assessment. Science of The Total Environment, Vol. 797. pp. 149134.

Ravetz, B. D., Tay, N. E. S., Joe, C. L., Sezen-Edmonds, M., Schmidt, M. A., Tan, Y., Janey, J. M., Eastgate, M. D. and Rovis, T. (2020). Development of a Platform for Near-Infrared Photoredox Catalysis. ACS Central Science, Vol. 6. No. 11, pp. 2053–2059

Ravi, S. K. and Tan, S. C. (2015). Progress and perspectives in exploiting photosynthetic biomolecules for solar energy harnessing. Energy & Environmental Science, Vol. 8. No. 9, pp. 2551–2573.

Reiser, O. (2016). Shining Light on Copper: Unique Opportunities for Visible-Light-Catalyzed Atom Transfer Radical Addition Reactions and Related Processes. Accounts of Chemical Research, Vol. 49. No. 9, pp. 1990–1996.

Romero, N. A. and Nicewicz, D. A. (2016). Organic Photoredox Catalysis. Chemical Reviews, Vol. 116. No. 17, pp. 10075–10166.

Rosenzweig, A. C. and Sazinsky, M. H. (2006). Structural insights into dioxygen-activating copper enzymes. Current Opinion in Structural Biology, Vol. 16. No. 6, pp. 729–735.

Roy, A., Shee, U., Mukherjee, A., Mandal, S. K. and Roy, P. (2019). Rhodamine-Based Dual Chemosensor for Al 3+ and Zn 2+ Ions with Distinctly Separated Excitation and Emission Wavelengths. ACS Omega, Vol. 4. No. 4, pp. 6864–6875.

Roy, P. (2021). Recent advances in the development of fluorescent chemosensors for Al3+. Dalton Transactions, Vol. 50. No. 21, pp. 7156–7165.

Sagami, T., Tahara, Y. O., Miyata, M., Miyake, H. and Shinoda, S. (2017). Luminescence sensing of weakly-hydrated anions in aqueous solution by self-assembled europium(III) complexes. Chemical Communications, Vol. 53. No. 28, pp. 3967–3970.

Sahana, A., Banerjee, A., Lohar, S., Chottapadhyay, A., Mukhopadhyay, S. K. and Das, D. (2013). Lighting of a rhodamine-based fluorescent lamp using ClO4- as a connector: Detection by the naked eye and cell imaging studies of trace amounts of ClO4- ions. RSC Advances, Vol. 3. No. 33, pp. 14044–14047.

Sahu, S., Sikdar, Y., Bag, R., Maiti, D. K., Cerón–Carrasco, J. P. and Goswami, S. (2019). Visual detection of fluoride ion based on ICT mechanism. Spectrochimica Acta Part A: Molecular and Biomolecular Spectroscopy, Vol. 213. pp. 354–360.

Samanta, S. S., Giri, P. K., Giri, S., Ghosh, A., & Misra, A. (2023). Flexible HSA-interactive phenolphthalein based probe proficient at selective turn-on sensing for Zn2+ & Al3+. J. Mol. Struct., Vol. 1278, pp. 134927.

Santra, S., Mukherjee, S., Bej, S., Saha, S. and Ghosh, P. (2015). Amino-ether macrocycle that forms CuII templated threaded heteroleptic complexes: a detailed selectivity, structural and theoretical investigations. Dalton Transactions, Vol. 44. No. 34, pp. 15198–15211.

Saravanan, A., Deivayanai, V. C., Kumar, P. S., Rangasamy, G., Hemavathy, R. V, Harshana, T., Gayathri, N. and Alagumalai, K. (2022). A detailed review on advanced oxidation process in treatment of wastewater: Mechanism, challenges and future outlook. Chemosphere, Vol. 308. pp. 136524.

Schmidtchen, F. P. and Berger, M. (1997). Artificial Organic Host Molecules for Anions. Chemical Reviews, Vol. 97. No. 5, pp. 1609–1646.

Schulze, M., Kunz, V., Frischmann, P. D. and Würthner, F. (2016). A supramolecular ruthenium macrocycle with high catalytic activity for water oxidation that mechanistically mimics photosystem II. Nature Chemistry, Vol. 8. No. 6, pp. 576–583.

Sedgwick, A. C., Wu, L., Han, H.-H., Bull, S. D., He, X.-P., James, T. D., Sessler, J. L., Tang, B. Z., Tian, H. and Yoon, J. (2018). Excited-state intramolecular proton-transfer (ESIPT) based fluorescence sensors and imaging agents. Chemical Society Reviews, Vol. 47. No. 23, pp. 8842–8880.

Sessler, J. L., Camiolo, S. and Gale, P. A. (2003). Pyrrolic and polypyrrolic anion binding agents. Coordination Chemistry Reviews, Vol. 240. No. 1–2, pp. 17–55.

Sharma, A. S., Sharma, V. S., Kaur, H. and Varma, R. S. (2020). Supported heterogeneous nanocatalysts in sustainable, selective and eco-friendly epoxidation of olefins. Green Chemistry, Vol. 22. No. 18, pp. 5902–5936.

Shaw, G. B., Grant, C. D., Shirota, H., Castner, E. W., Meyer, G. J. and Chen, L. X. (2007). Ultrafast Structural Rearrangements in the MLCT Excited State for Copper(I) bis-Phenanthrolines in Solution. Journal of the American Chemical Society, Vol. 129. No. 7, pp. 2147–2160.

She, M., Wang, Z., Chen, J., Li, Q., Liu, P., Chen, F., Zhang, S. and Li, J. (2021). Design strategy and recent progress of fluorescent probe for noble metal ions (Ag, Au, Pd, and Pt). Coordination Chemistry Reviews, Vol. 432. pp. 213712.

Sheldrick, G. M. SADABS (Version 2.03); University of Göttingen: Germany, 2002.

Sheldrick, G. M. (2000). SHELXS in SHELXTL v6. 12, Bruker AXS Inst. Inc., Madison (WI, USA), 10.

Shen, J., Wen, X. and Fan, Z. (2023). Tandem detection of aluminum ion and norfloxacin by Au-doped copper nanoclusters based on AIE and coordination reaction. Sensors and Actuators B: Chemical, Vol. 381. pp. 133436.

Shen, Y., Nie, C., Wei, Y., Zheng, Z., Xu, Z. L. and Xiang, P. (2022). FRET-based innovative assays for precise detection of the residual heavy metals in food and agriculture-related matrices. Coordination Chemistry Reviews, Vol. 469. pp. 214676.

Shon, J.-H. and Teets, T. S. (2019). Molecular Photosensitizers in Energy Research and Catalysis: Design Principles and Recent Developments. ACS Energy Letters, Vol. 4. No. 2, pp. 558–566.

Shrestha, R., Ban, S., Devkota, S., Sharma, S., Joshi, R., Tiwari, A. P., Kim, H. Y. and Joshi, M. K. (2021). Technological trends in heavy metals removal from industrial wastewater: A review. Journal of Environmental Chemical

Engineering, Vol. 9. No. 4, pp. 105688.

Shrivastava, K., Gill, F. S., Juyal, S., Lal, M. and Jain, A. (2025). Green Carbon for Clean Energy: Biomass-Derived Hierarchical Structures in Energy Storage. Wiley Interdisciplinary Reviews: Energy and Environment, Vol. 14. No 2, pp. e70007. p.)

Singh, H., Tiwari, K., Tiwari, R., Pramanik, S. K. and Das, A. (2019). Small Molecule as Fluorescent Probes for Monitoring Intracellular Enzymatic Transformations. Chemical Reviews, Vol. 119. No. 22, pp. 11718–11760.

Singh, S., Nautiyal, D., Thetiot, F., Le Poul, N., Goswami, T., Kumar, A. and Kumar, S. (2021). Bioinspired Heterobimetallic Photocatalyst (RuIIchrom-FeIIIcat) for Visible-Light-Driven C-H Oxidation of Organic Substrates via Dioxygen Activation. Inorganic Chemistry, Vol. 60. No. 21, pp. 16059–16064.

Singh, V. P., Tiwari, K., Mishra, M., Srivastava, N. and Saha, S. (2013). 5-[{(2-Hydroxynaphthalen-1-yl)methylene}amino]pyrmidine-2,4(1H,3H)-dione as Al3+ selective colorimetric and fluorescent chemosensor. Sensors and Actuators, B: Chemical, Vol. 182. pp. 546–554.

Singha, S., Jun, Y. W., Sarkar, S. and Ahn, K. H. (2019). An Endeavor in the Reaction-Based Approach to Fluorescent Probes for Biorelevant Analytes: Challenges and Achievements. Accounts of Chemical Research, Vol. 52. No. 9, pp. 2571–2581.

Smith, C. B., Days, L. C., Alajroush, D. R., Faye, K., Khodour, Y., Beebe, S. J. and Holder, A. A. (2022). Photodynamic Therapy of Inorganic Complexes for the Treatment of Cancer. Photochemistry and Photobiology, Vol. 98. No. 1, pp. 17–41.

Song, H., Liu, G., Fan, C. and Pu, S. (2021). A novel fluorescent sensor for Al3+ and Zn2+ based on a new europium complex with a 1,10-phenanthroline ligand. Journal of Rare Earths, Vol. 39. No. 4, pp. 460–468.

Song, Y., Wang, Y., Pan, B., Cheng, X., Yang, J. and Chen, Y. (2025). Recent Advances in Biocatalytic Preparation of Chiral Sulfoxides. Asian Journal of Organic Chemistry, Vol. 14. No. 4, pp. e202400708.

Sparling, D. W. and Lowe, T. P. (1996). Environmental hazards of aluminum

to plants, invertebrates, fish, and wildlife. Springer.

Srour, H., Le Maux, P., Chevance, S. and Simonneaux, G. (2013). Metal-catalyzed asymmetric sulfoxidation, epoxidation and hydroxylation by hydrogen peroxide. Coordination Chemistry Reviews, Vol. 257, pp. 3030–3050.

Steinmaus, C. M. (2016). Perchlorate in Water Supplies: Sources, Exposures, and Health Effects. Current Environmental Health Reports, Vol. 3. No. 2, pp. 136–143.

Streb, C. (2012). New trends in polyoxometalate photoredox chemistry: From photosensitisation to water oxidation catalysis. Dalton Transactions, Vol. 41. No. 6, pp. 1651–1659.

Su, Z., Li, Y., Li, J. and Dou, X. (2021). Ultrasensitive luminescent turn-on detection of perchlorate particulates by triggering supramolecular self-assembly of platinum(II) complex in hydrogel matrix. Sensors and Actuators, B: Chemical, Vol. 336. No. 129728.

Suárez, P. L., García-Cortés, M., Fernández-Argüelles, M. T., Encinar, J. R., Valledor, M., Ferrero, F. J., Campo, J. C. and Costa-Fernández, J. M. (2019). Functionalized phosphorescent nanoparticles in (bio)chemical sensing and imaging – A review. Analytica Chimica Acta, Vol. 1046. pp. 16–31.

Sun, T., Niu, Q., Li, Y., Li, T., Hu, T., Wang, E. and Liu, H. (2018). A novel oligothiophene-based colorimetric and fluorescent “turn on” sensor for highly selective and sensitive detection of cyanide in aqueous media and its practical applications in water and food samples. Sensors and Actuators, B: Chemical, Vol. 258. pp. 64–71.

Sundberg, R. J. (1974). Interactions of histidine and other imidazole derivatives with transition metal ions in chemical and biological systems. Chemical Reviews, Vol. 74. No. 4, pp. 471–517.

Szynkowska, M. I., Pawlaczyk, A. and Maćkiewicz, E. (2018). Bioaccumulation and Biomagnification of Trace Elements in the Environment. In Recent Advances in Trace Elements pp. 251–276.

Taha, A., Farooq, N., Singh, N. and Hashmi, A. A. (2024). Recent developments

in Schiff base centered optical and chemical sensors for metal ion recognition. Journal of Molecular Liquids, Vol. 401. pp. 124678.

Takeda, E., Taketani, Y., Sawada, N., Sato, T. and Yamamoto, H. (2004). The regulation and function of phosphate in the human body. BioFactors, Vol. 21. No. (1–4), pp. 345–355.

Tang, Y., Sun, J. and Yin, B. (2016). A dual-response fluorescent probe for Zn2+ and Al3+ detection in aqueous media: pH-dependent selectivity and practical application. Analytica Chimica Acta, Vol. 942. pp. 104–111

Tao, C., Wang, B., Sun, L., Liu, Z., Zhai, Y., Zhang, X. and Wang, J. (2017). Merging visible-light photoredox and copper catalysis in catalytic aerobic oxidation of amines to nitriles. Organic and Biomolecular Chemistry, Vol. 15. No. 2, pp. 328–332.

Tarai, A., Li, Y., Liu, B., Zhang, D., Li, J., Yan, W., Zhang, J., Qu, J. and Yang, Z. (2021). A review on recognition of tri-/tetra-analyte by using simple organic colorimetric and fluorometric probes. Coordination Chemistry Reviews, Vol. 445. pp. 214070.

Taylor, S. D., Howard, W., Kaval, N., Hart, R., Krause, J. A. and Connick, W. B. (2010). Solid-state materials for anion sensing in aqueous solution: Highly selective colorimetric and luminescence-based detection of perchlorate using a platinum(ii) salt. Chemical Communications, Vol. 46. No. 7, pp. 1070–1072.

Thanayupong, E., Suttisintong, K., Sukwattanasinitt, M. and Niamnont, N. (2017). Turn-on fluorescent sensor for the detection of cyanide based on a novel dicyanovinyl phenylacetylene. New Journal of Chemistry, Vol. 41. No. 10, pp. 4058–4064.

Tielrooij, K. J., Garcia-Araez, N., Bonn, M. and Bakker, H. J. (2010). Cooperativity in ion hydration. Science, Vol. 328. No. 5981, pp. 1006–1009.

Tigreros, A. and Portilla, J. (2022). Ecological and Economic Efforts in the Development of Molecular Sensors for the Optical Detection of Cyanide Ions. European Journal of Organic Chemistry, Vol. 2022. No. 29, pp. e202200249.

Ting, S. I., Garakyaraghi, S., Taliaferro, C. M., Shields, B. J., Scholes, G. D., Castellano, F. N. and Doyle, A. G. (2020). 3d-d Excited States of Ni(II) Complexes Relevant to Photoredox Catalysis: Spectroscopic Identification and Mechanistic Implications. Journal of the American Chemical Society, Vol. 142. No. 12, pp. 5800–5810.

Tohora, N., Mahato, M., Sahoo, R., Ahamed, S., Sultana, T., Selim Arif Sher Shah, M. and Kumar Das, S. (2023). Fabrication of a GUMBOS-based ratiometric organo nanosensor for selective and sensitive detection of perchlorate ions that works in 100% water. Journal of Photochemistry and Photobiology A: Chemistry, Vol. 445. pp. 115050.

Turro, N. J., Ramamurthy, V. and Scaiano, J. C. (2010). Modern molecular photochemistry of organic molecules (Vol. 188). University Science Books Sausalito, CA.

Tzeng, B. C., Chen, B. S., Chen, C. K., Chang, Y. P., Tzeng, W. C., Lin, T. Y., Lee, G. H., Chou, P. T., Fu, Y. J. and Chang, A. H. H. (2011). PH-dependent spectroscopic and luminescent properties, and metal-ion recognition studies of Re(I) complexes containing 2-(2′-pyridyl) benzimidazole and 2-(2′-pyridyl)benzimidazolate. Inorganic Chemistry, Vol. 50. No. 12, pp. 5379–5388.

Udhayakumari, D. (2018). Chromogenic and fluorogenic chemosensors for lethal cyanide ion. A comprehensive review of the year 2016. Sensors and Actuators, B: Chemical, Vol. 259. pp. 1022–1057.

Valdez, C. E., Smith, Q. A., Nechay, M. R. and Alexandrova, A. N. (2014). Mysteries of metals in metalloenzymes. Accounts of Chemical Research, Vol. 47. No. 10, pp. 3110–3117.

Vallee, B. L. and Williams, R. J. (1968). Metalloenzymes: the entatic nature of their active sites. Proceedings of the National Academy of Sciences of the United States of America, Vol. 59. No. 2, pp. 498–505.

Vidal, A., Adamo, F., Iengo, E. and Alessio, E. (2021). Models of molecular photocatalysts for water oxidation: Strategies for conjugating the Ru(bda) fragment (bda = 2,2′-bipyridine-6,6′-dicarboxylate) to porphyrin photosensitizers. Inorganica Chimica Acta, Vol. 516. pp. 120143.

Wan, H., Xu, Q., Gu, P., Li, H., Chen, D., Li, N., He, J. and Lu, J. (2021). AIE-based fluorescent sensors for low concentration toxic ion detection in water. Journal of Hazardous Materials, Vol. 403. No. 123656.

Wang, D. X. and Wang, M. X. (2020). Exploring Anion-πInteractions and Their Applications in Supramolecular Chemistry. Accounts of Chemical Research, Vol. 53. No. 7, pp. 1364–1380.

Wang, F., Wang, K., Kong, Q., Wang, J., Xi, D., Gu, B., Lu, S., Wei, T. and Chen, X. (2021). Recent studies focusing on the development of fluorescence probes for zinc ion. Coordination Chemistry Reviews, Vol. 429. pp. 213636.

Wang, F., Wang, L., Chen, X. and Yoon, J. (2014). Recent progress in the development of fluorometric and colorimetric chemosensors for detection of cyanide ions. Chemical Society Reviews, Vol. 43. No. 13, pp. 4312–4324.

Wang, R., Hua, S., Xing, Y., Wang, R., Wang, H., Jiang, T. and Yu, F. (2024). Organic dye-based photosensitizers for fluorescence imaging-guided cancer phototheranostics. Coordination Chemistry Reviews, Vol. 513. No. 215866.

Wang, R., Zhang, H., Wang, S., Meng, F., Sun, J., Lou, D. and Su, Z. (2023). A ratiometric fluorescent probe based on a dual-ligand lanthanide metal–organic framework (MOF) for sensitive detection of aluminium and fluoride ions in river and tap water. Inorganic Chemistry Frontiers, Vol. 10. No. 5, pp. 1534–1542.

Wang, Z., Cui, S., Qiu, S. and Pu, S. (2019). A dual-functional fluorescent sensor based on diarylethene for Zn 2+ and Al 3+ in different solvents. Journal of Photochemistry and Photobiology A: Chemistry, Vol. 376. pp. 185–195.

Wasielewski, M. R. (1992). Photoinduced electron transfer in supramolecular systems for artificial photosynthesis. Chemical Reviews, Vol. 92. No. 3, pp. 435–461.

Watson, J. (2018). Explosives Incident Report. United States Bomb Data Center (USBDC), Huntsville.

Weiss, J. A. and Stanbury, J. B. (1972). Spectrophotometric determination of microamounts of perchlorate in biological fluids. Analytical Chemistry, Vol. 44. No. 3, pp. 619–620.

Wilker, J. J., Dmochowski, I. J., Dawson, J. H., Winkler, J. R. and Gray, H. B. (1999). Substrates for rapid delivery of electrons and holes to buried active sites in proteins. Angewandte Chemie International Edition, Vol. 38. No. (1-2), pp. 89–92.

Wong, R. C. H., Lo, P. C. and Ng, D. K. P. (2019). Stimuli responsive phthalocyanine-based fluorescent probes and photosensitizers. Coordination Chemistry Reviews, Vol. 379. pp. 30–46.

Wu, D., Sedgwick, A. C., Gunnlaugsson, T., Akkaya, E. U., Yoon, J. and James, T. D. (2017). Fluorescent chemosensors: the past, present and future. Chemical Society Reviews, Vol. 46. No. 23, pp. 7105–7123.

Wu, J., Kwon, B., Liu, W., Anslyn, E. V, Wang, P. and Kim, J. S. (2015). Chromogenic/Fluorogenic Ensemble Chemosensing Systems. Chemical Reviews, Vol. 115. No. 15, pp. 7893–7943.

Wu, L., Huang, C., Emery, B. P., Sedgwick, A. C., Bull, S. D., He, X. P., Tian, H., Yoon, J., Sessler, J. L. and James, T. D. (2020). Förster resonance energy transfer (FRET)-based small-molecule sensors and imaging agents. Chemical Society Reviews, Vol. 49. No. 15, pp. 5110–5139.

Wu, S., Wang, Y., Iqbal, M., Mehmood, K., Li, Y., Tang, Z. and Zhang, H. (2022). Challenges of fluoride pollution in environment: Mechanisms and pathological significance of toxicity – A review. Environmental Pollution, Vol. 304. pp. 119241.

Xiong, S., Nanda Kishore, M. V., Zhou, W. and He, Q. (2022). Recent advances in selective recognition of fluoride with macrocyclic receptors. Coordination Chemistry Reviews, Vol. 461. 124642.

Xu, H., Chen, W., Ju, L. and Lu, H. (2021). A purine based fluorescent chemosensor for the selective and sole detection of Al3+ and its practical applications in test strips and bio-imaging. Spectrochimica Acta - Part A: Molecular and Biomolecular Spectroscopy, Vol. 247. pp. 119074.

Xu, J., Jiang, R., Feng, Y., Liu, Z., Huang, J., Ma, C. and Wang, K. (2022).

Functional nucleic acid-based fluorescent probes for metal ion detection. Coordination Chemistry Reviews, Vol. 459. pp. 214453.

Xu, Z., Chen, X., Kim, H. N. and Yoon, J. (2010). Sensors for the optical detection of cyanide ion. Chemical Society Reviews, Vol. 39. No. 1, pp. 127–137.

Xue, Y. and Chao, D. (2024). Organic and Non-Precious Metal Photosensitizers for Photocatalytic CO2 Reduction. ChemPhotoChem, Vol. 8. No. 12, pp. e202400246.

Yadav, R. N., Srivastava, A. K., Dey, S., Das, A., Banik, B. K. and Hossain, M. F. (2024). Transition metal complexes: A new era of photosensitizers for Dearomative photocycloaddition/annulation via energy and Electron transfer Photocatalysis. Coordination Chemistry Reviews, Vol. 520. pp. 216136.

Yang, B., Chen, Y. and Shi, J. (2019). Reactive Oxygen Species (ROS)-Based Nanomedicine. Chemical Reviews, Vol. 119. No. 8, pp. 4881–4985.

Yang, J., Tang, L., Li, L., Wu, X. and Yan, L. (2025). Recent Advances in Organic Small-Molecule Fluorescent Probes for the Detection of Zinc Ions (Zn2+). Journal of Fluorescence, Vol. 35. No. 5, pp. 2641–2674.

Yang, X., Zhang, S., Li, P., Gao, S. and Cao, R. (2020). Visible-light-driven photocatalytic selective organic oxidation reactions. Journal of Materials Chemistry A, Vol. 8. No. 40, pp. 20897–20924.

Yang, Y., Yin, C., Huo, F., Chao, J., Zhang, Y. and Cheng, F. (2014). A new highly selective and turn-on fluorescence probe for detection of cyanide. Sensors and Actuators, B: Chemical, Vol. 193. pp. 220–224.

Yao, J., Yang, M. and Duan, Y. (2014). Chemistry, Biology, and Medicine of Fluorescent Nanomaterials and Related Systems: New Insights into Biosensing, Bioimaging, Genomics, Diagnostics, and Therapy. Chemical Reviews, Vol. 114. No. 12, pp. 6130–6178.

Ye, L., You, H., Yao, J. and Su, H. (2012). Water treatment technologies for perchlorate: A review. Desalination, Vol. 298. pp. 1–12.

Yi, H., Crayston, J. A. and Irvine, J. T. S. (2003). Ruthenium complexes of 2-(2′-pyridyl)benzimidazole as photosensitizers for dye-sensitized solar

cellsElectronic supplementary information (ESI) available: details of the luminescence measurements and solar cell construction and testing; synthesis details; Dalton Transactions, Vol. 4. pp. 685–691.

Yilmaz, B., Keskinates, M., Aydin, Z. and Bayrakci, M. (2022a). A highly selective optical sensor for the detection of cyanide ions in aqueous solution and living cells. Journal of Photochemistry and Photobiology A: Chemistry, Vol. 424. pp. 113651.

Obali, A. Y. (2020a). Hydroxy- and Methoxy-Substituted Inorganic Receptor Design: Dual Selectivities for Ag+ and CN− in Aqueous Medium. Polycyclic Aromatic Compounds, Vol. 40. No. 5, pp. 1624–1636.

Yoon, J., Kim, S. K., Singh, N. J. and Kim, K. S. (2006). Imidazolium receptors for the recognition of anions. Chemical Society Reviews, Vol. 35. No. 4, pp. 355–360. pp.

You, L., Zha, D. and Anslyn, E. V. (2015). Recent Advances in Supramolecular Analytical Chemistry Using Optical Sensing. Chemical Reviews, Vol. 115. No. 15, pp. 7840–7892.

Zeng, L., Wang, X.-Y., Li, N., Pang, J. and Bu, X.-H. (2024). Low-power, non-coherent light-triggered two-photon absorption via extending the lifetime of the transition state. Coordination Chemistry Reviews, Vol. 511, pp. 215868.

Zhang, B. and Sun, L. (2019). Artificial photosynthesis: opportunities and challenges of molecular catalysts. Chemical Society Reviews, Vol. 48. No. 7, pp. 2216–2264.

Zhang, R. and Yuan, J. (2020). Responsive Metal Complex Probes for Time-Gated Luminescence Biosensing and Imaging. Accounts of Chemical Research, Vol. 53. No. 7, pp. 1316–1329.

Zhang, T., Wu, Q., Sun, H. W., Rao, J. and Kannan, K. (2010). Perchlorate and Iodide in Whole Blood Samples from Infants, Children, and Adults in Nanchang, China. Environmental Science & Technology, Vol. 44. No. 18, pp. 6947–6953.

Zhang, X., Yin, J. and Yoon, J. (2014). Recent Advances in Development of Chiral Fluorescent and Colorimetric Sensors. Chemical Reviews, Vol. 114.

No. 9, pp. 4918–4959.

Zhao, G., Wei, G., Yan, Z., Guo, B., Guang, S., Wu, R., & Xu, H. (2020). A multiple fluorescein-based turn-on fluorophore (FHCS) identified for simultaneous determination and living imaging of toxic Al3+ and Zn2+ by improved Stokes shift. Anal. Chim. Acta., Vol. 1095, pp. 185-196.

Zhao, X., Hou, Y., Liu, L. and Zhao, J. (2021). Triplet Photosensitizers Showing Strong Absorption of Visible Light and Long-Lived Triplet Excited States and Application in Photocatalysis: A Mini Review. Energy and Fuels, Vol. 35. No. 23, pp. 18942–18956.

Zhao, X., Liu, J., Fan, J., Chao, H. and Peng, X. (2021). Recent progress in photosensitizers for overcoming the challenges of photodynamic therapy: from molecular design to application. Chemical Society Reviews, Vol. 50. No. 6, pp. 4185–4219.

Zheng, Z. B., Huang, Q. Y., Han, Y. F., Zuo, J. and Ma, Y. N. (2017). Ruthenium(II) complex-based chemosensors for highly sensitive and selective sequential recognition of copper ion and cyanide. Sensors and Actuators, B: Chemical, Vol. 253. pp. 203–212.

Zhou, W., Saran, R. and Liu, J. (2017). Metal Sensing by DNA. Chemical Reviews, Vol. 117. No. 12, pp. 8272–8325.

Zhou, Z., Song, J., Nie, L. and Chen, X. (2016). Reactive oxygen species generating systems meeting challenges of photodynamic cancer therapy. Chemical Society Reviews, Vol. 45. No. 23, pp. 6597–6626.

Zhu, J. W., Ou, H. D., Xu, N., Deng, W. and Yao, Z. J. (2020). Ruthenium-based phosphorescent probe for selective and naked-eye detection of cyanide in aqueous media. Dyes and Pigments, Vol. 176, pp. 108196.

Zulkifli, S. N., Rahim, H. A. and Lau, W.-J. (2018). Detection of contaminants in water supply: A review on state-of-the-art monitoring technologies and their applications. Sensors and Actuators B: Chemical, Vol. 255, pp. 2657–2689.

LIST OF PUBLICATIONS

Name- Sudhanshu Naithani

ORCID ID: https://orcid.org/my-orcid?orcid=0009-0001-5503-7308

1. Nidhi Goswami, **Sudhanshu Naithani**, Sandeep Singh, Samar Layek, Franck Thetiot, Ritesh Dubey, Tapas Goswami, Sushil Kumar "Isolation of the labile and fluorogenic tetrahedral intermediate in the Al(III)-catalysed hydration of heteroaromatic aldehydes" ***Chem. Commun***. **2025**, *00*, 0000. ***Manuscript under review***

2. Nidhi Goswami, **Sudhanshu Naithani**, Ritesh Dubey, Brij Bhushan, Samar Layek, Tapas Goswami, Sushil Kumar "Fluorogenic probes based on 2,2'-thiobis(ethylamine) binding motifs: Selective analyte detection and emerging opportunities" ***Polyhedron*** **2025**, *00*, 0000. ***Manuscript in revision***

3. Pooja Sharma, **Sudhanshu Naithani**, Udisha Duhan, Arnab Pan, Samar Layek, Sushil Kumar, Tapas Goswami "Facile development of NIR-active upconverting Yb^{3+},Er^{3+}: ZrO_2 nanoparticles decorated over MoS_2 nanosheets for antibiotic degradation" ***J. Environ. Chem Eng.*** **2025**, *00*, 0000. ***Manuscript in revision***

4. Heena, **Sudhanshu Naithani**, Sangeeta, Biswajit Guchhait, Nandita Medda, Partha Roy, Tapas Goswami, Sushil Kumar "Multi-functional AIE active anthracene Schiff base: A luminescent probe for nitro explosive detection, photolabeling and antimicrobial applications" ***Anal. Method.*** **2025**, *00*, 0000. ***Manuscript under review***

5. **Sudhanshu Naithani,** Mousmee Sharma, Parteek Prasher, Sushil Kumar "Coordination chemistry of mefenamic acid with bioactive first-row transition metals: Insights into their DNA binding and anticancer potential" ***Coord. Chem. Rev.*** **2025,** *543*, 216943.

6. Nidhi Goswami, **Sudhanshu Naithani**, Jimmy Mangalam, Vikas Yadav, Saakshi Saini, Partha Roy, Tapas Goswami, Sushil Kumar "Imidazo-phenanthroline based ratiometric optical sensing platform for cyanide and fluoride ions" ***Spectrochim. Acta A Mol. Biomol. Spectrosc***. **2025**, *338*, 126123.

7. **Sudhanshu Naithani**, Pramod Kumar, Ritesh Dubey, Franck Thetiot, Samar Layek, Tapas Goswami, Sushil Kumar "Design principles for metal-organic receptors targeting optical recognition of Pd(II) in environmental and biological matrices" ***J. Mater. Chem. C.*** **2025**, *13*, 11562-11585.

8. **Sudhanshu Naithani**, Nidhi Goswami, Vikas Yadav, Jimmy Mangalam, Tapas Goswami, Sushil Kumar **"**Selective turn-on luminescent recognition of perchlorate ion using pyridyl-benzimidazole based probe" ***Luminescence*** **2024**, *40*, e70087.

9. **Sudhanshu Naithani**, Heena, Pooja Sharma, Samar Layek, Franck Thetiot, Tapas Goswami, Sushil Kumar "Nanoparticles and quantum dots as emerging optical sensing platforms for Ni(II) detection: Recent approaches and perspectives" ***Coord. Chem. Rev.*** **2025**, *524*, 216331.

10. **Sudhanshu Naithani**, Ritesh Dubey, Tapas Goswami, Franck Thetiot, Sushil Kumar "Optical detection strategies for Ni(II) ion using metal-organic chemosensors: From molecular design to environmental applications" ***Dalton Trans.*** **2024**, *53*, 17409-17428.

11. Heena, **Sudhanshu Naithani**, Sangeeta, Biswajit Guchhait, Tapas Goswami, Sushil Kumar "Designing a multifunctional AIE active fluorescent Schiff base probe: Sensitive heavy

metal ions recognition and water induced aggregation" ***New J. Chem.*** **2024**, *48*, 17423-17435.

12. Nidhi Goswami, **Sudhanshu Naithani**, Tapas Goswami, Pankaj Kumar, Pramod Kumar, Sushil Kumar "Turn-on detection of Al^{3+} ions by quinoline based tripodal probe: Mechanistic investigation and live cells imaging applications" ***Anal. Methods*** **2024**, *16*, 5022-5031.
13. **Sudhanshu Naithani**, Franck Thetiot, Vikas Yadav, Saakshi Saini, Partha Roy, Samar Layek, Tapas Goswami, Sushil Kumar "A pyridyl-benzimidazole based ruthenium(II) complex as optical sensor: Targeted cyanide detection and live cell imaging applications" ***J. Photochem. Photobiol. A: Chem.*** **2024**, *453*, 115610.
14. Pooja Sharma, **Sudhanshu Naithani**, Vikas Yadav, Sangeeta, Biswajit Guchhait, Sushil Kumar, Tapas Goswami "Indium nanocubes based recyclable fluorescent chemosensor for sustainable environmental monitoring: pH-induced fluorescence transition and selective detection of Pd(II) ions" ***Sci. Total Environ.*** **2024**, *920*, 171043.
15. Nidhi Goswami, **Sudhanshu Naithani**, Tapas Goswami, Pankaj Kumar, Sushil Kumar "A quinoline derived Schiff base as highly selective 'turn-on' probe for fluorogenic recognition of Al^{3+} ion" ***Spectrochim. Acta A Mol. Biomol. Spectrosc***. **2024**, *310*, 123971.
16. **Sudhanshu Naithani**, Nidhi Goswami, Sain Singh, Vikas Yadav, Sanjay Kumar, Pramod Kumar, Amit Kumar, Tapas Goswami, Sushil Kumar "Turn-on detection of Al^{3+} and Zn^{2+} ions by NSN donors probe: Reversibility, logic gates and DFT calculations" ***Anal. Methods*** **2023**, *15*, 6021–6030.
17. Nidhi Goswami, **Sudhanshu Naithani**, Jimmy Mangalam, Tapas Goswami, Ritesh Dubey, Pramod Kumar, Pankaj Kumar, Sushil Kumar "Fluorescent and chromogenic organic probes to detect group 10 metal ions: Design strategies and sensing applications" ***Dalton Trans.*** **2023**, *52*, 14704–14732.
18. Pooja Sharma, **Sudhanshu Naithani**, Samar Layek, Amit Kumar, Reema Rawat, Heena, Kaja Sravani, Amit Nag, Sushil Kumar, Tapas Goswami "Development of low-cost copper nanoclusters for highly selective "turn-on" sensing of Hg^{2+} ions" ***Spectrochim. Acta A Mol. Biomol. Spectrosc***. **2023**, *297*, 122697.
19. Tapas Goswami, **Sudhanshu Naithani**, Amit Kumar, Sushil Kumar "Morphology controlled Cu nanostructures grafted over rGO as highly efficient and recyclable heterogeneous catalysts to develop 1,2,3-triazole derivatives under click conditions" ***Colloids Surf. A Physicochem. Eng.*** **2023**, *662*, 130982.
20. **Sudhanshu Naithani**, Tapas Goswami, Franck Thetiot, Sushil Kumar "Imidazo[4,5-*f*][1,10]phenanthroline based luminescent probes for anion recognition: Recent achievements and challenges" ***Coord. Chem. Rev.*** **2023**, 475, 214894.

LIST OF CONFERENCES

- Received the **Best Poster Award** at the *International Analytical Conference and Exhibition* organized by the 2nd Indian Analytical Congress, held from May 26–28, **2022**, at Graphic Era, Dehradun.

- Participated in the National Workshop on '*Advanced Materials and Their Characterization*' at UPES, held from September 7–10, **2022**.

- Presented a poster at the *International Young Researcher Conclave (IYRC) 2023*, held on January 19–20, **2023**, at UPES, Dehradun.

- Presented a poster at the *Sustainability Fair 2.0 (HSFEA 2023)*, held on October 30–31, **2023**, at UPES, Dehradun.

- Delivered a short-invited lecture at the *International Conference on Ultrafast Nonlinear Optics and Optical Spectroscopy (UNOOS)*, held from December 10–12, 2024, at the Indian Institute of Science Education and Research (IISER), Mohali, Punjab, India.

- Presented a poster at the *2nd International Young Researcher Conclave (IYRC-2024)*, held from February 26–28, **2024**, at UPES, Dehradun.

Sudhanshu Naithani

Development of Molecular Photosensitizers for Luminescence Sensing and Catalytic Applications

Quick Submit

Quick Submit

UPES: University of Tomorrow

Document Details

Submission ID
trn:oid:::1:3296220619

Submission Date
Jul 15, 2025, 4:46 PM GMT+5:30

Download Date
Sep 14, 2026, 11:06 AM GMT+5:30

File Name
Sudhansuh_Naithani_thesis_for_plag_run.pdf

File Size
11.5 MB

200 Pages

51,405 Words

272,769 Characters

8% Overall Similarity

The combined total of all matches, including overlapping sources, for each database.

Filtered from the Report

- Bibliography
- Quoted Text
- Small Matches (less than 14 words)

Exclusions

- 7 Excluded Sources

Match Groups

145 Not Cited or Quoted 8%
Matches with neither in-text citation nor quotation marks

1 Missing Quotations 0%
Matches that are still very similar to source material

0 Missing Citation 0%
Matches that have quotation marks, but no in-text citation

0 Cited and Quoted 0%
Matches with in-text citation present, but no quotation marks

Top Sources

3% Internet sources
6% Publications
1% Submitted works (Student Papers)

Integrity Flags

1 Integrity Flag for Review

Replaced Characters
236 suspect characters on 61 pages
Letters are swapped with similar characters from another alphabet.

Our system's algorithms look deeply at a document for any inconsistencies that would set it apart from a normal submission. If we notice something strange, we flag it for you to review.

A Flag is not necessarily an indicator of a problem. However, we'd recommend you focus your attention there for further review.

Match Groups

145 Not Cited or Quoted 8%
Matches with neither in-text citation nor quotation marks

1 Missing Quotations 0%
Matches that are still very similar to source material

0 Missing Citation 0%
Matches that have quotation marks, but no in-text citation

0 Cited and Quoted 0%
Matches with in-text citation present, but no quotation marks

Top Sources

3% Internet sources
6% Publications
1% Submitted works (Student Papers)

Top Sources

The sources with the highest number of matches within the submission. Overlapping sources will not be displayed.

1	Internet	
www.rsc.org		2%
2	Publication	
Sushil Kumar, Ritesh Dubey, Tapas Goswami, Franck Thetiot, Sudhanshu Naithani...		1%
3	Publication	
Amit Chauhan, Satyam Singh, Atresh Kumar Singh, Alok Kumar Singh et al. "Phot...		<1%
4	Publication	
Sushil Kumar, Nidhi Goswami, Sudhanshu Naithani, Tapas Goswami, Pramod Ku...		<1%
5	Publication	
Nidhi Goswami, Sudhanshu Naithani, Jimmy Mangalam, Vikas Yadav, Saakshi Sai...		<1%
6	Publication	
Nidhi Goswami, Sudhanshu Naithani, Tapas Goswami, Pankaj Kumar, Sushil Kum...		<1%
7	Publication	
Jolly Kaushal, Sain Singh, Heena Ahlawat, Saakshi Saini, Partha Roy. "Easily synth...		<1%
8	Publication	
Pramod Kumar, Tapas Goswami, Sushil Kumar, Sudhanshu Naithani, Ritesh Dube...		<1%
9	Internet	
doras.dcu.ie		<1%
10	Publication	
Nidhi Goswami, Sudhanshu Naithani, Tapas Goswami, Pankaj Kumar, Pramod Ku...		<1%

11	Publication	Hao-Jun Mo, Yong Shen, Bao-Hui Ye. "Selective Recognition of Cyanide Anion via F... <1%
12	Publication	Sushil Kumar, Nidhi Goswami, Sudhanshu Naithani, Jimmy Mangalam, Tapas Gos... <1%
13	Publication	Chanchal Bhaumik, Shyamal Das, Debasish Saha, Supriya Dutta, Sujoy Baitalik. "S... <1%
14	Internet	www.frontiersin.org <1%
15	Publication	Sowmiya Ganesan, Angappan Sheela. "Ruthenium and platinum-based anticance... <1%
16	Publication	Pooja Sharma, Sudhanshu Naithani, Vikas Yadav, Sangeeta, Biswajit Guchhait, Su... <1%
17	Student papers	Curtin University of Technology <1%
18	Publication	Jolly Kaushal, Sain Singh, Heena, Saakshi Saini, Partha Roy. " An easily synthesiza... <1%
19	Publication	Ankita Roy, Mahasweta Nandi, Partha Roy. "Dual chemosensors for metal ions: A ... <1%
20	Publication	Gabr, Moustafa Tarek. "Tetraarylethylene-Based Probes for Biosensing Applicatio... <1%
21	Internet	www.db-thueringen.de <1%
22	Student papers	Indian Institute of Technology, Kharagpure <1%
23	Publication	Ying Zhou, Jun Feng Zhang, Juyoung Yoon. "Fluorescence and Colorimetric Chem... <1%
24	Internet	libweb.kpfu.ru <1%

25 Publication
Ankita Roy, Uday Shee, Abhishek Mukherjee, Sushil Kumar Mandal, Partha Roy. " ... <1%

26 Publication
Lecture Notes in Chemistry, 2016. <1%

27 Internet
www.science.gov <1%

28 Publication
Chanchal Bhaumik, Debasish Saha, Shyamal Das, Sujoy Baitalik. "Synthesis, Struct... <1%

29 Publication
Debasish Saha, Shyamal Das, Chanchal Bhaumik, Supriya Dutta, Sujoy Baitalik. " ... <1%

30 Publication
Cheng, Zehua. "Fluorescent Detection of Pesticide Residues and Heavy Metal Ions... <1%

31 Internet
core.ac.uk <1%

32 Internet
ebin.pub <1%

33 Internet
hdl.handle.net <1%

34 Student papers
National Institute Of Technology, Tiruchirappalli <1%

35 Publication
Ajeet Kumar, Satish Kumar. "Light-controlled receptors for environmentally and ... <1%

36 Publication
Aryadeep Roychoudhury. "Biology and Biotechnology of Environmental Stress Tol... <1%

37 Publication
Charles Immanuel David, Hyung-il Lee. "Cutting-edge advances in colorimetric an... <1%

38 Publication
Duraisamy Udhayakumari. "Mechanistic Innovations in Fluorescent Chemosenso... <1%

39 Student papers

University of KwaZulu-Natal <1%

40 Internet

idr.nitk.ac.in <1%

41 Publication

A. Afrin, P. Chinna Ayya Swamy. "Novel Schiff base derivatives for the detection o... <1%

42 Publication

Abha Sharma. "Small Organic Molecules-Based Fluorescent Biosensors and their ... <1%

43 Publication

Duraisamy Udhayakumari. "Detection of toxic fluoride ion via chromogenic and fl... <1%

44 Publication

Montgomery, Charlotte Loraine. "Mechanistic and Kinetic Evaluation of Cobalt Hy... <1%

45 Publication

Nidhi Goswami, Sudhanshu Naithani, Jimmy Mangalam, Tapas Goswami, Ritesh D... <1%

46 Student papers

Savitribai Phule Pune University <1%

47 Student papers

University of Sheffield <1%

48 Publication

Yuming Yang, Qiang Zhao, Wei Feng, Fuyou Li. "Luminescent Chemodosimeters f... <1%